Yong-Gang Li *Editor*

Earthquake and Disaster Risk: Decade Retrospective of the Wenchuan Earthquake

Higher Education Press

Springer

Earthquake and Disaster Risk: Decade Retrospective of the Wenchuan Earthquake

Yong-Gang Li
Editor

Earthquake and Disaster Risk: Decade Retrospective of the Wenchuan Earthquake

Higher Education Press

Springer

Editor
Yong-Gang Li
Department of Earth Sciences
University of Southern California
Los Angeles, CA, USA

ISBN 978-981-13-8014-3 ISBN 978-981-13-8015-0 (eBook)
https://doi.org/10.1007/978-981-13-8015-0

Jointly published with Higher Education Press, Beijing, China
The print edition is not for sale in China Mainland. Customers from China Mainland please order the print book from: Higher Education Press.
ISBN of the China Mainland edition: 978-7-04-051729-3

This Springer imprint is published by the registered company Springer Nature Singapore Pte Ltd.
The registered company address is: 152 Beach Road, #21-01/04 Gateway East, Singapore 189721, Singapore

Preface

This book is a monograph of the earth science specializing in observational, computational, and applied seismology and geophysics. The contents of this book mainly come out of the International Conference for the Decade Memory of the Wenchuan Earthquake held in Chengdu, China, on May 12–14, 2018. The 2018 *M*8 Wenchuan earthquake in Sichuan, China, highlighted the importance for an international discussion on the seismology, geology, and geodynamics of large earthquakes, their predictability and risk, and how to make full use of the present knowledge and techniques to reduce earthquake disasters. Authors from China Earthquake Administration and top universities and institutions in earthquake sciences in China and USA present and review principles, methods, and techniques for characterization of the Wenchuan earthquake. This book includes articles full of perceptive insights into the 2008 Wenchuan earthquake with cross-disciplinary and multiple thematic aspects in modern seismological, geophysical, geological, and stochastic methodology and technology. The new disciplines are illuminated by case study for readers to better understand the occurrence, dynamics, likelihood of earthquakes. This book covers: (1) a review of rupture process of the 2008 Wenchuan earthquake; (2) the methods used for fast inversion of the earthquake rupture process with applications to emergency response; (3) the Wenchuan earthquake fault scientific drilling project; (4) coordinated distributed experiments applied to earthquake forecast test sites; (5) annual earthquake potential consultation with a real forward prediction test in China; (6) structural relationship between the 2008 *M*8 Wenchuan and 2013 *M*7 Lushan earthquakes viewed by fault zone trapped waves; (7) analyzing earthquake events in the vicinity of Wenchuan using ETAS models; (8) full-3D seismic tomography for near-surface seismic structure; (9) self-correcting estimate of earthquake death toll. The Editor approaches this as a broad interdisciplinary effort, with well-balanced reviewing, policy-making, and research reporting aspects. Linked with these topics, the book highlights the importance for characterizing the Wenchuan earthquake rupture process, fault zone structure, earthquake hazards, and forecast in Western China. These contents make this book a must-read for researchers in the field of earthquake physics and prediction.

This book covers multidisciplinary topics, allowing readers to grasp the various methods and skills used in data processing, analysis, and numerical modeling for structural, geological, physical, and mechanical interpretation of geophysical and tectonic problems and earthquake phenomena.

Los Angeles, USA Yong-Gang Li
January 2019

Overview

The International Conference for a Decade Memory of the Wenchuan Earthquake with the 4th International Conference on Continental Earthquakes (ICCE) and the 12th General Assembly of the Asian Seismological Commission (ASC), organized by China Earthquake Administration (CEA) in collaboration with several national and international organizations and projects (IASPEI, UNISDR, IAEE, ISC, ASC, ACES, NSFC, etc.), was held on May 12–14, 2018 in Chengdu, China. The keynote presentations in this conference reviewed "the advancement of seismic risk mitigation in China since 2008, highlighting earthquake monitoring and prediction, earthquake emergency management. Behind these developments, legislation guided and supported by governance of society, science, and technology has been the principal dynamo, and international/regional collaboration played an important role." Mentioned by Administer of CEA G. G. Zheng (2018). The conference focused on the exchange and cooperation in earthquake science and technology for earthquake disaster risk reduction, earthquake emergency response, and post-earthquake rescue, relief, and recovery. Scientists, researchers, and managers of governmental offices from multiple countries participated in this conference to exchange their work and expertise in seismology, geodesy, geodynamics, and big data assimilation as well as the international/regional collaboration in science and governance of earthquakes disaster mitigation and preparedness. For instance, new ideas about earthquakes that have been learned at the Southern Earthquake Center (SCEC) and will be headed next were introduced by Director of SCEC J. E. Vidale (2018) in his keynote speech at the opening ceremony of the conference: "SCEC is allowing more apt emergency preparations and building and retrofitting laws and in the process giving us a deeper understanding of the physics of earthquakes and the geological evolution of the Southern California natural laboratory."

Ten years had passed since the 2018 *M*8 Wenchuan earthquake. A decade review of that disastrous event remained worth for further understanding the seismogeneises, preparation, and occurrence of continental earthquakes. The retrospective analyses of this great earthquake would help scientists and governmental agencies for more effectively reducing the risk of disasters through exchange of information and international cooperation in research and mitigation measurements

of the future global earthquakes. As one of outcomes from this international conference, a special book titled *Earthquake and Disaster Risk: Decade Retrospective of the Wenchuan Earthquake* was scheduled by conference organizers for publication to aim at sharing the results of this conference with diverse communities. While this book mainly contains the works presented in the International Conference for a Decade Memory of the Wenchuan Earthquake, it also includes relevant study of continental earthquakes using the state-of-the-art methods and technology, especially in the study of the predictability of major to great continental earthquakes.

The subject of this book is for a decade retrospective of the 2018 Wenchuan earthquake to foster the international and regional collaboration in earthquake research and disaster mitigation. This book introduces multi-disciplinary topics in observational, computational, and applied geophysics in a wide spectrum of solid earth system. Authors of nine chapters describe various disciplines, methods, and techniques in earthquake science through their investigation of Wenchuan earthquake and other significant global earthquakes. The book includes:

Chapter 1: "Inversion of the Earthquake Rupture Process: Methods, Case Studies and Applications to Emergency Response" by Yun-Tai Chen, Li-sheng Xu, Yong Zhang, and Xu Zhang.

In this chapter, authors briefly review the methods developed by themselves and illustrate their applications in three representative examples (i.e., the 2008 M_W7.9 Wenchuan earthquake, the 2010 M_W6.9 Yushu earthquake, and the 2016 M_W7.8 Kaikoura in New Zealand), for which the earthquake rupture processes were processed and were reported to the state authorities and released to the public immediately for the rapid emergency response. The methods for the inversion of earthquake rupture process are involved with moment tensor inversion, source time function retrieval, rupture process inversion either based on the apparent source time functions (ASTFs) or on the waveform data with fixed focal mechanism and that with changeable rakes based on the waveform data. The inverted results exhibit that the 2008 M_W7.9 Wenchuan earthquake occurred on the NE-striking Longmen Shan Fault (LF) which is the boundary of the Tibetan Plateau and the Sichuan Basin. The 350-km-long northeastern segment of the LF ruptured in this earthquake having seismic moment of about 9.4×10^{20} Nm released on the overall rupture area of approximately 350 km $\times$ 50 km and resulting the average stress drop of $\sim$18 MPa and the maximum stress drop of $\sim$65 MPa. Four major slip-concentrated patches or asperities on the fault plane are resolved in rupture process inversion, including two of them with slips up to 6.7–8.9 m, just beneath two meizoseismal areas of intensity I_0 = IX between Yingxiu-Dujiangyan and Wenchuan and the area around Beichuan, respectively.

The rupture process inversions for the 2010 M_W6.9 Yushu earthquake occurred on the Garze-Yushu Fault and the 2016 M_W7.8 Kaikoura, New Zealand, earthquake occurred on the Marlborough Fault System also resolve multiple slip patches involved in these two major earthquakes. The authors of this chapter have collected the data immediately after over 70 significant earthquakes occurred across the world

since 2009, conducted inversion process, and reported the results to the authorities to serve for the earthquake emergency response.

Chapter 2: "Rupture Process of the 2008 Wenchuan, China, Earthquake: A Review" by Thorne Lay.

The author of this chapter provides a profound review to summarize much of the intervening advance in understanding of the mainshock rupture process of the Wenchuan earthquake since this *M*7.9 earthquake occurred on May 12, 2008. This review updates and extends prior reviews of the earthquake by Zhang et al. (2010) and Yin (2010), therefore, can stand as a vast national undertaking in China, with the societal impact motivating the development of comprehensive understanding of the earthquake rupture process that is highlighted here. First, the author reviews field mapping work done on extensive surface ruptures and landslides occurred during the 2008 Wenchuan earthquake, which provides important constraints on the fault geometry and overall rupture process. Then, thorough investigations on focal mechanisms and aftershock distribution, back projection and surface wave finiteness constraints, strong motions observations, teleseismic inversions with either 1D or 3D Green's functions as well as geodetic constraints are reviewed in this chapter.

Based on GPS and InSAR displacements and rupture models, the most comprehensive representations of the faulting process are obtained by joint inversions of the seismic and geodetic data. Triggering interactions and stress transfer before and after the mainshock are also reviewed in this chapter. The detailed slip during dynamic rupture in the 2008 Wenchuan mainshock has been quite well resolved now. The event ruptured multiple faults with a mix of thrust- and right-lateral strike-slip faulting along the northeast-trending Longmen Shan thrust belt, with an overall oblique compressional deformation. The patchy distribution of large slip in the multi-segment Beichuan fault being constrained by field, seismological and geodetic observations (refer to extensive references in this chapter) that are relatively well reconciled by the more recent joint inversion analyses. The large-slip patches are less than 10 km deep, but slip extends deeper in the southwestern region and the fault appears to have listric extension into a mid-crustal décollement with shallow dip below 20 km depth.

The 2008 Wenchuan rupture clearly involved dynamic triggering of multiple fault segments representing a complex fault zone failure. Triggering interactions and stress transfer before and after the mainshock are also reviewed in this chapter. Some arguments were raised after occurrence of the 2008 Wenchuan earthquake; such as "Was this event triggered by the Zipingpu Reservoir?" and "If did this big event trig the nearby earthquakes, including the 2013 *M*7 Lushan earthquake?" are discussed here. There are still remaining questions about the Pengguan fault slip magnitude and geometry, and the down-dip extension of the crustal faults into a possible mid-crustal décollement. Because the recurrence interval estimate for the 2008 rupture is not really any clearer, than it was in 2010; definitive characterization of past events is very challenging due to the rough topography and near-surface faulting complexity along the zone. Large-scale issues of deep crustal

inflation versus brittle faulting uplift also remain unresolved. Finally, a comparison of rupture parameters with global subduction zone thrusts is shown in this chapter.

Chapter 3: "The Wenchuan Earthquake Fault Scientific Drilling (WFSD) Project" by Zhiqin Xu and Haibing Li.

The Wenchuan earthquake fault scientific drilling project (WFSD) is the first scientific drilling project for great earthquakes in mainland China and the world's fastest scientific drilling for great earthquakes. Authors of this chapter introduce the details of this abstractive project that consists of drilling, logging, monitoring, coring, and research on the Longman Shan fault which ruptured in the 2008 Wenchuan *M*8 earthquake. The project started drilling in Dujiangyan on November 7, 2008, and completed on June 30, 2014, spending a total of 6 years. A total of 425 scientists, researchers, and engineers from more than fifty domestic and international organizations, including many famous institutions, universities, and drilling companies, participated in this project. The purpose of the Wenchuan earthquake fault scientific drilling project is to explore the key scientific problems arising from the Wenchuan earthquake. The project directly samples the source areas of great earthquakes and microseisms and conducts multidisciplinary research on geological structures, seismic geology, rock mechanics, chemical physics, seismic physics, fluid interactions, and rheology using a series of advanced observation and analysis methods, to reveal the physical and chemical effects which control faulting and earthquakes and provide basic data for future monitoring, prediction, or early warning of earthquakes.

In the WFSD project, six boreholes with a total depth of about 9 km were drilled on the hanging wall of the Longmen Shan earthquake rupture zone to measure the fluid, stress, permeability, temperature, friction, and seismic wave velocity for establishing a series of logging, fluid, and geostress profiles to illustrate lithological, structural, and physicochemical properties of earthquake faults. These data are significance to reveal the relationship between large sliding distance with slip velocity and fracture friction, to study the relationship between temperature change and friction coefficient, to remodel the process of rupture evolution, and to understand the seismic energy state of the seismic fault zone, the period of earthquake healing and the constraints of the physicochemical behavior of the fault zone on the mechanism of earthquake occurrence. The project has achieved many important research progresses, especially the breakthrough in the study of the seismogenetic mechanism. These achievements include: (1) Graphite in the fault zone can be used to assess the occurrence of great earthquakes. (2) The lowest fault frictional coefficient in the world has been determined. (3) The rapid healing information of the fault zone after the great earthquake was recorded first time. However, the realization of the goal of scientific drilling requires the geoscientists to continue to strive for progress and breakthrough in the future. Such as combined with geological survey of the surface rupture area of the Longmen Shan fault zone, borehole data of the Wenchuan earthquake fault zone, and deep seismic reflection profiles, the tectonic framework of the Longmen Shan was reshaped and a new orogenic model was proposed.

Chapter 4: "Coordinated Distributed Experiments (CDEs) Applied to Earthquake Forecast Test Sites" by Zhongliang Wu, Yan Zhang and Jiawei Li.

Authors of this chapter discuss coordinated distributed experiments (CDEs) in connection with the top-level design of the China Seismic Experiment Site (CSES) project. Indeed in the history of earthquake forecast experiments, for most of the test sites, the "target earthquake" occurred either out of the range of the test area (such as the 1996 Lijiang earthquake which was just located out of the West-Yunnan Earthquake Prediction Experiment Site), or within the test area but after the test has formally closed (such as the 2004 Parkfield earthquake which happened long after the predicted earthquake although observational facilities were still functioning). It is because the duration of a funded project in earthquake science is usually much shorter than an earthquake cycle. Another problem met in earthquake science is that the "samples" are not sufficient. Therefore, there are many controlling parameters to be considered in the test of the hypotheses. To tackle these problems, the concept CDEs used in ecology and environmental science was proposed as an operational tool for hypothesis testing in earthquake science although the forms would be different. The CDEs for earthquake science need not only one or two but also several test sites with different tectonic settings. The Collaboratory for the Study of Earthquake Predictability (CSEP) carried by Southern California Earthquake Center (SCEC) is one of the significant advancements in implementing the field experiments in several testing areas selected with standardized data format and testing criteria. The first phase of the CSEP (2007–2018) was mainly concentrating on the "homogeneous" models of seismicity and deformation with emphases on statistical seismology, and it is now to take more account for the tectonic settings and earthquake rupture processes. For a certain segment of active fault or tectonic block boundary zone which would accommodate future earthquakes, an "earthquake rupture scenario" plays the role of the "coordination" and provides different versions of earthquake preparation models, taking guidelines from which the detection programs and monitoring systems are designed for consensus-based experiments.

Accordingly, at the opening ceremony of the International Conference for the Decade Memory of the Wenchuan Earthquake with the ICCE, it was officially announced that the China Seismic Experiment Site (CSES) be established in the Sichuan–Yunnan region. This natural laboratory, as a continuation and expansion of the West-Yunnan Earthquake Prediction Experiment Site since 1980 and the National Experiment Site for Earthquake Monitoring and Forecast since 2014, aims to make use of the cutting edge science and technology to deepen the understandings of the preparation and occurrence of continental earthquakes and the cause of seismic disasters. The establishment of the CSES is now underway. According to the Chinese earthquake catalog since 1965, there were in average 14 earthquakes with $M_S \geq 6.0$, among which 3 with $M_S \geq 7.0$ for every decade in this region, which provides the planning of the experiment with a statistical background.

Chapter 5: "Annual Earthquake Potential Consultation: A Real Forward Prediction Test in China" by Yongxian Zhang, Zhongliang Wu, Xiaotao Zhang, and Gang Li.

In this chapter, authors briefly review the annual consultation on the likelihood of earthquakes in continental China since 1970s. The National Annual Consultation (NAC) is one of the contributions of Chinese seismological community to the test of earthquake forecast schemes. In the perspective of statistical seismology, the long-term persistence, real forward forecast test, and combination of the information of different disciplines make this approach unique among the endeavors studying the predictability of earthquakes. This chapter summarizes the 40-year practice of NAC from 1970s to the present, its scientific outputs, methodology used for analysis, in-depth philosophy guiding the consultation, and proposed developments and improvements in the future. In early December of every year, the NAC is held in Beijing in which more than hundred delegates including scientists and leaders from provincial earthquake administrations, Institutions and Bureau Offices of China Earthquake Administration (CEA) together with invited scientists from universities participate. Through wide discussions at the meeting, it is very helpful to raise new ideas as well as the scientific problems in earthquake prediction to be studied further.

In the comprehensive analysis which combines the information from different disciplines, seismologists prefer the combination of quantitative calculation and qualitative experience. Some of the calculation tools, such as fuzzy logic, pattern recognition, artificial neural networks, and expert system, are used for learning and predicting. In order to evaluate the prediction ability of the annual consultation quantitatively, the R score test based on the statistics of alarm-based forecast prediction has been proposed. When all the predictions are successful, $R = 1$; when all the predictions are wrong, $R = -1$; for random prediction, $R = 0$. The highest R score is 0.73 in 2003, and the lowest R score is –0.08 in 2006. The test results of the annual consultation by R score for 27 years show that overall medium-term earthquake prediction is feasible even under limited monitoring ability and incomplete knowledge. The summary research reports on the national key earthquake potential areas in 2013 and 2014 were taken as two successful case studies. On the other hand, the failure forecast for Wenchuan $M8$ earthquake was simply reviewed in this chapter.

Chapter 6: "Structural Relationship Between the 2008 $M8$ Wenchuan and 2013 $M7$ Lushan Earthquakes Viewed by Fault-Zone Trapped Waves" by Yong-Gang Li, Jin-Rong Su, Tian-Chang Chen and Peng Wu.

Authors of this chapter use fault zone trapped waves (FZTWs) to evaluate fault connectivity and segmentation along the southern Longmen Shan Fault (LMSF) system, on which the $M8$ Wenchuan earthquake occurred in 2018 and the $M7$ Lushan earthquake occurred in 2013 for understanding fault evolution and earthquake potential in Sichuan, China. Because FZTWs arise from constructive interference of reflected waves at boundaries between the low-velocity fault zone and high-velocity surrounding rocks, the amplitude and dispersion of FZTWs are sensitive to the geometry and physical property of the fault zone as well as the

source location relative to the fault zone. There was no surface rupture found after the 2013 Lushan earthquake so that this event could not be obviously associated with any identified surficial geological faults in the epicentral area. Observations and 3D finite-difference simulations of FZTWs generated by Lushan aftershocks and recorded at particular stations in Lushn area help us distinguish the seismogenic fault of Lushan earthquake among multiple imbricated thrust faults in the complicated fold-faulting region. Furthermore, the FZTWs generated by Lushan aftershocks were also recorded at stations located within rupture zones of the 2018 *M*8 Wenchuan earthquake, and vice versa the FZTWs generated by Wenchuan aftershocks were recorded at stations close to the seismogenic fault of Lushan earthquake even though there is an ∼45-km-long "seismic gap" between two epicentral zones of the 2018 Wenchuan and 2013 Lushan earthquakes. These observations of FZTWs show the continuity of a low-velocity waveguide extending along the southern LMSF although the rock damage magnitude (inferred by the waveguide trapping effect) varies along multiple fault segments with the greater rock damage magnitude within rupture zones of Wenchuan and Lushan earthquakes than that within the un-ruptured fault in "seismic gap." FZTWs help us to obtain a better understanding of the structural relationship between the Lushan and Wenchuan events. From structural viewpoint, we consider the 2008 event and the 2013 event as being an earthquake sequence along the southern LMSF system, in favor that the 2013 Lushan *M*7 earthquake is a largest aftershock of the 2018 Wenchuan *M*8 earthquake.

Because the 2013 *M*7 Lushan earthquake only ruptured a small fault segment, increased seismic hazards in its adjacent regions, particularly in the "seismic gap," should be noticeable. Our investigation infers that the connectivity of the seismogenic faults of the Wenchuan and Lushan events may increase to a state where combined ruptures of them are a possibility for even a larger earthquake.

Chapter 7: "Analyzing Earthquake Events in the Vicinity of Wenchuan Using ETAS Models" by Annie Chu.

In this chapter, the author applies the spatial–temporal Epidemic-Type Aftershock Sequence (ETAS) model to regional seismicity of surrounding Wenchuan, China. The Preliminary Determination of Epicenters (PDE) data in a rectangular space window including the Wenchuan earthquake on May 12, 2008 (its epicenter located at 31.021°N, 103.367°E) approximately at the center of the rectangle are used in this study. The ETAS model is a type of Hawkes point process model and is also known as branching or self-exciting point process. The model used for data analysis in this chapter is the spatial–temporal ETAS model. The author implements a homogeneous model and four inhomogeneous models and compares them in model diagnostics and predicted intensity rate based on maximum likelihood estimates (MLEs), with calculation details provided and emphasized. By estimation of inhomogeneous background rate with ETAS model, the inhomogeneous model fits better than the other four models. The homogeneous model lacks adequacy to explain the seismic data of Wenchuan region while models with numerous background rate parameters like and are not optimal due to over-fitting the catalog of 2009 events. Since ETAS parameter MLEs help build

predicted intensity rate, it is possible to visualize the region and sub-regions' intensity rates. The author has found that the seismic activity of Wenchuan vicinity changes over the 45 years from 1973 to 2017. The seismicity appeared noticeably different in scatter plots and MLEs using the ETAS model with its background rates, triggering parameters, and predicted intensity rate. Additionally, foreshocks and aftershock pattern may be noticeably different as observed from the events of Wenchuan, Lushan, Ludian, and Jiuzhaigou earthquakes in Sichuan and earthquakes in Southern California. However, the incompleteness of data is an important factor to consider.

Finally, the author raises some interesting questions in the future work, such as the effects of grid pattern using irregular polygons and different time window intervals applied to the same region in catalogue data analysis, the negotiation between time consumption and stability in computation of model parameters, the seismicity quiescence along the Longmenshan fault before the 2008 *M*8 Wenchuan earthquake, and the possibility of improvement by using the event with magnitudes <4.0 in the PDF catalog.

Chapter 8: "Full-3D Seismic Tomography for Structure of the Critical Zone" by Wei Wang, Po Chen, En-Jui Lee, and Dawei Mu.

Recent advances in full-3D seismic tomography (F3DT), in which the starting model and the inverted model perturbations are 3D in space and the sensitivity (Fréchet) kernels are computed using purely numerical solutions of 3D (visco) elastodynamic equations, have opened up new possibilities for imaging the structures of the near surface, in which mechanical properties of materials play important roles in various geotechnical engineering applications. In this study, authors have successfully applied F3DT to image the near-surface structure under a granitic ridge in the Blair Wallis watershed, southeastern Wyoming. The seismic data used in our tomography consist of both 2D active-source seismic refraction data and 3D ambient-noise Green's functions obtained from a minimally invasive, "large-N" seismic survey using a square array of 400 autonomous geophones. Lateral variations of our 3D velocity model show strong correlations with surface topography. Depth variations of our velocity model may give clues about the depth interval within which chemical weathering plays a significant role. With the calibration of borehole casing depths and saprolite refusal depths, our F3DT technique can be a highly effective tool for investigating the structure of the near surface.

Chapter 9: "Self-correcting Estimate of Earthquake Death Toll Based on Field Reports: The April 25, 2015, Nepal, Earthquake" by Tengfei Ma, Zhongliang Wu, and Yingchun Li.

Uncertainty in the estimate of earthquake death toll is determined by many complicated factors. As a result, the modification of the estimate seems to be an inevitable stage for almost all the agencies providing information for earthquake emergency and rescue actions. Authors of this chapter demonstrate such uncertainty, and the resulted difficulty of the modification met in the case of the April 25, 2015, *M*7.8 Nepal earthquake. In order to overcome this difficulty, they adopted a "self-correcting" method for the estimation of earthquake death toll and kept updating such estimate. The method is based on a simple model of the temporal

variation of found deaths. The input data for the deaths found in the field come from news reports which have the limit dependent on the infrastructure of communication and the openness of the society. In this sense, the "dynamic" approach is to be used as a complement rather than a substitute for other "static" approaches. After the Nepal earthquake, news media collected and reported the deaths found by the rescue teams from a variety of resources. The estimate of the Prompt Assessment of Global Earthquakes for Response (PAGER) system of US Geological Survey (USGS) issued about 9 days after the earthquake was probably 1,000 to 10,000 fatalities in total. In the same day, news reports gave that the found deaths accounted 7000. The authors used their self-correction estimate method to fit the data and gave the estimate that the final death toll would be around 7750 ± 198, comparable for the news media reported deaths of 7365 at the date 9.5 days after the earthquake. The rescue efficiency coefficient, reflecting the efficiency of the rescue practice, is 0.29, falling into the empirical relation from previous earthquakes. Saving life is the most critical concern of earthquake emergency and rescue. A dynamic correct estimate of the earthquake fatalities helps much to manage, operate, and deploy and adjust the task forces, facilities, and supplies for rescue and relief actions after a devastating earthquake.

This book is a monograph of the earth science specializing in observational, computational, and applied seismology and geophysics. The contents of this book mainly come out of the International Conference for the Decade Memory of the Wenchuan Earthquake held in Chengdu, China, on May 12–14, 2018. The 2018 $M8$ Wenchuan earthquake in Sichuan, China, highlighted the importance for an international discussion on the seismology, geology, and geodynamics of large earthquakes, their predictability and risk, and how to make full use of the present knowledge and techniques to reduce earthquake disasters. Authors from China Earthquake Administration and top universities and institutions in earthquake sciences in China and USA present and review principles, methods, and techniques for characterization of the Wenchuan earthquake. This book includes articles full of perceptive insights into the 2008 Wenchuan earthquake with cross-disciplinary and multiple thematic aspects in modern seismological, geophysical, geological, and stochastic methodology and technology. The new disciplines are illuminated by case study for readers to better understand the occurrence, dynamics, likelihood of earthquakes. The book editor approaches this as a broad interdisciplinary effort, with well-balanced reviewing, policy-making, and research reporting aspects. Linked with these topics, the book highlights the importance for characterizing the Wenchuan earthquake rupture process, fault zone structure, earthquake hazards, and forecast in Western China. These contents make this book a must-read for researchers in study of Wenchuan earthquake physics and prediction. This book can also be taken as an expansion of previous four books in the series to allow readers to grasp the various methods and skills used in data processing, analysis, and numerical modeling for structural, geological, physical, and mechanical interpretation of geophysical and tectonic problems and earthquake phenomena.

The book editor wishes to thank Prof. Zhongliang Wu, Director of Institute of Earthquake Forecasting, China, Earthquake Administration and an organizer of the

International Conference for the Decade Memory of the Wenchuan Earthquake, for his support to foster this special book as one of products from the conference. Without his encouragement and consultancy, this special book will not come out. The book editor is grateful to Academicians Prof. Yun-Tai Chen, Prof. Thorne Lay, and Prof. Zhiqin Xu as well as other chapter authors and reviewers for their collaborations and contributions to this book. We also thank many organizations and individuals, including HEP Director Bingxiang Li and Editor Yan Guan, who help to make this book possible.

Yong-Gang Li

References

Vidale, J.E. 2018. Decade review and prospective of seismic risk reduction in China. In *International Conference for the Decade Memory of the Wenchuan Earthquake with 4th International Conference on Continental Earthquakes*, Conference Program, 18.

Yin, A. 2010. A special issue on the great 12 May 2008 Wenchuan earthquake (M_w7.9): Observations and unanswered questions. *Tectonophysics* 491: 1–9.

Zhang, P.-Z., X.-Z. Wen, Z.-K. Shen, and J.-h. Chen. 2010. Oblique, high-angle, listric-reverse faulting and associated development of strain: The Wenchuan earthquake of May 12, 2008, Sichuan, China. *Annual Reviews of Earth and Planetary Sciences* 38: 353–382.

Zheng, G.G. 2018. Decade review and prospective of seismic risk reduction in China. In *International Conference for the Decade Memory of the Wenchuan Earthquake with 4th International Conference on Continental Earthquakes*, Conference Program, 15.

Contents

Chapter 1
Inversion of the Earthquake Rupture Process: Methods, Case Studies and Applications to Emergency Response

Yun-Tai Chen, Li-sheng Xu, Yong Zhang and Xu Zhang

Abstract To understand the seismogenesis and the earthquake mechanism, and to find a way helping reduction of seismic disaster, in the last two and more decades, we have been devoting to the study of earthquake rupture process, developing new methods and applying the methods to earthquake case studies as well as earthquake emergency response. In this article, we briefly review the methods developed, present three representative examples to illustrate the methods and their applications and summarize the events for which the earthquake rupture processes were processed and were reported to the authorities and released to the public immediately for the rapid emergency response. In the three examples, the 2008 M_W7.9 Wenchuan earthquake, the 2010 M_W6.9 Yushu earthquake and the 2016 M_W7.8 Kaikoura, New Zealand, earthquake are included. The 2008 M_W7.9 Wenchuan earthquake ruptured an area 350 km $\times$ 50 km along the 470-km-long NE-SW striking Longmenshan Fault, released seismic moment of about 9.4 $\times$ 10^{20} Nm and resulted in the average stress drop of about 18 MPa and the maximum stress drop of about 65 MPa, respectively. There were two substantial concentrated-slip patches on the fault plane with slips of up to 8.9 and 6.7 m, just beneath the elongated area extending from Yingxiu-Dujiangyan to Wenchuan and the meizoseismal area near Beichuan, respectively. During the rupture process, irregular high rupture velocities of 3.6, 4.0, 4.4, 3.5 km/s in the four stages, respectively, were found. The spatiotemporal rupture process exhibited a complex asymmetric bilateral rupture, with overall direction of northeast azimuth. The 2010 M_W6.9 Yushu earthquake ruptured unilaterally and released the scalar seismic moment of about 2.7 $\times$ 10^{19} Nm, resulting in the average slip of about 0.6 m and the average stress drop of 15 MPa. The rupture process lasted about 16 s, including two clearly distinguishable sub-events. The first one was between 0 and 5 s, corresponding to the asperity with a maximum slip of 0.8 m. The

Y.-T. Chen (✉)
College of the Earth and Planetary Sciences, University of Chinese Academy of Sciences, Beijing 100049, China
e-mail: chenyt@cea-igp.ac.cn

Y.-T. Chen · Y. Zhang
School of the Earth and Space Sciences, Peking University, Beijing 100871, China

L. Xu · Y. Zhang · X. Zhang
Institute of Geophysics, China Earthquake Administration, Beijing 100081, China

Y.-G. Li (ed.), *Earthquake and Disaster Risk: Decade Retrospective of the Wenchuan Earthquake*, https://doi.org/10.1007/978-981-13-8015-0_1

second was between 5 and 16 s, corresponding to the asperity 17–54 km southeastern from the epicenter. The 2016 M_W7.8 Kaikoura earthquake had a very complex source process. It lasted for about 100 s, producing a rupture area about 160 km long along strike direction and about 50 km wide in down-dip direction and resulting in a release of scalar moment 1.01×10^{21} Nm. Spatially, the rupture area consisted of two asperities, with one close to the rupture initiation point having a maximal slip value of about 6.9 m while the other far away in north having a maximal slip value of about 9.3 m. Temporally, the first asperity slipped for about 65 s and the second initiated 40 s later and lasted for 40 s, with both of them slipping about 25 s simultaneously. As to focal mechanism, the first asperity had a nearly thrust slip while the second had both thrust and strike-slip components. The methods have been applied to over 70 significant earthquakes across the world for rapid emergency response since 2008. The applications show that the methods prove to be effective in the earthquake emergency response, and the results may be used to reduce the losses caused by the earthquakes.

Keywords Inversion · Earthquake rupture process · Case study · Rapid emergency response

1.1 Introduction

It is well known that as a natural phenomenon, the earthquake is a kind of manifestation of the active Earth, and its occurrence is inevitable. Up to date whether an earthquake is predictable remains in debate, but it has become a common recognition that the terrible impact of the earthquake disaster can and must be reduced.

In the last two and more decades, the present authors have been conducting two pieces of work. One is to keep improving the inversion methods to make the inversion efficiency higher, and the other is to apply the method to promote our understanding of earthquake phenomena and the rapid emergency response. Nowadays only around two hours are needed to accomplish an inversion process while three to five hours were required in 2010, and even five to eight hours for the same inversion process in 2009. From 2009 up to date, over 70 events have been processed. The importance of the results became apparent, especially in the emergency responses of the 2008 M_W7.9 (M_S8.0) Wenchuan, Sichuan, earthquake and the 2010 M_W6.9 Yushu, Qinghai, earthquake.

In the following sections, we will briefly present the methods used in the inversion of earthquake rupture process, introduce three representative examples of the application to real earthquakes in more details and summarize the events processed for the rapid emergency response.

1.2 Methods

1.2.1 Moment Tensor Inversion

Assuming that the earthquake source is at the origin of the coordinate system, as the linear dimension of the earthquake source is small compared to the wavelength of interest, the displacement at the field point $\boldsymbol{r}$ can be written as (Aki and Richards 2002)

$$u_i(\boldsymbol{r}, t) = G_{ij,k}(\boldsymbol{r}, t) * M_{jk}(t) \tag{1.1}$$

where the asterisk represents the convolution in the time domain, $u_i(\boldsymbol{r}, t)$ is the observed displacement, $M_{jk}(t)$ is the moment tensor function and $G_{ij,k}(\boldsymbol{r}, t)$ is the Green's function. Taking the Fourier transform, Eq. (1.1) in the frequency domain becomes

$$u_i(\boldsymbol{r}, \omega) = G_{ij,k}(\boldsymbol{r}, \omega) \cdot M_{jk}(\omega) \tag{1.2}$$

where ω is the angular frequency. The moment tensor functions are obtained by frequency-domain inversion.

1.2.2 Retrieval of the Source Time Function

In general, the recorded displacement generated by an earthquake with scalar seismic moment M_0 may be expressed as (Hartzell 1978; Mueller 1985)

$$u(t) = M_0 S(t) * P(t) * I(t) \tag{1.3}$$

where $S(t)$ is the normalized far-field source time function (STF) which is the time derivative of the normalized near-field STF, $P(t)$ is the impulse response of the transmitting path and $I(t)$ is the impulse response of the instrument. In the frequency domain, Eq. (1.3) becomes much simpler, *i.e.*,

$$u(\omega) = M_0 S(\omega) \cdot P(\omega) \cdot I(\omega) \tag{1.4}$$

By analogy with Eq. (1.4), we have a similar equation for a second earthquake:

$$u'(\omega) = M_0' S'(\omega) \cdot P'(\omega) \cdot I'(\omega) \tag{1.5}$$

where u', M', S', P' and I' are the respective quantities for this earthquake. For an earthquake with the identical hypocenter and focal mechanism as the first one,

recorded by the same instrument at the same site and small enough so that its far-field STF can be regarded as a Dirac δ-function in time, the seismogram of the smaller event is the impulse response of the transmitting path and instrument and can be regarded as an empirical Green's function (EGF) of the first event. The relationship between the displacements of these two earthquakes is

$$\frac{u(\omega)}{u'(\omega)} = \frac{M_0}{M_0'} S(\omega) \tag{1.6}$$

in the frequency domain, since $P(\omega) = P'(\omega)$, $I(\omega) = I'(\omega)$ and $S'(\omega) = 1$.

As Eq. (1.6) indicates, the STF of the larger earthquake is scaled by the ratio $M_0 \big/ M_0'$ of the scalar seismic moment of the larger earthquake (M_0) to that of the smaller earthquake (M_0') and is a relative STF. In some cases, there is no smaller event available to satisfy these requirements, and then synthetic seismograms have to be adopted. In the case of the synthetic seismograms are used to retrieve the STF of the larger earthquake, the ratio of the scalar seismic moments is simply the scalar seismic moment of the larger earthquake since the synthetic seismograms are calculated for unit seismic moment. The shortcoming of using a synthetic Green's function is that the retrieved STFs are affected by the inaccuracy of the synthetic Green's function. For this reason, EGFs are preferred.

The STFs of the larger earthquake used in the next step of this study are obtained by spectral division in the frequency domain (Xu and Chen 1996).

1.2.3 Construction of the Slip Distribution Based on the Apparent Source Time Functions (ASTFs)

If the final rupture area of an earthquake fault is A and the scalar seismic moment as a function of time is $M_0(t)$, the average slip as a function of time, $D(t)$, on the fault plane is

$$D(t) = \frac{M_0(t)}{\mu A}, \tag{1.7}$$

where μ is the rigidity of the material in the earthquake source region. For a finite earthquake fault, the slip is generally non-uniform and variable with time and space, and the rupture area is irregular in shape. In this case, the finite fault can be divided into numerous sub-faults, each of which can be regarded as a point source. The slip as a function of time, $D_j(t)$, of the j-th sub-fault is expressed as

$$D_j(t) = \frac{M_j(t)}{\mu A_j} \tag{1.8}$$

where $M_j(t)$ and A_j are the scalar seismic moment and the area of the j-th sub-fault, respectively. The far-field STF observed at the i-th station, $S_i(t)$, is the sum of the weighted far-field STF of the j-th sub-fault, $s_j(t)$,

$$S_i(t) = \sum_{j=1}^{J} w_j s_j\left(t - \tau_{ij}\right), \tag{1.9}$$

where J is the number of the sub-faults, τ_{ij} is the time delay associated with the wave propagation and w_j is a weight defined by the ratio of the scalar seismic moment of the j-th sub-fault, M_j, to the total scalar seismic moment, M_0,

$$w_j = \frac{M_j}{M_0} \tag{1.10}$$

Let $m_j(t)$ denotes the weighted far-field STF of the j-th sub-fault,

$$m_j(t) = w_j s_j(t) \tag{1.11}$$

The weight for each sub-fault is obtained by normalizing the weighted far-field STF of the sub-fault,

$$w_j = \int_0^\infty m_j(t)\, \mathrm{d}t \tag{1.12}$$

Equation (1.9) can be rewritten as

$$S_i(t) = \sum_{j=1}^{J} m_j\left(t - \tau_{ij}\right) \tag{1.13}$$

Hence, the time derivative of the slip as a function of time of the j-th sub-fault is determined by

$$\dot{D}_j(t) = \frac{\dot{M}_j(t)}{\mu A_j} = \frac{M_j s(t)}{\mu A_j} = \frac{M_0}{\mu A_j} m_j(t) \tag{1.14}$$

The STFs observed at different distances and/or different azimuths are identical if the linear dimension of a fault is small enough to be considered as a point source. However, the shapes of the STFs vary with azimuth for a finite fault. If a finite fault is considered as a combination of numerous sub-faults, as indicated by Eq. (1.13), the observed STF for the finite fault is the sum of all the weighted STFs of the sub-faults. Equation (1.13) can be rewritten as

$$S_i(t) = \sum_{j=1}^{J} \delta\left(t - \tau_{ij}\right) * m_j(t) \tag{1.15}$$

$$\tau_{ij} = \frac{r_j}{v_i} \tag{1.16}$$

where r_j is the distance between the j-th sub-fault and the reference point on the fault plane and v_i is the apparent velocity, which depends on the wave velocity and propagation direction and the location of the j-th sub-fault. In practice, we obtain this time delay by calculating the difference of theoretical travel times and the rupture time.

In matrix form, Eq. (1.15) can be written as

$$\mathbf{S} = \mathbf{KM} \tag{1.17}$$

where $\mathbf{S}$ is the data vector, consisting of the observed STFs, $\mathbf{M}$ is the unknowns vector made up of the weighted STFs of all the sub-faults and $\mathbf{K}$ is the coefficient matrix determined by the time delay associated with the wave propagation.

Usually, this problem is underdetermined since the number of the unknowns is larger than the number of observation equations and there is no constraint imposed on the STFs of sub-faults. In order to stabilize the solution, the following condition is imposed:

$$m_j(t) \geq 0 \tag{1.18}$$

which physically means that no backward slip occurs during the rupture process and is apparently a kinematic rather than dynamic constraint. This condition is very easy to apply if the conjugate gradient method is employed (e.g., Ward and Barrientos 1986). The conjugate gradient method is very helpful and powerful in solving underdetermined problems such as Eq. (1.17). This method has the advantages that it is unnecessary to find the inverse matrix and that any non-negative initial model can be usable.

1.2.4 Construction of the Slip Distribution Based on the Waveform Data

For a finite fault, the seismic waves recorded by the n-th station $u_n(\boldsymbol{x}, t)$ can be expressed as (Aki and Richards 2002; Zhang et al. 2012)

$$u_n(\boldsymbol{x}, t) = \sum_{k=1}^{K} M_{pq}\left(\boldsymbol{\xi}_k, t\right) * G_{np,q}\left(\boldsymbol{x}, t; \boldsymbol{\xi}_k, 0\right) \tag{1.19}$$

where $M_{pq}(\boldsymbol{\xi}_k, t)$ is the components of time- and space-dependent moment tensor, $G_{np,q}(\boldsymbol{x}, t; \boldsymbol{\xi}_k, 0)$ is Green's function, $\boldsymbol{\xi}_k$ is spatial coordinates of the k-th sub-fault. With the assumption that the spatial components and temporal components of moment tensor are mutually independent, the Eq. (1.19) could be rewritten as

$$u_n(\boldsymbol{x}, t) = \sum_{k=1}^{K} \left[M_{pq}(\boldsymbol{\xi}_k) \cdot s_k(t) \right] * G_{np,q}(\boldsymbol{x}, t; \boldsymbol{\xi}_k, 0) \tag{1.20}$$

where $M_{pq}(\boldsymbol{\xi}_k)$ is the spatial components of moment tensor and $s_k(t)$ is the temporal components of moment tensor (i.e., moment rate functions or source time functions of each sub-faults). If we only consider double-couple component of moment tensor, then $M_{pq}(\boldsymbol{\xi}_k)$ could be rewritten as (Aki and Richards 2002; Lay and Wallace 1995)

$$M_{pq}(\boldsymbol{\xi}_k) = M_0(\boldsymbol{\xi}_k)\left(e_p(\boldsymbol{\xi}_k)\nu_q(\boldsymbol{\xi}_k) + e_q(\boldsymbol{\xi}_k)\nu_p(\boldsymbol{\xi}_k)\right) \tag{1.21}$$

In Eq. (1.21), $M_{pq}(\boldsymbol{\xi}_k)$ is the equivalent scalar seismic moment of the k-th sub-fault, $e_p(\boldsymbol{\xi}_k)$ and $e_q(\boldsymbol{\xi}_k)$ are components of unit slip vector at k-th sub-fault, $\nu_p(\boldsymbol{\xi}_k)$ and $\nu_q(\boldsymbol{\xi}_k)$ are components of unit normal vector at k-th sub-fault. Combined with Eq. (1.21), then Eq. (1.20) could be rewritten as

$$u_n(\boldsymbol{x}, t) = \sum_{k=1}^{K} \hat{s}_k(t) * \left[\left(e_p(\boldsymbol{\xi}_k)\nu_q(\boldsymbol{\xi}_k) + e_q(\boldsymbol{\xi}_k)\nu_p(\boldsymbol{\xi}_k)\right) \cdot G_{np,q}(\boldsymbol{x}, t; \boldsymbol{\xi}_k, 0) \right] \tag{1.22}$$

by supposing

$$\hat{s}_k(t) = M_0(\boldsymbol{\xi}_k) s_k(t).$$

1.2.4.1 Case of the Unchangeable Focal Mechanisms

Given that all the sub-faults have the same focal mechanism, the slip vectors and normal vectors will be unchangeable for all the sub-faults. Then Eq. (1.22) may be rewritten as

$$u_n(\boldsymbol{x}, t) = \sum_{k=1}^{K} \hat{s}_k(t) * G_{nk}(\boldsymbol{x}, t) \tag{1.23}$$

Since

$$G_{nk}(\boldsymbol{x}, t) = \left(e_p \nu_q + e_q \nu_p\right) \cdot G_{np,q}(\boldsymbol{x}, t; \boldsymbol{\xi}_k, 0)$$

where the components of the slip vector e_p and e_q are constants for all the sub-faults, and the components of the unit normal vector ν_p and ν_q are also constants for all the sub-faults. In the matrix form, the above Eq. (1.23) can be written as

$$\mathbf{u} = \mathbf{G}\hat{\mathbf{s}} \tag{1.24}$$

where $\mathbf{u}$ is vector of observed data, $\mathbf{G}$ is matrix of Green's functions and $\hat{\mathbf{s}}$ is vector of unknowns, consisting of the moment rate functions of sub-faults.

1.2.4.2 Case of the Changeable Rakes

If the rake of each sub-fault is allowed to be changeable, one may always decompose the slip vector into two components perpendicular to each other in an orthogonal source Cartesian coordinate system (x, y, z), in which x and y indicate the two orthogonal slip directions on fault plane, and z, the normal direction of the fault plane. In this case, Eq. (1.22) can be rewritten as

$$u_n(\boldsymbol{x}, t) = \sum_{k=1}^{K} G_{knx,z}(\boldsymbol{x}, t) * s_{kx}(t) + G_{kny,z}(\boldsymbol{x}, t) * s_{ky}(t) \tag{1.25}$$

since $\nu_x = \nu_y = e_z = 0$ and $\nu_z = 1$, and $\hat{s}_{kx}(t) = e_x M_{k0} s_k(t)$ and $\hat{s}_{ky}(t) = e_y M_{k0} s_k(t)$. The corresponding matrix form of Eq. (1.25) is as the following

$$\mathbf{u} = \begin{pmatrix} \mathbf{G}_x & \mathbf{G}_y \end{pmatrix} \begin{pmatrix} \hat{\mathbf{s}}_x \\ \hat{\mathbf{s}}_y \end{pmatrix} \tag{1.26}$$

In order to mitigate the impact caused by the errors in observation and the Green's functions and to obtain physically acceptable solution, we introduce constraints such as the minimization of scalar seismic moment (Antolik and Dreger 2003; Hartzell and Heaton 1983; Zhang et al. 2012) and the smoothness in time and space (Yagi et al. 2004; Zhang et al. 2012). Taking into account these constraints, we may change Eqs. (1.24) and (1.26) into,

$$\begin{pmatrix} \mathbf{u} \\ \mathbf{0} \\ \mathbf{0} \\ \mathbf{0} \end{pmatrix} = \begin{pmatrix} \mathbf{G} \\ \lambda_1 \mathbf{T} \\ \lambda_2 \mathbf{D} \\ \lambda_3 \mathbf{Z} \end{pmatrix} \hat{\mathbf{s}} \tag{1.27}$$

and

$$\begin{pmatrix} \mathbf{u} \\ \mathbf{0} \\ \mathbf{0} \\ \mathbf{0} \end{pmatrix} = \begin{pmatrix} \begin{pmatrix} \mathbf{G}_x & \mathbf{G}_y \end{pmatrix} \\ \lambda_1 \begin{pmatrix} \mathbf{T} & \mathbf{0} \\ \mathbf{0} & \mathbf{T} \end{pmatrix} \\ \lambda_2 \begin{pmatrix} \mathbf{D} & \mathbf{0} \\ \mathbf{0} & \mathbf{D} \end{pmatrix} \\ \lambda_3 \begin{pmatrix} \mathbf{Z} & \mathbf{0} \\ \mathbf{0} & \mathbf{Z} \end{pmatrix} \end{pmatrix} \begin{pmatrix} \hat{\mathbf{s}}_x \\ \hat{\mathbf{s}}_y \end{pmatrix}, \tag{1.28}$$

respectively, where **T** is temporal smoothness matrix, **D** is spatial smoothness matrix and **Z** is the matrix of minimization of scalar seismic moment, and λ_1, λ_2 and λ_3 are the corresponding relative weights, respectively.

1.3 The 2008 M_W7.9 (M_S8.0) Wenchuan Earthquake

1.3.1 Tectonic Setting

The 2008 M_W7.9 (M_S8.0) Wenchuan earthquake occurred on the eastern margin of the Bayan Har Block of the eastern Tibetan Plateau. The NE-striking Longmen Shan Fault (LF) lies to the northeast of the SSE-moving Sichuan-Yunnan Block of southwest China (Fig. 1.1). Southwest China is a region characterized by a strong northeastward motion of the Indian Plate with respect to southwest China, by the westward subduction of the Pacific Plate under east China, and by the northwestward impact of the Philippine Sea Plate. As a result of the continental collision between the Indian and Eurasian Plates at about 40–42 mm/year at N20°E, and an eastward extrusion transfer of crustal material from underneath the Tibetan Plateau to South China Block; a predominantly thrust motion with a minor component of right-lateral motion at a rate of about 18–20 mm/year has been associated with NW-SE thrusting of southwest China with respect to South China Block along the NE-SW striking LF. The southeastward motion of South China Block at a rate of 12–14 mm/ayr incompletely accommodates the accumulation of stress due to the NW-SE thrusting of Bayan Har Block with respect to South China Block along the LF. Thus the LF is an active tectonic structure with the highest degree of vulnerability for earthquake ruptures.

Despite its active tectonic setting, historically the LF has experienced only moderate seismic activity. Frequently earthquakes of small to moderate size occur on or near it, but no earthquakes as large as magnitude 7 have been documented along this fault. Some earthquakes with magnitudes around 6 have occurred here historically (Fig. 1.1) including the April 21, 1657 Wenchuan earthquake (M6.5) (epicentral location: 31.3°N, 103.5°E), the February 8, 1958 Maowen-Beichuan earthquake (M_S6.2)

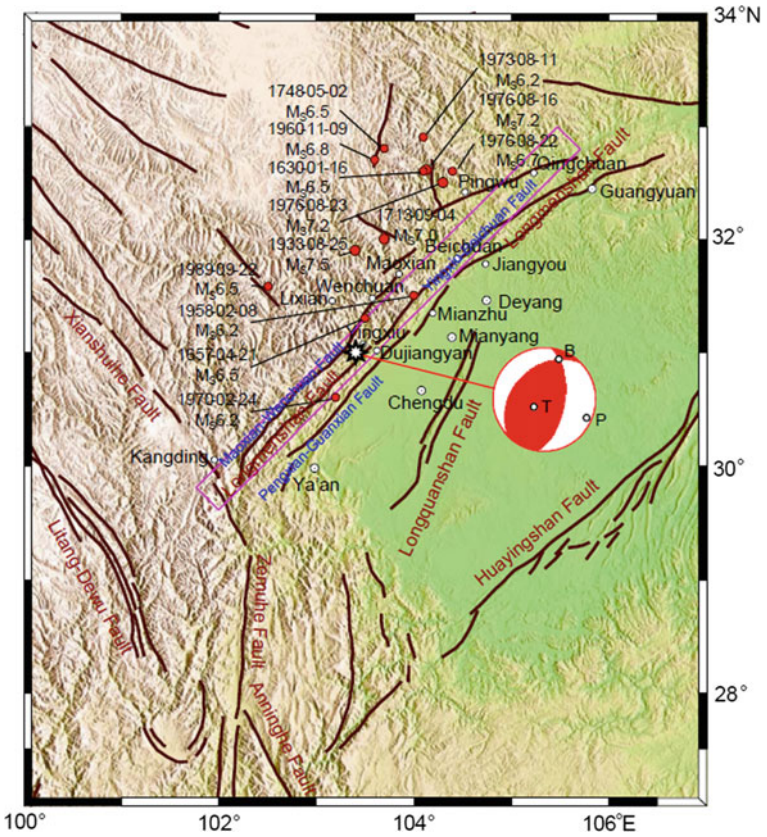

Fig. 1.1 Epicenter (white octagonal star) location of the 2008 M_W7.9 Wenchuan earthquake, main faults (modena lines) in epicentral area, historical earthquakes (red circles), and main cities (white circles) along Longmen Shan Fault (LF). "Beach-ball" represents the lower hemisphere projection of focal mechanism (NP1: strike 12°/dip 56°/rake 70°; NP2: strike 225°/dip 39°/rake 117°) of the Wenchuan earthquake

(epicentral location: 31.7°N, 104.3°E) which occurred to the northeast of the epicenter of the 2008 Wenchuan earthquake, and the February 24, 1970 Dayi earthquake (M_S6.2) (epicentral location: 30.65°N, 103.28°E, focal depth: 15 km) which occurred to the SSW of the epicenter of the 2008 Wenchuan earthquake. Based on the relocation of 10,057 earthquakes that occurred in central-western China from 1992 to 1999, Yang et al. (2003) noted that the LF is 470 km in length and about 2400 earthquakes with magnitudes between 1.0 and 5.0 occurred on or near the fault zone during this interval. Several magnitude 7 earthquakes have occurred nearby but outside the fault zone (Fig. 1.1), including the August 25, 1933, M_S7.5 Maowen-Diexi and the July 16, 1976 and July 23, 1976, M_S7.2 Songpan earthquakes.

About 89,000 people were confirmed killed or missing in the Wenchuan earthquake. Soon after the occurrence of the earthquake, we started to analyze available

seismic recordings and released the information on the earthquake source mechanism and rupture process to the authorities and public within 12 h for earthquake disaster emergency response.

After the emergency response task ended, we collected more teleseismic data from the globally distributed stations, and seriously selected and processed the data for the details of the rupture process of this event. Here, we exhibit them in the following.

1.3.2 Focal Mechanism and Aftershocks

Time-domain moment tensor inversion was used to obtain the focal mechanism of the Wenchuan earthquake. The results are that one of the nodal planes (NP2) has a strike of 225° with dip 39° and rake 117°, and the other (NP1) has a strike of 12° with dip 56° and rake 70°. The epicenters of aftershocks relocated by the double-difference earthquake location algorithm are located in a NE-SW trending zone about 320 km in length and 50 km in width which clearly coincides with the strike direction of the NP2 of the two nodal planes (Fig. 1.2).

Vertical cross-sections along the strike direction NE-SW and the direction perpendicular to the strike NW-SE (Fig. 1.2) of the projections of the relocated hypocenters also show that the aftershocks are clustered around this nodal plane. We identify the plane (NP2) striking 225° as the causative fault due to its agreement with the NE-SW trending hypocentral distribution of the aftershocks and the NE-SW strike, SE thrust of the LF. Overall, the 2008 Wenchuan mainshock rupture was a predominantly thrust event with a small right-lateral strike-slip component on a plane dipping 39° with a strike of 225° and rake 117°. Our solution NP2 (strike 225°/dip 39°/rake 117°) for the Wenchuan earthquake is very close to the moment tensor solution (strike 238°/dip 59°/rake 128°) obtained by USGS/NEIC and the Global Centroid Moment Tensor (GCMT) solution (strike 229°/dip 33°/rake 141°) obtained by GCMT Project. The scalar seismic moment M_0 we obtained is 9.4×10^{20} Nm, corresponding to a moment magnitude of $M_W 7.9$, and is in good agreement with that obtained by the USGS/NEIC ($M_0 = 7.5 \times 10^{20}$ Nm, $M_W = 7.8$) and GCMT Project ($M_0 = 9.4 \times 10^{20}$ Nm, $M_W = 7.9$).

1.3.3 Distribution of Static Slip

Figure 1.3 shows the static slip distribution on the fault plane. The slip vector represents the direction and amount of displacement of the hanging wall with respect to the footwall at each sub-fault. The Wenchuan earthquake has a slip distribution with predominantly thrust faulting and a small right-lateral strike-slip component. There are four major concentrated-slip patches on the fault plane. From the southwest to the northeast, the focal mechanisms varied in the order of oblique thrust and right-lateral strike-slip faulting of $M_W 7.3$ just underneath the southwestern most segment near

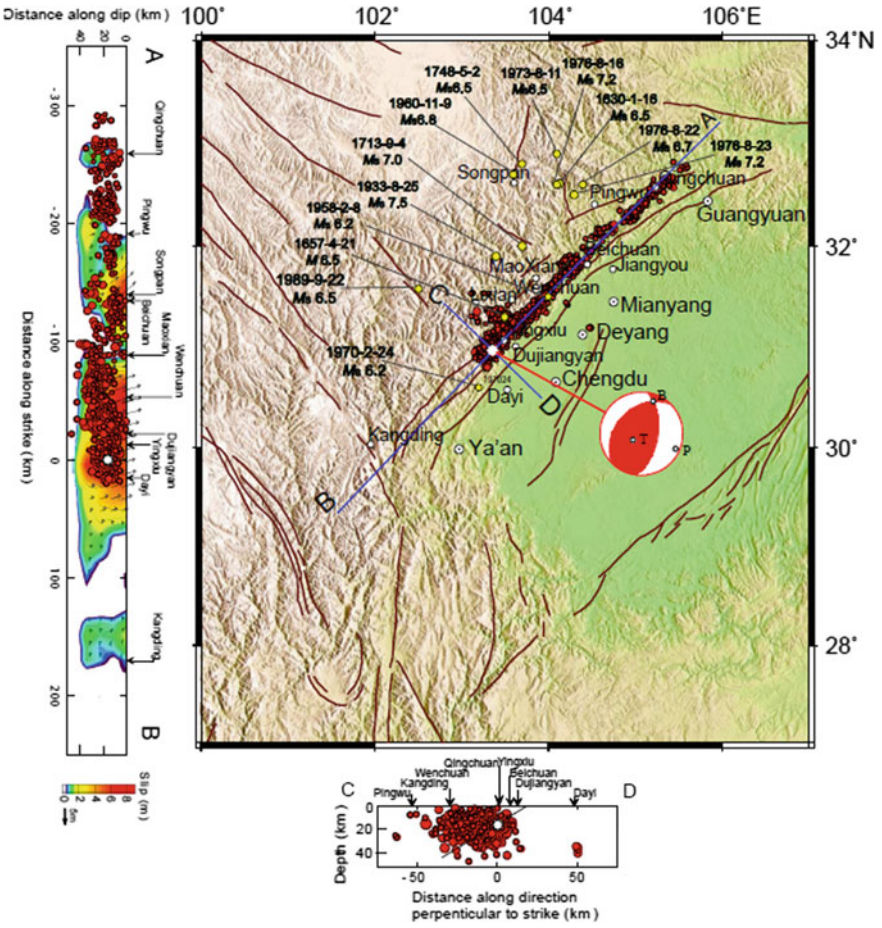

Fig. 1.2 Map showing topography and major faults (solid modena lines) in northeast Sichuan, the 2008 Wenchuan M_W7.9 earthquake epicenter (white octagonal star), the locations of relocated aftershocks (red dots), and locations of historical earthquakes (yellow dots) in and near the Longmen Shan Fault (LF) which consists of three nearly parallel NE-SW striking faults: From NW to SE, Maoxian-Wenchuan Fault (MWF), Yingxiu-Beichuan Fault (YBF) and Pengxian-Guanxian Fault (PGF). On the left, vertical cross-section A-B along the strike direction NE-SW shows that the aftershocks are clustered around the fault plane NP2 striking 225°, dipping 39° with a rake 117°. At the bottom, vertical cross-section C-D along the direction perpendicular to the strike direction NW-SE shows that the aftershocks are clustered around the LF which consists of three nearly parallel NE-SW striking faults: MWF, YBF and PGF

Kangding, predominant thrust with small right-lateral strike-slip faulting of M_W7.8 just underneath the elongated Yingxiu-Dujiangyan-Wenchuan area, oblique thrust and right-lateral strike-slip faulting of M_W7.5 just underneath the Beichuan area, and a predominantly right-lateral strike-slip faulting with minor normal faulting of M_W6.9 just underneath the Qingchuan area. The overall focal mechanism of the Wenchuan earthquake is similar to that of the second or largest concentrated-slip patch of M_W7.8 which is one of predominantly thrust faulting with a minor right-lateral strike-slip component and in good agreement with the general NE-SW strike of the LF. The overall focal mechanism of the Wenchuan earthquake is consistent with the tectonic setting of the generally NE-SW striking LF and is due to the NW-SE thrusting of Bayan Har Block with respect to South China Block.

The inversion shows that the Wenchuan earthquake ruptured an area 350 km in length by 50 km in width, of the 470-km-long NE-SW striking LF (Fig. 1.3). A seismic moment of about 9.4×10^{20} Nm was released in the Wenchuan earthquake, corresponding to a moment magnitude of M_W7.9. The average stress drop and the maximum stress drop in this earthquake are about 18 and 65 MPa, respectively, and are comparable with an intraplate earthquake with magnitude M_W8.0.

The two substantial concentrated-slip patches of M_W7.8 and M_W7.5 on the fault plane with slips of up to 8 and 6.7 m were just beneath the elongated area extending from Yingxiu-Dujiangyan to Wenchuan and the area near Beichuan, respectively (Fig. 1.3). These two patches breached the surface and were responsible for the tremendous destruction in these two meizoseismal areas (Fig. 1.4). Additionally, the

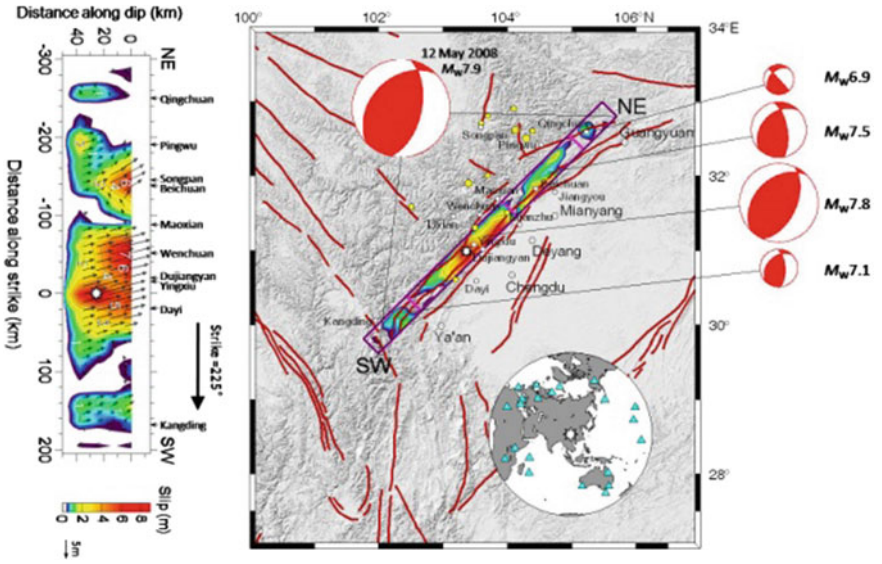

Fig. 1.3 Static slip distribution on the fault plane. Four major concentrated-slip patches with varied focal mechanisms and of seismic moment M_W7.1, M_W7.8, M_W7.5, M_W6.9, respectively, were specially shown

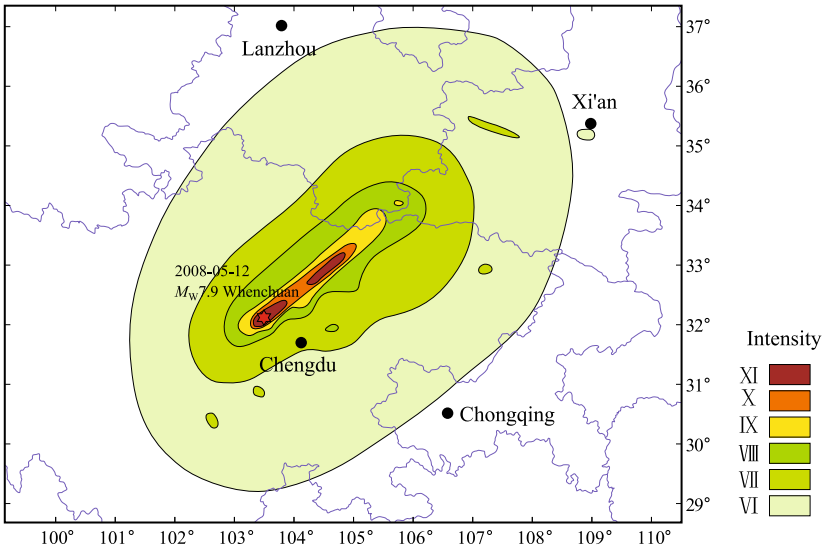

Fig. 1.4 Isoseismals of the 2008 M_W7.9 Wenchuan earthquakes. Two substantial concentrated-slip patches of M_W7.8 and M_W7.5 on the fault plane in Fig. 1.3 are correspondent to the two meizoseismal areas of the epicentral intensity $I_0 = \text{XI}$

other two concentrated-slip patches of M_W7.2 and M_W6.9 on the fault plane with slips of up to 2.3 m and 1.6 m were just underneath the Qingchuan and the Kangding areas, respectively.

1.3.4 Source Rupture Process

The inverted spatiotemporal rupture process of the Wenchuan earthquake shows that the earthquake is a complex asymmetric bilateral rupture with overall strong northeast directivity, with high irregular rupture velocities and long rupture duration of about 90 s (Fig. 1.5). These characteristics account for the northeastward elongated meizoseismal areas and the asymmetric distribution of aftershocks that are significantly more numerous to the northeast of the instrumental epicenter than to the southwest. As theoretical studies have indicated, and the field observations have confirmed, in thrust earthquakes the motion at a point on the ground surface of the hanging wall is usually stronger than that at the point on the foot wall, which is symmetrical with respect to the fault trace. The significant difference in damage between the meizoseismal areas with severe damage (Yingxiu-Dujiangyan-Wenchuan and Beichuan-Qingchuan areas) which are located in the hanging wall and relatively minor damage areas such as Chengdu-Deyang-Guang'an areas which are located in

the foot wall can be attributed at least partly to the effect of the asymmetric dipping fault geometry, i.e., the hanging wall/footwall effect.

It is recognized that the predominantly thrust motion with a minor component of right-lateral motion of the M_W7.9 Wenchuan earthquake was consistent with the tectonic setting of the generally NE-SW striking LF and was due to the NW-SE thrusting of Bayan Har Block with respect to South China Block along the NE-SW striking LF. It is also recognized that the rupture process of the Wenchuan earthquake was extremely complicated. During the rupture process of the Wenchuan earthquake, not only the two substantial concentrated-slip patches of M_W7.2 and M_W6.9 on the fault plane breached the surface and were responsible for the tremendous destruction in the two meizoseismal areas, but also the irregular high rupture velocities of 3.6, 4.0, 4.4, 3.5 km/s in the four stages 1, 2, 3, 4, respectively, as shown in Fig. 1.5 and high rupture velocity enhanced the devastating damage in the meizoseismal areas. It is

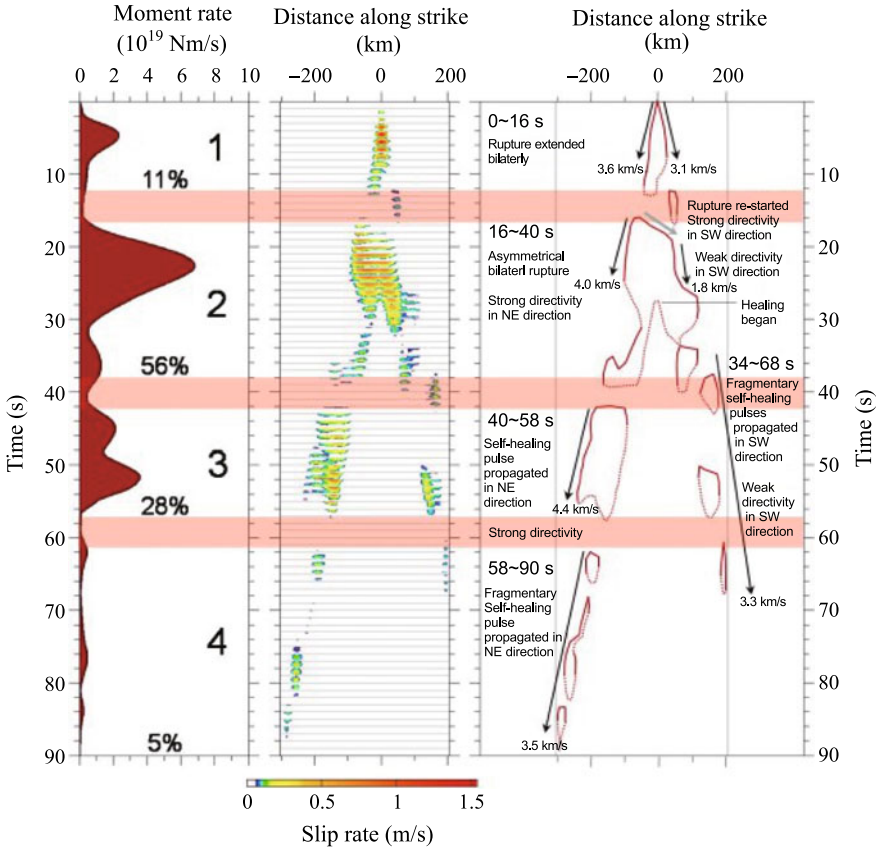

Fig. 1.5 Spatiotemporal rupture process of the 2018 M_W7.9 (M_S8.0) Wenchuan earthquake. On the left is source time function (STF). In the middle is the spatiotemporal variation of slip-rate on the fault. On the right is analysis of the spatiotemporal rupture process of the Wenchuan earthquake

worthy to notice that the Wenchuan earthquake is a complicated rupture event which involved rupturing of several fault segments, and it should be taken into account that in the assessment of the earthquake disaster risk, not only one segment of the fault, but also more segments are possible to rupture.

1.4 The 2010 M_W6.9 Yushu, Qinghai, Earthquake

1.4.1 Tectonic Setting

The M_W6.9 (M_S7.1) Yushu earthquake occurred on April 14, 2010, at 07:49 am Beijing Time (April 13, 2010, 23:49 UTC). The epicenter of the Yushu earthquake was at (33.2°N, 96.6°E), 44 km northwestern of Yushu city, and the focal depth was 14 km (Fig. 1.6). By May 30, 2010, the Yushu earthquake caused about 3000 people killed or missing, over 10,000 people injured, and a large number of houses and buildings collapsed. The Yushu earthquake occurred on the Garze-Yushu Fault, a southeast-striking, left-lateral strike-slipping fault, which lies on southern boundary of the Bayan Har Block. Historically, there has been high seismicity on the fault. The Yushu earthquake was the largest event on the northwestern segment of the Garze-Yushu fault in recent 100 years.

For fast emergency response to the earthquake disaster, we obtained the source rupture process of the Yushu earthquake, by inverting the seismic recordings and had it released about 2.5 h after its occurrence. About 5 h and 2 days after the earthquake occurrence when more data became available, we updated twice the results, respectively (http://www.csi.ac.cn).

In order to better understand the source rupture process of the Yushu earthquake, after the fast emergency response activity, once again we inverted the carefully selected waveform data to improve the results of the source rupture process (Fig. 1.7). It is worthy to note that overall the latest improved results are well consistent with the fast and the two updated results.

1.4.2 Focal Mechanism

The inverted result (Fig. 1.7) shows that the focal mechanism of the Yushu earthquake was strike 119°/dip 83°/rake −2°, and that the scalar seismic moment was about 2.7×10^{19} Nm, yielding a moment magnitude of M_W6.9. The average slip on the whole fault plane was about 0.6 m, and the average stress drop was 15 MPa, which was in a good agreement with the typical value of the stress drop (about 10 MPa) for the intraplate earthquakes.

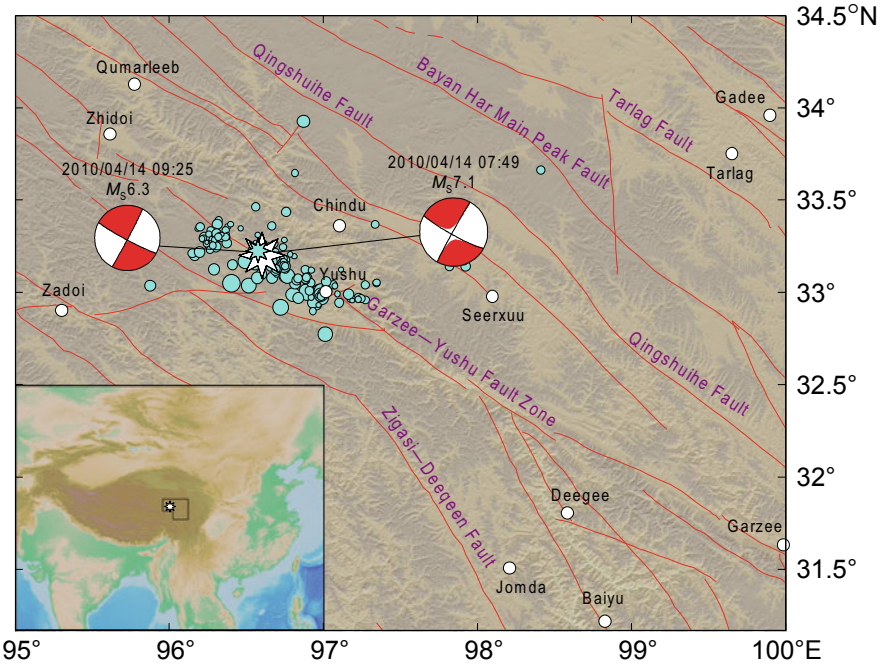

Fig. 1.6 Tectonic setting of the 2010 Yushu earthquake. White and cyan octagonal stars are epicenters of the M_W6.9 (M_S7.1) mainshock and the largest aftershock of M_S6.3, respectively. Red lines denote the major faults. Beach balls represent the focal mechanisms of the mainshock and the largest aftershock of M_S6.3 (equal-area projection of the lower hemisphere of the focal sphere). Cyan circles are locations of the aftershocks in the first 5 days after the occurrence of the mainshock (from Qinghai Province Earthquake Administration). Black frame in the left-bottom inset outlines the area of the main plot

1.4.3 Distribution of Static Slip

The rupture duration time of the Yushu earthquake was about 16 s, with two clearly distinguishable sub-events (Fig. 1.7b). The first one was between 0 and 5 s, corresponding to the concentrated-slip patch 10 km northwestern to 10 km southeastern of the epicenter, with a maximum slip of 0.8 m. The second one was between 5 and 16 s, corresponding to the concentrated-slip patch 17–54 km southeastern of the epicenter in the strike direction (red-orange-yellow area in Fig. 1.7c and e), with a maximum slip of 1.8 m and breached the ground surface.

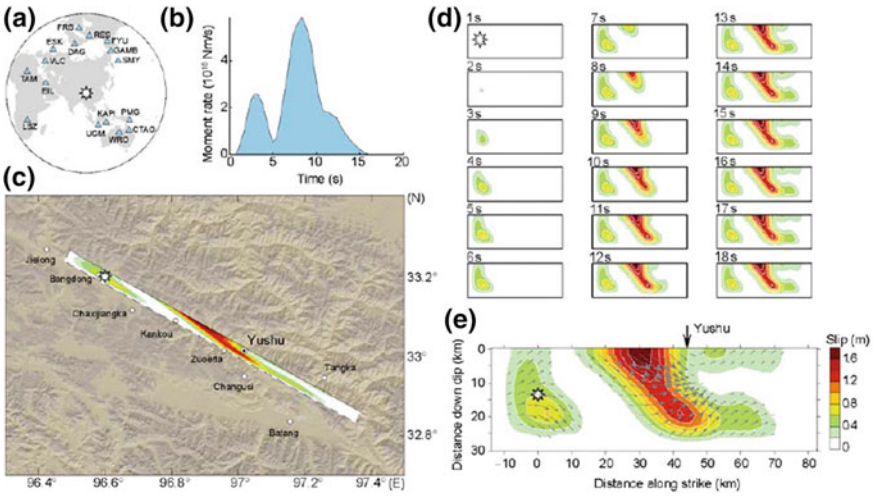

Fig. 1.7 Inverted spatiotemporal rupture process of the 2010 Yushu earthquake. **a** Locations of the epicenter and seismic stations; **b** Moment rate or source time function; **c** Projection of the static (final) slip distribution on the ground surface; **d** Spatiotemporal distribution of slip on the fault plane; **e** Static slip distribution on the fault plane. White octagonal star represents the epicenter in (**a**) and (**c**), but the rupture initiation point in (**d**) and (**e**). Gray arrows in (**e**) denote the slip vectors

1.4.4 Source Rupture Process

The waveform analysis shows that the Yushu M_W6.9 (M_S7.1) earthquake consists of two distinct sub-events (Fig. 1.7). The first one occurred in the first 5 s releasing less seismic moment, and the second occurred in the later 11 s releasing more seismic moment. These two principal sub-events correspond to two concentrated-slip patches located near the hypocenter and in southeast of the epicenter, respectively. The second patch breached the ground surface. The peak slip and peak slip rate are about 2.1 m and 1.1 m/s, respectively. This indicates that the Yushu earthquake is an event with large slip-velocity on the fault plane. Overall, the Yushu earthquake is a unilateral rupture event with the rupture mainly propagating southeastward. It was inferred that the Yushu city, 44 km southeastern of the epicenter, would be heavily destroyed due to the facts that the concentrated-slip patch to the southeast of the epicenter breached the ground surface, and that the strong focusing of the seismic energy caused by the seismic Doppler effect. These results have been reported to the authorities and released to the public on the Web site about 2.5 h after the earthquake occurrence and confirmed later by the tremendous damage in the Yushu city, and proved to be very informative in the Yushu earthquake relief work.

1.5 The 2016 M_W7.8 Kaikoura, New Zealand, Earthquake

1.5.1 Tectonic Settings

As Fig. 1.8 shows, the 2016 M_W7.8 Kaikoura, New Zealand, earthquake occurred in the Marlborough Fault System (MFS), which is composed of several major faults such as Hope fault, Clarence fault, Awatere fault and Wairau fault (Langridge et al. 2003). The MFS is an intricate system consisting of almost right-lateral strike-slip faults, which links two subduction zones with opposite dipping directions, Pyusegur and Hikurangi (e.g., Hamling et al. 2017). Therefore, it has been regarded as a seismically high-risk region (Stirling et al. 2012). The islands of New Zealand and their surrounding regions have been considered as an active zone of earthquakes, with a lot of damaging earthquakes with varieties of focal mechanisms in history. The islands situate on boundary between Pacific Plate and Australian Plate. The Pacific Plate is subducting under the Australian Plate at a speed of about 46–51 mm/year, whereas in the south of New Zealand, the Australian Plate is subducting under the Pacific Plate (DeMets et al. 2010). The interaction of the two plates resulted in the complex tectonic setting and stress or strain field, and the 2016 M_W7.8 Kaikoura earthquake just occurred in this special location and had such a focal mechanism solution, implying that the event seems to have an unusual source.

The rupture process of this event was obtained by inverting teleseismic data and released only about 2.5 h after it took place for the emergency response (http://www.csi.ac.cn). Afterward, we collected more data, including more stations of teleseismic data and two tracks of coseismic InSAR data, to analysis this event for its source complexity (Du et al. 2018). In the following, we show only the primary part of the inverted results.

1.5.2 Focal Mechanism

The USGS W-phase moment tensor solution shows that one of the nodal planes is of strike 219°, dip 38°, and rake 128° while the GCMT solution indicates that one of the nodal planes is of strike 226°, dip 33°, and rake 141°, which are consistent with the spatial distribution of the aftershocks (Fig. 1.8). Both solutions suggest that it was a right-lateral strike and thrust event and had prominent non-double-couple component (Duputel and Rivera 2017). However, our analysis showed that the strike should be at azimuth of 208°, and the rake should be changing from around 106° to around 151° from south to north (Du et al. 2018).

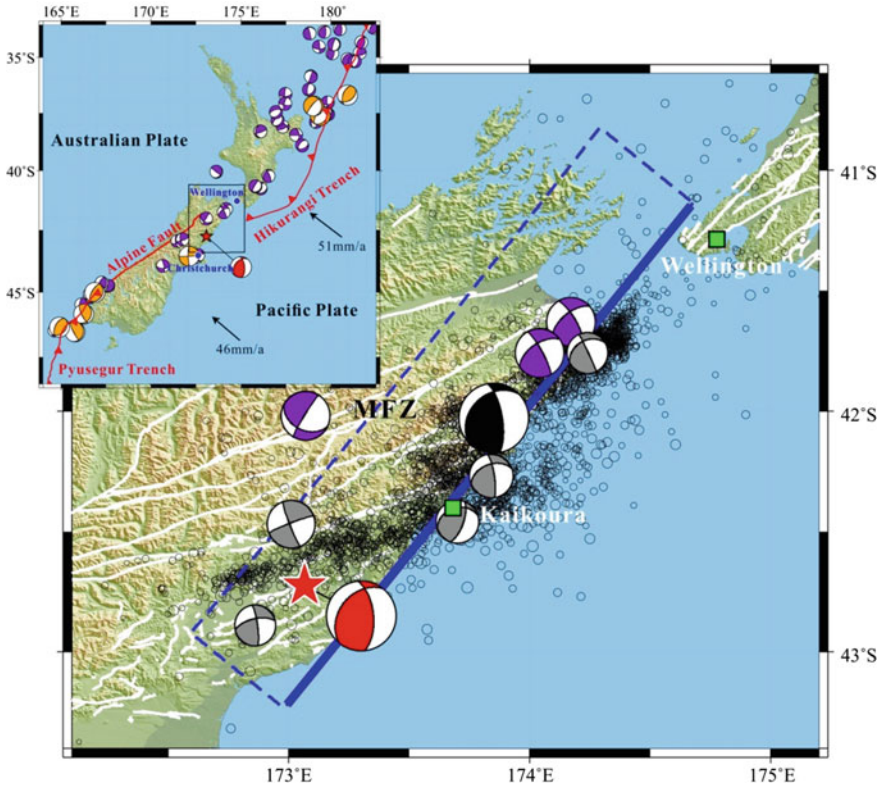

Fig. 1.8 Tectonic setting of the 2016 M_W7.8 Kaikoura, New Zealand, earthquake. The blue box shows the initial fault model projected on the ground surface, with the blue solid line indicating the surface intersection of the model. The red star is the epicenter of this event while the black empty circles are the epicenters of the aftershocks for one week since the mainshock (GeoNet: http://quakesearch.geonet.org.nz/). The white solid curves are the major active faults (Langridge et al. 2016). The red beach ball denotes the W-phase moment tensor solution of the mainshock from USGS and the black one does the GCMT solution of the mainshock. The gray beach balls indicate the GCMT solutions of the aftershocks ($M_W \geq 5.5$). Inset: regional tectonic and relative movement of plates. The Pacific Plate has been going under the Australian Plate at a rate of 40–50 mm/a (DeMets et al. 2010). The purple and orange beach balls denote the GCMT solutions of earthquakes ($M_W \geq 6.0$) since 1979, where the purple ones are for the M_W6–7 earthquakes while the orange ones are for the M_W7–8 earthquakes

1.5.3 Static Slip

The inverted static slip distribution, as shown in Fig. 1.9b, suggests that the slip mainly concentrated on two asperities A and B, with A close to the initial rupture point and relatively weaker while B far away and much stronger. The asperity A produced a maximal slip of about 6.9 m, releasing about 30% of the total moment. It

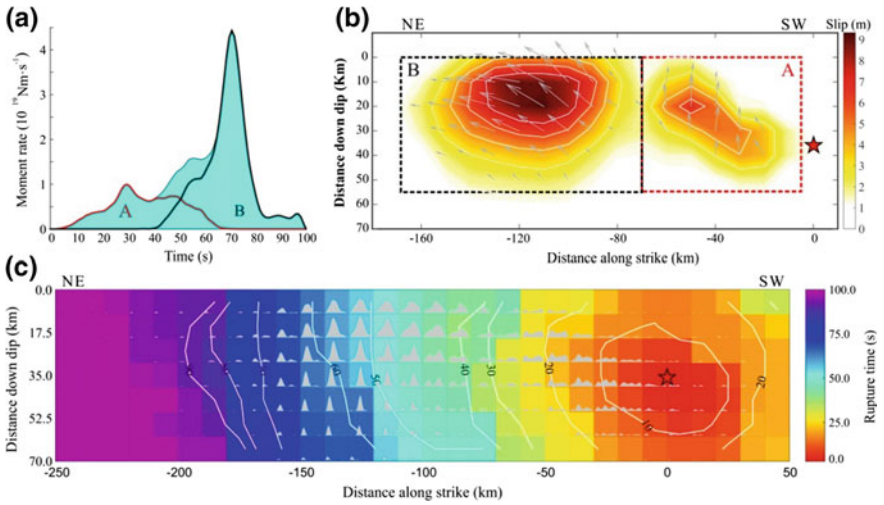

Fig. 1.9 Results of jointly inverted rupture process. **a** Seismic moment rate function, where the red part labeled A is for the patch A while the black part labeled B is for the patch B. **b** Distribution of the static coseismic slip, where the red star denotes initial rupture point, and the red discontinued box surrounds the patch A while the black one does the patch B. The patch A lasted for about 65 s, releasing the seismic moment corresponding to M_W7.6, with the average rake 106° (over all the sub-faults) and the maximal slip 6.9 m. The patch B lasted about 40 s, releasing the moment corresponding to M_W7.8, with the average rake 151° and the maximal slip 9.3 m. **c** Slip functions of all the sub-faults (gray shading) and the rupture times (colorful shading with white contours)

is equivalent to an event of M_W7.6. The asperity B produced a maximal slip of about 9.3 m, releasing about 70% of the total moment released. It is equivalent to an event of M_W7.8.

1.5.4 Source Rupture Process

The inverted STF (Fig. 1.9a) shows that the rupture lasted for a little bit less than 100 s and released scalar moment of 1.01×10^{21} Nm, and the dominant moment was released in the first 80 s. Combining the two-peak feature of the STF with the spatial distribution of asperities on the fault plane as shown in Fig. 1.9b, we divided the whole process into two sub-events A and B. The sub-event A lasted for 65 s, covering about 70 km along strike. The sub-event B started 40 s later and also lasted for about 40 s, covering about 90 km along strike. It is worthy to stress that the event A was nearly thrust while the event B had both strike and thrust components.

We also noticed that the sub-event A had not ended before the sub-event B started (Fig. 1.9a). In order to illustrate the spatiotemporal complexity of the rupture process, we made the snapshots of slip rates as shown in Fig. 1.10. In the first 10 s, the slip was very weak and had no observable directivity, which can be considered to

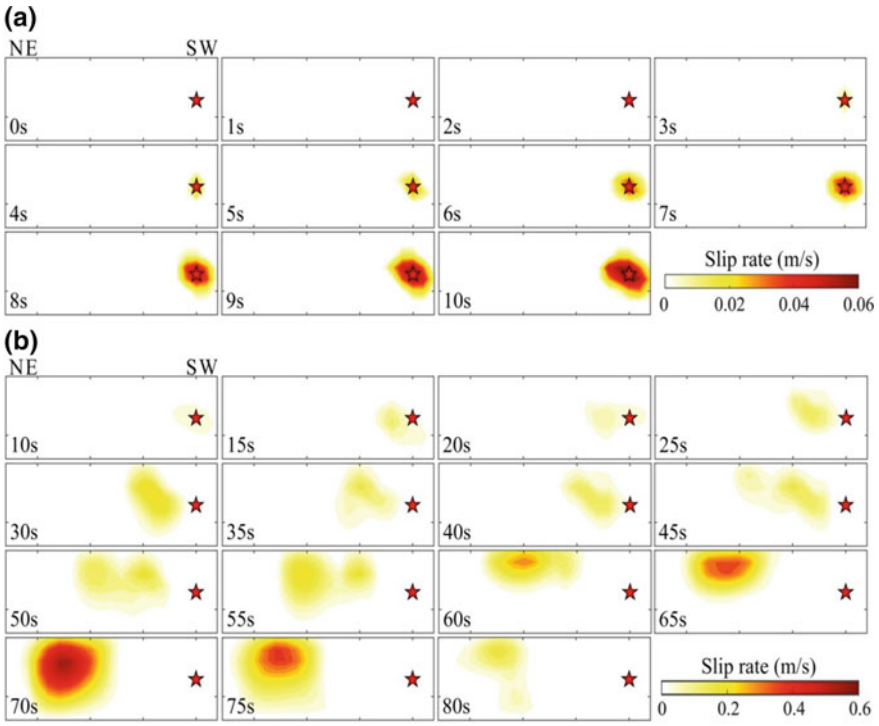

Fig. 1.10 Snapshots of the slip rate. **a** For the first 10 s; **b** For the period of 10–80 s. The star denotes the initial rupture point

be bilateral. Afterward, the slipping area started moving obviously toward the left, and its slipping amplitude was gradually increasing till about 80 s later, which was absolutely unilateral. More details on the rupture propagate are exhibited in Fig. 1.9c.

1.6 Applications to the Earthquake Emergency Response

The fast and robust inversion methods of earthquake rupture process developed in the past two and more decades proved to be effective in providing information on the source characteristics. Except for the usual earthquake source parameters, such as epicentral location, focal depth, focal mechanism, the spatiotemporal rupture process inversion provided still more important information, such as the heavy disastrous areas, etc. The prompt release of these results proved very useful for earthquake emergency response and mitigation of the earthquake disaster. In the past decade, we applied these methods to some significant earthquakes. Since the Wenchuan earthquake occurred on May 12, 2008, a total of 71 worldwide earthquakes were

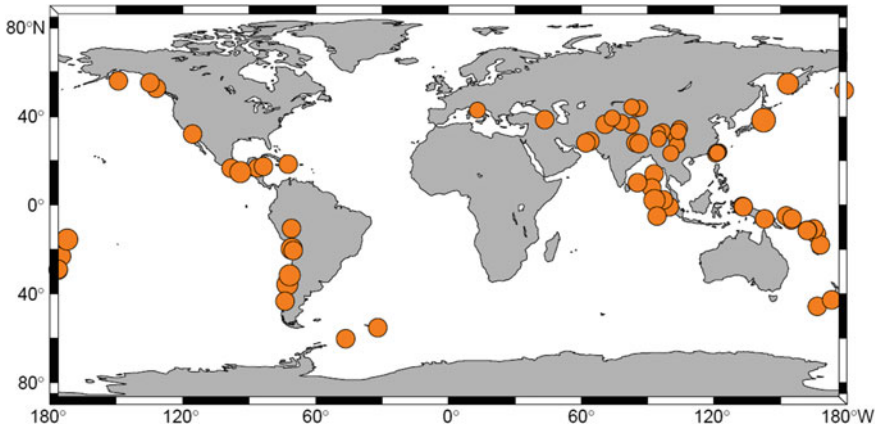

Fig. 1.11 Distribution of the significant earthquakes processed and released since May 12, 2008 in this study

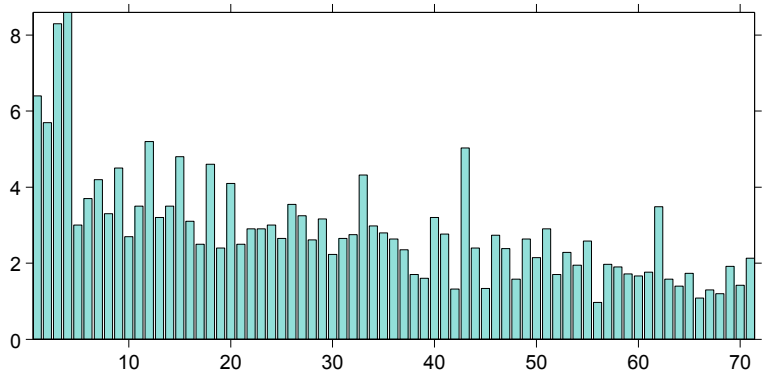

Fig. 1.12 Time consumed on each of the significant earthquakes in Table 1.1 for which the source rupture processes were inverted and released immediately after the earthquake occurrence in the time period of 2009–2018. The abscissa represents serial number (No.) of the significant earthquake. The ordinate represents the time consumed for data processing in an hour

processed for their source processes (Fig. 1.11). At the earlier stage, more time was spent on each event. Gradually, the time consumed became less. As Fig. 1.12 shows, currently, usually around 2 h are enough for each event.

All the fast inversion results were directly emailed to China Earthquake Administration (CEA) as well as some of the institutes of the CEA before 2014. Later they were demanded to send to http://www.cenc.ac.cn/cenc/_300651/index.html, a Web site of China Earthquake Network Center (CENC).

Table 1.1 Source parameters of the significant earthquakes for which the earthquake rupture processes were inverted and released immediately after the earthquake occurrence in the time period of 2009–2018

No.	Epicentral region	Origin time (UTC)	Epicentral location (Lat., Long.)	Focal depth (km)	M_W	Time consumed (h)
1	North of Papua	2009-01-04 04:43	(−0.5°, 132.8°)	33	7.7	6.4
2	North of Papua	2009-01-04 06:33	(−0.7°, 133.2°)	33	7.5	5.7
3	Tonga	2009-03-19 18:17	(−23.0°, −174.7°)	10	7.8	8.3
4	Offshore Honduras	2009-05-28 08:24	(16.8°, −86.2°)	15	7.2	8.6
5	Hualian, Taiwan, China	2009-07-13 18:05	(24.1°, 122.2°)	6	6.4	3.0
6	South Island, N.Z.	2009-07-15 09:22	(−45.7°, 166.6°)	33	7.8	3.7
7	Andaman Islands	2009-08-10 19:55	(14.1°, 92.9°)	33	7.8	4.2
8	Samoa Islands	2009-09-29 17:48	(−15.5°, −172.2°)	33	8.0	3.3
9	Southern Sumatra	2009-09-30 10:16	(−0.8°, 99.8°)	60	7.6	4.5
10	Vanuatu	2009-10-07 22:03	(−13.0°, 166.3°)	33	7.8	2.7
11	Hualian, Taiwan, China	2009-12-19 13:02	(23.8°, 121.7°)	30	6.6	3.5
12	Haiti	2010-01-12 21:53	(18.5°, −72.4°)	10	7.1	5.2
13	Central Chile	2010-02-27 06:34	(−35.8°, −72.7°)	33	8.6	3.2
14	Central Taiwan, China	2010-03-04 00:18	(23.0°, 120.7°)	5	6.5	3.5
15	Northern Mexico	2010-04-04 22:40	(32.1°, −115.5°)	10	7.2	4.8
16	Southern Sumatra	2010-04-06 22:15	(2.4°, 97.1°)	31	7.8	3.1
17	Yushu, Qinghai, China	2010-04-13 23:49	(33.1°, 96.7°)	10	6.9	2.5

(continued)

Table 1.1 (continued)

No.	Epicentral region	Origin time (UTC)	Epicentral location (Lat., Long.)	Focal depth (km)	M_W	Time consumed (h)
18	Nicobar Islands	2010-06-12 19:26	(7.7°, 91.9°)	30	7.6	4.6
19	Vanuatu	2010-12-25 13:16	(−19.7°,168.9°)	20	7.4	2.4
20	Southwestern Pakistan	2011-01-18 20:23	(28.8°, 63.9°)	10	7.1	4.1
21	Tohoku, Japan	2011-03-11 05:46	(38.3°, 142.4°)	24	9.0	2.5
22	Kermadec Islands	2011-07-06 19:03	(−29.3°, −176.2°)	10	7.7	2.9
23	Kermadec Islands	2011-10-21 17:57	(−29.0°, −176.2°)	33	7.5	2.9
24	Eastern Turkey	2011-10-23 10:41	(38.6°, 43.5°)	20	7.3	3.0
25	Mexico	2012-03-20 18:02	(16.7°, −98.2°)	20	7.5	2.7
26	Northern Sumatra	2012-04-11 08:38	(2.3°, 93.1°)	23	8.6	3.6
27	Xinyuan, Xinjiang, China	2012-06-29 21:07	(43.4°, 84.8°)	7	6.3	3.3
28	Costa Rica	2012-09-05 14:42	(10.1°, 85.3°)	41	7.6	2.6
29	Haida Gwaii	2012-10-28 03:04	(52.8°, −131.9°)	18	7.8	3.2
30	Southeastern Alaska	2013-01-05 08:58	(55.2°, −134.8°)	10	7.5	2.2
31	Solomon Islands	2013-02-06 01:12	(−10.8°, 165.1°)	6	7.8	2.7
32	Nantou, Taiwan, China	2013-03-27 02:03	(23.8°, 121.1°)	21	6.0	2.8
33	Khash, Iran	2013-04-16 10:44	(28.1°, 62.1°)	82	7.7	4.3
34	Lushan, Sichuan, China	2013-04-20 00:02	(30.3°, 103.0°)	12	6.8	3.0
35	Sea of Okhotsk	2013-05-24 05:44	(54.9°, 153.3°)	610	8.3	2.8

(continued)

Table 1.1 (continued)

No.	Epicentral region	Origin time (UTC)	Epicentral location (Lat., Long.)	Focal depth (km)	M_W	Time consumed (h)
36	Nantou, Taiwan, China	2013-06-02 05:43	(23.8°, 121,1°)	20	6.2	2.6
37	Minxian-Zhangxian, Gansu, China	2013-07-21 23:45	(34.5°, 104.2°)	10	6.0	2.4
38	Hualian, Taiwan, China	2013-10-31 12:02	(23.6°, 121.4°)	12	6.3	1.7
39	Scotia Sea	2013-11-17 09:04	(−60.3°, −46.4°)	10	7.8	1.6
40	Yutian, Xinjiang, China	2014-02-12 09:19	(35.9°, 82.6°)	13	6.9	3.2
41	Northern Chile	2014-04-01 23:46	(−19.6°, −70.8°)	20	8.2	2.8
42	Northern Chile	2014-04-03 02:43	(−20.4°, −70.1°)	20	7.7	1.3
43	Solomon Islands	2014-04-12 20:14	(−11.3°, 162.2°)	29	7.6	5.0
44	Solomon Islands	2014-04-13 12:36	(−11.5°, 162.1°)	35	7.5	2.4
45	Papua New Guinea	2014-04-19 13:27	(−6.7°, 154.9°)	31	7.5	1.3
46	Alaska	2014-06-23 20:53	(51.8°, 178.8°)	114	7.9	2.7
47	Ludian, Yunnan, China	2014-08-03 08:30	(27.1°, 103.3°)	12	6.1	2.4
48	Jinggu, Yunnan, China	2014-10-07 13:49	(23.4°, 100.5°)	5	6.0	1.6
49	Papua New Guinea	2015-03-29 23:48	(−4.8°, 152.6°)	18	7.5	2.6
50	Nepal	2015-04-25 06:11	(28.1°, 84.6°)	40	7.9	2.2
51	Nepal	2015-05-12 07:05	(27.8°, 86.1°)	15	7.2	2.9
52	Pishan, Xinjiang, China	2015-07-03 01:07	(37.5°, 78.1°)	15	6.3	1.7
53	Central Chile	2015-09-16 22:54	(−31.6°, −71.7°)	13	8.2	2.3

(continued)

Table 1.1 (continued)

No.	Epicentral region	Origin time (UTC)	Epicentral location (Lat., Long.)	Focal depth (km)	M_W	Time consumed (h)
54	Farkhar, Afghanistan	2015-10-26 09:09	(36.4°, 70.7°)	213	7.5	2.0
55	Tarauaca, Brazil	2015-11-24 22:45	(−10.5°, −70.9°)	600	7.4	2.6
56	Sumatra	2016-03-02 12:49	(−4.9°, 94.2°)	10	7.7	1.0
57	South Georgia Island	2016-08-19 07:32	(−55.3°, −31.9°)	10	7.4	2.0
58	Zaduo, Qinghai, China	2016-10-17 07:14	(32.8°, 94.9°)	9	5.8	1.9
59	Norcia, Italy	2016-10-30 06:40	(42.9°, 13.1°)	10	6.3	1.7
60	South Island, N.Z.	2016-11-13 11:02	(−42.8°, 173.1°)	10	7.9	1.7
61	Aketao, Xinjiang, China	2016-11-25 14:24	(39.3°, 74.0°)	12	6.5	1.8
62	Hututi, Xinjiang, China	2016-12-08 05:15	(43.8°, 86.4°)	6	6.2	3.5
63	Chile	2016-12-25 14:22	(−43.4°, −73.8°)	40	7.5	1.6
64	Solomon Islands	2017-01-22 04:30	(−6.1°, 155.2°)	168	7.9	1.4
65	Jiuzhaigou, Sichuan, China	2017-08-08 13:19	(33.2°, 103.8°)	10	6.5	1.7
66	Jinghe, Xinjiang, China	2017-08-08 23:27	(44.3°, 82.9°)	11	6.3	1.1
67	Mexico	2017-09-08 12:49	(14.9°, −94.0°)	30	8.1	1.3
68	Milin, Tibet, China	2017-11-17 22:34	(29.8°, 94.9°)	10	6.4	1.2
69	Northern Honduras	2018-01-10 02:51	(17.5°, −83.5°)	10	7.7	1.9
70	Alaska	2018-01-23 09:31	(56.0°, −149.1°)	10	7.9	1.4
71	Papua New Guinea	2018-02-25 17:44	(−6.1°, 142.8°)	20	7.4	2.1

1.7 Summary

In the past two and more decades, we have developed a series of the inversion methods for the earthquake rupture process and verified these methods by applying them to real earthquakes. Moreover, we successfully applied the methods to the post-earthquake emergency response. In this article, we have had briefly reviewed the methods we have developed, present three significant earthquakes as examples, i.e., the 2008 M_W7.9 Wenchuan earthquake, the 2010 M_W6.9 Yushu earthquake and the 2016 M_W7.8 Kaikoura, New Zealand, earthquake, and display the significant earthquakes for which the earthquake rupture processes were inverted and released immediately after they took place during the time period 2009–2018.

The methods for the inversion of earthquake rupture process include moment tensor inversion, source time function retrieval, rupture process inversion based on the ASTFs, rupture process inversion with fixed focal mechanism based on the waveform data, and that with changeable rakes based on the waveform data.

The inverted results exhibited that the 2008 M_W7.9 Wenchuan earthquake occurred on eastern margin of the Bayan Har Block on Tibetan Plateau, where there is a NE-striking fault named Longmen Shan Fault (LF). The LF is the boundary of the Tibetan Plateau and the Sichuan Basin. This earthquake ruptured the 350-km-long northeastern segment of the 470-km-long LF. The overall rupture area reached about 350 km $\times$ 50 km, released seismic moment of about 9.4×10^{20} Nm and resulted in the average stress drop of about 18 MPa and the maximum stress drop of about 65 MPa, respectively. Our inversion resolved four major slip-concentrated patches or asperities on the fault plane, among them two substantial concentrated-slip patches or asperities had slips as large as up to 8.9 and 6.7 m, respectively. The two substantial slip-concentrated patches are just beneath the two meizoseismal areas both of intensity $I_0 =$ IX, i.e., the elongated area between Yingxiu-Dujiangyan and Wenchuan, and the area around Beichuan, respectively. During the rupture process, the rupture velocities were found changing in succession of about 3.6, 4.0, 4.4, 3.5 km/s for the four stages. In general, the spatiotemporal distribution of the slip exhibited a complex asymmetric bilateral rupture, but with overall a unilateral rupture from southwest to northeast.

The inverted results also exhibited that the 2010 M_W6.9 Yushu earthquake occurred on the Garze-Yushu Fault, a southeast-striking, left-lateral strike-slipping fault, which lies on southern boundary of the Bayan Har Block. This event was a unilateral rupture from northwest to southeast. It released scalar seismic moment of about 2.7×10^{19} Nm, resulting in average slip of about 0.6 m and average stress drop of 15 MPa. The rupture process lasted for about 16 s, including two clearly distinguishable sub-events. The first one was between 0 s and 5 s in time and 10 km northwestern and 10 km southeastern to the hypocenter in space, corresponding to the asperity or the slip-concentrated area with a maximum slip of about 0.8 m. The second was between 5 and 16 s in time and 17–54 km southeastern to the hypocenter, corresponding to the asperity or the slip-concentrated area with a maximum slip of 1.8 m.

The 2016 M_W7.8 Kaikoura, New Zealand, earthquake occurred in the Marlborough Fault System (MFS), which is composed of several major faults such as Hope fault, Clarence fault, Awatere fault and Wairau fault. This event lasted for about 100 s and had a very complex source process. It produced a rupture area about 160 km long along strike direction and about 50 km wide in down-dip direction and resulted in a release of scalar moment 1.01×10^{21} Nm. Spatially, the rupture area consisted of two asperities, with one close to the initial rupture point having a maximal slip value of about 6.9 m while the other far away in north having a maximal slip value of about 9.3 m. Temporally, the first asperity slipped for about 65 s and the second initiated 40 s later and lasted for 40 s, with both of them slipping about 25 s simultaneously. It is more interesting that, similarly to the 2008 Wenchuan earthquake, the focal mechanism of the 2016 Kaikoura earthquake was changing during the rupture process, with the first asperity having a nearly thrust slip while the second having both thrust- and strike-slip components.

Finally, we have applied the methods developed in the past two and more decades to over 70 significant earthquakes which have occurred across the world in the time period of 2009 up to date. Each time when the significant earthquake occurred, we routinely started the work immediately after the earthquake occurrence by collecting the observation data, and conducting inversion process, and reported the results to the authorities to serve for the earthquake emergency response. Our application practices show that the methods were effective in the earthquake emergency response and the results played an important role in the mitigation of earthquakes disaster.

References

Aki, K., and P.G. Richards. 2002. *Quantitative seismology*, 2nd ed., 700. Sausalito: University Science Books.

Antolik, M., and D.S. Dreger. 2003. Rupture process of the 26 January 2001 M_W7.6 Bhuj, India, earthquake from teleseismic broadband data. *Bulletin of the Seismological Society of America* 93: 1235–1248.

DeMets, C., R.G. Gordon, and D.F. Argus. 2010. Geologically current plate motions. *Geophysical Journal International* 181: 1–80.

Du, H.L., X. Zhang, L.S. Xu, W.P. Feng, L. Yi, and P. Li. 2018. Source complexity of the 2016 M_W7.8 Kaikoura (New Zealand) earthquake revealed from teleseismic and InSAR data. Earth and Planetary Physics 2 (4): 1–17. http://doi.org/10.26464/epp2018029.

Duputel, Z., and L. Rivera. 2017. Long-period analysis of the 2016 Kaikoura earthquake. *Physics of the Earth and Planetary Interiors* 265: 62–66.

Hamling, I.J., S. Hreinsdóttir, K. Clark, J. Elliott, C. Liang, E. Fielding, N. Litchfield, P. Villamor, L. Wallace, T.J. Wright, E. D'Anastasio, S. Bannister, D. Burbidge, P. Denys, P. Gentle, J. Howarth, C. Mueller, N. Palmer, C. Pearson, W. Power, P. Barnes, D.J.A. Barrell, R. Van Dissen, R. Langridge, T. Little, A. Nicol, J. Pettinga, J. Rowland, and M. Stirling. 2017. Complex multifault rupture during the 2016 M_W7.8 Kaikōura earthquake, New Zealand. *Science* 356. http://doi.org/10.1126/science.aam7194.

Hartzell, S.H. 1978. Earthquake aftershocks as Green's functions. *Geophysical Research Letters* 5: 1–4.

Hartzell, S.H., and T.H. Heaton. 1983. Inversion of strong ground motion and teleseismic waveform data for the fault rupture history of the 1979 Imperial Valley, California, earthquake. *Bulletin of the Seismological Society of America* 73: 1553–1583.

Langridge, R., J. Campbell, N. Hilland, and V. Pere. 2003. Paleoseismology and slip rate of the Conway Segment of the Hope Faultat Greenburn Stream, South Island, New Zealand. *Annals of Geophysics* 46: 1119–1139.

Langridge, R.M., W.F. Ries, N.J. Litchfield, P. Villamor, R.J. Van Dissen, D.J.A. Barrell, M.S. Rattenbury, D.W. Heron, S. Haubrock, and M.W. Stirling. 2016. The New Zealand Active Faults Database. *New Zealand Journal of Geology and Geophysics* 59: 86–96.

Lay, T., and T.C. Wallace. 1995. *Modern global seismology*, 534. San Diego: Academic Press.

Mueller, C.S. 1985. Source pulse enhancement by deconvolution of an empirical Green's function. *Geophysical Reseach Letters* 12: 33–36.

Stirling, M., G. McVerry, M. Gerstenberger, N. Litchfield, R. Van Dissen, K. Berryman, P. Barnes, L. Wallace, P. Villamor, R. Langridge, G. Lamarche, S. Nodder, M. Reyners, B. Bradley, D. Rhoades, W. Smith, A. Nicol, J. Pettinga, K. Clark, and K. Jacobs. 2012. National seismic hazard model for New Zealand: 2010 Update. *Bulletin of the Seismological Society of America* 102: 1514–1542.

Ward, S.N., and S.E. Barrientos. 1986. An inversion for slip distribution and fault shape from geodetic observations of the 1983, Borah Peak, Idaho, Earthquake. *Journal Geophysical Research* 91: 4909–4919.

Xu, L.S., and Y.T. Chen. 1996. Source time functions of the Gonghe, China earthquake retrieved from long-period digital waveform data using empirical Green's function technique. *Acta Seismologica Sinica* 9 (2): 209–222.

Yagi, Y., T. Mikumo, J. Pacheco, and G. Reyes. 2004. Source rupture process of the Tecomán, Colima, Mexico earthquake of 22 January 2003, determined by joint inversion of teleseismic body-wave and near-source data. *Bulletin of the Seismological Society of America* 94: 1795–1807.

Yang, Z.X., Y.T. Chen, Y.J. Zheng, and X.H. Yu. 2003. Accurate relocation of earthquakes in central-western China using the double difference earthquake location algorithm. Science in China Series D-Earth Sciences 33 (suppl.), 123–149.

Zhang, Y., W.P. Feng, Y. Chen, L. Xu, Z. Li, and D. Forrest. 2012. The 2009 L'Aquila M_W6.3 earthquake: a new technique to locate the hypocentre in the joint inversion of earthquake rupture process. *Geophysical Journal International* 191: 1417–1426.

Chapter 2
Rupture Process of the 2008 Wenchuan, China, Earthquake: A Review

Thorne Lay

Abstract The May 12, 2008, Wenchuan earthquake (M_W 7.9, M_S 8.1) is the largest continental intraplate event to strike globally in the last 60 years. It caused great destruction and loss of life along the steep eastern margin of the Tibetan Plateau, adjacent to the Sichuan Basin. The event ruptured multiple faults with a mix of thrust- and right-lateral strike-slip faulting along the northeast-trending Longmen Shan thrust belt, with an overall oblique compressional deformation. Surface displacements of up to ~11 m, the distribution of thousands of aftershocks and landslides, geodetic observations, and seismic wave imaging indicate a total rupture extent of ~280 km, extending unilaterally northeastward from the hypocenter. The primary slip has a patchy distribution along the segmented out-of-sequence Beichuan fault, with large-slip patches in the region from Yingxiu to Xiaoyudong, near Beichuan, and near Nanba. The southwestern segment near Yingxiu, where the hanging wall is comprised of the high seismic velocity Pengguan massif, has primarily thrust displacement with minor right-lateral component. Strongly oblique slip occurred near Beichuan and progressively more steeply dipping right-lateral strike-slip dominates toward the northeast. The large-slip patches are less than 10 km deep, but slip extends deeper in the southwestern region and the fault appears to have listric extension into a mid-crustal décollement with shallow dip below 20 km depth. The rupture expanded with an average rupture velocity of ~2.8 ± 0.2 km/s along this segmented fault zone with a total rupture duration of ~110 s, with faster rupture speed in the northeastern region, possibly being supershear. Most aftershocks are concentrated from 10 to 20 km deep, below the large-slip zones. Predominantly thrust slip with vertical offset of ~3.5 m occurred at shallow depth along ~72 km of the imbricate Pengguan fault located 6–7 km to the southeast of the southern Beichuan fault. Shallower dip of the Pengguan fault may cause it to converge with the Beichuan fault at depth, and/or to flatten into the same mid-crustal décollement. Oblique compressional left-lateral slip occurred on

The original version of this chapter was revised: Incorrect figure has been replaced. The correction to this chapter is available at https://doi.org/10.1007/978-981-13-8015-0_10

T. Lay (✉)
Department of Earth and Planetary Sciences, University of California Santa Cruz, Santa Cruz, CA 95064, USA
e-mail: tlay@ucsc.edu

Y.-G. Li (ed.), *Earthquake and Disaster Risk: Decade Retrospective of the Wenchuan Earthquake*, https://doi.org/10.1007/978-981-13-8015-0_2

the short conjugate southward-dipping Xiaoyudong fault, connecting the two range-parallel faults. The moment-scaled radiated energy of the Wenchuan event is higher than for typical interplate thrust faulting, likely contributing to the extensive damage.

Keywords Wenchuan earthquake · Rupture process · Slip distribution · Intraplate faulting · Surface rupture · Aftershocks · Sichuan earthquake

2.1 Introduction and Tectonic Setting

The May 12, 2008, Wenchuan earthquake was an event of profound consequences. Located along the eastern margin of the Tibetan Plateau, adjacent to the Sichuan Basin, the large magnitude (M_W 7.9, M_S 8.1) shallow rupture produced devastating ground shaking and landsliding, impacting many towns and villages along the Longmen Shan thrust belt. The Chinese government reports that 69,227 people were confirmed killed and 17,923 are missing, with 374,643 injured by September 18, 2008. This includes 158 workers killed in landslides while attempting to repair roads in the source region. The catastrophic event has stimulated new generations of Chinese students to pursue earthquake research, and the impressive quantitative analysis of the earthquake performed by many Chinese geophysicists evident in this review demonstrates the high quality of data collection and sophisticated signal analysis that has been achieved in the Chinese earthquake research community over the past several decades. The geophysical and field observations of the earthquake have been extensively studied, and much of the literature addressing the rupture process during the event is discussed here, prompted by a keynote speech that the author delivered at the International Conference for the Decade Memory of the Wenchuan Earthquake held in Chengdu, Sichuan, May 12–14, 2018. This review updates and extends prior reviews of the earthquake by Zhang et al. (2010) and Yin (2010). The extraordinary efforts for recovery, reconstruction, and relocation of communities to safer locations are not discussed here, but stand as a vast national undertaking in China, with the societal impact motivating the development of comprehensive understanding of the earthquake rupture process that is highlighted here.

The 2008 Wenchuan earthquake struck during a global increase in the annual rate of great earthquakes around the world between 2004 and 2014 (Fig. 2.1; Lay 2015). Most of these earthquakes are located around the Pacific and Indo-Australian plate subduction zone margins, in regions where most global $M \geq 7.9$ events have been recorded throughout the last century. The 2008 event stands out as the largest continental intraplate event during this time, and it is located within the continental environment of eastern Asia with the most extensive history of large earthquakes. This is emphasized in Fig. 2.2, which shows the ISC-GEM catalog distribution of major ($M \geq 7.0$) earthquakes in China and surrounding countries since 1900. The 2008 event is the largest continental intraplate event since the 1957 Mongolian earthquake, and Fig. 2.2 provides a stark reminder that there is broad exposure to events of this size throughout China and southeastern Eurasia generated by the India-Eurasia continental collision.

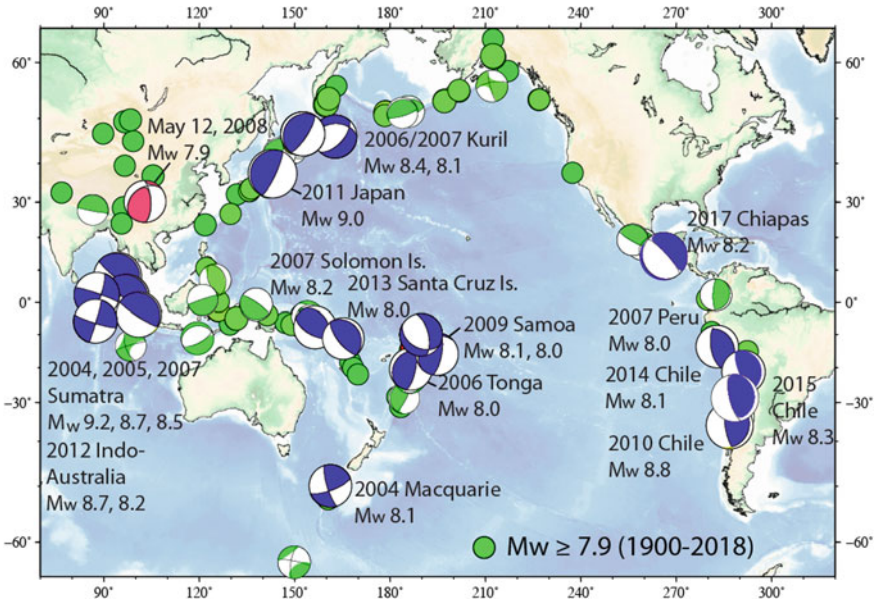

Fig. 2.1 Global distribution of shallow (depth ≤ 70 km) earthquakes with moment magnitudes, $M \geq 7.9$ from the USGS-NEIC/ISC-GEM catalog (green dots) for 1900–1976, and global centroid-moment-tensor mechanisms for events from 1976 to 2018 shown in green or, for labeled great events with $M_W \geq 8.0$ from 2004 to 2015, shown in blue. The centroid-moment-tensor mechanism for the M_W 7.9 May 12, 2008, Wenchuan, China earthquake is shown in red. Modified from Lay (2015)

The source region of the 2008 Wenchuan earthquake has over 4 km of topographic relief over a ~50 km wide plateau margin, with the rupture extending northeastward from a region of high topography to lower relief valleys along the Longmen Shan (Fig. 2.3). The steep, high relief represents a dominance of uplift over erosion. The long-term rock uplift rate, corrected for denudation, is estimated as 0.7–1.2 mm/yr (Burchfiel et al. 2008), while the dip-slip shortening rate measured from GPS is about 1 ± 1 mm/yr. Based on an average uplift of 5 m during the 2008 event, Burchfiel et al. (2008) estimate a recurrence interval for 2008 size events of 2000–10,000 yr. There is only modest accommodation of compression in the foreland, although a 17.5 km deep detachment with blind fault splays detected by reflection profiles does appear to extend into Sichuan Basin (Jia et al. 2010; Li et al. 2010b).

Densmore et al. (2007) studied active faults in the region, asserting that the Beichuan and Pengguan faults (Fig. 2.4) are dominantly dextral-slip structures with prior surface ruptures during the latest Pleistocene and Holocene. They estimate a dextral-slip rate of about 1 mm/yr along the Beichuan fault. Their inference that there is significant seismic hazard in the region, despite a lack of large historic earthquakes in the Longmen Shan overall (e.g., Zhang et al. 2008; Lin et al. 2010), proved prescient. Ran et al. (2010) examined three trenches in the Beichuan and Pengguan faults, finding no evidence for large paleoearthquakes within the last 2300 years,

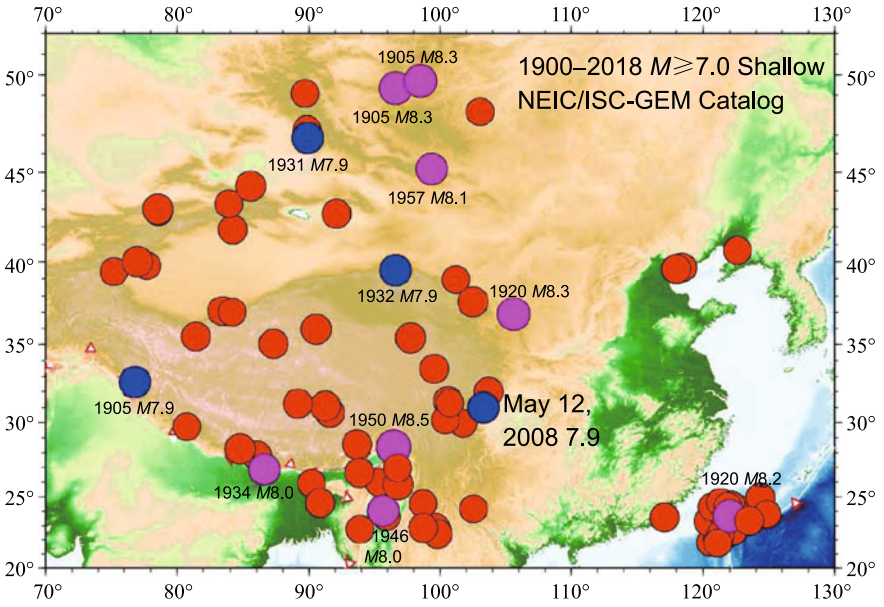

Fig. 2.2 Distribution of major ($M \geq 7.0$) earthquakes in China and immediately surrounding countries from 1900 to 2018 from the USGS-NEIC/ISC-GEM catalog. Red dots indicate events with $M \leq 7.8$, labeled blue dots are M 7.9 events, and labeled magenta dots are great earthquakes with $M \geq 8.0$

which corresponds to the historical record in Chengdu. However, occurrence of an $M \sim 8$ earthquake along the Beichuan fault with 2–3 m average slip in the late Tang-Song Dynasty (800–1000 C.E.) has been inferred based on fault exposures by Lin et al. (2010). The Beichuan fault has experienced some historic activity, with 12 earthquakes with $M > 4$ since 1168, including the 1958 Beichuan earthquake with M 6.2. The eastern margin Pengguan fault was historically seismically inactive but has an uplift rate of ~0.2 mm/yr since the middle Pleistocene (Ma et al. 2005). The Wenchuan-Maoxian (Maowen) fault to the northwest of the Pengguan Massif (Fig. 2.4) has experienced some prior seismicity, but did not rupture in 2008.

The large-scale crustal deformation driving the uplift of the Pengguan Massif bounded by the Wenchuan and Beichuan faults is the subject of continuing debate. Royden et al. (2008) argue that rapidly eastward-flowing deep crust in a channel under eastern Tibet inflates in the mid-lower crust to give upthrust of the Massif, accounting for the presence of strong topography despite low present-day convergence rate, modest shortening and little accommodation by large-scale low-angle thrusts. Hubbard and Shaw (2009) and Hubbard et al. (2010) balance geologic cross sections including the blind structures extending into the Sichuan Basin and argue that the observed crustal shortening and associated folding and faulting are compatible with the structural relief, with no need for inflation of low-viscosity material in the lower crust. Modeling by Zhu and Zhang (2013) with a viscoelastic finite element method for the interseismic and coseismic deformation around the 2018 event indicates that

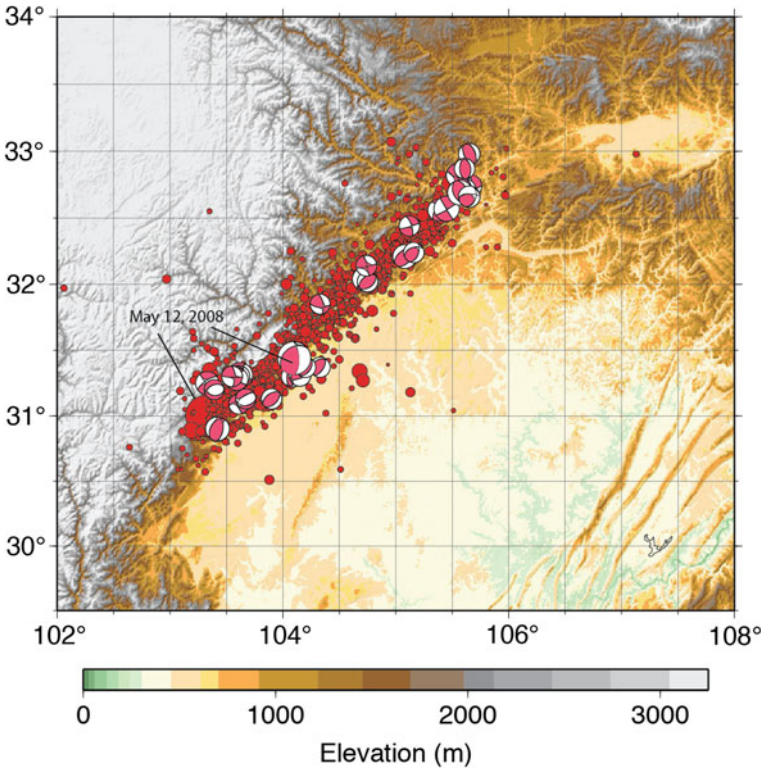

Fig. 2.3 Aftershock distribution for the May 12, 2008, Wenchuan earthquake from the USGS-NEIC catalog (through May 26, 2008) along with global centroid-moment-tensor (GCMT) source mechanisms (through September 12, 2008) plotted at their centroid locations. Note that the mainshock centroid location is located northeast of the NEIC epicenter, which is at the southwestern end of the aftershock zone. Figure courtesy of C. J. Ammon

the lower crust in eastern Tibet and in the Sichuan Basin does not accumulate large elastic strain energy, while the Longmen Shan fault zone does, with concentrated uplift along high-angle listric reverse faults. Li et al. (2018) integrate 2-D and 3-D structural constraints from seismic reflection profiles, borehole data, and field observations to infer the subsurface structural architecture. They estimate that the eastern Tibet margin has experienced east–west shortening since 5–2 Ma, oblique to the Longmen Shan. The regional fault geometries are inferred by Xu et al. (2009d) to not be favorably oriented for frictional slip from the horizontal compression, resulting in long recurrence times. This tectonic setting is thus less well constrained and has slower deformation rates than the subduction zone context for most of the great earthquakes shown in Fig. 2.1 and reflects the challenge for seismic hazard assessment common to all of the intraplate deformation regions shown in Fig. 2.2.

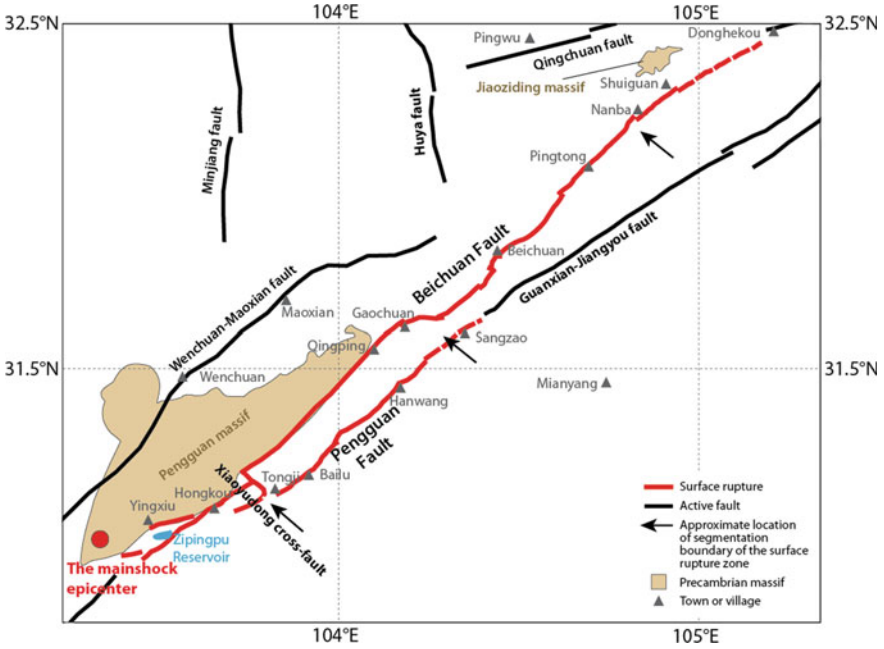

Fig. 2.4 Base map of the Wenchuan earthquake source region. Surface rupture along the Beichuan, Pengguan, and Xiaoyudong faults is indicated in red. The USGS-/NEIC epicenter is the red dot. Other large mapped faults in the Longmen Shan thrust belt are marked with black lines. The Pengguan and Jiaoziding massifs are outlined in brown. The Zipingpu Reservoir is indicated in cyan. Modified from Zhang et al. (2010)

2.2 Surface Rupture and Landslide Constraints on Fault Geometry

Extensive surface rupturing occurred during the 2008 Wenchuan earthquake, and field mapping provides important constraints on the overall rupture process (e.g., Dong et al. 2008; He et al. 2008; Li et al. 2008a, b; Xu et al. 2008, 2009a, b; Chen et al. 2009a; Jia et al. 2010; Li and Wei 2009; Liu et al. 2008, 2009, 2010; Lin et al. 2009; Wang et al. 2009a, c, 2010a; Wu et al. 2009a, b; Densmore et al. 2010; Li et al. 2010a; Yu et al. 2010; Zhou et al. 2010; Fu et al. 2011; Pan et al. 2014). Rupture occurred on three primary faults; the multi-segment Beichuan fault, the parallel Pengguan fault, and the Xiaoyudong cross-fault (Fig. 2.4). These field studies detected right-lateral reverse faulting along the Beichuan fault over ~240 km extending from the epicenter to near Donghekou, finding oblique slip of up to 7.6 m near Yingxiu, 5–6 m near Hongkou, 6.6 m near Beichuan, 4.4 m near Pingtong, and 2.5 m near Nanba. A localized peak vertical offset of 11 m occurred near Beichuan (Liu et al. 2009), but this reduces rapidly to about 6 m within 1–2 km along strike. Pure reverse faulting along the more shallowly dipping Pengguan fault extended ~72 km

with maximum vertical offset of 3.5 m. The northwest-trending, 30°–45° southwest-dipping Xiaoyudong fault, which had not been recognized before 2008, experienced left-lateral slip of up to 2.2 m, and a scarp height of 3.5 m at the northwestern end diminishes to less than 0.2 m near the Pengguan fault (Liu et al. 2012). This salient appears to have strongly influenced the rupture segmentation (Chang et al. 2012). There are offsets of 3–4 km in the Beichuan fault and 2–3 km in the Pengguan fault near the intersections with the cross-fault (Fig. 2.4). Of 20 mapped surface ruptures, the rupture zone is <40 m wide for 17 cases, with 3 zones up to 59 m wide (Zhou et al. 2010).

The rough topography and variability of scarps due to inheritance of shallow southeast-dipping faults (e.g., Liu et al. 2010; Yu et al. 2010) make interpretation of many of the surface ruptures uncertain. For example, Lin et al. (2009) reported left-lateral slip of <2 m on the southern Beichuan fault, but this is not supported by other field studies or by geodesy. Lin et al. (2009, 2012) reported 0.3–0.6 m right-lateral strike-slip with 0.2–0.5 m vertical slip on the Qingchuan fault, but this small slip is not confirmed by InSAR or aftershock distributions so it is not clear whether it represents coseismic slip during the mainshock. The Qingchuan fault does appear to be active, with an estimated 3–5 mm/yr deformation rate in the late Pleistocene-Holocene (Lin et al. 2014).

Some of the fault exposures have been analyzed for surface roughness using portable laser scanners, displaying self-affine roughness with power spectral density and rms roughness having power law relationships with length of the profiles (Wei et al. 2010). Roughness is greater perpendicular to the slip direction than along the striations. Two boreholes were drilled through the Beichuan fault zone 400 m and 1 km west of a 4.3 m nearly vertical surface rupture, intersecting the inferred fault zone at depths of ~589 and 1230 m, respectively (Li et al. 2013, 2014a). Repeated temperature measurements were made in the first of these boreholes from 1.3 to 5.3 years after the rupture in an effort to detect frictional heating (Li et al. 2015). Multiple cataclasites intersect the borehole and it is ambiguous to identify the precise 2008 rupture surface in the vicinity of 576–589 m depth, with a zone of breccia extending down to 760 m. The lack of any thermal anomaly (<0.02 °C) near the assumed rupture surface bounds the dissipated heat energy to <1.2 MJ/m^2, suggesting an effective coefficient of dynamic friction of <0.02 during rupture. Tidal response of water level in the deep borehole tracks changes in permeability over 18 months and indicates a high hydraulic diffusivity in the damage zone of 2.4×10^{-2} m^2/s (Xue et al. 2013). The permeability appears to decrease with time due to fault healing, but is apparently intermittently increased by shaking from remote earthquakes.

A 16 station 400-m-long seismic array was deployed across the shallow fault rupture zone to record fault zone-trapped waves for aftershocks, supplemented by recordings of the Sichuan Seismic Network (Li et al. 2012, 2014b). The waveforms show complexities that can be well modeled by 3D finite-difference calculations with a 200-m-wide fault core zone within a 400-m-wide damage zone with seismic velocities in the damage zone reduced by 30–55% relative to the wall rock, extending to ~10 km deep, with the slowest velocities near the surface. The shallower dipping

Pengguan fault is unlikely to favor fault zone-trapped waves based on modeling for a wide range of fault zone dip.

The Wenchuan earthquake triggered landslides over a broad area, with earthquake-induced mass wasting contributing significantly to the overall erosion rate. Ouimet (2010) characterizes a 240-km-long area along the Beichuan and Pengguan faults where >10% of the surface is affected by landslides. The strongly affected zone is 25–30 km wide in the southwestern region and 3–5 km wide in the northeast. Dai et al. (2011) identify 56,000 triggered slides along the rupture zone, with some located 50–100 km to the northwest. Gorum et al. (2011) use satellite images and air photographs to map 60,000 landslide scarps, 57% of which are in the Pengguan Massif hanging wall of the Beichuan fault and 13% in the Pengguan fault hanging wall. Of particular note is the Donghekou rock avalanche, near the northeastern end of the rupture (Fig. 2.4). This so-called ejection landslide involved 10–15 $\times$ 10^6 m^3 of rock that experienced as much as 700 m drop and 2400 m runout, resulting in great loss of life in Donghekou. The landslide appears to have started with material being ballistically ejected by large local seismic acceleration, launching large boulders with parabolic trajectories (Yuan et al. 2010). The steep topography and lithologic structures may have influenced this, but it is also possibly a manifestation of enhanced ground motion from a mach cone produced by supershear rupture velocity in the northeastern steeply dipping dextral shearing portion of the rupture.

2.3 Seismological Constraints

The 2008 Wenchuan earthquake has been analyzed by a wide range of seismological approaches, including hypocentral location, seismic velocity tomography of the source region, moment tensor determination, aftershock analysis, back-projection and directivity analysis, strong motion modeling, and teleseismic inversion for finite-fault rupture process. Many of these constraints on the source process are noted here.

The USGS National Earthquake Information Center (NEIC) located the May 12, 2008 hypocenter at 31.002°N, 103.322°E, 19 km deep at 06:28:01.6 UTC (https://earthquake.usgs.gov/earthquakes/eventpage/usp000g650#executive). The NEIC also reports $M_S = 8.1$ based on observations from 199 stations. Using local data from the Sichuan Province Seismic Network and the Zipingpu Reservoir Seismic Network, Yang et al. (2012) relocated the hypocenter as 31.018°N, 103.365°E, 15.5 km deep at 14:27:57.59 local time. An et al. (2010) relocated the event at 31.001°N, 103.280°E, 17 km deep. Various other estimates of the hypocentral location (most being slightly south of the values above), origin time, and M_S have been reported (e.g., China Earthquake Administration; Chen et al. 2009a, b).

The crustal structure around the source region is clearly heterogeneous (Fig. 2.3), and regional tomography indicates high P and S wave velocity in the upper 15 km of the Pengguan Massif, which forms the hanging wall of the southern Beichuan fault (e.g., Wang et al. 2009c; Wu et al. 2009a; Pei et al. 2010; Xu et al. 2010b). Wang et al. (2009c) analyzed 200,000 local P and S travel times, detecting some offsets in

structure between segments of the Beichuan fault. The rupture initiated in a region of high Poisson's ratio in the southwest that extends to the lower crust around 20 km deep, where velocities are low.

2.3.1 Focal Mechanisms and Aftershock Distribution

Point-source focal mechanisms for large earthquakes provide an overall measure of the strain release. The global centroid-moment-tensor (GCMT) solution for the 2008 Wenchuan earthquake has a predominantly (93%) double-couple solution with strike 231°, dip 35°, rake 138°, centroid time shift 38.8 s, centroid depth 12.8 km and seismic moment 8.97×10^{20} Nm (M_W 7.9) (http://www.globalcmt.org/CMTsearch.html). The W-phase solution from Duputel et al. (2012) has a much smaller (48%) double-couple component, with the best double couple having strike 222°, dip 29°, and rake 152°, and seismic moment 1.19×10^{21} Nm (M_W 8.0). These mechanisms both indicate an overall oblique thrusting moment tensor with significant right-lateral component.

A vigorous aftershock sequence followed the 2008 rupture, with many events being located by the USGS-NEIC (Fig. 2.3), and many more located by regional networks and portable seismometer deployments (Zhang et al. 2010). Huang et al. (2008) relocated 2553 events with $M > 2$ using double-difference locations. The events are distributed along 330 km from southwest to northeast, with some indication of listric faulting around 20 km deep in the southwest. Double-difference relocations of 3622 events with a 350-km-long distribution were also performed by Chen et al. (2009b) using data from a movable seismic array. Most aftershocks are in the depth range 10–22 km. They found narrower aftershock distribution in the northeast consistent with more steeply dipping fault and broader aftershock distribution along the Pengguan Massif extending from 4 to 24 km deep.

After relocating aftershocks, Zheng et al. (2009) used regional Chinese network waveforms in the Cut-and-Paste method to estimate focal mechanisms and source depths of larger ($M \geq 5.6$) aftershocks. Thrust faulting dominates overall, even in the northeast, with few strike-slip solutions. 2878 aftershocks were located by double-difference using a temporary network deployed from July to October 2008 by An et al. (2010). They found that most aftershocks are shallower than 20 km. A region of low seismicity through Yingxiu Town separates two blocks along the Beichuan fault. Cai et al. (2011) used an 89 station network to locate 1376 aftershocks from May 12 to August 3, 2008, by cross-correlation, and then determined 89 P wave first-motion mechanisms showing sub-horizontal compression axes, with a mix of thrust and strike-slip faulting. Moment tensor inversions for 160 events with $M \geq 4$ from May 12 to September 8, 2010, were obtained by Lin et al. (2018), again with a mix of reverse and strike-slip mechanisms and a handful of normal faulting solutions. Yin et al. (2018) used data from a temporary array and 1273 events in a relocated catalog as templates to search the first 7 days after the mainshock, detecting 12,914 events. Most aftershocks are below 10 km depth and in the regions down-dip

of peak mainshock slip. Migration with time along strike suggests afterslip at depth. The locations support the possibility of high-angle listric faulting shallowing into a 20-km-deep décollement for both the southwestern Beichuan and Pengguan faults. The northeastern segment of the Beichuan fault is steeply dipping. The Xiaoyudong cross-fault shows some post-seismic deformation. The overall aftershock distribution extends southwest of the epicenter by about 20 km and northeast of Donghekou to beyond the Qingchuan fault (Fig. 2.4), suggesting extension of the Beichuan fault into the Bikou Massif to the northeast (Zhang et al. 2010). Minor activity spreads along the Qingchuan fault, possibly related to the small surface slip noted earlier. While there is clearly segmentation along the Beichuan fault, the aftershocks and surface ruptures of the Wenchuan event indicate a generally continuous rupture along the fault zone.

The abundant aftershock recordings enable examination of period and amplitude parameters for *P* waves of 24 events, allowing some calibration of potential early warning applications for future events (Wang et al. 2009b). This is particularly relevant as activation of nearby faults in the Longmen Shan due to stress adjustments to the 2008 event is a serious concern, as discussed below.

2.3.2 Back-Projection and Surface Wave Finiteness Constraints

Constraints on the rupture velocity and directivity for the 2008 Wenchuan earthquake have been obtained by back-projection of teleseismic short-period *P* waves and directivity analysis of global Rayleigh waves. These constraints are valuable for constraining finite-fault inversions. Du et al. (2009) analyze high-frequency energy in Alaska to infer a 90-s-rupture process with northeastward expansion. They infer an average speed of 2.2 km/s during the 50 s, with rupture extending about 110 km, and then faster, supershear rupture at 4.8 km/s for the next 40 s, with rupture extending another 190 km. The possibility of supershear rupture of the northeastern predominantly strike-slip region of faulting is supported by finite element modeling by Zhu (2018), who finds that as dynamic rupture models traverse the Gaochuan bend (Fig. 2.4), rupture speed can increase to 5.02 km/s. Xu et al. (2009c) analyzed *P* wave data in large aperture networks of global, Alaskan, Australian, and European stations, inferring unilateral rupture extending ~300 km to the northeast of the epicenter with a duration of about 110 s, with average rupture speed of 2.8 km/s. Similarly, Zhang and Ge (2010) analyzed Australian data, finding a 98 s duration and rupture length of 290 km, with rupture speed of about 3 km/s. These studies detected bursts of coherent short-period energy along strike, but these need not correspond to large-slip regions. Wang et al. (2016) back-project short-period data from networks in Europe and Alaska and infer an overall process with a rupture velocity of 1.8 km/s during the first 40 s of rupture and 3.5 km/s during the next 60 s of rupture. They note that even faster speed of the latter portion of the rupture at about 4.3 km/s

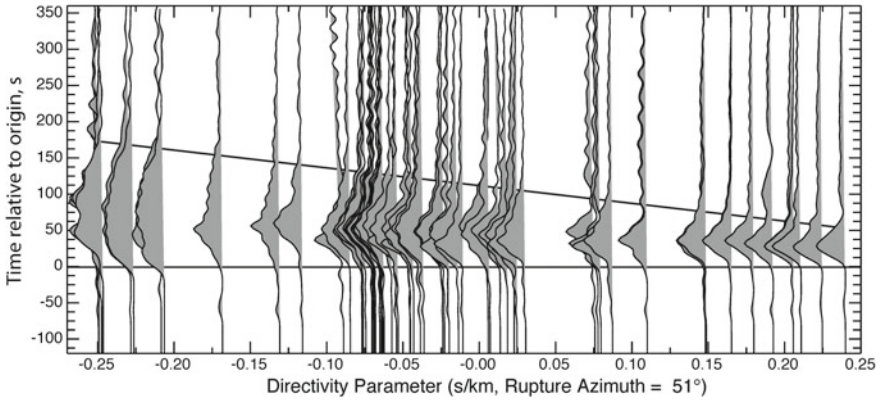

Fig. 2.5 Rayleigh wave source time functions obtained by iteratively deconvolving point-source synthetic waveforms from corresponding observations for the May 12, 2008, Wenchuan earthquake. The deconvolutions use a positivity constraint and are aligned on the origin time of the earthquake. The slanted line is an approximate fit to the termination of the source time functions, which are plotted as a function of unilateral directivity parameter assuming a rupture azimuth of 51°. Figure courtesy of C. J. Ammon

is indicated by moment release from near-field strong motion inversion by Zhang et al. (2012). Okuwaki and Yagi (2018) apply a hybrid back-projection method, finding concentrations of high-frequency radiation near fault segment boundaries and fault steps. Huang and Yao (2018) apply compressive-sensing back-projection to detect frequency-dependence of the along-strike rupture, with low-frequency radiation along smooth rupture segments and concentrations of high frequency near the complexities like the Xiaoyudong cross-fault and the Nanba fault step-over. Rupture speed accelerates near the complexities.

Rayleigh waves also exhibit strong directivity toward the northeast. Hwang et al. (2011) analyzed 100-s period Rayleigh wave phase velocity delay time, inferring a unilateral rupture azimuth of N59°E, with a rupture length of 210 km, a rise time of 9.3 s, and duration of 70 s, giving an average rupture velocity estimate of 3 km/s. Figure 2.5 displays the clear Rayleigh wave directivity apparent in Rayleigh wave relative source time functions (RSTF), which have been obtained by iterative deconvolution of point-source synthetic seismograms computed at the hypocenter with the GCMT focal mechanism. A positivity constraint was used. The data are aligned with respect to the directivity parameter, $\Gamma = \cos(\phi_{sta} - \phi_{rup})/c$, where ϕ_{sta} is the station azimuth, ϕ_{rup} is an assumed unilateral rupture azimuth (N51°E), and c is a reference phase velocity of 4 km/s. Assuming a simple unilateral rupture, the maximum RSTF duration is $T_{max} = 170$ s and the minimum is $T_{min} = 50$ s, giving an average total rupture duration of $T_{avg} = 110$ s. The estimated fault length, $L = (c/2) \times (T_{max} - T_{min}) = 240$ km. Assuming a rise time of $0.2 \times T_{avg}$, these values give an average rupture velocity of ~2.7 km/s.

2.3.3 Strong Motions Observations

An extensive data set of strong motion observations was produced by the Wenchuan earthquake. A preliminary summary of the observations by Li et al. (2008b) documented 460 free-field stations in 17 provinces, municipalities, and autonomous regions, along with several arrays and portable deployments after the mainshock. Among the 1400 components recorded, the largest peak acceleration is 957.7 gal, and there are 7 values larger than 600 gal. Initial numerical simulations of the strong motions were explored by Wei et al. (2008).

Bjerrum et al. (2010) used three early finite-slip models from Koketsu et al. (2009), Ji (2008), and Nishimura and Yagi (2008) for deterministic and semi-stochastic simulation of strong motion. They found that the models predict large variation in ground shaking due to the slip heterogeneity and width of the fault plane. Similarly, strong motions were simulated using stochastic finite-fault models with two segments with two large asperities 45 and 170 km northeast of the hypocenter by Ghasemi et al. (2010), evaluating predictions against the observations from 108 accelerograms at 54 stations within 150 km. An empirical Green's function (EGF) method using records from an event in Japan was applied by Kurahashi and Irikura (2010) in hybrid modeling with the model of Koketsu et al. (2009), with three asperity locations. Directivity in the strong motions was overpredicted by the assumed kinematic effects.

In a more deterministic analysis, a multi-time window finite-fault inversion using 26 strong motion recordings was performed by Zhang et al. (2012). Using an average rupture velocity of 3 km/s, they found large slip 20–50 km northeast of the hypocenter, with rupture spreading around a large asperity that broke abruptly about 25 s after rupture initiation. Their model had variable dip along a three-segment model of the Beichuan fault and included slip on the Pengguan fault.

2.3.4 Teleseismic Inversions with 1D Green's Functions

Far-field seismic waves intrinsically provide limited resolution of the details of earthquake ruptures, but in the case of a long unilateral rupture like the 2008 Wenchuan event, the overall slip distribution can be quite well determined. Early inversions (e.g., Yamanaka 2008; Nishimura and Yagi 2008; Ji 2008; Yagi et al. 2012) assumed a single uniformly dipping (30°–33°) fault plane adopted from the point-source moment tensor estimates. These models had one or two large-slip patches along strike, but limited detail. For example, the model of Ji (2008) used 17 *P* waves, 15 *SH* waves, and 30 surface waves, finding large-slip regions 30–40 and 170–180 km from the hypocenter about 10 km deep, along a 33° dipping plane striking 229°, with an average rupture velocity of ~2.4 km/s. Teleseismic and strong motion data were inverted by Koketsu, et al. (2009) giving comparable models.

An example of the author's early teleseismic body wave inversion for a single-plane rupture model with a dip of 35° is shown in Fig. 2.6a. This model was obtained by linear least squares multiple time window inversion of 35 *P* and 20 *SH* waves.

Minor, poorly resolved, slip is found southwest of the hypocenter, and a large-slip patch with predominantly oblique thrust motion is located 40–60 km northeast of the hypocenter, with increasingly right-lateral strike-slip motion to the northeast. The subfaults all have six 2.0-s rise-time triangles, and the estimated seismic moment is 1.12×10^{21} Nm. A two-segment fault model obtained by inversion of the same data set is shown in Fig. 2.6b, with dip in the northwestern segment increased to 70°. This causes rake to vary with depth. The effect of listric reduction of dip with depth for a two-segment model is shown in Fig. 2.6c. In the southwestern region, the fault dip smoothly decreases from 45° at the surface to 25° at a depth of 22 km. In the northeastern region, the fault dip smoothly decreases from 80° to 60°. The inverted slip model is very similar to the uniformly dipping case in Fig. 2.6b, suggesting that there is little resolution of listric geometry from the teleseismic body wave data. Comparison of observed and predicted waveforms for the model in Fig. 2.6c is shown in Fig. 2.7. Major features in the waveforms are well matched; the model accounts for ~80% of the power in the signals, but small features are not matched.

Zhang et al. (2009) used 21 long-period *P* waves for a single-dip (39°) fault model, finding average slip of 2.4 m along a 300 km long fault with strike 225°. Their model indicates large-slip patches near Yingxiu, Beichuan, Kandig, and Qingchuan. They estimate an 18 MPa average stress drop. Nakamura et al. (2010) inverted teleseismic body waves for a fault model with two segments, finding predominantly thrust motion near the epicenter and strike-slip motion from 110 km northeast to the end of the fault. The maximum slip was 11 m, and the seismic moment is 1.2×10^{21} Nm. They used the slip model to simulate broadband waveforms using 3D spectral element calculations, supporting the basic model. Zhao et al. (2010) inverted 39 *P* and *SH* waveforms for a 100 s duration model with dip of 42° extending 280 km long. Similar to the model in Fig. 2.6a they found large oblique slip in the southwest with nearly pure dip-slip at shallow depth and horizontal slip in the northeast from Beichuan to Qingchuan with 5 large-slip subevents distributed along strike.

An updated version of the inversion of Ji (2008) using the same data set (https://earthquake.usgs.gov/earthquakes/eventpage/usp000g650#finite-fault) is posted on the USGS-NEIC Web site. This model has two segments representing the Beichuan fault, dipping 46° and 50° from southwest to northeast, along with a 28° dipping plane representing the Pengguan fault. The hypocenter is on the latter fault, near its intersection with the Beichuan fault 14 km deep. The seismic moment estimate is 8.8×10^{20} Nm, and there are 4 large-slip patches along the Beichuan fault.

Deconvolution of teleseismic waves using three thrust and strike-slip aftershocks to obtain empirical Green's functions for teleseismic waves was performed by Wen et al. (2012). Their fault model has three segments with high spatial variability of slip and rupture velocity. They infer that the rupture starts with thrust motion and low rupture velocity of 1.7 km/s, and the rupture speed increases to 3.1–3.3 km/s with large slip in a region of overlapping fault segments, then it slows to 2.5–2.9 km in the northeastern strike-slip region. The total rupture extends 300 km with 2.6–2.9 km/s average rupture speed. A linear inversion of teleseismic signals then gives a final slip model with variable rupture velocity with three large-slip patches near Yingxiu, Beichuan, and Nanba.

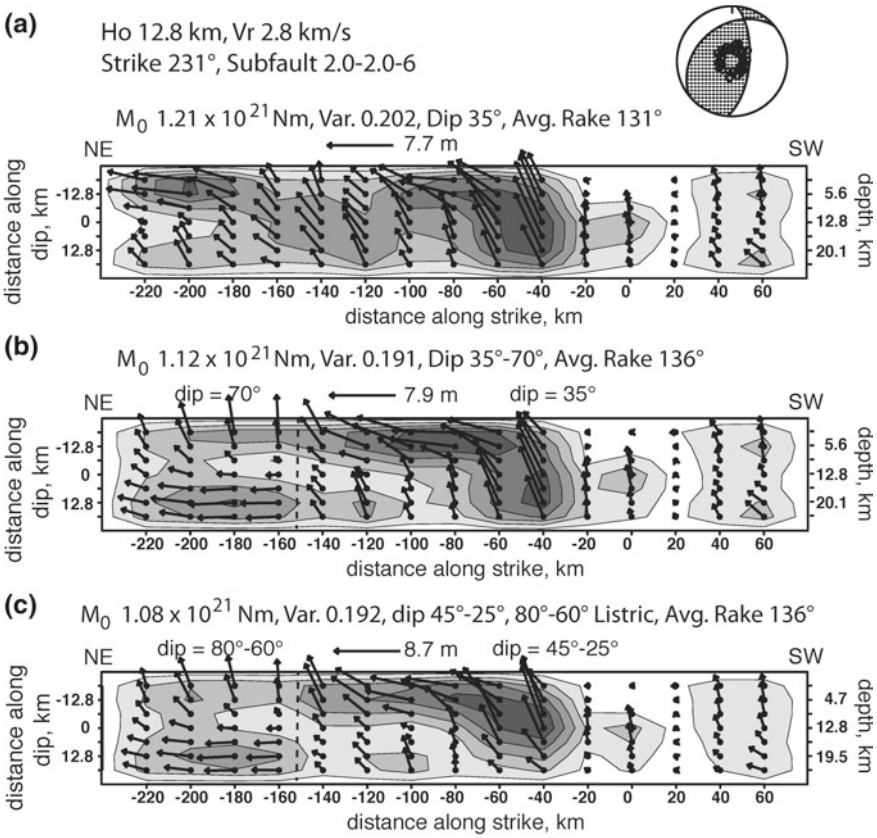

Fig. 2.6 Early finite-fault slip inversions using teleseismic *P* and *SH* data for **a** a single planar fault model dipping 35°, **b** two fault segments (separated by the vertical dashed line) with 35° dip in the southwest and 70° dip in the northeast, and **c** two fault segments (separated by the vertical dashed line) with listric decreases in dip as depth increases, from 45° to 25° in the southwest and from 80° to 60° in the northeast. In all cases, the strike is 231° and the rupture expansion velocity is 2.8 km/s, with the hypocenter being 12.8 km deep. The source time function for each subfault is comprised of six 2-s rise-time symmetric triangles staggered by 2-s, allowing up to 14 s subfault source durations. The magnitude of slip is contoured, with the peak slip indicated in each case and the arrows indicating variability of average rake on each subfault. The focal mechanism indicates the average fault geometry for model (**a**) and shows the azimuthal distribution of *P* wave data used in the inversion. Figure 2.7 shows comparisons of the observed and predicted data *P* and *SH* data for the listric model in (**c**). All three models have residual waveform misfit power of about 0.2

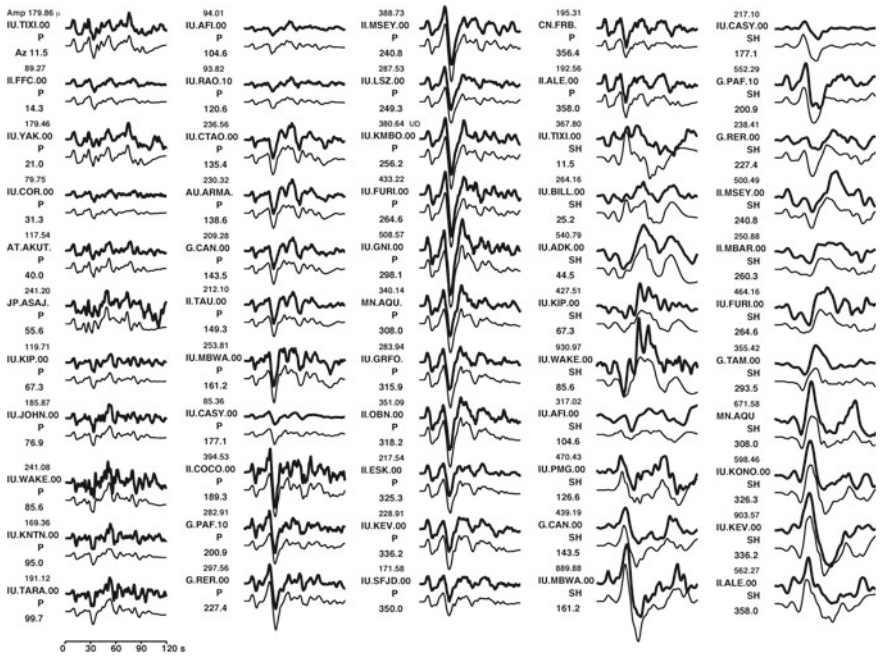

Fig. 2.7 Comparisons of observed *P* and *SH* data (bold lines) and model predictions for the finite-fault inversion solution with listric faulting and variable dip along strike shown in Fig. 2.6c. The peak-to-peak amplitude in microns is shown above each station name and the azimuth is shown below. *SH* waves were given 0.2 times the weight of *P* waves in the inversion

2.3.5 Teleseismic Inversions with 3D Green's Functions

The 2008 Wenchuan earthquake occurred in a region of acute crustal heterogeneity and surface topography, raising the issue of how the 3D surface topography affects seismic wave ground motions both locally and teleseismically. Chavez et al. (2010) computed finite-difference calculations of local ground motion velocity predictions using 3D structure and the model of Ji (2008). Patterns of along-rupture ground velocities demonstrate the effects of northeastward directivity that correspond with asymmetry in intensity isoseismals.

The influence of rough surface topography along the rupture on teleseismic body waves used in finite-fault inversions presents a difficult challenge, particularly given the extent of the rupture and magnitude of the surface roughness. Calculation of teleseismic *P* wave Green's functions using a hybrid approach was performed by Avants (2014). The 3D finite-difference code WPP, from Livermore National Laboratory, was used to compute displacement and stress time series on a dense grid near the bottom of the computational model below the rough surface topography along the fault. The representation theorem was then used to compute far-field *P* wave Green's functions including the *pP* and *sP* interactions with the rough surface topography, for

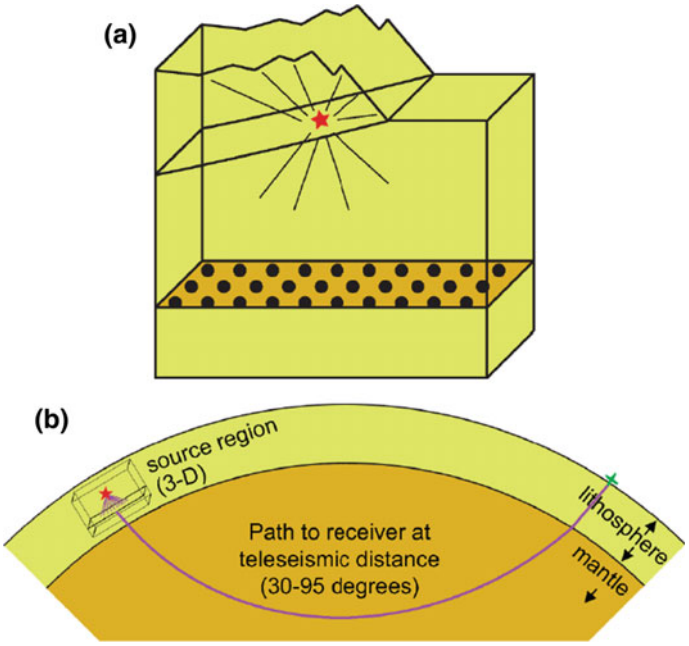

Fig. 2.8 Schematics of the modeling procedure for including rough surface topography in the calculation of Green's functions for teleseismic *P* wave inversion for finite-fault models for the 2008 Wenchuan event. **a** Depiction of the rough surface topography, which ranges over 4 km above the westward dipping faults beneath the Longmen Shan and the flat Sichuan Basin. A finite-difference method is used to calculate the wavefields from a grid of source locations on specified faults collecting the space and time history of stress and displacement at each point on the horizontal sampling grid at depth below the source region. **b** The space-time varying stress and displacement wavefields computed on the sampling grid are then used in the representation theorem with generalized ray theory to predict the far-field *P* wave observations at teleseismic station locations, applying corrections for attenuation and geometric spreading

generalized ray theory first-motion approximations, including geometric spreading and attenuation operators (Fig. 2.8). This approach is only able to compute about 20 s duration Green's functions to avoid interference of down-doing *S* waves from the source, but it does predict the effects of the free surface interactions in the *P* wave packet. Comparison of Green's functions for teleseismic *P* waves at different azimuths for a flat free surface and a rough free surface is shown in Fig. 2.9 for strike, dip and rake values used in fault segments along the rough topography. Steeper dip of 70° is used in the northeast, 50° dip is used in the central fault, and 35° dip is used in the southwestern portion of the fault.

Linear inversions using 40 teleseismic *P* waves for a relatively coarse fault model grid with 3 subfaults along dip and 19 along strike, with three planar segments having varying dip from 35° to 70°, are shown in Fig. 2.10. A model is shown for Green's functions with a flat free surface (Fig. 2.10a) and for Green's functions for the 3D

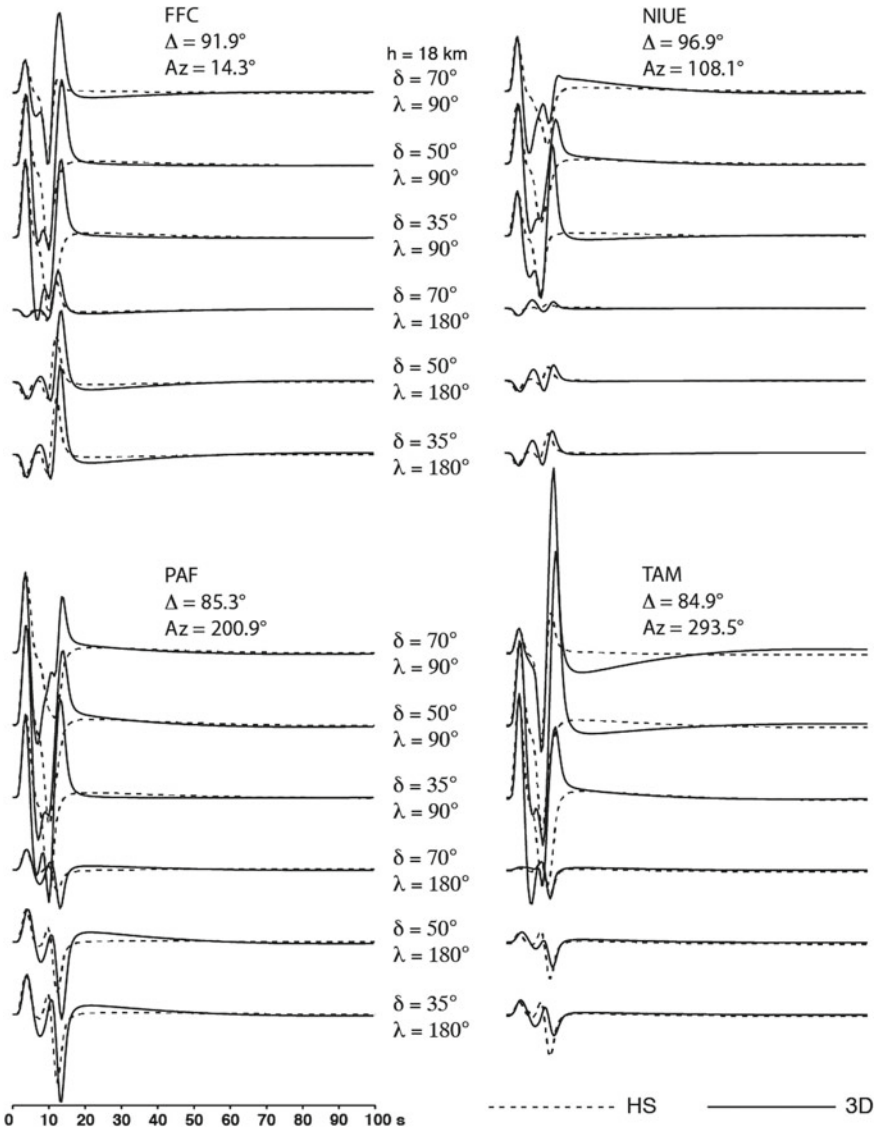

Fig. 2.9 Examples of individual station teleseismic *P* wave Green's function for a source depth of 18 km for a flat surface uniform half-space (HS) and for the 3D rough surface over uniform half-space (3D) case. The Green's functions span the range of dip (35°–70°) and rake (90°–180°) considered in the finite-fault inversions at appropriate along-strike positions under the 3D topography. The *P* wave signals include direct down-going *P*, *pP,* and *sP* surface reflections, and any early out of plane scattering for the 3D case

topography (Fig. 2.10b). The rupture velocity is 2.8 km/s for both cases. Two large-slip patches are found along strike, with oblique thrusting in the southwest and more strike-slip motion in the steeper dipping northeast, similar to models in Fig. 2.6. The effect of the laterally varying 3D topography on the slip inversions is rather subtle, despite the substantial differences in Green's functions apparent in Fig. 2.9. This is due to the intrinsic low-pass nature of projection of data into the slip model, with rapidly varying differences in far-field Green's functions from finite wavelength interactions with the rough free surface tending to be averaged over in the finite-fault imaging. The moment rate functions are quite similar, although the 3D model does recover a somewhat lower total moment. This is a first-cut approach, at the time it was perhaps the first use of truly 3D Green's functions for teleseismic distances for developing a finite-fault model for a large earthquake. A method that can account for the later coda generated by the rough topography (longer Green's functions) may lead to stronger systematic effect of the 3D structure in the finite-fault imaging. The rather subtle differences in models obtained with 1D and 3D Green's functions do provide some assurance that the first-order features of the models based on 1D calculations are relatively stable.

2.4 Geodetic Constraints

The Wenchuan earthquake provided extensive geodetic observations that have been analyzed by many researchers. Continuous observations were not acquired, and there is some contribution from early post-seismic deformation to the GPS and InSAR measurements that dominate the geodetic observations. High-rate GPS acquisition was not yet broadly practiced at the time of the event. With this caveat, the geodetic data provide high-resolution information about the source process that adds precision to the smoothed images from the far-field seismic observations.

2.4.1 GPS and InSAR Displacements and Rupture Models

The Working Group of the Crustal Motion Observation Network of China Project (2008) consolidated early geodetic measurements for the 2008 source, including 435 campaign and 35 permanent GPS sites, 42 spirit leveling vertical displacements and triangulation sites. Wang et al. (2008) used the GPS data to construct a source model with a two-segment Beichuan fault and the Pengguan fault. Slip distributions were derived from 122 GPS stations by Diao et al. (2010), for Beichuan and Pengguan fault models with dip decreasing with depth. The peak slip on the Beichuan model had 9 m slip near Beichuan and Jiangyou and involved right-lateral and reverse faulting, while the Pengguan fault model has 2–3 m reverse slip. They assert that listric models with dip shallowing to 20° in the mid-crust perform better than constant dip models. They noted that the aftershocks tend to be down-dip of regions with large slip.

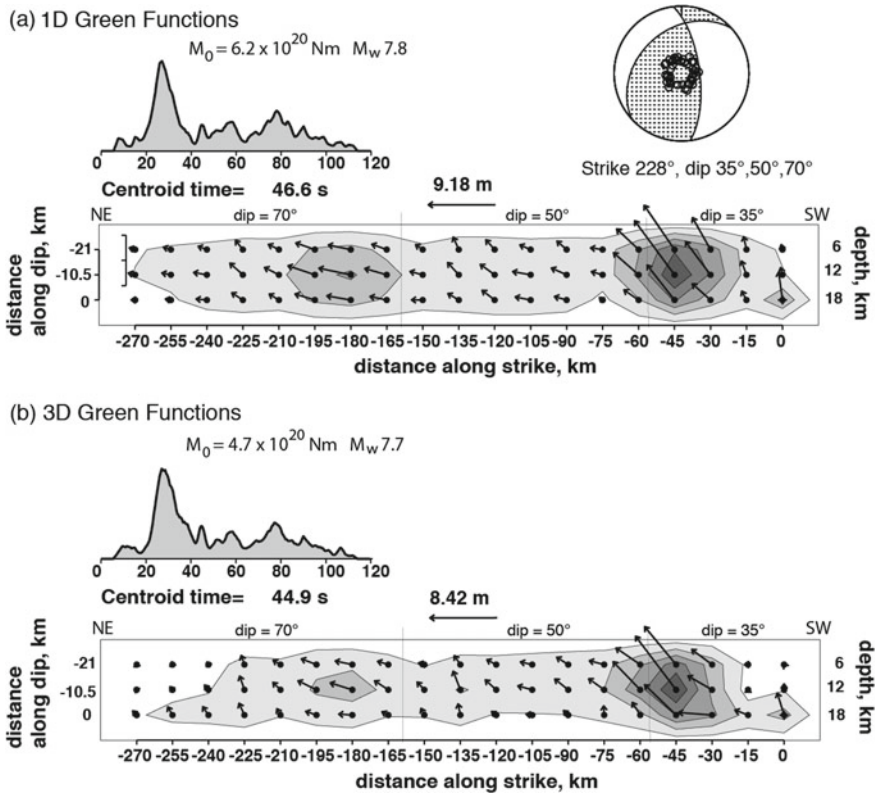

Fig. 2.10 Finite-fault slip inversions using teleseismic *P* wave data for three-segment models with dip varying along strike from 35° to 50° to 70° (separated by vertical dashed lines), for **a** Green's functions from a uniform elastic half-space with flat free surface, and **b** Green's functions for a uniform elastic half-space with 3D rough surface topography smoothed from the actual topography shown in Fig. 2.3. In all cases, the strike is 228° and the rupture expansion velocity is 2.8 km/s, with the hypocenter being 12 km deep. The source time function for each subfault is comprised of six 2-s rise-time symmetric triangles staggered by 2-s, allowing up to 14 s subfault source durations. The magnitude of slip is contoured, with the peak slip indicated in each case and the arrows indicating variability of average rake on each subfault. The focal mechanism indicates the average fault geometry in the first segment for model (**a**) and shows the azimuthal distribution of *P* wave data used in the inversion

Wang et al. (2010b) compare the GPS predictions of slip models from teleseismic inversions by Ji (2008) and Zhang et al. (2009), with those of the geodetic inversion by Wang et al. (2008), demonstrating the expected greater detail provided by the geodetic data. They then inverted teleseismic data assuming a listric Beichuan fault model 308 km long and including the Pengguan fault. As in earlier models, they found large-slip patches near Hongkou and Beichuan-Pingtong.

InSAR data have also played a significant role for constraining the rupture process although there were limitations in azimuth offset measures due to strong ionospheric

signals for much of the data. Early investigations by Sun et al. (2008), Hao et al. (2009), Kobayashi et al. (2009), Shan et al. (2009a, b), Hashimoto et al. (2010), and Furuya et al. (2010) used six to eight ascending orbits from L-Band ALOS/PALSAR differential SAR Interferometry to estimate continuous surface deformations. Unlike the earliest seismic models, these studies clearly detected the deformation on both the Beichuan and Pengguan faults, as observed by the field observations, with dominant shallowly dipping thrust component in the southwest and steeper-dipping strike-slip in the northeast. Pixel-offset methods were used to improve resolution in the decorrelated near-fault regions, improving resolution of slip and subfault segmentation along the Beichuan fault. de Michele et al. (2010a) used a sub-pixel correlation method to estimate slip along 270 km of the Beichuan fault and 70 km of the Pengguan fault. Oblique thrusting with dextral component is observed along the Beichuan fault. They note that using ascending data only does not provide a unique sense of displacement and additional data are needed to interpret the data. Qu et al. (2012) extended pixel-offset tracking for six tracks of ALOS/PALSAR data, inferring slip along 238 km of the Beichuan fault and offsets on the Xiaoyudong cross-fault.

Combining GPS and InSAR observations helps to retrieve longer wavelength surface displacements, and addition of descending track data less affected by ionospheric signals improves the resolution of slip. Shen et al. (2009) used data from 158 GPS sites and ALOS PALSAR range-change data to obtain a fault model with dip varying from 43° in the southwestern Beichuan fault to 96° in the northeast. Three regions of high slip near Yingxiu, Beichuan, and Nanba (Fig. 2.4) were detected, with large slip near fault bifurcations and conjugate junctions. They estimated a seismic moment of 8.03×10^{20} Nm, possibly enhanced by some post-seismic data. GPS, InSAR, and field observations were incorporated into a fault model by Tong et al. (2010), with four subfaults with variable geometry and dip. Faults dip 35° in the southwest and 70° in the north. Mainly thrust slip less than 10 km deep is found on the southern segment of the Beichuan fault with slip up to 13 m, with right-lateral slip of up to 7 m in the northeast. Similarly, Feng et al. (2010) use GPS and six ALOS/PALSAR ascending orbits with pixel offsets to determine slip on 3 planar fault segments along the Beichuan fault and a single Pengguan fault. They estimate 6.7 m thrust slip near Yingxiu and Beichuan, and 4 m strike-slip offset near Pingtong and Nanba. Small slip on the Pengguan fault is detected. The resolution of strike-slip motion is not as good as for vertical motion.

Optimal weighting of information from GPS horizontals, GPS verticals, and ALOS/PALSAR L-band data was evaluated by Xu et al. (2010a). They obtained a slip model with 4 large-slip patches, with 10 m slip near Hongkou/Yingxiu and Beichuan and substantial slip near Yuejiashan and Nanba. Right-lateral oblique thrusting occurred in the southwest and right-lateral slip of 1–2 m occurred in the northeast. Most slip is shallower than 10 km, but deeper slip may occur in the southwest. Their estimate of the seismic moment was 8.19×10^{20} Nm.

Slip on the Beichuan and Pengguan faults was also inferred from 1521 components of GPS campaign data, 42 spirit leveling vertical displacements and 342 InSAR line-of-site range changes from 8 L-band ALOS/PALSAR orbits by Wang et al. (2011). They allowed for listric fault geometry in the southwest, finding 2–6 m of slip on a

deep décollement fault. Slip along a two-segment Beichuan fault with southwestern dip of 55° and northeastern dip of 70° has four large patches above 20 km near Hongkou, Qingping, Beichuan, and Nanba, in basic agreement with the models of Shen et al. (2009), Tong et al. (2010), and Feng et al. (2010). The Beichuan fault and 35°-dipping Pengguan fault both root into the décollement. Zhang et al. (2011) combined GPS and InSAR data in a linear inversion for slip, stabilizing rake variations and exploring the effect of crustal layering. They find 3 peak-slip asperities near Yingxiu, Yuejiashan, and Beichuan, with predominantly thrust in the southwest and right-lateral strike-slip in the northeast, along with modest pure-thrust slip on the Pengguan fault. Layered models place 15–20% more slip at greater depth than half-space models.

Use of ascending and descending track SAR data along with geologic data improves resolution of slip and can overcome some of the ionospheric contamination of the ascending tracks (e.g., Tong et al. 2010; de Michele et al. 2010b). Tong et al. (2010) combine L-band ALOS/PALSAR line-of-sight displacements from ascending track data with descending track ScanSAR ALOS interferograms. Having multiple radar look directions greatly improves the resolution of slip along a rupture. Jointly inverting with 109 GPS displacement vectors and geologic scarp height measurements, a 4-fault slip model is obtained, with three segments along the Beichuan fault with dip varying from 35° in the southwest to 50° in the central segment to 70° in the northeast, and the Pengguan fault dipping 25°. Maximum slip depth was from 21 to 23 km along the Beichuan fault and 7 km on the Pengguan fault. Maximum slip was 13 m in the southwestern segment, 12 m in the central segment and 7 m in the northeastern segment, and 12 m on the Pengguan. The geodetic seismic moment is 6.79×10^{20} Nm. Aftershocks locate below the average slip at shallow depth on each segment. de Michele et al. (2010b) used C-band and L-band data from ascending and descending tracks with sub-pixel correlation analyses to constrain 3-D surface displacements. Their processing of correlograms reduces sensitivity to tropospheric phase delays. Field measurements from Xu et al. (2009a) were used to validate the near-fault displacements. The average motion on the southwestern Beichuan fault has 3.5 m vertical motion, 4.8 m perpendicular to strike, and 3.5 m parallel to strike, while the northeastern region has up to 5 m of dextral slip. The left-lateral slip on the Xiaoyudong cross-fault was resolved. The possible role of a blind thrust along the northeastern portion of the fault to accommodate compression was proposed, but no slip on such a structure was resolved.

Wan et al. (2017) analyze the available InSAR and GPS data, exploring layered elastic structure variations across the Beichuan fault, which varies in dip from 36° in the southwest to 83° at the northeast end of the rupture. 8.4 m of thrust motion and 5 m of dextral slip are found near Hongkou and 6 m of thrust motion and 8.4 m of dextral slip near Beichuan. Peak slip is located near changes in fault geometry and complexities that act as geometric barriers.

Reanalysis of the InSAR data to eliminate strong ionospheric signals was performed by Feng et al. (2017). They estimate fully 3D surface displacements (Fig. 2.11) from InSAR and compare the image offsets with GPS and field observations. They assert that prior studies using ascending ALOS data have biased coseismic

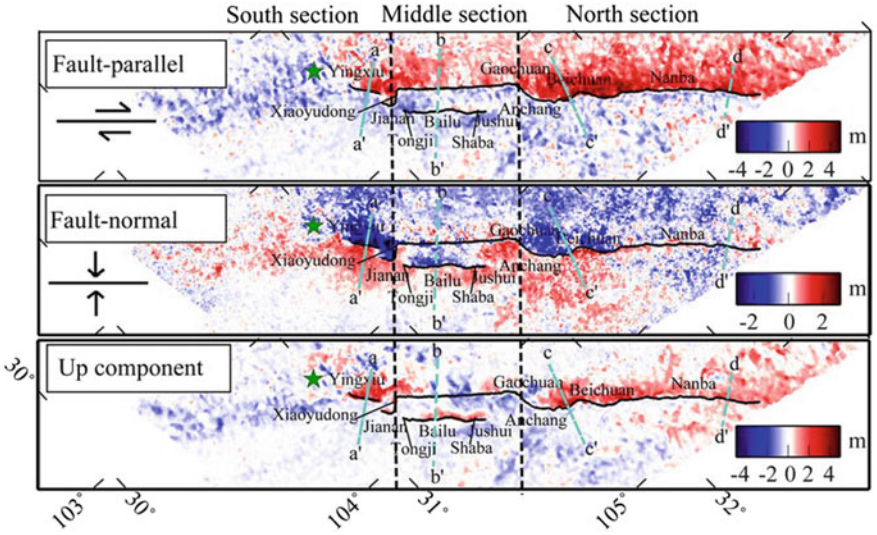

Fig. 2.11 Derived 3D surface displacement distribution inferred from sub-pixel correlation analysis of combined ascending ALOS and descending Envisat synthetic aperture radar data. Displacement is shown as fault-parallel, fault-normal, and vertical displacement (positive = right lateral/up, negative = left lateral/(down). Figure from Feng et al. (2017)

deformation maps and dissimilar slip at depth due to strong ionospheric distortions and that pixel-offset tracking is also affected by ionospheric disturbance. By adding in post-event SAR data free of strong ionospheric signals, the early long-period contamination can be suppressed, improving consistency with the GPS data and allowing use of both range and azimuth SAR image offsets. Their processing indicates some faulting along a northeastward extension of the Beichuan fault, but no clear rupture of the Qingchuan fault. They infer that the southern tip of rupture is at 31.065°N, 103.551°E, near the estimates of the hypocentral location, with the northeastern terminus being less clear, but near 32.424°N, 106.126°E. They find vertical slip of up to 6.5 m with dextral slip of up to 5.5 m on the Beichuan fault and up to 3.5 m on the Pengguan fault.

2.5 Joint Inversions from Seismic and Geodetic Data

Given that the geodetic data resolve overall faulting offset with no time evolution and with some contribution of post-seismic deformation, the most comprehensive representations of the faulting process are obtained by joint inversions of the seismic and geodetic data. Two fault model solutions from such joint inversions are shown in Fig. 2.12, with their consistencies and inconsistencies representing what we do and do not know about the rupture process.

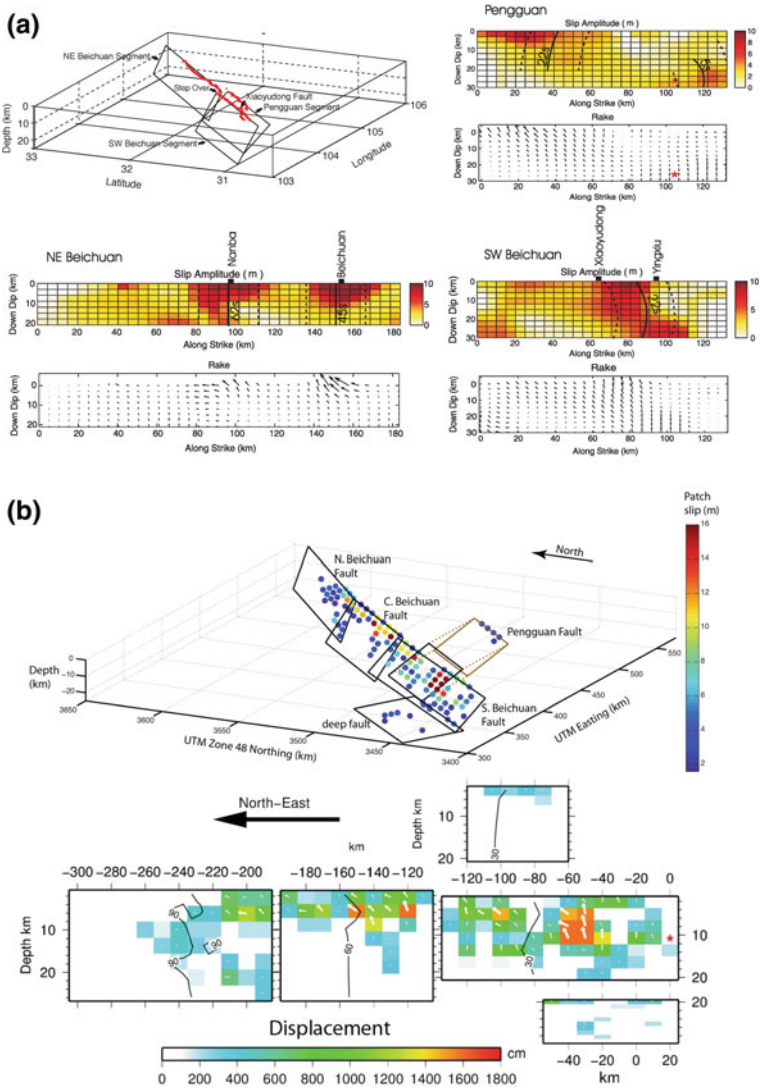

Fig. 2.12 Multiple-fault slip models from joint inversion of seismic and geodetic data. **a** The linear, multiple time window inversion of teleseismic, strong motion, and geodetic data by Hartzell et al. (2013). The 3D plot shows the placement of each of the three faults, along with the Xiaoyudong strike-slip cross-fault. Red lines indicate mapped surface slip. The rupture front is shown at times 5, 22, 45, and 52 s after initiation of rupture in the fault slip maps. Slip amplitude is indicated by the color scale, and slip direction and magnitude are shown in the lower panels. The slip duration allowed at each position is up to 10 s. The rupture hypocenter is the red star on the Pengguan fault. **b** 3D plot of the 5-fault slip model from joint inversion of teleseismic, SAR and GPS data by Fielding et al. (2013). The Beichuan fault has three segments with dip of 45° in the south, 55° in the center, and 70° in the north. The Pengguan fault dips 34°; note that it is displayed twice with the brown offset version clarifying the lack of deep slip. The deep fault dips 5°. The hypocenter is at the southern end of the S. Beichuan Fault

Figure 2.12 summarizes the joint inversion of geodetic, teleseismic, and strong motion data by Hartzell et al. (2013). They applied a linear multiple time window inversion to obtain slip on the Pengguan and Beichuan faults, connected by the Xiaoyudong cross-fault. The hypocenter was placed on the Pengguan fault, which differs from most other studies, and the rupture expansion proceeds to the northeast, triggering the cross-fault and then spreading bilaterally onto the Beichuan fault. The overall seismic moment estimate is 1.0×10^{21} Nm. Figure 2.12b summarizes the kinematic model from inversion of SAR (ALOS and Envisat tracks, with pixel-offset tracking to constrain the fault placement), GPS and teleseismic data by Fielding et al. (2013). They find rupture velocity of 2.5–3.0 km/s with 110 s duration. The hypocenter is on the Beichuan fault. Slip is largely thrust in the south along the imbricate faults, and increasingly right-lateral to the northeast with steeper dip. The southern Beichuan segment dips 45°, converging with a 34° dipping Pengguan fault about 20 km deep, and then connecting to a 5° dipping décollement fault. The central Beichuan segment dips 55° and the northern segment dips 70°. The Pengguan fault is dynamically triggered in this model, but the timing of this is not well resolved, and could involve post-seismic deformation. A total seismic moment estimate of 9.5×10^{20} Nm is obtained. In both cases, inversions were conducted for the various data sets separately. The geodetic and field data give best constraint on the precise fault geometry, but the seismic data resolve the rupture expansion velocity of 2.8 ± 0.2 km/s. The estimated amount of slip on the Pengguan fault varies substantially, with large slip found by Hartzell et al. (2013) but weak slip by Fielding et al. (2013). This is clearly influenced by choice of placement of the hypocenter. Large-slip patches are found between Yingxiu to Xiaoyudong, near Beichuan and near Nanba (Figs. 2.4 and 2.12). Generally, these features are compatible with the earlier inversions described above. Overall, the resolution is most consistent for the segmented Beichuan fault system, but questions remain about the timing and strength of failure of the Pengguan fault.

2.6 Triggering Interactions

The 2008 Wenchuan rupture clearly involved dynamic triggering of multiple fault segments representing a complex fault zone failure. Uncertainty in the precise faulting geometry at depth complicates assessment of precise offsets of the segments and their interactions, compounded by the great topographic variation and obscurity of some of the surface ruptures. Triggering interactions and stress transfer before and after the mainshock are also of interest.

2.6.1 Was the Event Triggered by the Zipingpu Reservoir?

The Wenchuan earthquake epicenter is within ~12 km from the closest portion of the Zipingpu reservoir and ~24 km from its dam (Fig. 2.3). This reservoir began impoundment in September 2005 and rose from 760 m level to a maximum water level at 875 m in October 2006, followed by seasonal fluctuation in level to no lower than 817 m. Soon after the earthquake, debate commenced as to whether the earthquake was triggered by the reservoir (e.g., Lei et al. 2008; Ge et al. 2009; Kerr and Stone 2009, 2010; Deng et al. 2010; Gahalaut and Gahalaut 2010; Lu et al. 2010; Lei 2011; Ma et al. 2011; Klose 2012; Sun et al. 2014; Tao et al. 2015). Elastic and poroelastic calculations have been performed to evaluate the stress changes on the Beichuan fault prior to the 2008 rupture. This is complicated by uncertainty in the precise hypocentral parameters, the precise fault geometry of the southern Beichuan fault, and limited information on the crustal hydrologic properties. Early assessments of whether the reservoir loading increased driving stress at the hypocenter ranged from quite skeptical to cautiously probable.

Lei (2011) computes a few tens of kPa increase in driving stress at the hypocenter, but reported no clear increase in daily event rate close to it, concluding that the possibility of triggering cannot be ruled out. Sun et al. (2014) used a 3D numerical finite element model with poroelasticity to compute pore pressure and Coulomb stress change on the Beichuan fault, estimating only 1 kPa change at the hypocenter. There is a clear seismicity increase along a trend between the hypocenter and the reservoir (Ma et al. 2011), but the events involved are less than M 2.2. Small events prior to the mainshock are located in regions of predicted increase in Coulomb stress. Additional 3D poroelastic calculations were performed by Tao et al. (2015), with seismicity migration indicating a pore pressure front propagation in the direction of the Beichuan fault following reservoir impoundment. They also computed minor or no increase of Coulomb stress at the hypocenter, but increase of 9.3–69.1 kPa at depths from 1 to 8 km on the southwestern Beichuan fault. This corresponds to an advance in tectonic loading of on the order of 60–450 years. While direct triggering was considered inconclusive, the weakening effect on the shallow fault may have facilitated growth of the rupture by cascade from an initial small rupture. At this time, the issue appears to still be open, and it is not clear how to unambiguously resolved the question.

2.6.2 Triggering of Nearby Earthquakes

The effect of the 2008 rupture on surrounding faults in China has also received much attention, both for remote triggering from passage of dynamic waves and for static stress effects on nearby faults. Remote triggering during the passage of the mainshock waves was evaluated by Jiang et al. (2010), by high-pass (>5 Hz) filtering of three component recordings at 271 stations. Comparing the high-frequency signals

in the hour before and after the earthquake, 17 sites were found to have a statistically significant increase in activity after the mainshock, with 11 sites located in the north China block, along the rupture direction. However, many sites were not triggered, so the effect is subtle.

Static Coulomb stress changes on faults around the rupture zone have been computed by Parsons et al. (2008), Toda et al. (2008), Wan et al. (2009), Shan et al. (2009a, b), Luo and Liu (2010), Wan and Shen (2010), and Nalbant and McCloskey (2011) using elastic, viscoelastic, or viscoelastoplastic models. Most of these early studies used relatively simple rupture models from early teleseismic and geodetic inversions and give generally similar spatial patterns of regional increases or decreased of driving stress. Neighboring faults to the southwest and northeast show fairly consistent predictions of increased driving stress. This includes the Qingchuan fault in the north.

The occurrence of the April 20, 2013, Lushan earthquake (M_W 6.6) on the Pengxian-Guanxian fault or the Ya'an fault southwest of the Wenchuan rupture zone has naturally raised the question of whether the event is triggered. Shan et al. (2013) and Wang et al. (2014b) compute an increase of driving stress on the faults near the Lushan hypocenter, as found in earlier studies, with the loading clock advanced by up to 60 years, depending on the friction coefficient. Wang et al. (2014b) estimate an 85% chance that the event is essentially a delayed aftershock. Jia et al. (2014) compute an increase in driving stress of 0.25 bar at the Lushan location and report an increase in local background activity following the Wenchuan event. The confidence level of there being a direct interaction between the Wenchuan and Lushan event (and the effect on other faults that have not yet ruptured) is dependent on details of the slip model and geometry of the mainshock as well as the dip angle and geometry of the receiver fault (e.g., Wang et al. 2014a), all of which have significant uncertainty in this case. Li et al. (2019, see Chap. 6) examine fault zone-trapped waves for aftershocks of the Lushan and Wenchuan earthquakes, finding prominent coda for stations along the Xinkaidian fault which extends southwestward from the Pengxian-Guanxian fault. They infer rupture of the Xinkaidian fault in 2013, with continuity of a less-damaged low-velocity fault zone waveguide extending along the seismic gap between the 2008 and 2013 events. Overall, the case for the timing and location of the Lushan earthquake being influenced by the Wenchuan event appears moderately strong, so it can be viewed as a large aftershock of the 2008 event in a general sense.

2.7 Comparison of Rupture Parameters with Global Subduction Zone Thrusts

The global context of the 2008 Wenchuan earthquake in Fig. 2.1 raises the issue of how the faulting in this major continental event compares to that in the abundant distribution of large events in subduction zones. Figure 2.13 compares the rupture duration, moment-scaled radiated energy, and apparent stress estimated for the 2008

Wenchuan event with corresponding measurements for all interplate thrust events with $M_W \geq 7.0$ from 1990 to 2016 obtained by Ye et al. (2016). The Wenchuan event centroid duration, Tc, scaled by the average trend of centroid durations with seismic moment is within the upper half of the distribution for interplate thrust events (Fig. 2.13a). However, the radiated energy ($E_R = 3.78 \times 10^{13}$ J, https://doi.org/10.17611/DP/EQE.1) (Convers and Newman 2011) scaled by the GCMT moment gives a ratio near the maximum of interplate thrust events (Fig. 2.13b) and a similarly high apparent stress. The radiated energy may be even higher, as a relatively short source duration estimate was used, but even with this value the comparison indicates that high radiated energy may have influenced the strong shaking and widespread damage during the 2008 rupture. Future work can compare the 2008 Wenchuan earthquake parameters with those of other large continental events to evaluate whether it is unusual among that population.

2.8 Summary

The ten-year anniversary of the 2008 Wenchuan earthquake has recently occurred, and this review summarizes much of the intervening advance in our understanding of the mainshock rupture process. In his introduction to the 2010 special issue in *Tectonophysics*, Yin (2010) made a list of unanswered questions, among which was the detailed slip along the rupture. That is quite well resolved now, with the patchy distribution of large slip in the multi-segment Beichuan fault being constrained by field, seismological and geodetic observations that are relatively well reconciled by the more recent joint inversion analyses. There are remaining questions about the Pengguan fault slip magnitude and geometry, and the down-dip extension of the crustal faults into a possible mid-crustal décollement. The recurrence interval estimate for the 2008 rupture is not really any clearer than it was in 2010; definitive characterization of past events is very challenging due to the rough topography and near-surface faulting complexity along the zone. Large-scale issues of deep crustal inflation versus brittle faulting uplift also remain unresolved.

Acknowledgements All seismological data used in finite-fault inversions by the author were obtained from the Incorporated Research Institutions for Seismology (IRIS) data management service (DMS) (https://www.iris.edu/hq/). Editor Yong-Gang Li provides helpful comments on the manuscript. The author's research on earthquake processes is supported by the U.S. National Science Foundation grant EAR1802364. This chapter was prepared following the International Conference for the Decade Memory of the Wenchuan Earthquake (4th International Conference on Continental Earthquakes), May 12–14, 2018 in Chengdu, China. The author's participation in that excellent conference was supported by the China Earthquake Administration.

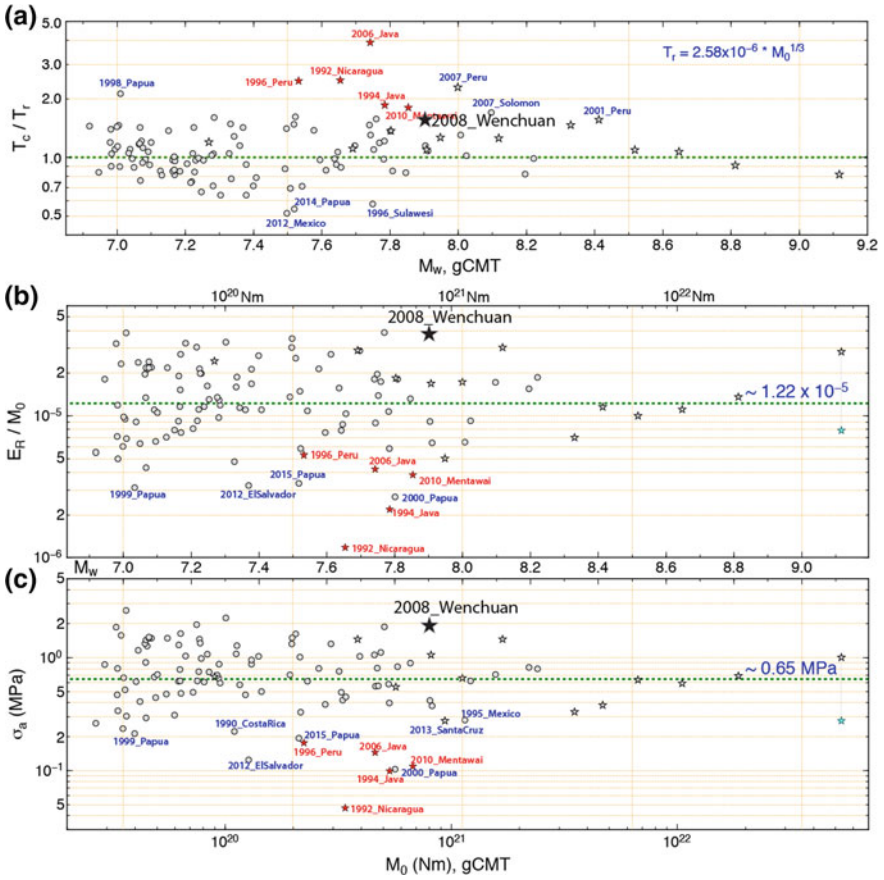

Fig. 2.13 Comparison of measurements of rupture duration (**a**), moment-scaled radiated energy (**b**), and apparent stress (**c**) for the 2008 Wenchuan intraplate thrust (black stars) with measurements for interplate thrusts from subduction zones in the Pacific and Indian Oceans. Modified from Ye et al. (2016)

References

An, M., M. Feng, and C. Long. 2010. Deep ruptures around the hypocenter of the 12 May 2008 Wenchuan earthquake deduced from aftershock observations. *Tectonophysics* 491: 96–104. https://doi.org/10.1016/j.tecto.2009.12.024.

Avants, M.S. 2014. Effects of near-source heterogeneity on wave fields emanating from crustal sources observed at regional and teleseismic distances. Ph.D. Thesis, University of California, Santa Cruz, 135 pp.

Bjerrum, L.W., M.B. Sorensen, and K. Atakan. 2010. Strong ground-motion simulation of the 12 May 2008 Mw 7.9 Wenchuan earthquake, using various slip models. *Bulletin of the Seismological Society of America* 100 (5B): 2396–2424. https://doi.org/10.1785/0120090239.

Burchfiel, B.C., L.H. Royden, R.D. van der Hilst, B.H. Hager, Z. Chen, R.W. King, C. Li, J. Lü, H. Yao, and E. Kirby. 2008. A geological and geophysical context for the Wenchuan earthquake of 12 May 2008, Sichuan, People's Republic of China. *GSA Today* 18: 4–11. https://doi.org/10.1130/GSATG18A.1.

Cai, C., C.Q. Yu, K. Tao, X.P. Hu, Y. Tian, H. Zhang, et al. 2011. Spatial distribution and focal mechanism solutions of the Wenchuan earthquake series: Results and implications. *Earthquake Science* 24 (1): 115–125. https://doi.org/10.1007/s11589-011-0775-5.

Chang, C.-P., G.-H. Chen, X.-W. Xu, R.-M. Yuan, Y.-T. Kuo, and W.-S. Chen. 2012. Influence of the pre-existing Xiaoyudong salient in surface rupture distribution of the M_W 7.9 Wenchuan earthquake, China. *Tectonophysics* 530–531: 240-250. https://doi.org/10.1016.j.tecto.2011.12038.

Chavez, M., E. Cabrera, R. Madariaga, H. Chen, N. Perea, D. Emerson, A. Salazar, M. Ashworth, Ch. Moulinec, X. Li, M. Wu, and G. Zhao. 2010. Low-frequency 3D wave propagation modeling of the 12 May 2008 M_W 7.9 Wenchuan earthquake. *Bulletin of the Seismological Society of America* 100: 2561–2573.

Chen, G.H., X.W. Xu, G.H. Yu, Y.F. An, R.M. Yuan, T.T. Guo, X. Gao, H. Yang, and X.B. Tan. 2009a. Co-seismic slip and slip partitioning of multi-faults during the Ms 8.0 2008 Wenchuan earthquake. *Chinese Journal of Geophysics* 52 (5): 1384–1394.

Chen, J.-H., Q.-Y. Liu, S.-C. Li, B. Guo, Y. Li, J. Want, and S.-H. Qi. 2009b. Seismotectonic study by relocation of the Wenchuan MS8.0 earthquake sequence (in Chinese with English abstract). *Chinese Journal of Geophysics* 52 (2): 390–397.

Convers, J.A., and A.V. Newman. 2011. Global evaluation of large earthquake energy from 1997 through mid-2010. *Journal Geophysical Research* 116: B08304. https://doi.org/10.1029/2010JB007928.

Dai, F.C., C. Xu, X. Yao, L. Xu, X.B. Tu, and Q.M. Gong. 2011. Spatial distribution of landslides triggered by the 2008 Ms 8.0 Wenchuan earthquake, China. *Journal of Asian Earth Sciences* 40: 883–895. https://doi.org/10.1016/j.jseaes.2010.04.010.

de Michele, M., D. Raucoules, C. Lasserre, E. Pathier, Y. Klinger, J. Van Der Woerd, J. de Sigoyer, and X. Xu. 2010a. The M_W 7.9 12 May 2008 Sichuan earthquake rupture measured by sub-pixel correlation of ALOS pALSAR amplitude images. *Earth Planets Space* 62: 875–879. https://doi.org/10.5047/eps.2009.05.002.

de Michele, M., D. Raucoules, J. de Sigoyer, M. Pubellier, and N. Chamot-Rooke. 2010b. Three-dimensional surface displacement of the 2008 May 12 Sichuan earthquake (China) derived from Synthetic Aperture Radar: evidence for rupture on a blind thrust. *Geophysical Journal International* 183: 1097–1103. https://doi.org/10.1111/j.1365-246X.2010.04807.x.

Deng, K., S. Zhou, R. Wang, R. Robinson, C. Zhao, and W. Cheng. 2010. Evidence that the 2008 M_W 7.9 Wenchuan earthquake could not have been induced by the Zipingpu reservoir. *Bulletin of the Seismological Society of America* 100: 2805–2814. https://doi.org/10.1785/0120090222.

Densmore, A.L., M.A. Ellis, Y. Li, R. Zhou, G.S. Hancock, and N. Richardson. 2007. Active tectonics of the Beichuan and Pengguan faults at the eastern margin of the Tibetan Plateau. *Tectonics* TC4005. https://doi.org/10.1029/2006tc001987.

Densmore, A.L., Y. Li, N.J. Richardson, R. Zhou, M. Ellis, and Y. Zhang. 2010. The role of late quaternary upper-crustal faults in the 12 May 2008 Wenchuan earthquake. *Bulletin of the Seismological Society of America* 100: 2700–2712. https://doi.org/10.1785/0120090294.

Diao, F., X. Xiong, R. Wang, Y. Zheng, and H. Hsu. 2010. Slip model of the 2008 M_W 7.9 Wenchuan (China) earthquake derived from co-seismic GPS data. *Earth Planets Space* 62: 869–874. https://doi.org/10.5047/eps.2009.05.003.

Dong, S., Y. Zhang, Z. Wu, N. Yang, Y. Ma, W. Shi, Z. Chen, C. Long, and M. An. 2008. Surface rupture and co-seismic displacement produced by the Ms 8.0 Wenchuan earthquake of May 12th, 2008, Sichuan, China: Eastwards growth of the Qinghai-Tibet Plateau. *Acta Geological Sinica* 82: 938–948.

Du, H.-L., L.-S. Xu, and Y.-T. Chen. 2009. Rupture process of the 2008 great Wenchuan earthquake from the analysis of the Alaska-array data. *Chinese Journal of Geophysics* 52 (2): 372–378.

Duputel, Z., L. Rivera, H. Kanamori, and G. Hayes. 2012. W phase source inversion for moderate to large earthquakes (1990-2010). *Geophysical Journal International* 189: 1125–1147. https://doi.org/10.1111/j.1365-246X.2012.05419.x.

Feng, G., E.A. Hetland, X.L. Ding, Z.W. Li, and L. Zhang. 2010. Coseismic fault slip of the 2008 M_W 7.9 Wenchuan earthquake estimated from InSAR and GPS measurements. *Geophysical Research Letters* 37: L01302. https://doi.org/10.1029/2009gl041213.

Feng, G., S. Jónsson, and Y. Klinger. 2017. Which fault segments ruptured in the 2008 Wenchuan earthquake and which did not? New evidence from near-fault 3D surface displacements derived from SAR Image offsets. *Bulletin of the Seismological Society of America* 107: 1185–1200. https://doi.org/10.1785/0120160126.

Fielding, E.J., A. Sladen, Z. Li, J.-P. Avouac, R. Bürgmann, and I. Ryder. 2013. Kinematic sfault slip evolution source models of the 2008 M7.9 Wenchuan earthquake in China from SAR interferometry, GPS and teleseismic analysis and implications for Longmen Shan tectonics. *Geophysical Journal International* 194: 1138–1166. https://doi.org/10.1093/gji/ggt155.

Fu, B., P. Shi, H. Guo, S. Okuyama, Y. Ninomiya, and S. Wright. 2011. Surface deformation related to the 2008 Wenchuan earthquake, and mountain building of the Longmen Shan, eastern Tibetan Plateau. *Journal of Asian Earth Sciences* 40: 805–824. https://doi.org/10.1016/j.jseaes.2010.11.011.

Furuya, M.T., Y.Takada Kobayashi, and M. Murakami. 2010. Fault source modeling of the 2008 Wenchuan earthquake based on ALOS/PALSAR data. *Bulletin of the Seismological Society of America* 100: 2750–2766. https://doi.org/10.1785/0120090242.

Gahalaut, K., and V.K. Gahalaut. 2010. Effect of the Zipingpu reservoir impoundment on the occurrence of the 2008 Wenchuan earthquake and local seismicity. *Geophysical Journal International* 183: 277–285. https://doi.org/10.1111/j.1365-246X.2010.04715.x.

Ge, S., M. Liu, N. Lu, J.W. Godt, and G. Luo. 2009. Did the Zipingpu Reservoir trigger the 2008 Wenchuan earthquake? *Geophysical Reseach Letters* 36: L20315. https://doi.org/10.1029/2009GL040349.

Ghasemi, H., Y. Fukushima, K. Koketsu, H. Miyake, Z. Wang, and J.G. Anderson. 2010. Ground-motion simulation for the 2008 Wenchuan, China, earthquake using the stochastic finite-fault method. *Bulletin of the Seismological Society of America* 100: 2476–2490.

Gorum, T., X. Fan, C.J. van Westen, R.Q. Huang, Q. Xu, C. Tang, and G. Wang. 2011. Distribution pattern of earthquake-induced landslides triggered by the 12 May 2008 Wenchuan earthquake. *Geomorphology* 133: 152–167. https://doi.org/10.1016/j.geomorph.2010.12.030.

Hao, K. X., H. Si, H. Fujiwara, and T. Ozawa. 2009. Coseismic surface-ruptures and crustal deformations of the 2008 Wenchuan earthquake Mw7.9, China. *Geophysical Reseach Letters* 36: L11303. https://doi.org/10.1029/2009gl037971.

Hartzell, S., C. Mendoza, L. Ramirez-Guzman, Y. Zeng, and W. Mooney. 2013. Rupture history of the 2008 MW 7.9 Wenchuan, China, Earthquake: Evaluation of separate and joint inversions of geodetic, teleseismic, and strong-motion data. *Bulletin of the Seismological Society of America* 103: 353–370. https://doi.org/10.1785/0120120108.

Hashimoto, M., M. Enomoto, and Y. Fukushima. 2010. Coseismic deformation from the 2008 Wenchuan, China earthquake derived from ALOS/PALSAR images. *Tectonophysics* 491: 59–71. https://doi.org/10.1016/j.tecto.2009.08.034.

He, H. L., Z.M. Sun, Z.Y. Wei, S.P. Dong, X. Gao, S.Y. Wang, and J.Q. Wang. 2008. Rupture of the M_W 8.0 Wenchuan earthquake along Baishahe river (in Chinese). *Seismology and Geology* 30 (3): 658–673.

Huang, T., and H. Yao. 2018. Coseismic radiation of the 2008 M_W 7.9 Wenchuan earthquake and its relationship with fault complexities. *Pure and Applied Geophysics*. https://doi.org/10.1007/s00024-018-2050-3.

Huang, Y., J.-P. Wu, T.-Z. Zhang, and D.-N. Zhang. 2008. Relocation of the M8.0 Wenchuan earthquake and its aftershock sequence. *Science in China, Series D: Earth Sciences* 51: 1703–1711.

Hubbard, J., and J.H. Shaw. 2009. Uplift of the Longmen Shan and Tibetan plateau, and the 2008 Wenchuan (M = 7.9) earthquake. *Nature* 458: 194–197. https://doi.org/10.1038/nature07837.

Hubbard, J., J.H. Shaw, and Y. Klinger. 2010. Structural setting of the 2008 Mw 7.9 Wenchuan, China, earthquake. *Bulletin of the Seismological Society of America* 100: 2713–2735. https://doi.org/10.1785/0120090341.

Hwang, R.-D., J.-P. Chang, C.-Y. Wang, J.-J. Wu, C.-H. Kuo, Y.-W. Tsai, W.-Y. Chang, and T.-W. Lin. 2011. Rise time and source duration of the 2008 MW 7.9 Wenchuan (China) earthquake as revealed by Rayleigh waves. *Earth Planets Space* 63: 427–434. https://doi.org/10.5047/eps.2011.01.002.

Ji, C. 2008. Preliminary result of the May 12, 2008 Mw7.97 Sichuan, China earthquake. http://www.geol.ucsb.edu/faculty/ji/big_earthquakes/2008/05/12/ShiChuan.html.

Jia, D., Y. Li, A. Lin, M. Wang, W. Chen, X. Wu, Z. Ren, Y. Zhao, and L. Luo. 2010. Structural model of 2008 Mw 7.9 Wenchuan earthquake in the rejuvenated Longmen Shan thrust belt, China. *Tectonophysics* 491: 174–184. https://doi.org/10.1016/j.tecto.2009.08.040.

Jia, K., S. Zhou, J. Zhuang, and C. Jiang. 2014. Possibility of the independence between the 2013 Lushan earthquake and the 2008 Wenchuan earthquake on Longmen Shan fault, Sichuan, China. *Geophysical Reseach Letters* 85: 60–67. https://doi.org/10.1785/0220130115.

Jiang, T., Z. Peng, W. Wang, and Q.-F. Chen. 2010. Remotely triggered seismicity in continental China following the 2008 MW 7.9 Wenchuan earthquake. *Bulletin of the Seismological Society of America* 100: 2574–2589. https://doi.org/10.1785/0120090286.

Kerr, R.A., and R. Stone. 2009. A human trigger for the great quake of Sichuan? *Science* 323: 322.

Kerr, R.A., and R. Stone. 2010. Two years later, new rumblings over origins of Sichuan quake. *Science* 327: 1184.

Klose, C.D. 2012. Evidence for anthropogenic surface loading as trigger mechanism of the 2008 Wenchuan earthquake. *Environmental Earth Science* 66: 1439–1447. https://doi.org/10.1007/s12665-011-1355-7.

Kobayashi, T., Y. Takada, M. Furuya, and M. Murakami. 2009. Locations and types of ruptures involved in the 2008 Sichuan earthquake inferred from SAR image matching. *Geophysical Reseach Letters* 36: L07302. https://doi.org/10.1029/2008GL036907.

Koketsu, K., Y. Yokota, H. Ghasemi, K. Hikima, H. Miyake, and Z. Wang. 2009. Source Process and Ground Motions of the 2008 Wenchuan Earthquake, Investigation report of the May 12th 2008, Wenchuan earthquake, China, Grant-in-Aid for Special Purposes of 2008, Ministry of Education, Culture, Sports, Science and Technology (MEXT), No. 20900002, 201–212.

Kurahashi, S., and K. Irikura. 2010. Characterized source model for simulating strong ground motions during the 2008 Wenchuan earthquake. *Bulletin of the Seismological Society of America* 100: 2450–2475.

Lay, T. 2015. The surge of great earthquakes from 2004 to 2014. *Earth and Planetary Science Letters* 409: 133–146. https://doi.org/10.1016/j.epsl.2014.10.047.

Lei, X. 2011. Possible roles of the Zipingpu Reservoir in triggering the 2008 Wenchuan earthquake. *Journal of Asian Earth Sciences* 40: 844–854.

Lei, X., S. Ma, X. Wen, J. Su, and F. Du. 2008. Integrated analysis of stress and regional seismicity by surface loading—A case study of Zipingpu reservoir (in Chinese with English abstract). *Seismology and Geology* 30 (4): 1046–1064.

Li, C.-Y., and Z.-Y. Wei. 2009. Deformation styles of the northeasternmost surface rupture zone of the MS 8.0 Wenchuan earthquake (in Chinese). *Seismology and Geology* 31 (1): 1–8.

Li, H., X. Fu, J. van der Woerd, J.L. Si, Z.X. Wang, L.W. Hou, Z.L. Qiu, N. Li, F.Y. Wu, Z.Q. Xu, and P. Tapponnier. 2008a. Surface rupture associated with the Wenchuan earthquake and its oblique slip. *Acta Geologica Sinica* 82: 1623–1643.

Li, X., Z. Zhou, M. Huanng, R. Wen, H. Yu, D. Lu, Y. Zhou, and J. Cui. 2008b. Preliminary analysis of strong-motion recordings from the magnitude 8.0 Wenchuan, China, earthquake of 12 May 2008. *Seismological Research Letters* 79: 844–854. https://doi.org/10.1785/gssrl.79.6.844.

Li, C.-Y., Z.-Y. Wei, J.-Q. Ye, Y.-B. Han, and W.-J. Zheng. 2010a. Amounts and styles of coseismic deformation along the northern segment of surface ruptures, of the 2008 Wenchuan Mw 7.9 earthquake, China. *Tectonophysics* 491: 35–58. https://doi.org/10.1016/j.tecto.2009.09.023.

Li, Y., D. Jia, J.H. Shaw, J. Hubbard, A. Lin, M. Wang, L. Luo, H. Li, and L. Wu. 2010b. Structural interpretation of the coseismic faults of the Wenchuan earthquake: Three-dimensional modeling of the Longmen Shan fold-and-thrust belt. *Journal Geophysical Research* 115: B04317. https://doi.org/10.1029/2009JB006824.

Li, Y.G., J.R. Su, and T.C. Chen. 2012. Fault-zone trapped waves at a dip fault: Documentation of rock damage on the thrusting Longmen Shan fault ruptured in the 2008 M8 Wenchuan earthquake. In *Imaging modeling and assimilation in seismology*, ed. Y.G. Li, 151–198. Beijing: Higher Education Press; Boston: De Gruyter.

Li, H., H. Wang, Z. Xu, J. Si, J. Pei, T. Li, Y. Huang, S.-R. Song, L.-W. Kuo, Z. Sun, M.-L. Chevalier, and D. Liu. 2013. Characteristics of the fault-related rocks, fault zones and the principal slip zone in the Wenchuan Earthquake Fault Scientific Drilling Project Hole-1 (WFSD-1). *Tectonophysics* 584: 23–42.

Li, H., Z. Xu, Y. Niu, G. Kong, Y. Huang, H. Wang, J. Si, Z. Sun, J. Pei, Z. Gong, M.-L. Chevalier, and D. Liu. 2014a. Structural and physical property characterization of the Wenchuan earthquake Fault Scientific Drilling project—hole 1 (WFSD-1). *Tectonophysics* 619–620: 86–100.

Li, Y.G., Z.Q. Xu, and H.B. Li. 2014b. Rock damage structure of the south Longmen Shan fault in the 2008 M8 Wenchuan earthquake viewed with fault-zone trapped waves and scientific drilling. *Acta Geologica Sinica (English Edition)* 88 (2): 444–467.

Li, H., L. Xue, E.E. Brodsky, J.J. Mori, P.M. Fulton, H. Wang, Y. Kano, K. Yun, R.N. Harris, Z. Gong, C. Li, J. Si, Z. Sun, J. Pei, Y. Zheng, and Z. Xu. 2015. Long-term temperature records following the M_W 7.9 Wenchuan (China) earthquake are consistent with low friction. *Geology* 43 (2): 163–166. https://doi.org/10.1130/g35515.

Li, Z., P. Zhang, W. Zheng, D. Jia, J. Hubbard, R. Almeida, C. Sun, X. Shi, and T. Li. 2018. Oblique thrusting and strain partitioning in the Longmen Shan fold-and-thrust belt, eastern Tibetan plateau. *Journal of Geophysical Research: Solid Earth* 123: 4431–4453. https://doi.org/10.1029/2018jb015529.

Li, Y.G., J.R. Su, T.C. Chen, and P. Wu. 2019. Structural relationship between the 2008 M8 Wenchuan and 2013 M7 Lushan earthquakes viewed by fault-zone trapped waves, this volume.

Lin, A., Z. Ren, D. Jia, and X. Wu. 2009. Co-seismic thrusting rupture and slip distribution produced by the 2008 Mw 7.9 Wenchuan earthquake, China. *Tectonophysics* 471: 203–215. https://doi.org/10.1016/j.tecto.2009.02.014.

Lin, A., Z. Ren, D. Jia, and Y. Miyairi. 2010. Evidence for a Tang-Song Dynasty great earthquake along the Longmen Shan thrust belt prior to the 2008 MW 7.9 Wenchuan earthquake, China. *Journal of Seismology* 14: 615–628. https://doi.org/10.1007/s10950-010-9186-7.

Lin, A., G. Rao, and B. Yan. 2012. Field evidence of rupture of the Qingchuan Fault during the 2008 Mw7.9 Wenchuan earthquake, northeastern segment of the Longmen Shan Thrust Belt, China. *Tectonophysics* 522: 243–252.

Lin, A., G. Rao, and B. Yan. 2014. Structural analysis of the right-lateral strike-slip Qingchuan fault, northeastern segment of the Longmen Shan thrust belt, central China. *Journal of Structural Geology* 68: 227–244. https://doi.org/10.1016/j.jsg.2014.09.014.

Lin, X., D. Dreger, H. Ge, P. Xu, M. Wu, A. Chiang, G. Zhao, and H. Yuan. 2018. Spatial and temporal variations in the moment tensor solutions of the 2008 Wenchuan earthquake aftershocks and their tectonic implications. *Tectonics* 37: 989–1005. https://doi.org/10.1002/2017TC004764.

Liu, J., Z. Zhang, L. Wen, J. Sun, X. Xing, G. Hu, Q. Xu, P. Tapponier, L. Zeng, L. Ding, and Y. Liu. 2008. The Ms 8.0 Wenchuan earthquake coseismic rupture and its tectonic implications-an out-of-sequence thrusting event with slip partitioned on multiple faults. *Acta Geologica Sinica* 82 (12): 1707–1722.

Liu, J., Z. Zhang, L. Wen, P. Tapponnier, J. Sun, X. Xing, G. Hu, Q. Xu, L. Zeng, L. Ding, C. Ji, K.W. Hudnut, and J. van der Woerd. 2009. Co-seismic ruptures of the 12 May 2008, MS 8.0 Wenchuan earthquake, Sichuan: East-west crustal shortening on oblique, parallel thrusts along the eastern edge of Tibet. *Earth and Planetary Science Letters* 286: 355–370. https://doi.org/10.1016.j.epsl.2009.07.017.

Liu, J., L. Wen, J. Sun, Z. Zhang, G. Hu, X. Xing, L. Zeng, and Q. Xu. 2010. Surficial slip and rupture geometry on the Beichuan fault near Hongkou during the Mw 7.9 Wenchuan earthquake, China. *Bulletin of the Seismological Society of America* 100: 2615–2650.

Liu, J., J. Sun, P. Wang, K.W. Hudnut, C. Ji, Z. Zhang, Q. Xu, and L. Wen. 2012. Surface ruptures on the transverse Xiaoyudong fault: A significant segment boundary breached during the 2008 Wenchuan earthquake, China. *Tectonophysics* 580: 218–241. https://doi.org/10.1016/j.tecto.2012.09.024.

Lu, X., X. Zhang, L. Zhou, et al. 2010. Research and analysis on accurate positioning of earthquakes in the Zipingpu reservoir area. *Seismology* 30 (20): 10–19.

Luo, G., and M. Liu. 2010. Stress evolution and fault interactions before and after the 2008 Great Wenchuan earthquake. *Tectonophysics* 491: 127–140. https://doi.org/10.1016/j.tecto.2009.12.019.

Ma, B.Q., G. Su, Z.H. Hou, and S.B. Shu. 2005. Late quaternary slip rate in the central part of the Longmenshan fault zone from terrace deformation along the Minjiang River (in Chinese). *Seismology and Geology* 27 (2): 234–242.

Ma, W., C. Xu, and X. Zhang. 2011. Discussion on the relationship between Zipingpu reservoir and the Wenchuan earthquake (in Chinese with English abstract). *Seismology and Geology* 33 (1): 175–190.

Nakamura, T., S. Tsuboi, Y. Kaneda, and Y. Yamanaka. 2010. Rupture process of the 2008 Wenchuan, China earthquake inferred from teleseismic waveform inversion and forward modeling of broadband seismic waves. *Tectonophysics* 491: 72–84. https://doi.org/10.1016/j.tecto.2009.09.020.

Nalbant, S.S., and J. McCloskey. 2011. Stress evolution before and after the 2008 Wenchuan, China earthquake. *Earth and Planetary Sciences Letters* 307: 222–232. https://doi.org/10.1016/j.epsl.2011.04.039.

Nishimura, N., and Y. Yagi. 2008. A huge earthquake occurred in Sichuan Province, China on May 12, 2008 (provisional). http://www.geol.tsukuba.ac.jp/~yagi-y/EQ/20080512/index.html.

Okuwaki, R., and Y. Yagi. 2018. Role of geometric barriers in irregular-rupture evolution during the 2008 Wenchuan earthquake. *Geophysical Journal International* 212: 1657–1664. https://doi.org/10.1093/gji/ggx502.

Ouimet, W.B. 2010. Landslides associated with the May 12, 2008 Wenchuan earthquake: Implications for the erosion and tectonic evolution of the Longmen Shan. *Tectonophysics* 491: 244–252. https://doi.org/10.10106/j.tecto.2009.09.012.

Pan, J., H. Li, J. Si, J. Pei, X. Fu, M.-L. Chevalier, and D. Liu. 2014. Rupture process of the Wenchuan earthquake (Mw 7.9) from surface ruptures and fault striations characteristics. *Tectonophysics* 619–620: 13–28. https://doi.org/10.1016.j.tecto.2013.06.028.

Parsons, T., C. Ji, and E. Kirby. 2008. Stress changes from the 2008 Wenchuan earthquake and increased hazard in the Sichuan basin. *Nature* 454: 509–510. https://doi.org/10.1038/nature07177.

Pei, S., J. Su, H. Zhang, Y. Sun, M.N. Toksöz, Z. Whang, X. Gao, J. Liu-Zeng, and J. He. 2010. Three-dimensional seismic velocity structure across the 2008 Wenchuan M_S 8.0 earthquake, Sichuan, China. *Tectonophysics* 491: 211–217. https://doi.org/10.1016/j.tecto.2009.08.039.

Qu, D., X. Shan, Y. Liu, G. Zhang, X. Song, G. Zhang, L. Guo, and Y. Han. 2012. Ground surface ruptures and near-fault, large-scale displacements caused by the Wenchuan M_S8.0 earthquake derived from pixel offset tracking on synthetic aperture radar images. *Acta Geologica Sinica* 86: 510–519.

Ran, Y., L. Chen, J. Chen, H. Wang, G. Chen, J. Yin, X. Shi, C. Li, and X. Xu. 2010. Paleoseismic evidence and repeat time of large earthquakes at three sites along the Longmenshan fault zone. *Tectonophysics* 491: 141–153. https://doi.org/10.1016/j.tecto.2010.01.009.

Royden, L.H., B.C. Burchfiel, and R.D. van der Hilst. 2008. The geological evolution of the Tibetan Plateau. *Science* 321: 1054–1058. https://doi.org/10.1126/science.1155371.

Shan, B., X. Xiong, Y. Zheng, and F. Diao. 2009a. Stress changes on major faults caused by M_w7.9 Wenchuan earthquake May 12, 2008. *Science in China Series D-Earth Sciences* 52: 593–601.

Shan, X., C. Qu, X. Song, G. Zhang, Y. Liu, et al. 2009b. Coseismic surface deformation caused by the Wenchuan earthquake from InSAR data analysis. *Chinese Journal of Geophysics* 52: 496–504.

Shan, B., X. Xiong, Y. Zheng, B. Jin, C. Liu, X. Xie, and H. Hsu. 2013. Stress changes on major faults caused by 2013 Lushan earthquake and its relationship with 2008 Wenchuan earthquake. *Science China Earth Sciences* 56: 1169–1176. https://doi.org/10.1007/s11430-013-4642-1.

Shen, Z.-K., J. Sun, P. Zhang, Y. Wan, M. Wang, R. Bürgmann, Y. Zeng, W. Gan, H. Liao, and Q. Wang. 2009. Slip maxima at fault junctions and rupturing of barriers during the 2008 Wenchuan earthquake. *Nature Geosciences* 2: 718–724. https://doi.org/10.1038/NGEO636.

Sun, J., F. Liang, Z.K. Shen, and X. Xu. 2008. InSAR deformation observation and preliminary analysis of the Ms 8.0 Wenchuan earthquake (in Chinese with English abstract). *Seismology and Geology* 30: 489–495.

Sun, Y.-J., H. Zhang, S.-W. Dong, L. Zheng, B. Zhang, H.-H. Cheng, and Y.-L. Shi. 2014. Study on the effect of Zipingpu reservoir on the occurrence of 2008 Wenchaun M_S 7.9 earthquake based on a 3D-poroelastic model. *Chinese Journal of Geophysics* 57: 209–218.

Tao, W., T. Masterlark, Z.-K. Shen, and E. Ronchin. 2015. Impoundment of the Zipingpu reservoir and triggering of the 2008 MW 7.9 Wenchuan earthquake, China. *Journal of Geophysical Research: Solid Earth* 120: 7033–7047. https://doi.org/10.1002/2014jb011766.

Toda, S., J. Lin, M. Meghraoui, and R.S. Stein. 2008. 12 May 2008 M = 7.9 Wenchuan, China, earthquake calculated to increase failure stress and seismicity rate on three major fault systems. *Geophysical Research Letters* 35: L17305. https://doi.org/10.1029/2008gl034903.

Tong, X., D.T. Sandwell, and Y. Fialko. 2010. Coseismic slip model of the 2008 Wenchuan earthquake derived from joint inversion of interferometric synthetic aperture radar, GPS, and field data. *Journal Geophysical Research* 115: B04314. https://doi.org/10.1029/2009JB006625.

Wan, Y., and Z.K. Shen. 2010. Static Coulomb stress changes on faults caused by the 2008 Mw7.9 Wenchuan, China earthquake. *Tectonophysics* 491: 105–118.

Wan, Y.G., Z.K. Shen, S.Z. Sheng, and X.F. Xu. 2009. The influence of 2008 Wenchuan earthquake on surrounding faults (in Chinese with English Abstract). *Acta Seismologica Sinica* 31 (2): 128–139.

Wan, Y., Z.-K. Shen, R. Bürgmann, J. Sun, and M. Wang. 2017. Fault geometry and slip distribution of the 2008 M_W 7.9 Wenchuan, China earthquake, inferred from GPS and InSAR measurements. *Geophysical Journal International* 208: 748–766. https://doi.org/10.1093/gji/ggw421.

Wang, W.M., L.F. Zhao, J. Li, and Z.X. Yao. 2008. Rupture process of the Ms 8.0 Wenchuan earthquake in Sichuan, China. *Chinese Journal of Geophysics* 51 (5): 1403–1410 (in Chinese).

Wang, Q., D. Cui, X. Zhang, W. Wang, J. Liu, K. Tian, and Z. Song. 2009a. Coseismic vertical deformation of the M_S8.0 Wenchuan earthquake from repeated levelings and its constraint on listric fault geometry. *Earthquake Science* 22: 595–602. https://doi.org/10.1007/s11589-009-0595-z.

Wang, W., S. Ni, Y. Chen, and H. Kanamori. 2009b. Magnitude estimation for early warning applications using the initial part of P waves: A case study on the 2008 Wenchuan sequence. *Geophysical Reseach Letters* 36: L16305. https://doi.org/10.1029/2009GL038678.

Wang, Z., Y. Fukao, and S. Pei. 2009c. Structural control of rupturing of the Mw7.9 2008 Wenchuan earthquake, China. *Earth and Planetary Science Letters* 279: 131–138. https://doi.org/10.1016/j.epsl.2008.12.038.

Wang, H., Y.K. Ran, L.C. Chen, X. Shi, R.C. Liu, and F. Gomez. 2010a. Determination of horizontal shortening and amount of reverse-faulting from trenching across the surface rupture of the 2008 M_W 7.9 Wenchuan earthquake, China. *Tectonophysics* 491: 10–20.

Wang, W., W. Sun, and Z. Jiang. 2010b. Comparison of fault models of the 2008 Wenchuan earthquake (M_S8.0) and distributions of co-seismic deformations. *Tectonophysics* 491: 85–95. https://doi.org/10.1016/j.tecto.2009.08.035.

Wang, Q., Q. Xuejun, L. Qigui, J. Freymueller, Y. Shaomin, X. Caijun, Y. Yonglin, Y. Xinshao, T. Kai, and C. Gang. 2011. Rupture of deep faults in the 2008 Wenchuan earthquake and uplift of the Longmen Shan. *Nature Geosciences* 4: 634–640. https://doi.org/10.1038/NGEO1210.

Wang, J., C. Xu, J.T. Freymueller, Z. Li, and W. Shen. 2014a. Sensitivity of Coulomb stress change to the parameters of the Coulomb failure model: A case study using the 2008 M_W 7.9 Wenchuan earthquake. *Journal of Geophysical Research: Solid Earth* 119: 3371–3392. https://doi.org/10.1002/2012jb009860.

Wang, Y., F. Wang, M. Wang, Z.-K. Shen, and Y. Wan. 2014b. Coulomb stress change and evolution induced by the 2008 Wenchuan earthquake and its delayed triggering of the 2013 M_W 6.6 Lushan earthquake. *Seismological Research Letters* 85: 52–59. https://doi.org/10.1785/0220130111.

Wang, D., J. Mori, and K. Koketsu. 2016. Fast rupture propagation for large strike-slip earthquakes. *Earth and Planetary Science Letters* 440: 115–126. https://doi.org/10.1016/j.epsl.2016.02.022.

Wei, Z., S. Yang, and X. Chen. 2008. Numerical simulation of strong ground motion for the M_S 8.0 Wenchuan earthquake of 12 May 2008. *Science in China Series D: Earth Sciences* 51: 1673–1682.

Wei, Z., H. He, F. Shi, X. Gao, and C. Xu. 2010. Topographic characteristics of rupture surface associated with the 12 May 2008 Wenchuan earthquake. *Bulletin of the Seismological Society of America* 100: 2669–2680. https://doi.org/10.1785/0120090260.

Wen, Y.-Y., K.-F. Ma, and D.D. Oglesby. 2012. Variations in rupture speed, slip amplitude and slip direction during the 2008 Mw 7.9 Wenchuan earthquake. *Geophysical Journal International* 190: 379–390. https://doi.org/10.1111/j.1365-246X.2012.05476.x.

Working Group of the Crustal Motion Observation Network of China Project. 2008. Coseismic displacement field of the 2008 M_W 8.0 Wenchuan earthquake determined by GPS (in Chinese). *Science in China Series D* 38: 1195–1206.

Wu, J.-P., Y. Huang, T.-Z. Zhang, Y.-H. Ming, and L.-H. Fang. 2009a. Aftershock distribution of the Ms 8.0 Wenchuan earthquake and 3-D P-wave velocity structure in and around source region. *Chinese Journal of Geophysics* 52: 102–111.

Wu, Z., S. Dong, P.J. Barosh, Z. Zhang, and H. Liao. 2009b. Dextral-slip thrust faulting and seismic events of the Ms 8.0 Wenchuan earthquake, Longmenshan Mountains, eastern margin of the Tibetan Plateau. *Acta Geologica Sinica* 83: 685–693.

Xu, X.W., X.Z. Wen, J.Q. Ye, B.Q. Ma, J. Chen, R.J. Zhou et al. 2008. The Ms8.0 Wenchuan earthquake surface ruptures and its seismogenic structure. *Seismology and Geology* 30 (3): 597–629 (in Chinese with an English abstract).

Xu, X., G. Yu, G. Chen, Y. Ran, C. Li, Y. Chen, and C. Chang. 2009a. Parameters of coseismic reverse- and oblique-slip surface ruptures of the 2008 Wenchuan earthquake, Eastern Tibetan plateau. *Acta Geologica Sinica* 83: 673–684.

Xu, X., X.Z. Wen, G.H. Yu, G.H. Chen, Y. Klinger, J. Hubbard, and J. Shaw. 2009b. Coseismic reverse- and oblique-slip surface faulting generated by the 2008 Mw 7.9 Wenchuan earthquake, China. *Geology* 37: 515–518. https://doi.org/10.1130/G25462A.1.

Xu, Y., K.D. Koper, O. Sufri, L. Zhu, and A.R. Hutko. 2009c. Rupture imaging of the Mw 7.9 12 May 2008 Wenchuan earthquake form back projection of teleseismic P waves. *Geochemistry Geophysics Geosystems* 10: Q04006. https://doi.org/10.1029/2008gc002335.

Xu, Z., S. Ji, H. Li, L. Hou, Z. Fu, and Z. Cai. 2009d. Uplift of the Longmen Shan range and the Wenchuan earthquake. *Episodes* 31: 291–301.

Xu, C., Y. Liu, Y. Wen, and R. Wang. 2010a. Coseismic slip distribution of the 2008 MW 7.9 Wenchuan earthquake form join inversion of GPS and InSAR data. *Bulletin of the Seismological Society of America* 100: 2736–2749. https://doi.org/10.1785/0120090253.

Xu, Y., Z. Li, R. Huang, and Y. Xu. 2010b. Seismic structure of the Longmen Shan region from S-wave tomography and its relationship with the Wenchuan MS 8.0 earthquake on 12 May 2008, southwestern China. *Geophysical Research Letters* 37: L02304. https://doi.org/10.1029/2009gl041835.

Xue, L., H.-B. Li, E.E. Brodsky, Z.-Q. Xu, Y. Kano, H. Wang, J.J. Mori, J.-L. Si, et al. 2013. Continuous permeability measurements record healing inside the Wenchuan earthquake fault zone. *Science* 340: 1555–1559. https://doi.org/10.1126/science.1237237.

Yagi, Y., N. Nishimura, and A. Kasahara. 2012. Source process of the 12 May 2008 Wenchuan, China, earthquake determined by waveform inversion of teleseismic body waves with a data covariance matrix. *Earth Planets Space* 64: e13–e16. https://doi.org/10.5047/eps.2012.05.006.

Yamanaka, Y. 2008. Earthquake M7.5 in Sichuan, China, on May 12, Ver.2, NGY Seismology Notes. http://www.seis.nagoya-u.ac.jp/sanchu/Seismo_Note/2008/NGY8a.html.

Yang, Z.X., Y.T. Chen, J.R. Su, T.C. Chen, and P. Wu. 2012. The hypocenter and origin time of the Mw 7.9 Wenchuan earthquake of May 12, 2008. *Acta Seismologica Sinica* 34 (2), 127–136. https://doi.org/10.3969/j.issn.0253-3782.2012.02.001.

Ye, L., T. Lay, H. Kanamori, and L. Rivera. 2016. Rupture characteristics of major and great ($M_w \geq$ 7.0) megathrust earthquakes from 1990 to 2015: 1. Source parameter scaling relationships. *Journal of Geophysical Research: Solid Earth* 121: 826–844. https://doi.org/10.1002/2015jb012426.

Yin, A. 2010. A special issue on the great 12 May 2008 Wenchuan earthquake (Mw7.9): Observations and unanswered questions. *Tectonophysics* 491: 1–9. https://doi.org/10.1016/j.tecto.2010.05.019.

Yin, X.Z., J.H. Chen, Z. Peng, X. Meng, Q.Y. Liu, B. Guo, and S.C. Li. 2018. Evolution and distribution of the early aftershocks following the 2008 Mw 7.9 Wenchuan earthquake in Sichuan, China. *Journal of Geophysical Research: Solid Earth*, in press. https://doi.org/10.1029/2018jb015575.

Yu, G., X. Xu, Y. Klinger, G. Diao, G. Chen, X. Feng, C. Li, A. Zhu, R. Yuan, T. Guo, X. Sun, X. Tan, and Y. An. 2010. Fault-scarp features and cascading-rupture model for the Mw 7.9 Wenchuan earthquake, eastern Tibetan Plateau, China. *Bulletin of the Seismological Society of America* 100: 2590–2614.

Yuan, R.-M., X.-W. Xu, G.-H. Chen, X.-B. Tan, Y. Klinger, and H.-L. Xing. 2010. Ejection landslide at northern terminus of Beichuan rupture triggered by the 2008 M_W 7.9 Wenchuan earthquake. *Bulletin of the Seismological Society of America* 100: 2689–2699. https://doi.org/10.1785/0120090256.

Zhang, H., and Z. Ge. 2010. Tracking the rupture of the 2008 Wenchuan earthquake by using the relative back-projection method. *Bulletin of the Seismological Society of America* 100: 2551–2560. https://doi.org/10.1785/0120090243.

Zhang, P.-Z., X.-W Xu, X.-Z Wen, and R.K. Rang. 2008. Slip rates and recurrence intervals of the Longmen Shan active fault zone and tectonics implications for the mechanism of the May 12 Wenchuan earthquake, 2008, Sichuan, China (in Chinese with English abstract). *Chinese Journal of Geophysics* 51: 1066–1073.

Zhang, Y., W.-P. Feng, L.-S. Xu, C.-H. Zhou, and Y.-T. Chen. 2009. Spatio–temporal rupture process of the 2008 great Wenchuan earthquake. *Science in China Series D-Earth Sciences* 38 (10): 1186–1194.

Zhang, P.-Z., X.-Z. Wen, Z.-K. Shen, and J.-H. Chen. 2010. Oblique, high-angle, listric-reverse faulting and associated development of strain: The Wenchuan earthquake of May 12, 2008, Sichuan, China. *Annual Reviews of Earth and Planetary Sciences* 38: 353–382. https://doi.org/10.1146/annurev-earth-040809-152602.

Zhang, G., C. Qu, X. Shan, X. Song, G. Zhang, C. Want, J.-C. Hu, and R. Wang. 2011. Slip distribution of the 2008 Wenchuan M_S 7.9 earthquake by joint inversion from GPS and InSAR measurements: a resolution test study. *Geophysical Journal International* 186: 207–220. https://doi.org/10.1111/j.1365-246X.2011.05039.x.

Zhang, G., M. Vallée, X. Shan, and B. Delouis. 2012. Evidence of sudden rupture of a large asperity during the 2008 Mw7.9 Wenchuan earthquake based on strong motion analysis. *Geophysical Research Letters* 39: L17303. https://doi.org/10.1029/2012gl052516.

Zhao, C., Z. Chen, L. Zhou, Z. Li, and Y. Kang. 2010. Rupture process of the 8.0 Wenchuan earthquake of Sichuan, China: The segmentation feature. *Chinese Science Bulletin* 55: 284–292.

Zheng, Y., H.-S. Ma, J. Lü, S. Ni, Y.-C. Li, and S.-J. Wei. 2009. Source mechanism of strong aftershocks (Ms5.6) of the 2008/05/12 Wenchuan earthquake and the implication for seismotectonics. *Science in China Series D* 52 (6): 739–753. https://doi.org/10.1007/s11430-009-0074-3.

Zhou, Q., X. Xu, G. Yu, X. Chen, H. He, and G. Yin. 2010. Width distribution of the surface ruptures associated with the Wenchuan earthquake: Implication for the setback zone of the seismogenic faults in postquake reconstruction. *Bulletin of the Seismological Society of America* 100: 2660–2668. https://doi.org/10.1785/0120090293.

Zhu, S. 2018. Why did the most severe seismic hazard occur in the Beichuan area in the 2008 Wenchuan earthquake, China? Insight from finite element modelling. *Physics of the Earth and Planetary Interiors* 281: 79–91. https://doi.org/10.1016/j.pepi.2018.05.005.

Zhu, S., and P. Zhang. 2013. FEM simulation of interseismic and coseismic deformation associated with the 2008 Wenchuan earthquake. *Tectonophysics* 584: 64–80. https://doi.org/10.1016/j.tecto.2012.06.024.

Chapter 3
The Wenchuan Earthquake Fault Scientific Drilling (WFSD) Project

Zhiqin Xu and Haibing Li

Abstract After the devastating Wenchuan earthquake on May 12, 2008, the Wenchuan earthquake Fault Scientific Drilling (WFSD) project was carried out in the Longmenshan fault zone, eastern margin of the Tibetan Plateau, which is the world's most rapid scientific drilling response to large earthquakes. The WFSD project provides an excellent opportunity for geoscientists to explore the formation mechanism of earthquakes. For now, six boreholes have been drilled along the coseismic ruptures of the Yingxiu–Beichuan and Guanxian–Anxian faults. The WFSD project aims to reveal the composition, structure, morphology, and tectonic properties of the Wenchuan earthquake fault zone at deep depths based on multidisciplinary observations, measurements, and analyses, to explore the physical and chemical behavior of the seismogenic faults and their energy states, as well as their rupture processes during the Wenchuan earthquake. All these studies provide evidence to further understand the stress conditions, the causes of rupture nucleation and propagation, the role of fluids in earthquake nucleation, propagation and cessation, and the seismogenic mechanism of seismic faults. At present, some important research results have been achieved: (1) The structure of the Wenchuan earthquake fault zone has been verified; (2) thermal pressurization was an important fault-weakening mechanism during the Wenchuan earthquake, and graphite can be considered as an indicator for the large earthquakes; (3) the lowest faulting frictional coefficient in the world has been obtained, and for the first time, prompt fault healing has been recorded; (4) a tectonic framework of the Longmenshan fault belt and a new formation model for the Wenchuan earthquake have been proposed; (5) the spatial relationship between seismic activities and the different sections of the Longmenshan thrust belt has been

The original version of this chapter was revised: Incorrect figure has been replaced. The correction to this chapter is available at https://doi.org/10.1007/978-981-13-8015-0_10

Z. Xu (✉)
State Key Laboratory for Mineral Deposits Research, School of Earth Sciences and Engineering, Nanjing University, Nanjing 210046, China
e-mail: xzq@nju.edu.cn; 3077864156@qq.com

Z. Xu · H. Li
Key Laboratory of Deep-Earth Dynamics, Natural Resources Ministry, Beijing 100037, China

Institute of Geology, Chinese Academy of Geological Sciences, Beijing 100037, China

Y.-G. Li (ed.), *Earthquake and Disaster Risk: Decade Retrospective of the Wenchuan Earthquake*, https://doi.org/10.1007/978-981-13-8015-0_3

established based on accurate aftershocks relocation and seismic array observations near the boreholes; (6) the relationship between the characteristics of fluid and seismic activities in the fault zone at deep depth has been discovered, which provides the scientific basis for determining the formation process of large earthquakes.

Keywords Longmenshan fault belt · Wenchuan Earthquake Fault Scientific Drilling (WFSD) project · Wenchuan earthquake · Earthquake mechanism · Tectonic framework

3.1 Introduction

The May 12, 2008, Wenchuan earthquake (M_W 7.9) occurred along the Longmenshan fault on the eastern margin of the Tibetan Plateau (Fig. 3.1). The Wenchuan earthquake ruptured two large parallel faults in the Longmenshan (Yingxiu–Beichuan thrust fault and Guanxian–Anxian thrust fault), producing ~270 and ~80 km of coseismic surface ruptures in 90s, respectively (Xu et al. 2008a, b; Fu et al. 2008; Li et al. 2008; Liu et al. 2008; Zhang et al. 2008; Liu-Zeng et al. 2009; Fu et al. 2011). The earthquake and the induced secondary disasters affected a large area, causing more than 70,000 deaths, at least 370,000 injuries, and about 45 million people lost their homes, with property loss exceeding one trillion renminbi. The disaster was extremely damaging, shocking China and the world. The Chinese government promptly led the people to carry out earthquake relief, rebuilding their homes, and heal the wounds. The Wenchuan earthquake area was reborn. However, this tragedy cannot be forgotten.

The Longmenshan, located along the eastern margin of the Tibetan Plateau, is a special orogenic belt with disparate elevation differences, a large difference in crustal thickness, numerous Neoproterozoic basement outcrops, no Cenozoic sediments in the foreland basin, and showing a crustal shortening in the GPS signal. Because the Wenchuan earthquake occurred along the Longmenshan fault zone with no previous record of earthquakes $\geq M$ 7 and minimal surface movements, the Longmenshan area was listed as a safe zone where great earthquakes are unlikely to occur. The Wenchuan earthquake has brought unprecedented shock and lessons to Chinese earthquake geologists. It warned us that there are potential blind spots in the surface geological survey and GPS monitoring, and it also presents a serious challenge to geoscientists: recognizing the kinematic and dynamic processes of great earthquakes, strengthening the prediction, and monitoring the methods of great earthquakes in potentially dangerous zones, thereby avoiding a repetition of the Wenchuan earthquake tragedy.

Scientific drilling of active (earthquake) fault zones can provide an important basis for solving the fundamental problems of seismic mechanisms through in situ observations, well in situ experiments, laboratory analyses of fault zone materials, and long-term monitoring (Brodsky et al. 2009; Zoback et al. 2007; Boullier 2011). The successful experience of scientific drilling in seismic fault zones in Taiwan of China, Japan, the USA, and New Zealand was inspiring (Ma et al. 2006; Kuo et al.

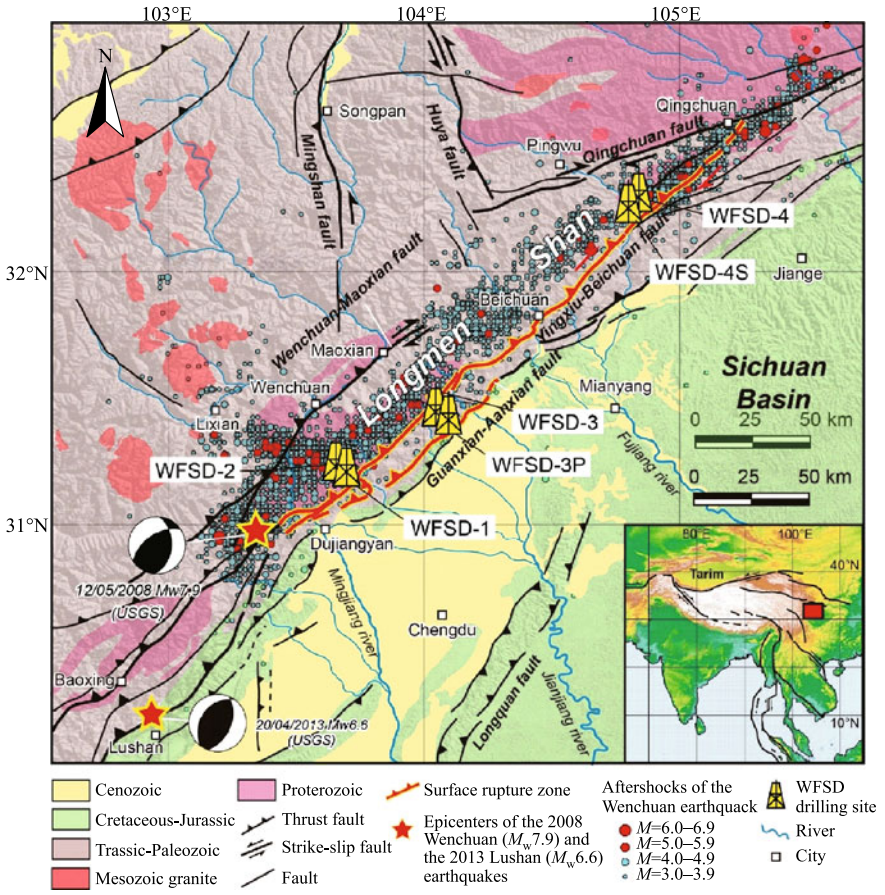

Fig. 3.1 Active tectonic of the Longmenshan and western Sichuan Basin, showing the WFSD drilling sites, epicenters, and focal mechanism of the 2008 Wenchuan and the Lushan earthquakes, and epicenter of aftershocks until August 31, 2009. Surface rupture zones follow the preexisting Yingxiu–Beichuan and Guanxian–Anxian faults

2009; Lin et al. 2013; Fulton et al. 2013; Niu et al. 2008; Ma et al. 2012; Sutherland et al. 2012; Carpenter et al. 2014). However, we know that the heat generated by seismic friction will gradually decay with time; that the porosity of the fracture will heal with time; and that the new material changes with time and with fluids interaction. In order to obtain important seismic information, we need scientific drilling through seismic faults as quickly as possible following a large earthquake.

178 days after the Wenchuan earthquake, while the aftershocks were still happening, with the support of the Chinese government, the Ministry of Science and Technology, the Ministry of Land and Resources, and the China Earthquake Administration jointly organized a scientific team, including Chinese geologists, seismic scientists, and drilling-logging experts. The scientific and technological team

implemented the Wenchuan earthquake Fault Scientific Drilling (WFSD) project, which consists of six wells and 9 km of drilling. This is the first scientific drilling project for seismic fault zone in mainland China (Fig. 3.1). It is also an excellent opportunity to understand the mechanism of earthquake occurrence, effectively monitor aftershocks, and improve seismic monitoring and early warning capabilities. The Wenchuan earthquake Fault Scientific Drilling Project is the world's fastest response to great earthquakes.

3.2 Tectonic Setting

The place where the Wenchuan earthquake occurred is located at the eastern margin of the Tibetan Plateau, east of the NWW-SEE trending Bayan Har block of central Tibet and west of the Sichuan Basin of the Yangtze block (Figs. 3.1 and 3.2). Different types of large faults are present along the boundary of the Bayan Har block (Fig. 3.2). The south and north borders of the block are left-lateral strike-slip faults: The northern boundary is the Kunlun left-lateral strike-slip fault, the southern boundary is the Xianshuihe left-lateral strike-slip fault, the eastern boundary is the Longmenshan thrust fault system, and the western boundary is the Altyn Tagh left-lateral strike-slip fault. Different types of large earthquakes occurred along the above-mentioned fault zones (Fig. 3.2). Focal mechanism shows the Manyi earthquake (1997, M_S 7.5, western Kunlun fault), the Yushu earthquake (2010, M_S 7.1, western Xianshuihe fault system), and the Kokoxili earthquake (2001, M_S 8.1, Kunlun fault) are all strike-slip earthquakes. The rupture lengths are 130, 61, and 426 km, respectively. The horizontal displacements are 3–4, 2, and 7.6 m, respectively. The Wenchuan earthquake and the Lushan earthquake (2013, M_S 7.0) occurred along the Longmenshan fault zone of the eastern boundary of the Bayan Har block are thrust earthquakes. The coseismic rupture zone of the Wenchuan earthquake has two rupture zones: 270 km along the Yingxiu–Beichuan fault and 80 km along the Guanxian–Anxian fault. The coseismic rupture of the Yingxiu–Beichuan fault is a right-lateral thrust fault, and the coseismic vertical displacement is more than 10 m (Li et al. 2008; Liu et al. 2008; Fu et al. 2008). The Guanxian–Anxian fault is a pure reverse fault, and the coseismic vertical displacement is 3.5 m (Li et al. 2008; Liu et al. 2008). In contrast, the northwestern boundary of the Bayan Har block is an extensional normal fault. In 2008, the coseismic fault of the Yutian M_S 7.3 earthquake was a strike-slip fault, coseismic vertical displacement is 3.1 m, the left-lateral horizontal displacement is 1.8 m, and the vertical displacement component is larger than the horizontal displacement component (Li et al. 2010). In April 2014, the new Yutian M_S 7.3 earthquake occurred east of the southwestern end of the Altyn Tagh fault. The strike-slip characteristics of the seismogenic fault are more clear with a greater strike-slip component than the vertical component of the normal fault. The left-lateral horizontal displacement of the coseismic fault is about 1 m, and the vertical displacement is about 0.4 m (Li et al. 2014a, b).

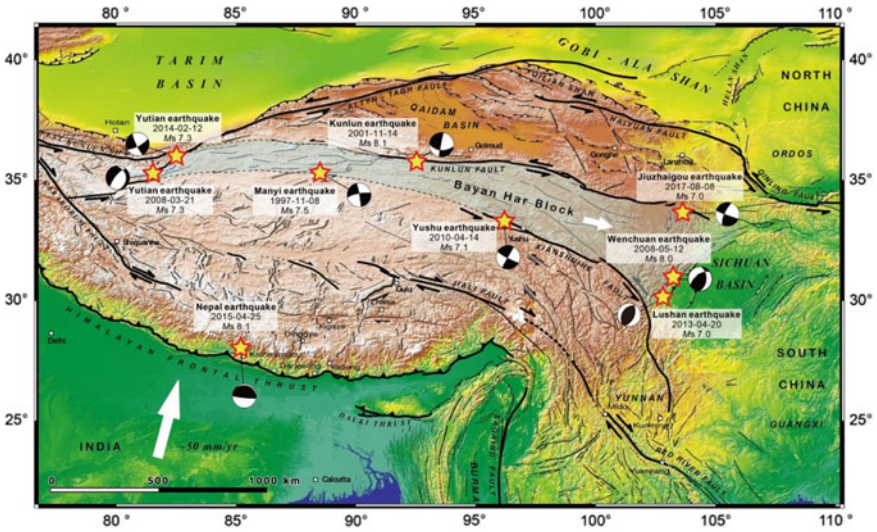

Fig. 3.2 Distribution of different types of large earthquakes ($\geq M7$) which occurred along the Bayan Har block of central Tibet since 1997 (active tectonic of the Tibet from Tapponnier et al. 2001)

The NNE-SSW trending Longmenshan is a compressive thrust belt composed of a number of active reverse faults. The horizontal shortening rate is small, only 3–4 mm/yr, but its vertical displacement is large, the maximum elevation of the mountain can reach more than 7000 m, and GPS measurements show that the vertical uplift rate can reach 3.5 mm/yr (Deng et al. 1994; Wang et al. 2010a, b, c). From the seismic activity record, this tectonic belt has had low activity in history. Before the Wenchuan M_S 8.0 earthquake, no $M \geq 7.0$ earthquake was recorded in the Longmenshan tectonic belt, and only several M 6-6.5 earthquakes occurred in the middle and southern sections. Unfortunately, the Wenchuan earthquake occurred indicating that we must study this active tectonic belt and its seismic hazard.

New research shows that on the west side of the exposed Neoproterozoic crystalline basement of the Longmenshan, a detachment shear zone that slides westward is found, the Longmenshan detachment zone. Together with the Yingxiu–Beichuan fault which is the main thrust fault of the Longmenshan, at 120–100 Ma, it extruded the ancient basement of the Longmenshan to form west-dipping sheets covered on the foreland basin and the Paleozoic–Mesozoic caprocks of the Yangtze Craton (Xu et al. 2008a, b). The epicenter of the Wenchuan earthquake is located within the damaged Yangtze Craton, which is 16–15 km below the extrusion rocks. This is a very special tectonic setting.

3.3 The Wenchuan Earthquake Fault Scientific Drilling (WFSD) Project

The Wenchuan earthquake Fault Scientific Drilling (WDSD) project is the first scientific drilling project about the earthquake disaster in mainland China. It is the first scientific attempt to explore the earthquake mechanism and improve earthquake prediction and early warning capability. It features 'Drilling—Well Detection—Scientific Research' and high-tech well detection, and closely integrates the forefront of science and technology.

The project started drilling in Dujiangyan on November 7, 2008, and completed on June 30, 2014, spending a total of 6 years. Domestic participating organizations are the Institute of Geology, Chinese Academy of Geological Sciences; Institute of Geology, China Earthquake Administration, Chinese Academy of Sciences; Peking University; China University of Geosciences (Wuhan); China University of Geosciences (Beijing); Jilin University; Chengdu University of Technology; Hefei University of Technology School of Resources and Environment; Chang'an University Applied Geophysics Institute; Sichuan Geological Survey; Beijing Geological Engineering Design and Research Institute; Beijing Exploration Engineering Institute; Jiangsu Sixth Geological Team; China Geological Equipment Group Co., Ltd.; Bureau of Geophysical Prospecting INC.; China National Petroleum Corporation Bohai Drilling Engineering Co., Ltd.; Sinopec Southwest Oil and Gas Company; Sinopec Shengli Oilfield Logging Company, as well as 36 other organizations. A total of 425 researchers participated in this study. International and regional participants include: University of California (Santa Cruz), US Southern Illinois University, German Geoscience Research Center (GFZ), Kyoto University Disaster Prevention Research Institute, Japan Marine Science and Technology Center Kochi Core Research Institute, Paris Institute of Geophysics, France Strasbourg, Institute of Geophysics, University of Lyon, Dalhousie University, Utrecht University, University of Padua, University of Taiwan, China, Central University of Taiwan, China, and Academia Sinica, China, etc. The chief scientist of the project is Professor Xu Zhiqin, the co-principal scientist is Professor Wu Zongliang, the chief geologist is Professor Li Haibing, and the chief engineer is Zhang Wei.

3.3.1 Key Scientific Problems

The purpose of the Wenchuan earthquake Fault Scientific Drilling project is to explore the key scientific problems arising from the Wenchuan earthquake. The Wenchuan earthquake caused rupture along two faults. This type of earthquakes is rare in global history, which made geoscientists wonder about the following questions: In which kind of stress environment did the Wenchuan earthquake occur? How did large coseismic ruptures occur? How did underground fluid affect the nucleation, occurrence, and halt of earthquakes? How strong were the aftershocks and how long did

aftershocks last after the Wenchuan earthquake? Why did the epicenter of the Wenchuan earthquake occur on the Yangtze Craton?

3.3.2 Scientific Objectives of the Project

The scientific goals of the Wenchuan earthquake fault scientific drilling project are to conduct multidisciplinary observations, testing and research on cores, drill cuttings, and fluid samples of boreholes, revealing the deep material composition, structure and tectonic properties of the Wenchuan earthquake fault zone; to explore the physical and chemical behavior, energy state and fracture evolution of rocks during the earthquake; to understand the stress environment of the Wenchuan earthquake, the causes of great earthquake ruptures and propagation, and the role of underground fluids in the process of nucleation, occurrence, and stopping of earthquakes, thus testing and deeply understanding the mechanism of earthquake fault.

3.3.3 Project Content

Through the WFSD project, six boreholes on the hanging wall of the Longmenshan earthquake rupture zone were carried out, with a total depth of about 9 km, to measure and research the fluid, stress, permeability, and seismic wave velocity; to establish a series of lithology, structure, physicochemical properties, logging, temperature, friction, fluid, and geostress profiles of earthquake faults; to reveal the relationship between large sliding distance with slip velocity and fracture friction; to study the relationship between temperature change and friction coefficient; to remodel the process of rupture evolution; to deepen the understanding of the seismic energy state of the seismic fault zone, the period of earthquake healing, and the constraints of the physicochemical behavior of the fault zone on the mechanism of earthquake occurrence. The project directly samples the source areas of great earthquakes and microseisms, and conducts multidisciplinary research on geological structures, seismic geology, rock mechanics, chemical physics, seismic physics, fluid interactions, and rheology using a series of advanced observation and analysis methods, to reveal the physical and chemical effects which control faulting and earthquakes, and provide basic data for future monitoring, prediction, or early warning of earthquakes. The project includes the following seven aspects:

(1) Identify the structure and structural properties of the fault zone

Under the premise of accurately correcting the well logging and core depths, by integrating geophysical logging, well-preserved core and active source seismic imaging and observation, to accurately identify active fault location, structure, behavior, and various structural elements, to accurately measure the width of the damage zone and

damage strength, and to classify the type of fault rocks to identify the structure and structural properties of the Wenchuan earthquake fault zone.

(2) Explore the mechanism of the Wenchuan earthquake

Through comprehensive research of scientific drilling, including petrology, geochemistry, physical properties, structure, and other aspects of observation and research, to reveal the deep material composition, structure and structural properties of the Wenchuan earthquake fault zone; to restore the physical and chemical behavior, energy state and fracture evolution of the rocks during the earthquake; to deepen our understanding of the stress environment caused by the Wenchuan earthquake, the causes of large earthquake ruptures and the spread from southwest to northeast, and the role of underground fluids in the nucleation, occurrence, and stopping of earthquakes; to test and deepen our understanding of the nature of earthquake faults and the mechanism of earthquake.

(3) Track the thermal history of the Wenchuan earthquake fault zone

Through the study of geochemical characteristics and local melting of rocks, minerals, and fluids in seismic fault zones, the thermal history of fault zones is defined, and evidence of thermal anomalies and their spatio-temporal variations is provided. The understanding of the role of fluids in the process of earthquake nucleation, occurrence, and halt is deepened.

(4) Microseismic array observation and aftershock study near the borehole and continuous dynamic monitoring of seismic wave travel time in the fault zone

Through the precise location of the Wenchuan earthquake aftershocks, seismic array observation and location near the boreholes, and microseismic data processing, the spatial relationship between seismic activity and the different segments of the Longmenshan fault zone is determined. Using vibroseis to conduct shallow seismic exploration of the fault zone, the stratigraphic structure of the borehole area has been determined. Through the precise control of artificial seismic source and high-precision receiving system, the continuous dynamic monitoring of seismic wave travel time in the fault zone is carried out. Therefore, the stress change and healing process of fault zone, and the relationship with the aftershock are studied, which provides a basis for the study of the mechanism of earthquake occurrence.

(5) Long-term observation and post-earthquake effects of fluid geochemistry

Through the comparative analysis of the geochemical profile of the Wenchuan earthquake preparation and occurrence process, and the long-term observation of fluid geochemistry before and after the Wenchuan earthquake and the post-earthquake effect of fluid geochemistry, the relationship between the dynamic diffusion of pore pressure and the spatio-temporal evolution of earthquakes is discussed. The dynamic relationship between deep fluid characteristics and tectonic activity provides a scientific basis for determining the behavior of deep fluid during the process of great earthquakes.

(6) Reconstruct the Wenchuan earthquake tectonic setting and deep structure

Through the WFSD project and the study of surface ruptures and tectonic setting, the Longmenshan tectonic framework and orogenic evolution process were reshaped; the 3D deep structure was revealed with the exploration of geophysical profiles across the Longmenshan; the study of the Tibetan Plateau activity structure and the background of the Wenchuan earthquake clarify the causes of material movement and stress concentration caused by the collision between India and Asia, and reveal the mechanism of the Wenchuan earthquake.

(7) Long-term observation in the boreholes

Deep seismic activities are observed and monitored; post-earthquake stress attenuation is measured and recorded by borehole seismometers and integrated geophysical detectors. From the perspective of 3D seismic array, a new analysis and discussion on the aftershock trend, aftershock magnitude, and influence range of the Wenchuan earthquake fault zone are carried out.

3.4 Main Preliminary Research Results

3.4.1 Establishing a Series of Profiles of Scientific Drilling of the Wenchuan Earthquake Fault Zone

The WFSD project implemented six holes: WFSD-1 (1201 m), WFSD-2 (2284 m), WFSD-3P (552 m), WFSD-3 (1502 m), WFSD-4 (2339 m), and WFSD-4S (1204 m), i.e., a total depth of 9000 m, including lithology charts, tectonic profiles (rock characteristics, microfractures, and fractures), fluid, petrophysical, mineralization, logging, geostress, and gravity profiles (Zhang et al. 2012; Yang et al. 2012c; Wang et al. 2013; Li et al. 2013, 2014a, b, 2016; Si et al. 2014; Zhang et al. 2017a, b). These profiles respectively show that different parameters vary with depth. It can help us to more fully understand the characteristics of the fault zone under the surface and determine the location of the principal slip zone (PSZ) of the earthquake by abnormal value, thus identifying the Longmenshan earthquake fault system and earthquake mechanism.

3.4.1.1 WFSD-1

The WFSD-1 drilling site is located along the southern segment of the YBF, in the Bajiaomiao village (Fig. 3.1).

The lithologies revealed in the drilling cores contain volcanic rocks, granite, sandstone (rich in coal material), siltstone, liquefied breccia, and other fault-related rocks (Fig. 3.3). The rocks above 585.75 m depth are volcanic rocks and granite, belonging to the Neoproterozoic Pengguan complex; the strata beneath 585.75 m depth belong

to the Late Triassic Xujiahe Formation, mostly composed of sandstone, siltstone, mudstone, and liquefied breccia, with some of them characterized as fault-related rocks (Fig. 3.3) (Li et al. 2013). The fault zone lies between 585 and 598 m depth. The fault-related rocks present within the cores are primarily fault gouge, cataclasite, and fault breccia. The thickness of the fault gouge layers varies from millimeters to meters (Li et al. 2013). Based on the distribution of the fault-related rocks, it is clear that many secondary faults formed along the southern part of the YBF, most of them with fault gouge layers; therefore, the YBF zone (575.7–759 m) is typical of a multiple fault core structure (Fig. 3.3) (Li et al. 2014a, b). The gamma radiation of the cataclasite varies greatly and is generally smaller than the black fault gouge, the dark gray fault gouge, and the fault breccia. The acoustic travel time difference is also relatively small, and the resistivity is significantly higher than the lower fault gouge and fault breccia. All the fault-related rocks correspond well with the high magnetic susceptibility. The magnetic susceptibility values of the Pengguan complex vary greatly (Li et al. 2018). The partial magnetic susceptibility and resistivity of the Xujiahe Formation are relatively low and the change is small, and the acoustic travel time difference is larger than that of the Pengguan complex.

3.4.1.2 WFSD-2

The WFSD-2 drilling site is located at Dujiangyan, east side of the Longmenshan (Figs. 3.1 and 3.4).

The WFSD-2 lithology chart is the deepest of the six wells, and the main rock units of the central segment of the Longmenshan are fairly completely presented. The cores of WFSD-2 borehole consist of the Pengguan complex and the Upper Triassic Xujiahe Formation (Fig. 3.5b). The lithology of the Pengguan complex is mainly granite, diorite, and pyroclastic rocks (Fig. 3.5a), including the first section (499.03–599.31 m), the second section (1211.49–1360.25 m), the third section (1361.26–1679.51 m), and the fourth section (1715.48–2081.47 m). The lithology of the Xujiahe Formation is mainly sandstone, siltstone, mudstone, shale, coal bed (seam), and conglomerate (Fig. 3.5a), including the upper section (599.31–1211.49 m), the middle section (1679.51–1715.48 m), and the lower section (2081.47–2283.56 m). Figure 3.6 shows that different fault zones of different sizes are present in the WFSD-2 cores, and each fault zone is composed of different fault rocks. The thickness of the fault gouge varies from a few millimeters to a few meters, the thickest of which reaches 6 m and is distributed at depths of 1679.51–1698.66 m. The cataclasite usually mixes with fault gouge and fault breccia (Fig. 3.5a). It can be seen from Fig. 3.5c–h that except for the diameter of the borehole, the variation of other log values and the distribution of rock units show a certain regularity. The natural gamma curve and P-wave velocities of the Pengguan complex are lower than those of the Xujiahe Formation, and their resistivity, density, and porosity are higher than those of the Xujiahe Formation. Figure 3.5i reflects the degree of fragmentation of the entire cores from WFSD-2. In the macroscopic view, the WFSD-2 cores are highly damaged. The crack density indicates that there are a large number of

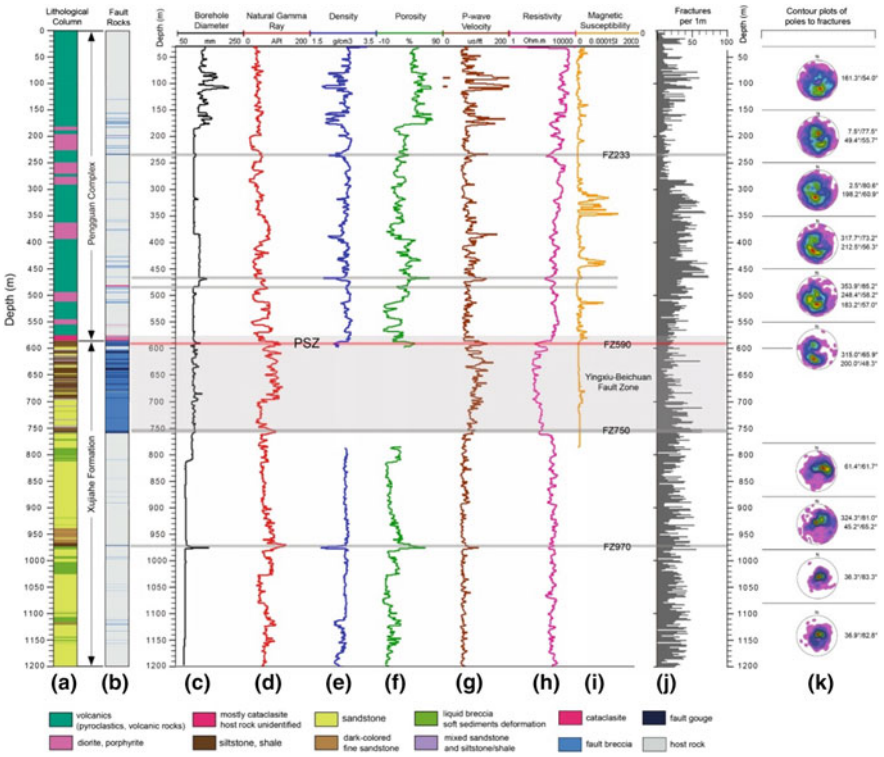

Fig. 3.3 Lithology chart and comprehensive well logging curves of the WFSD-1. **a** Lithological column; **b** distribution of fault-related rocks in the drilling core; **c** well diameter; **d** natural gamma radiation; **e** density; **f** neutron porosity; **g** P-wave velocity; **h** electric resistivity; **i** magnetic susceptibility; **j** cracks density in the drilling core; **k** pole projection of fractures at different depth (down semi-sphere)

fractures under the lower part of the first member of the Pengguan complex in the WFSD-2 cores. The largest crack density is more than 110 per meter, and the average is about 33.01 per meter (Fig. 3.5i). This indicates that the great earthquakes in the Longmenshan area not only affect the vicinity of the fault zone, but also have a wide range of influences, suggesting that the tectonic activities in the Longmenshan area are very strong (Zhang et al. 2012).

3.4.1.3 WFSD-3P and WFSD-3

The WFSD-3P and WFSD-3 drilling sites are located in Jiulong County, Mianzhu, in the hanging wall of the Guanxian–Anxian fault in the Triassic Xujiahe Formation (Fig. 3.1).

Fig. 3.4 Site of the WFSD-2 borehole

The drilling cores of WFSD-3P and WFSD-3 appear mainly gray to dark gray and are composed of sandstone, siltstone, carbonaceous siltstone, liquefied breccia, coal seam, and fault breccia, as well as fault gouge (Figs. 3.6 and 3.7). Combined with regional stratigraphic characteristics, the cores mainly consist of the middle (T3x2) and upper (T3x3) segments of the Xujiahe Formation in a reversed sequence (Li et al., 2016). In the WFSD-3P cores, the zone of fault rocks is mainly distributed at depths of 440.59–511.11 m (actual thickness is 50 m) (Fig. 3.6). Fault gouges are mainly present at depths of 451–464 m and 490–507 m. The gamma radiation and neutron porosity of the fault zone clearly increase. The resistivity, density, and sonic velocity tend to decrease. The damage zone is mainly distributed in the fault zone and its hanging wall. In the WFSD-3 cores, the zone of fault rocks has been identified at 1192–1250 m depth with an actual width of ~50 m (Fig. 3.8). The gamma radiation at the fault zone increases slightly, and the resistivity, density, neutron porosity, and wave velocity decrease. The thickness of the Anxian–Guanxian fault zone is 40–50 m, which is a typical low-angle listric thrust fault zone (Fig. 3.9). The fault zone has low resistivity, low wave velocity (high acoustic travel time difference), and high natural gamma characteristics. The fracture zone is distributed on the hanging wall and exhibits an asymmetrical fault structure. The fault gouge has a low magnetic susceptibility characteristic.

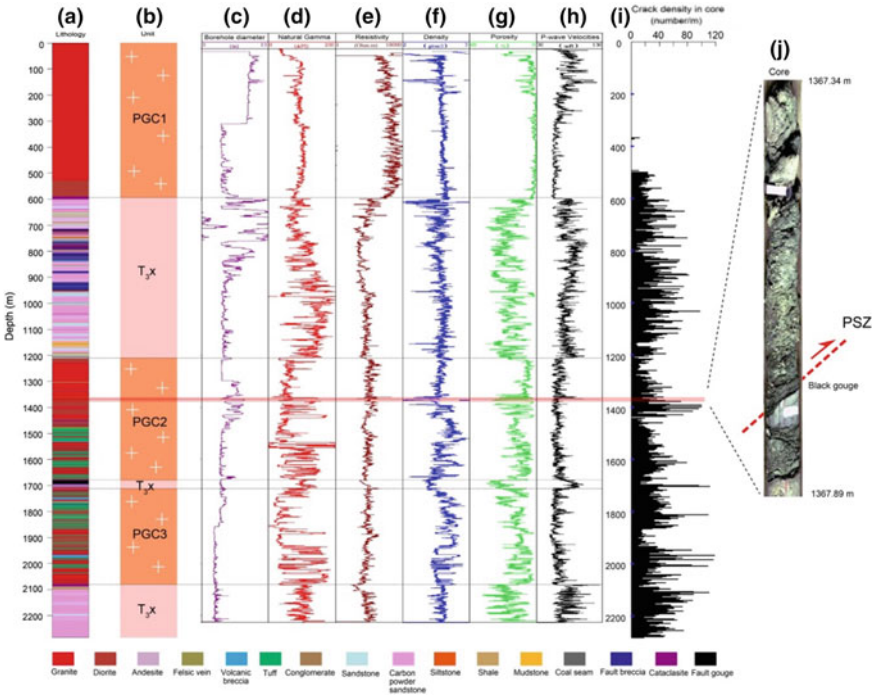

Fig. 3.5 Lithologic chart, logging profile, and crack density in the cores of the WFSD-2 borehole. **a** Lithology chart; **b** rock units; **c** borehole diameter; **d** natural gamma; **e** resistivity; **f** density; **g** porosity; **h** P-wave velocities; **i** crack density in cores; **j** core of PSZ of the Wenchuan earthquake. PGC: Neoproterozoic Pengguan complex; T3x: Xujiahe Formation; PSZ: principal slip zone. The black dashed lines represent the boundaries of the rock units

3.4.1.4 WFSD-4 and WFSD-4S

WFSD-4 and WFSD-4S drilling sites are located in Nanba County, Pingwu (Fig. 3.1). The drilling cores of WFSD-4 and WFSD-4S are composed of Qiujiahe Formation and Youfang Formation of the low series of Cambrian. The Qiujiahe Formation is mainly composed of slate and carbonate slate, and the Youfang Formation is mainly composed of metasandstone. In the WFSD-4 cores, there are seven main secondary fault zones mainly distributed from 2070 to 2225 m depths (Fig. 3.10). Fault rocks are mostly fault breccia. These secondary fault zones are located in the hanging wall of the north segment of the Yingxiu–Beichuan fault zone. In the WFSD-4S cores, a large number of fault rocks are present, such as fault breccia, cataclasite, and fault gouge which can reflect cataclastic deformation (Fig. 3.11). Through the analysis of fault rocks, nine secondary thrust fault zones with different scales and different structures are confirmed. As a whole, the cores of WFSD-4S are relatively damaged. Part of the cores is extremely crushed. Cracks are well developed in the entire cores.

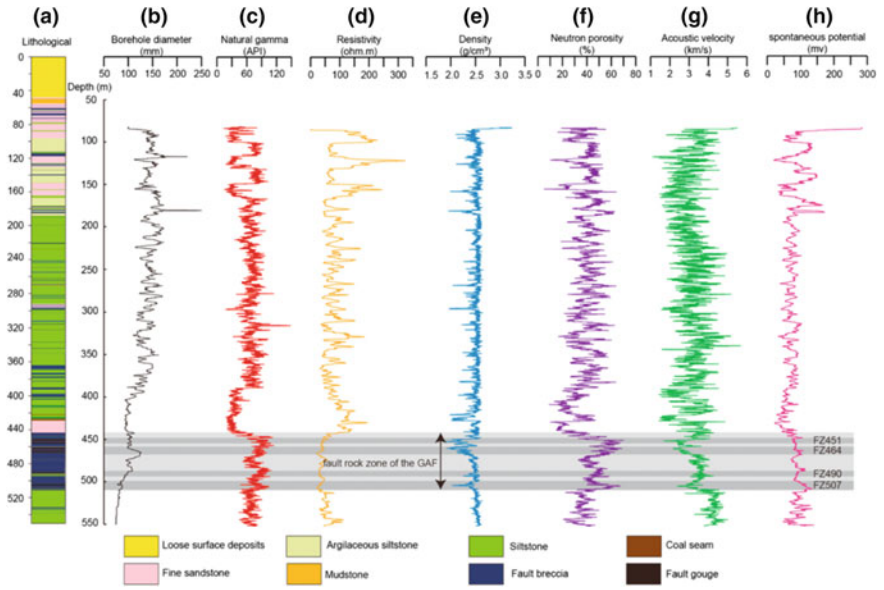

Fig. 3.6 Lithology chart and logging profile of the WFSD-3P borehole (after He et al. 2018)

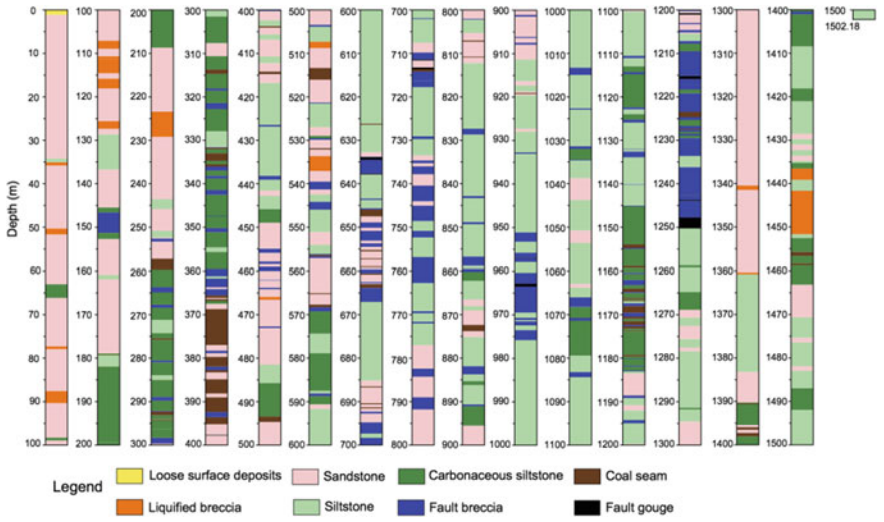

Fig. 3.7 Lithology chart and fault rock distributions in the WFSD-3 cores, with depths being the borehole depths (after Li et al. 2016)

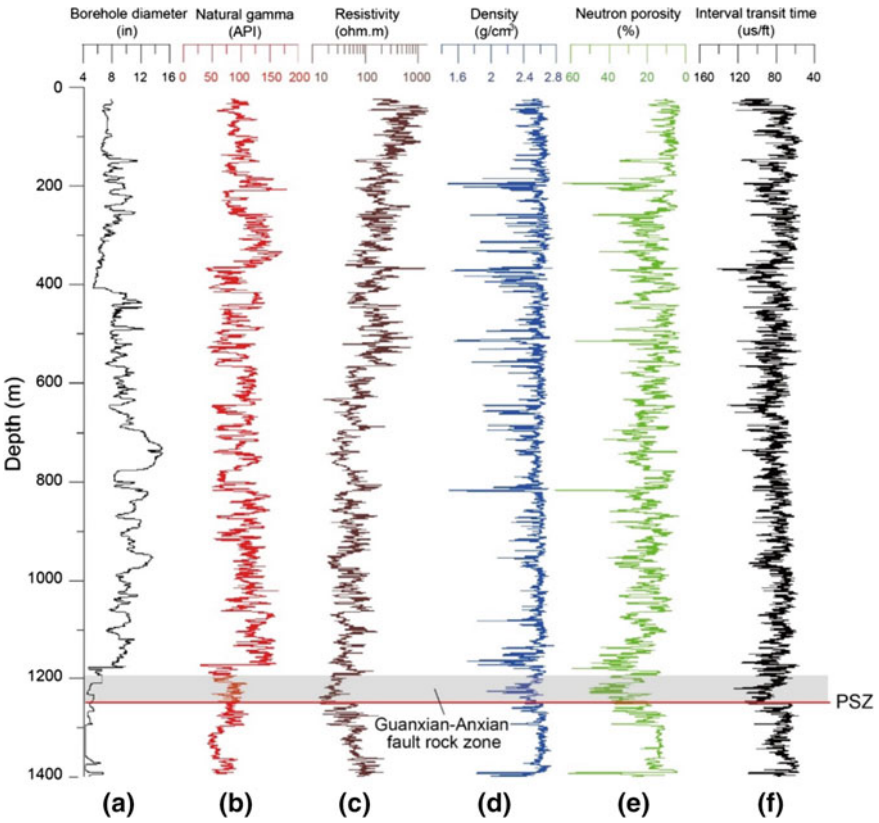

Fig. 3.8 Logging data from 24 to 1400 m depth in the WFSD-3 boreholes. **a** Borehole diameter; **b** natural gamma; **c** deep lateral resistivity; **d** density; **e** neutron porosity; **f** interval transit time (inversely proportional to the wave velocity) (after Li et al. 2016)

The mean crack density of the upper principal slip zone is approximately equal to the lower part, showing a symmetric fault structure.

3.4.2 Determination of the Structure, Deformation Characteristics, and Process of the Wenchuan Earthquake Fault Zone

The Wenchuan earthquake formed a 270-km rupture zone along the Yingxiu–Beichuan fault of the Longmenshan. Through the study of the surface outcrop in Bajiaomiao (Hongkou County) in the southern part of the Yingxiu–Beichuan fault as well as from the drilling cores, the Yingxiu–Beichuan fault with the west-dipping listric

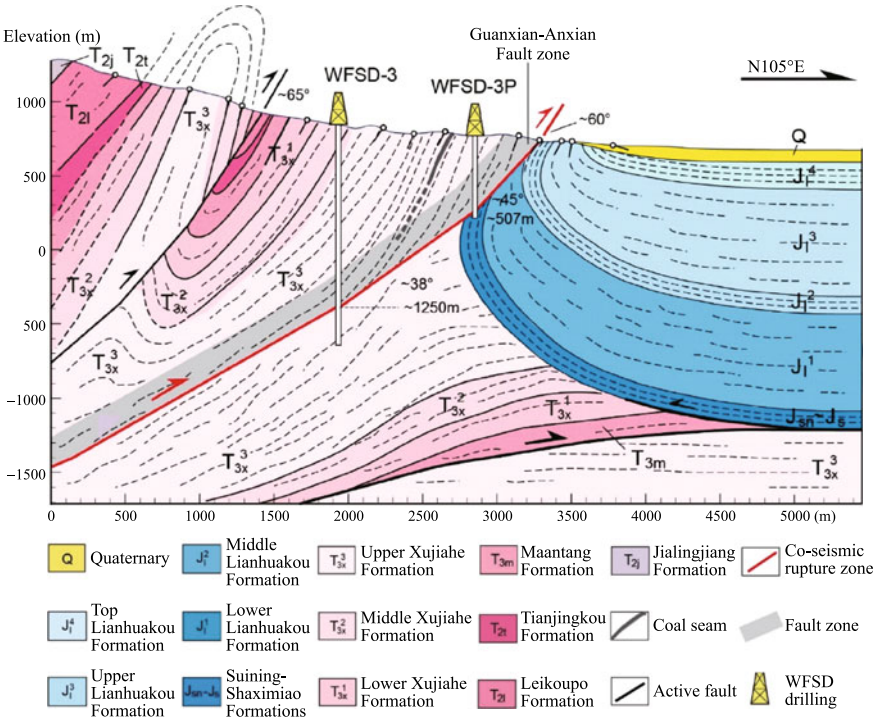

Fig. 3.9 Geological section across WFSD-3 drilling site and coseismic rupture zone of the Wenchuan earthquake. The width of the Guanxian–Anxian fault zone (gray stripe) is about 210 m. The surface rupture zone strikes ~N30°E and dips 60°NW at the bottom of the fault zone at the outcrop. The dip angle of the Guanxian–Anxian fault zone is about 38° at a depth of ~1250 m

appears as a high-angle thrust strike-slip fault with developed fractured rocks, pseudotachylite, fault gouge, fault breccia, and other types of fault rocks. Its overall trend is N55°–65°E, and the width of the fault zone is about 240 m. Pseudotachylites formed by multistage melting of fault rocks are found both at the surface and in the borehole cores (Wang et al. 2015a, b; Zhang et al. 2017a, b), suggesting that many large earthquakes occurred in the geological history. Comprehensive investigation found that the Yingxiu–Beichuan fault zone is composed of five fault rock units with different characteristics and has multi-core structural features (Wang et al. 2014). Different combinations of fault rocks and their structural characteristics show that each earthquake has a tendency to migrate downward the footwall (Wang et al. 2010a, b, c, 2013).

The cores from 575.7 to 759 m depths in WFSD-1 represent cataclasite and fault gouge (183.3 m) between the Pengguan complex and the T_3 coal-bearing strata which constitute the Yingxiu–Beichuan fault. The Yingxiu–Beichuan fault zone is a long-term locked high-angle thrust strike-slip fault zone that is prone to large earthquakes and has a long-term seismic evolution history. Based on a detailed study of the cores

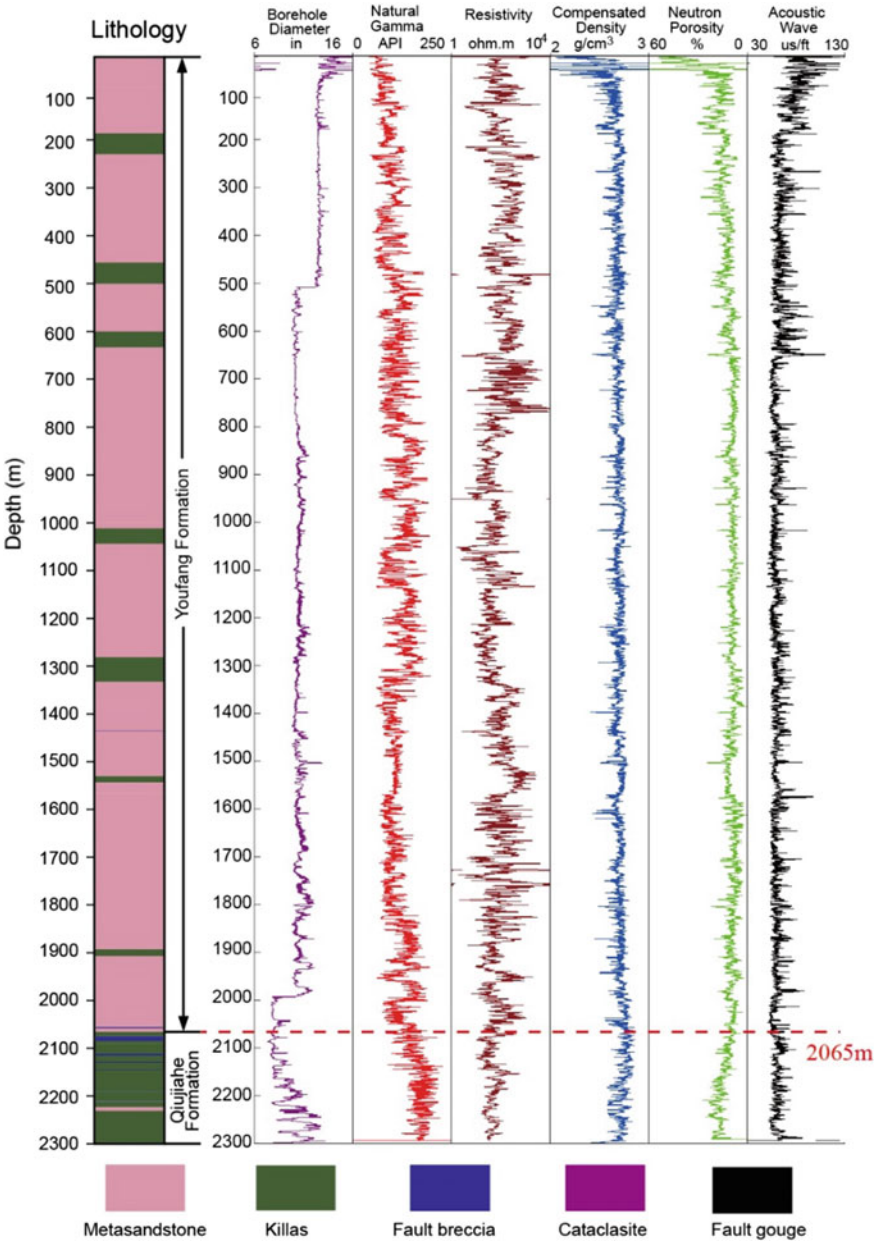

Fig. 3.10 Lithology chart and logging profile of the WFSD-4 borehole

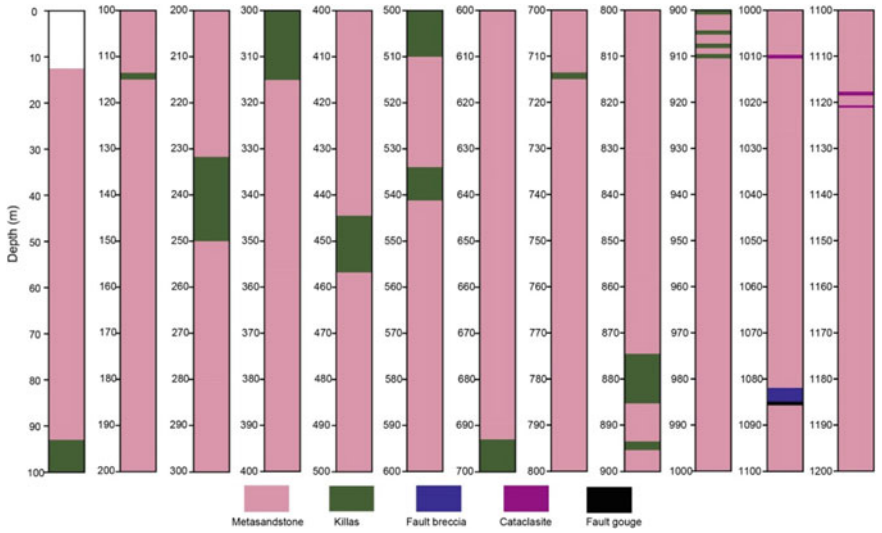

Fig. 3.11 Lithology chart of the WFSD-4S borehole

and fault rocks in WFSD-1, the location of the principal slip zone of the Wenchuan earthquake is identified at a depth of about 590 m, including a fresh dark black fault gouge (589.17–589.25 m core depth) (Figs. 3.12 and 3.13), whose particles are relatively thin and uniform.

From the photomicrographs, well-developed structural foliation of the fault gouge with S-C structures and asymmetric rotational structures indicates clear shear direction (Fig. 3.13) (Li et al. 2013; Wang et al. 2015a, b). Striation left by fault slip is present on the fault plane (Kuo et al. 2014). Graphite with lubrication and low friction coefficient (Li et al. 2015) is also found in the fault gouge (Kuo et al. 2014) and has high magnetic susceptibility characteristics (Li et al. 2013) and abnormal temperature, logging, drilling fluids, and clay mineral composition (Tang et al. 2013; Li et al. 2013, 2014a, b; Si et al. 2014). This indicates that the plane is the principal slip zone. The high magnetic susceptibility value of fault gouge may be due to the high temperature caused by friction during fault sliding to form new magnetic minerals or increased content of magnetic minerals (Hirono et al. 2006, 2008; Mishima et al. 2006, 2009; Tanikawa et al. 2007, 2008; Chou et al. 2012; Yang et al. 2012a, b, 2013). This illustrates that the frictional sliding of fault during the earthquake produces high temperatures and thus causes a series of physical and chemical changes.

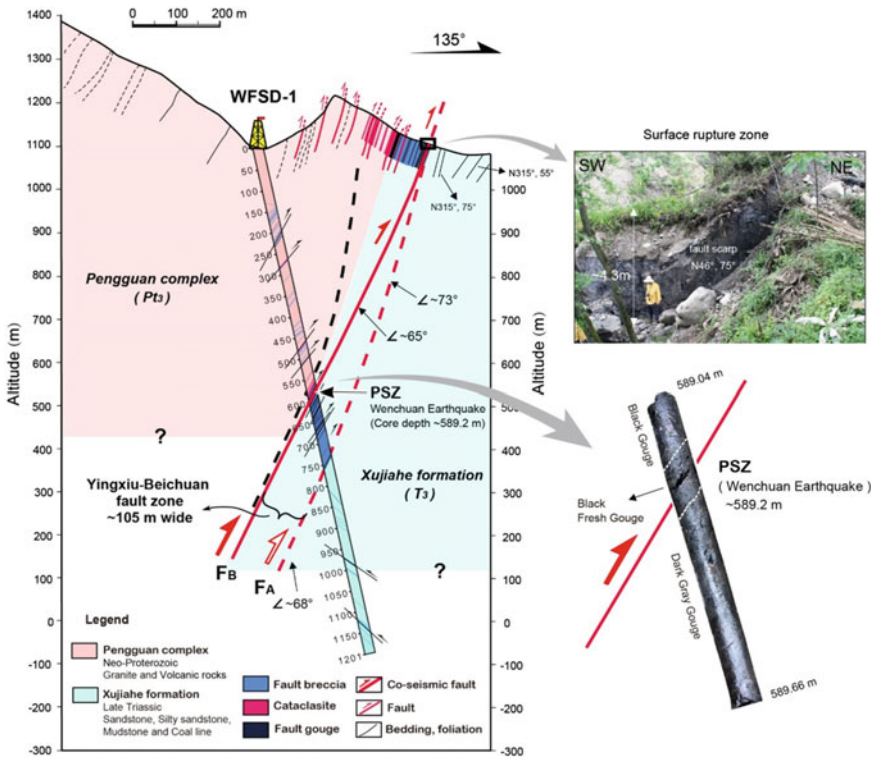

Fig. 3.12 Geologic cross-section across WFSD-1 drilling site of the 1200-m hole and coseismic surface rupture zone of the Wenchuan earthquake (after Li et al. 2013). The width of the Yingxiu–Beichuan fault zone (consisting of cataclasite, fault breccia, and fault gouge) is about 190 m at the outcrop. The surface rupture zone strikes N46°E and dips 75°NW at the bottom of the fault zone at the outcrop. FA: coseismic fault inferred from the dip angle observed at the surface and joins to the bottom of the fault zone in WFSD-1 cores. FB: coseismic fault inferred in this study (see text for details). The Yingxiu–Beichuan fault zone is about 100 m wide in WFSD-1 cores, similar to the 190 m width of the fault zone at the outcrop. The dip angle of the Yingxiu–Beichuan fault zone is about 68°–73° at a depth of ~760 km

3.4.3 Fault-Slip Mechanism and Post-earthquake Healing Process of Wenchuan Earthquake

3.4.3.1 Discovery of Fossils of Earthquakes, Proving Thermal Pressure as a Mechanism of Fault Slip and Weakening

Scanning electron microscopy (SEM) and transmission electron microscopy (TEM) analyses of the relatively fine and uniform particles of the principal slip zone at 589.21–589.22 m depths were carried out (Fig. 3.14a, b). A sliding layer was found with smaller particle sizes ($\leq$10 μm) about 100–200 μm thick (Fig. 3.14b).

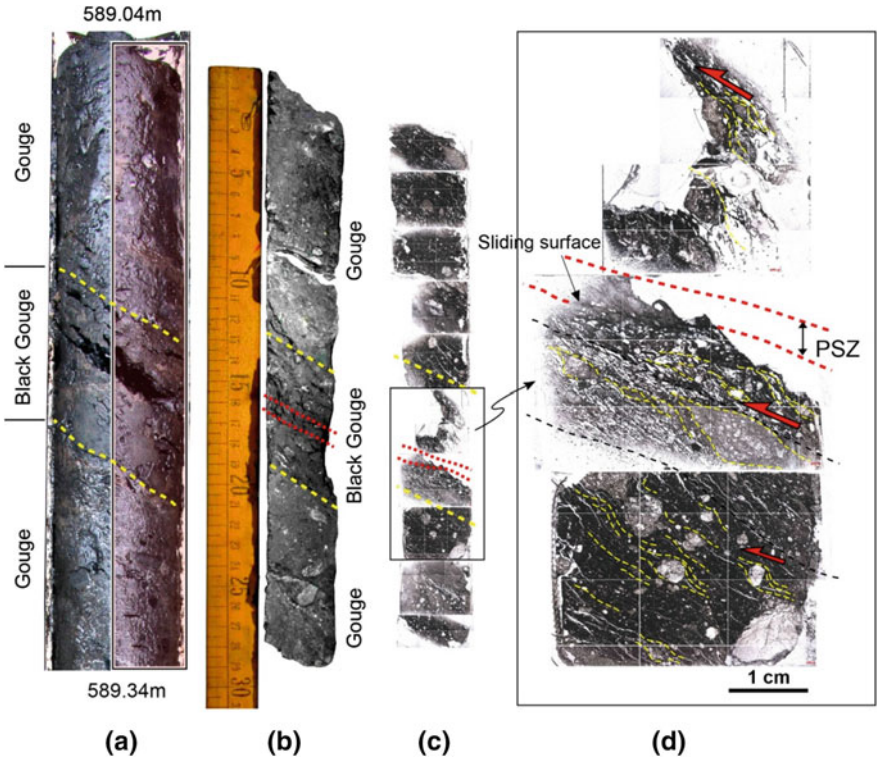

Fig. 3.13 Characteristics of fresh gouge and the principal slip zone (PSZ) of the Wenchuan earthquake in the WFSD-1 cores (after Li et al. 2013). **a** The central part of the gouge is broken due to water loss and is located close to the slip plane. The pink area to the right is the location of thin sections; **b** the broken part shows the bands of calcite (white fragments). The section between red dotted lines is darker and generally without calcite; **c** the continuous thin sections (plane-polarized light) correspond to (**b**); **d** foliated gouge micrograph (plane-polarized light). The PSZ of the Wenchuan earthquake is outlined by red dotted lines where fine and uniform grains as well as the slip plane can be observed

Combined with testing and analyses of synchrotron radiation X-ray diffraction (XRD), not only smectite minerals but also graphite was found enriched in this layer (Fig. 3.14d, e). This graphite is progressively and irreversibly converted from unordered organic compounds or amorphous carbonaceous materials to stable graphite by thermal activation (Buseck and Beyssac 2014). Therefore, the increase in crystallographic order of carbonaceous materials is associated with graphitization, which is widely used to indicate the highest temperatures reached by sedimentary and metamorphic rocks (Barker and Goldstein 1990; Beyssac et al. 2002). The presence of graphite in the slip zone indicates that during the earthquake the fault-slip mechanism is dominated by thermal pressurization, and that the fault strength of the Wenchuan earthquake is extremely low (Kuo et al. 2014; Wang et al. 2015a, b). The enrichment of graphite along the slip zone can be used not only as

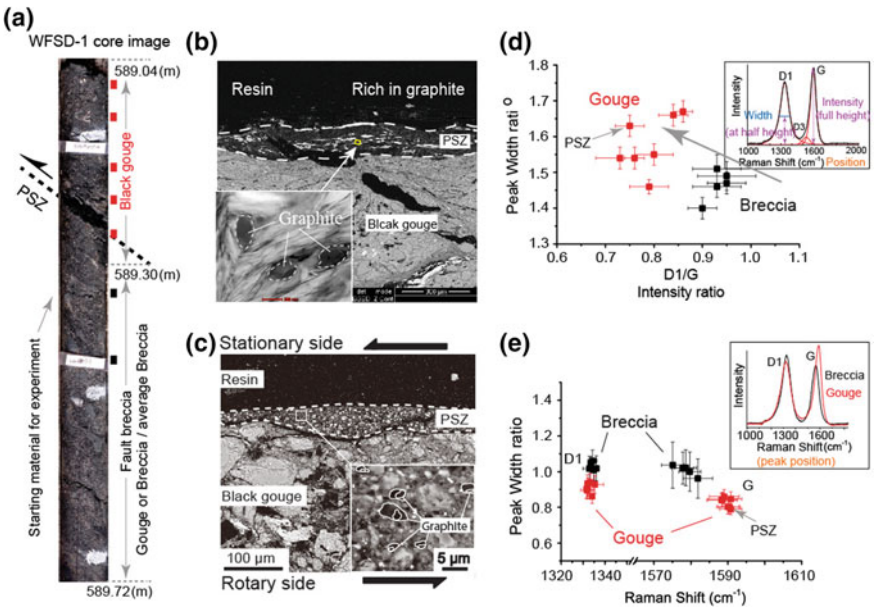

Fig. 3.14 Seismic fossils, coseismic graphitization, were found in the principal slip zone (PSZ) of the Wenchuan earthquake fault at 589 m depth in the WFSD-1 cores (modified after Kuo et al. 2014, 2017). **a** Core images exhibiting the PSZ of the Wenchuan earthquake. Locations of analyzed samples are indicated by red (black gouge) and black (breccia) boxes. **b** Backscattered scanning electron microscope (SEM) image of a thin section cut through part of the PSZ (within white dashed lines). Thickness of the PSZ in this location is ~200 μm and the PSZ is characterized by a local enrichment of graphite-rich layers (the insert backscattered SEM image). **c** Backscattered SEM image of thin section cut approximately parallel to the slip direction and perpendicular to the experimentally deformed gouge layer. White dashed lines enclose localized and fine-grained PSZ between 25 and 125 μm thick that developed adjacent to the stationary side of the gouge holder. Inset backscattered SEM image shows detail of small graphite particles. **d** Defect band (D1) to graphite band (G) (D1/G) peak width ratio versus D1/G intensity ratio. Inset shows representative first-order region of Raman spectrum and defines relevant spectrum decomposition parameters (width, intensity, etc.). The D3 band is attributed to out-of-phase defects. **e** Ratio of D1 or G peak width of gouge to average breccia peak width versus G band peak position. Inset shows systematic shift toward higher frequencies of G band observed in black gouge with respect to fault breccia. PSZ—principal slip zone. **a**, **d,** and **e** are from Kuo et al. (2017); **b** and **c** are modified after Kuo et al. (2014)

a mark of instantaneous frictional heating during the seismic slip of the upper crust, but also as a mark for quantifying the occurrence of great earthquakes (Kuo et al. 2014, 2017). This result is of great significance for understanding the fault process of the Wenchuan earthquake and the determination of ancient earthquakes.

3.4.3.2 Finding and Determining Extremely Low Fault Friction Coefficients

After WFSD-1 was completed, the temperature and water level changes in the well were continuously measured (Fig. 3.15). The long-term temperature measurement profile shows that the temperature anomaly of the principal slip zone of the Wenchuan earthquake decreased from 0.15 °C (one year after the earthquake) to 0.02 °C during the monitoring period (Fig. 3.15b, c). After that, the anomaly did not change significantly with time. The heat caused by friction during the Wenchuan earthquake is much less than 29 MJ/m^2 (Li et al. 2015). Through the frictional heat generated during the sliding process, the peak temperature conforms to the one-dimensional attenuation formula on the planar fault. The normal stress on the fault equals the lithostatic overburden less the hydrostatic pore pressure; the maximum value of 0.02 °C at 589 m implies that the effective coefficient of friction during the earthquake is <0.02 (Li et al. 2015). Considering that the coseismic displacement is 7 m, this is the lowest friction coefficient obtained in a natural fault so far, which is much lower than 0.1, the lowest value observed in the general high-speed friction experiments (Di Toro et al. 2011) (Fig. 3.15d), and 0.06 obtained in the high-speed friction experiments of the Longmenshan fault gouge in a wet environment (Togo et al. 2016). Organic carbon, clay minerals, and graphite in the fault zone are all possible factors leading to this phenomenon (Zhang and He 2013; Kuo et al. 2014). The discovery and determination of the lowest coefficient of friction worldwide indicate that the fault with extremely low friction coefficient during the Wenchuan earthquake may experience a strong weakening effect, thus directly answering the key problem in the field of seismic geology and seismic physics for decades—why can earthquakes cause the fault to slide and rupture for hundreds of kilometers?

3.4.3.3 Rapid Fault Healing After the Wenchuan Earthquake

The change of permeability in the fault zone can reflect the development and healing of the fracture, and is also an indication of regaining energy by seismic fault strengthening (Gratier 2011). Through the relationship between the effective permeability and the permeability coefficient, the average permeability of the Wenchuan fault zone at depths of 800–1201 m during the measurement period is calculated to be 1.4×10^{-15} m^2, which is higher than the permeability of the measured fault rock samples in the laboratory and of the whole rock of the Xujiahe Formation, as well as of other known fault zones (Lockner et al. 2000; Zhou and He 2009). The difference is likely to be controlled by the development of cracks (Caine et al. 1996). It also indicates that there was significant groundwater flow near the fault during the Wenchuan earthquake, and that the flow of groundwater can affect the effective normal stress and frictional heat near the fault, thus affecting the earthquake rupture process. Long-term water level monitoring shows a rapid decline in

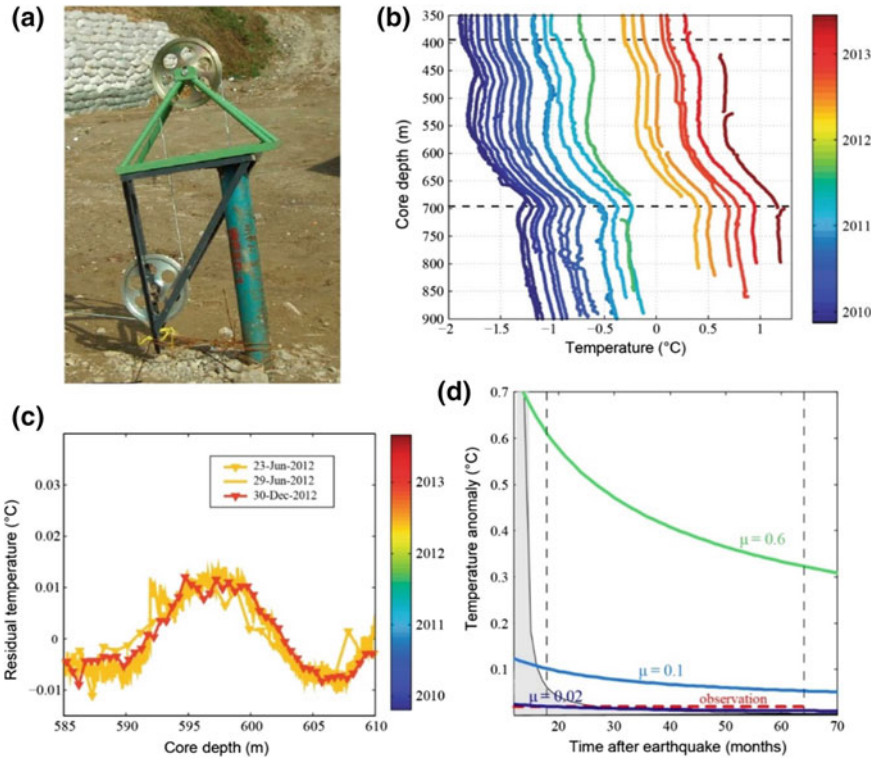

Fig. 3.15 Long-term temperature measurement from WFSD-1 borehole (after Li et al., 2015). **a** WFSD-1 drilling and measurement equipment; **b** 21 long-term temperature profiles (ground temperature gradient 0.02 °C/m is already deducted); **c** residual heat 0.02 °C; **d** fault effective coseismic friction coefficient ($\mu = 0.02$) estimated by maximum amplitude of across-fault temperature anomaly in the WFSD-1 borehole

permeability of the Yingxiu–Beichuan fault zone (Fig. 3.16), which reflects the fault sealing or reduced connectivity after the earthquake, i.e., the post-earthquake rapid healing process of the Yingxiu–Beichuan fault zone (Xue et al. 2013). It attests to local seismogenic mechanism and earthquake period.

Studies show that the average value of the hydraulic diffusion coefficient of the Wenchuan earthquake fault zone is 0.024 m^2/s, which is higher than the value measured in the Chelungpu fault zone after the 1999 Chichi earthquake (7×10^{-5} m^2/s). This means that the degree of rupture development and coseismic water permeability during the earthquake is very important. Through water level monitoring in the WFSD-1 borehole, the rapid decline of permeability in the fault zone after the great earthquake was recorded and analyzed, reflecting the rapid healing process of the fault zone. This is the first information recorded in the world that the fault quickly healed after the earthquake. The post-earthquake healing of the fault is of great significance for understanding the seismogenic mechanism and the earthquake period.

It may reveal the earthquake period and provide a scientific basis for earthquake prediction.

In addition, combined with the spatial and temporal distribution characteristics of the aftershock moment tensor of the Wenchuan earthquake (Lin et al. 2012) and well water level data analyses, the aftershocks of the Wenchuan earthquake are mainly dominated by thrust and strike-slip, and consistent with the slip distribution characteristics of the main shock rupture. The main types of moment tensor change from reverse fault and strike-slip fault to reverse fault with time, and the change of permeability analyzed by well water level data gradually decreases with time to the level before the earthquake. In general, the Longmenshan fault zone had healed after May 2009 (Lin et al. 2012).

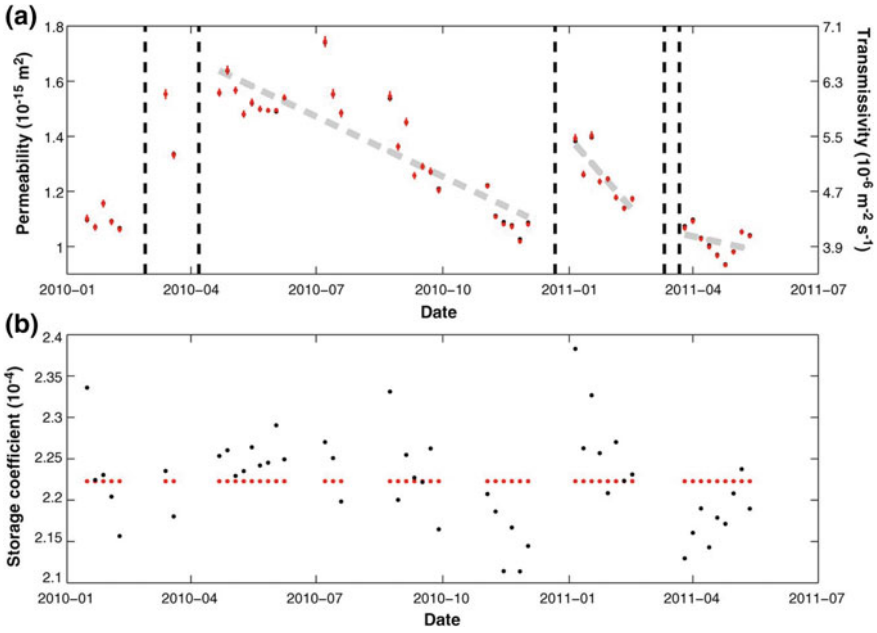

Fig. 3.16 Hydrogeologic properties of the well-aquifer system over time in the WFSD-1 borehole (after Xue et al. 2013). **a** Permeability and transmissivity; **b** storage coefficient. Segments that overlap the remote earthquakes (vertical dashed lines) were not inverted. The black dots denote an unconstrained inversion; the red dots are the results of inversion with the storage coefficient fixed to a single value. Because the two separate inversions have identical results for transmissivity, the red dots cover the black dots in (**a**). The vertical dashed lines show the time of the selected teleseismic events, which correspond to sudden increases in permeability. The best-fit linear trends between each set of permeability increases are shown as light gray dashed lines. Permeability errors are estimated by propagating the range of phase errors

3.4.3.4 Creeping Along the Guanxian–Anxian Fault in the Longmenshan Thrust Belt

Crustal active faults can slip either steadily by aseismic creep or abruptly by earthquake rupture. Creep can continuously relax the stress and reduce the magnitude of earthquakes. Identifying the slip behavior of active faults plays a crucial role in predicting and preventing earthquake disasters. According to the detailed structure analyses of fault rocks from the 551.51-m-long WFSD-3P cores and of the surface rupture zone along the Guanxian–Anxian fault (GAF), as well as the XRD analysis results, the fault rocks at different depths are characterized by distributed R1 shears and are dominated by pressure solution structures and abundant clay minerals (Fig. 3.17).

Such characteristics demonstrate that the GAF that ruptured during the 2008 Mw 7.9 Wenchuan earthquake has long-term creeping behavior. The majority of clay minerals in fault gouges of the GAF are newly formed by pressure solution. The growth of new phyllosilicates prevents soluble grains from coalescing and maintains fast diffusive paths along solution seams, thus promoting pressure solution. Both clay-rich fault gouges and pressure solution can control fault frictional behavior in the velocity-strengthening mode that generates aseismic stable slide. Therefore, the creeping mechanism of the GAF is mainly attributed to the interplay between new phyllosilicate minerals and pressure solution. Based on the P-wave distribution, it is proposed that the GAF is creeping at shallow depths and locked at greater depths; this provides a possible explanation for the rupture mechanism during the Wenchuan earthquake. However, more data are needed to better constrain the depth at which the behavior of the GAF changes from creeping to locked.

3.4.4 Real-Time Drilling Mud Gas Response to Small–Moderate Earthquakes in the WFSD-1 Borehole

We investigated the real-time drilling mud gas of the Wenchuan earthquake Fault Scientific Drilling Hole-1 and their responses to 3918 small–moderate aftershocks happened in the Longmenshan fault zone. Gas profiles for Ar, CH_4, He, ^{222}Rn, CO_2, H2, N_2, O_2 are obtained (Fig. 3.18a). Seismic wave amplitude, energy density, and static strain are calculated to evaluate their power of influence to the drilling site. Mud gases two hours before and after each earthquake are carefully analyzed. In total, 25 aftershocks have major mud gas response, and the mud gas concentrations vary dramatically immediately or minutes after the earthquakes. Different gas species respond to earthquakes in different manners according to local lithology encountered during the drill. The gas variations are likely controlled by dynamic stress changes, rather than static stress changes. They have the seismic energy density between 10^{-5} and 1.0 J/m^3 (Fig. 3.18b), whereas the static strain is mostly less

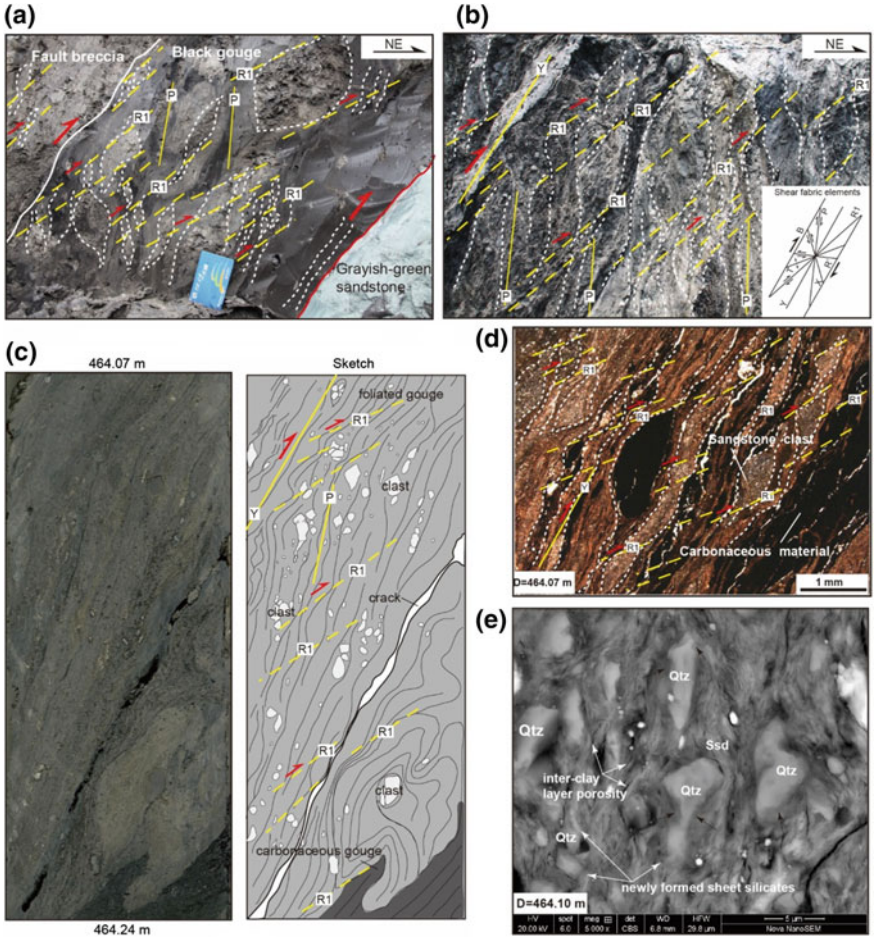

Fig. 3.17 Macroscopic and microstructural characteristics of creeping deformation of fault rocks in the Guanxian–Anxian fault zone (after He et al. 2018). **a** and **b** Deformed fault gouge and fault breccia with distributed R1 shears and some P and Y shears in the surface rupture outcrop. **c** Scan images and detailed sketches of the WFSD-3P core at 464.07–464.24 m depth: Foliation in the fault gouge was deformed with distributed R1 shears. **d** Fault gouge from WFSD-3P core at 464.07 m depth, with distributed R1 shears and banded carbonaceous materials with wavy boundaries. **e** SEM images of the fault gouge at 464.10 m depth shows that phyllosilicate minerals newly formed around the boundaries of partly dissolved quartz particles; the black arrows indicate the transition from the dissolved particle boundary to the newly formed clay grains. Terminology used to describe the geometry of shear fabric elements following Logan et al. (1979). Red arrows show the compression direction and red half arrows indicate the shear directions. D is the depth of the sample from WFSD-3P, as shown at the bottom left corner of each image. Red half arrows show the shear directions and red arrows show the compression direction. Qtz: quartz; Ssd: stacked sheet silicate domains

than 10^{-8}. We suggest that the limitation of the gas sources and the high hydraulic diffusivity of the newly ruptured fault zone could have inhibited the drilling mud gas behaviors; they are only able to respond to a small portion of the aftershocks. This work is important for the understanding of earthquake-related hydrological changes.

3.4.5 Aftershock Records and Precise Location of the Wenchuan Earthquake

Based on the data of fixed and mobile seismic stations distributed around the Longmenshan fault after the Wenchuan earthquake, the precise location of the aftershocks of the Wenchuan earthquake was studied to explore the relationship between the aftershock distribution of the great earthquake and the deep structure. In order to accurately obtain the seismic arrival time, based on digital seismic data, a waveform cross-correlation technology is used to obtain reliable relative arrival time between stations, and then, the double difference positioning technology is used to obtain more accurate aftershock positioning results.

Based on the aftershocks recorded by the China Seismological Network in the Longmenshan and neighboring areas during the 4 years after the Wenchuan earthquake (Fig. 3.19), the precise seismic location was studied. The precise position data of 43,297 earthquakes were obtained by Hyp2000 absolute positioning method and 32,797 earthquakes by HypoDD relative positioning method (double difference positioning method). The spatial and temporal distribution and evolution characteristics of the Wenchuan earthquake aftershock sequence were analyzed. During the 4 years from May 12, 2008, to May 12, 2012, 80,995 aftershocks were recorded, none > M7.0, 5 > M6.0, 70 > M5.0, 690 > M4.0, 4576 > M3.0, and 22,587 > M2.0, their depths are concentrated at 10–20 km, and the seismic distribution along the Longmenshan fault has clear segmentation. The southwestern segment is horizontally zonally distributed, demonstrating thrust activity, while the northeastern segment is close to a vertical distribution, which is consistent with strike-slip characteristics (Li et al. 2018). Wenchuan aftershocks' precise positioning is applied to the tracking of fluid pore pressure diffusion characteristics during aftershock activity (Chen et al. 2012). Based on the similarity of precise positioning data and focal mechanisms, the spatio-temporal distribution of aftershocks is analyzed by pore pressure diffusion mechanism. It is believed that the migration of deep fluids affects the spatio-temporal evolution process of aftershocks (Liu et al. 2014). Numerical simulation is used to analyze the temporal and spatial distribution of aftershocks activity and the change of pore pressure. The pore pressure diffusion formula can be used to represent the information about aftershock migration of the Longmenshan fault zone. The aftershock activity between May and December 2008 is divided into three stages related to fluid diffusion processes. With time, the pore pressure diffusion gradually increases, and in space, the pore pressure diffusion coefficient increases gradually from north to south. Moreover, the strong aftershocks of the Wenchuan earthquake mainly occurred along

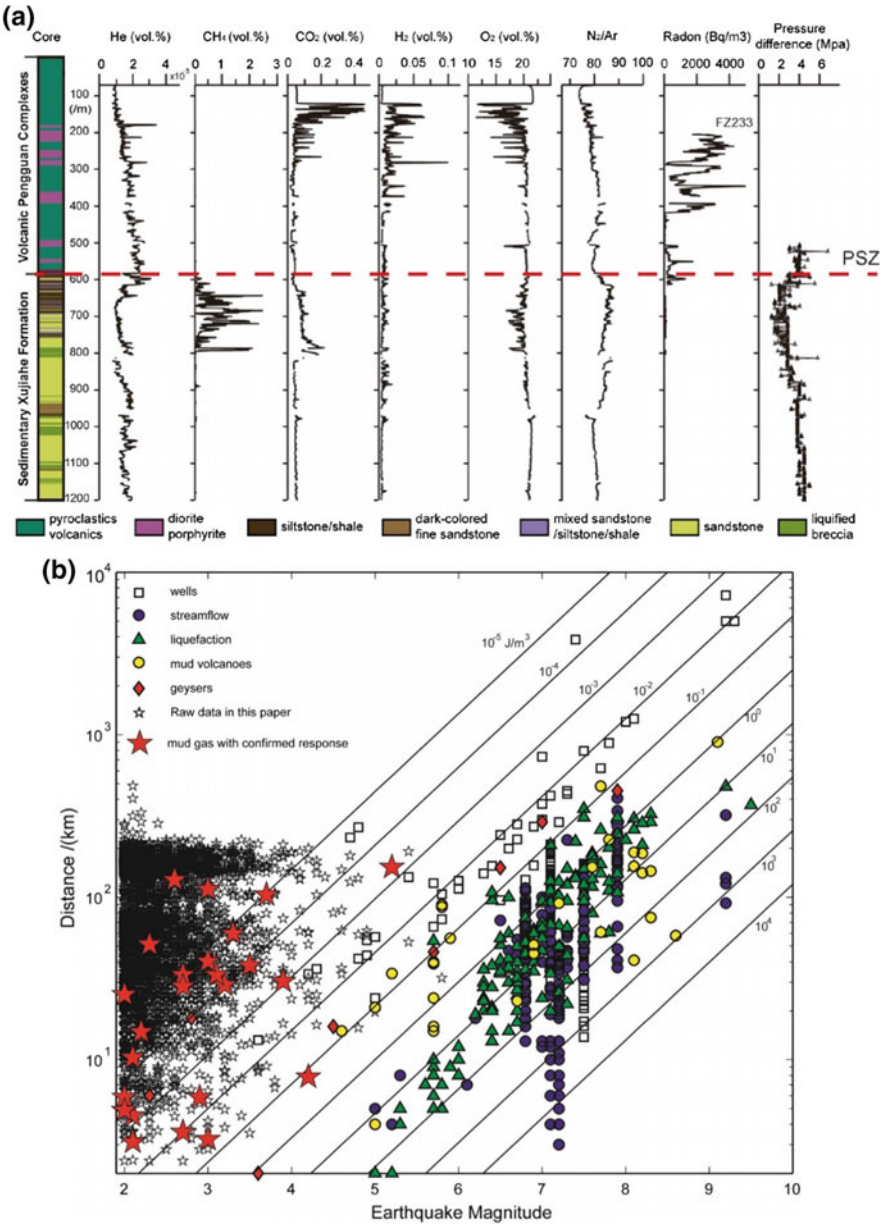
(a)
Core
He (vol.%)
CH4 (vol.%)
CO2 (vol.%)
H2 (vol.%)
O2 (vol.%)
N2/Ar
Radon (Bq/m3)
Pressure difference (Mpa)
Volcanic Pengguan Complexes
Sedimentary Xujiahe Formation
FZ233
PSZ
pyroclastics volcanics
diorite porphyrite
siltstone/shale
dark-colored fine sandstone
mixed sandstone /siltstone/shale
sandstone
liquified breccia
(b)
wells
streamflow
liquefaction
mud volcanoes
geysers
Raw data in this paper
mud gas with confirmed response
Distance /(km)
Earthquake Magnitude

◀**Fig. 3.18** Real-time drilling mud gas and earthquakes response in the WFSD-1 borehole (after Gong et al. 2017). **a** Mud gases distribution in depth coordinate. The red dashed line marks the position of the principle slip zone during the 2008 Wenchuan earthquake. The pressure difference is calculated by adding the pump pressure with the mud column and minus the formation pressure. No pumping pressure data are available for runs above 495 m. All gas data are averaged over 1 m interval. **b** A compilation of the mud gas data in WFSD-1 and many other types of hydrological response reported by Wang and Manga (2010). The black stars mark all the aftershocks considered in this paper, and the 25 red stars denote the aftershocks which confirmed having significant mud gas response

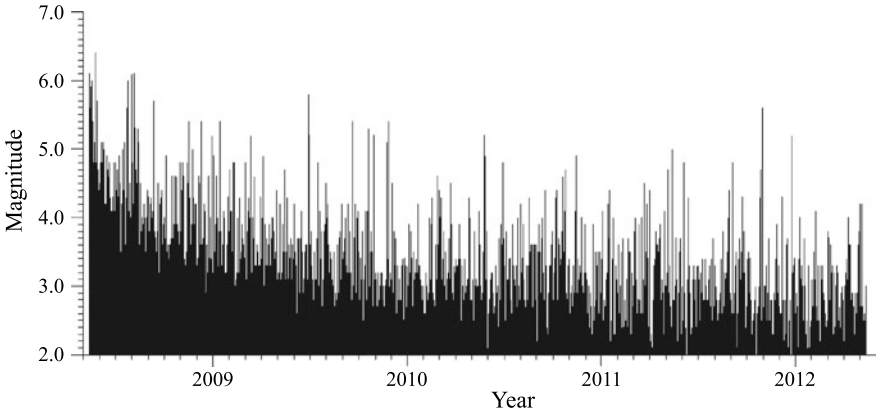

Fig. 3.19 Wenchuan earthquake aftershocks record from 2008.5.12 to 2012.5.12. During the four years from May 12, 2008, to May 12, 2012, 80,995 aftershocks of the Wenchuan earthquake were recorded, none > M7.0, 5 > M6.0, 70 > M5.0, 690 > M4.0, 4576 > M3.0, and 22,587 > M2.0

the northern segment of the fault, indicating that the north–south difference of pore pressure diffusion is related to the magnitude of aftershocks (Liu et al. 2014). Some scholars believe that deep fluids play an important role in the Wenchuan earthquake and aftershocks activity. For example, Lei et al. (2009) inverted the fine structure of the crust in the Longmenshan fault zone and its surrounding areas through P-wave arrival time data, and found that there are clear low-velocity anomalies below the epicenter region of the Wenchuan main earthquake, and the fluids in the Longmenshan fault zone play a direct role in the earthquake. Zhou and He (2009) established the crustal rheological structure of the Wenchuan earthquake-related tectonic units and considered that the complex rheological structure is the basis of the Wenchuan earthquake. The high fluid pore pressure in the Longmenshan fault zone is a necessary condition for triggering the Wenchuan earthquake. A comprehensive analysis of this subject can help us gain a deeper understanding of the role of fluid in seismic spatio-temporal evolution and better assess seismic hazards.

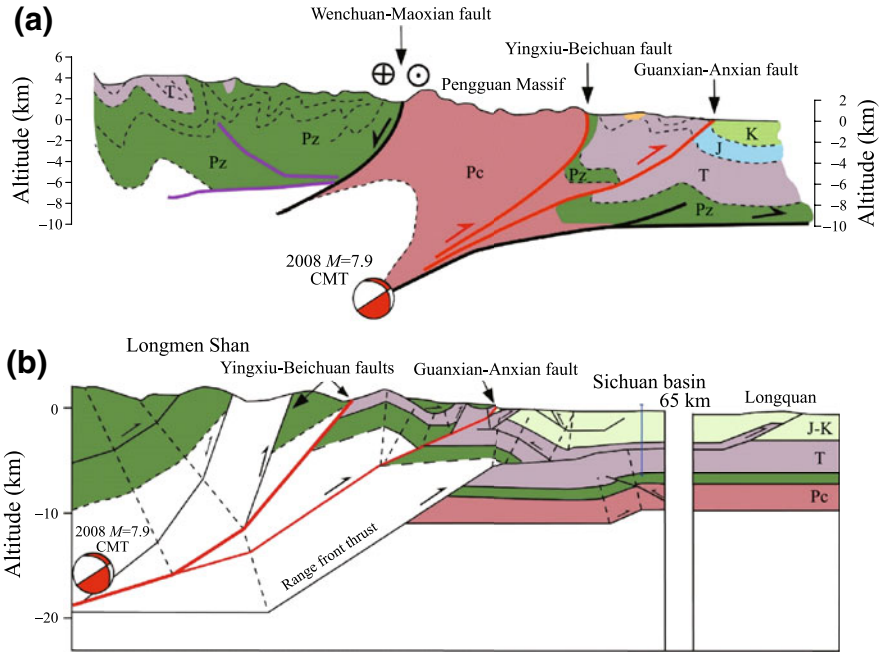

Fig. 3.20 Two models of the Longmenshan uplift. **a** The low velocity of the crustal channel flow is blocked by the rigid Yangtze block (after Burchfiel et al. 2008); **b** crustal thickening caused by thrust faults (after Hubbard and Shaw 2009). Pc—Precambrian; Pz—paleozoic; T—Triassic; J—Jurassic; K—Cretaceous

3.4.6 Tectonic Framework Reconstruction of Eastern Tibet

The Longmenshan is located in the eastern margin of the Tibetan Plateau, connecting the Songpan–Garze orogenic belt to the west and the Sichuan Basin to the east. It is a peculiar mountain range with steep terrain (3000–4500 m height difference, Densmore et al. 2007), significant differences in crustal thickness (52.5 km under the Longmenshan to 41.5 km below the Sichuan Basin, Wang et al. 2010a, b, c), low crustal horizontal shortening, and no Cenozoic sedimentation (Chen et al. 2000; Shen et al. 2005; Burhfield et al. 2008). The eastward growth of the lithosphere and asthenosphere of Tibet is blocked by the rigid Sichuan Basin. For a long time, two viewpoints have explained the uplift of the Longmenshan: The eastward movement of the low-velocity mid-lower crustal channel flow is blocked by the rigid Yangtze block (Fig. 3.20a; Royden et al. 1997; Clark and Royden 2000; Cook and Royden 2008; Burchfiel et al. 2008), and crustal thickening is caused by the thrust faults (Fig. 3.20b; Hubbard and Shaw 2009).

Combined with geological survey of the surface rupture area of the Longmenshan main earthquake fault zone, borehole data of the Wenchuan earthquake fault zone,

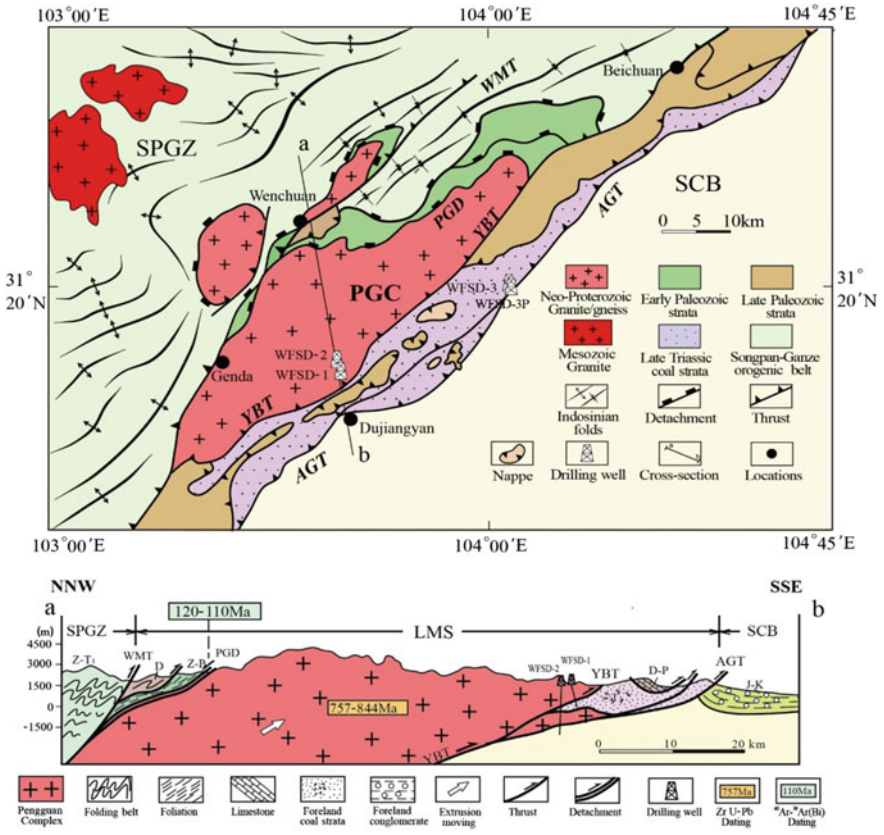

Fig. 3.21 Schematic diagram of the structural framework of the Longmenshan. The Longmenshan is made up of extrusion rocks and stack thrust rocks of the Pengguan complex extrusion. SCB—Sichuan basin; SPGZ—Songpan–Garze orogenic zone; LMS—Longmenshan; PGC—Pengguan complex; GAT—Guanxian–Anxian thrust belt; YBT—Yingxiu–Beichuan thrust belt; PGD1 & PGD2—Pengguan detachment fault system; WMT—Wenchuan–Maoxian thrust

and deep seismic reflection profiles, the tectonic framework of the Longmenshan was reshaped and a new orogenic model was proposed.

(1) WFSD-1 and WFSD-2 borehole data reveal the existence of multiple stack thrust rocks in the central segment of the Longmenshan (Fig. 3.21). Therefore, the Longmenshan tectonic framework consists of extrusion rocks and stack thrust rocks since the Cretaceous (Fig. 3.21). It is found that the west side of the Neoproterozoic Pengguan–Kangding complex in the Longmenshan is a large-scale Pengguan ductile detachment shear zone (PGD) with an age of 120–110 Ma, and the Yingxiu–Beichuan ductile shear zone located on the east side (YBT). The Pengguan–Kangding complex, which is clamped by two boundaries, constitutes the main tectonic unit of the Longmenshan—the Pengguan extrusion

rocks formed in the Cretaceous. The WFSD-1 and WFSD-2 borehole joint profiles and the reflection seismic section across the central Longmenshan reveal that the bottom boundary of the Pengguan extrusion rocks which is rootless extends westward to 6 km below the Wenchuan–Maoxian fault.

(2) The front edge of the Longmenshan Pengguan extrusion rocks is a series of Cenozoic west-dipping stack thrust rocks. The detachment fault between the Neoproterozoic basement and caprock under the Sichuan Basin is present to the east, and basement exists in the west-dipping thrust system (Fig. 3.21).

(3) The PGD on the west side of the Longmenshan extends westward to the basement and caprock of the Danba area of Songpan–Garze, and reveals that the rapid uplift age of the PGD is 40 Ma, combined with magnetotelluric data (Zhao et al. 2012). It explains the correlation between the high-conductivity, low-resistivity, and low-velocity zone representing the weak middle-lower crustal flow at 20–30 km depth in the Songpan–Garze orogenic belt and the uplift since 40 Ma. The lower part of the Longmenshan and Sichuan Basins, with low conductivity, high resistivity, and low velocity, represents the rigid body properties of the Yangtze block and the lower part of the Longmenshan, revealing the extruded stack thrust rocks which have 60 km vertical reduction and 12 km vertical uplift of upper crust, and have nothing to do with the channel flow. The epicenter of the earthquake occurred near the detachment fault between the basement and caprocks of the Yangtze Craton under the Longmenshan. Therefore, the formation of the Longmenshan caused long-term destruction and stress accumulation of the craton, which led to the outbreak of the Wenchuan earthquake.

3.5 Conclusion

The Wenchuan earthquake Fault Scientific Drilling (WFSD) project is the first scientific drilling project for great earthquakes in mainland China and the world's fastest scientific drilling for great earthquakes. It has attracted great attention from the geological circles in China and abroad. Drilling, logging, monitoring, coring, and research on the steep mountains with strong aftershocks and on the strongly fractured Wenchuan earthquake fault zone are highly risky and exploratory. Despite the difficulties, the project has achieved much important research progress, especially the breakthrough in the study of the seismogenetic mechanism. For example, the graphite in the fault zone can be used to assess the occurrence of great earthquakes, and the lowest fault frictional coefficient in the world has been determined, and for the first time recorded the rapid healing information of the fault zone after the great earthquake. This has attracted the attention of international scientists in the seismic field. However, the realization of the goal of scientific drilling is very exploratory in itself, and it requires the geoscientists to continue to strive for progress and breakthrough in the future.

Acknowledgements The implementation of this project has been strongly supported by the Ministry of Science and Technology, the Ministry of Land and Resources, the China Earthquake Administration, and the People's Government of Sichuan Province. The direct leadership of the China Geological Survey, the participation of all staff involved in the project, and the assistance of international collaborators made the project successful.

References

Barker, C.E., and R.H. Goldstein. 1990. Fluid-inclusion technique for determining maximum temperature in calcite and its comparison to the vitrinite reflectance geothermometer. *Geology* 18: 1003–1006.

Beyssac, O., J.N. Rouzaud, B. Goffe, et al. 2002. Graphitization in a high-pressure, low-temperature metamorphic gradient: A Raman microspectroscopy and HRTEM study. *Contributions to Mineralogy and Petrology* 143: 19–31.

Boullier, A.-M. 2011. Fault-zone geology: Lessons from drilling through the Nojima and Chelungpu faults. *Geological Society, London, Special Publications* 359: 17–37.

Brodsky, E.E., K.-F. Ma, J. Mori, et al. 2009. Rapid response fault drilling past, present, and future. *Scientific Drilling* 8: 66–74.

Burchfiel, B.C., L.H. Royden, R.D. Hilst, et al. 2008. A geological and geophysical context for the Wenchuan earthquake of 12 May 2008, Sichuan, People's Republic of China. *GSA Today* 18: 5.

Buseck, P.R., and O. Beyssac. 2014. From organic matter to graphite: Graphitization. *Elements* 10: 421–426.

Caine, J.S., J.P. Evans, and C.B. Forster. 1996. Fault zone architecture and permeability structure. *Geology* 24: 1025–1028.

Carpenter, B.M., H. Kitajima, R. Sutherland, et al. 2014. Hydraulic and acoustic properties of the active Alpine Fault, New Zealand: Laboratory measurements on DFDP-1 drill core. *Earth and Planetary Science Letters* 390: 45–51.

Chen, T., Y. Liu, D. Yang, et al. 2012. The role of pore pressure in earthquake triggering and process of swarm earthquakes and aftershocks. *Progress in Geophysics* 27 (6): 261. (In Chinese).

Chen, Z., B. Burchfiel, Y. Liu, et al. 2000. Global positioning system measurements from eastern Tibet and their implications for India/Eurasia intercontinental deformation. *Journal of Geophysical Research: Solid Earth* 105: 16,215–16,227.

Chou, Y.-M., S.-R. Song, C. Aubourg, et al. 2012. An earthquake slip zone is a magnetic recorder. *Geology* 40: 551–554.

Clark, M.K., and L.H. Royden. 2000. Topographic ooze: Building the eastern margin of Tibet by lower crustal flow. *Geology* 28: 703–706.

Cook, K. L., and L.H. Royden. 2008. The role of crustal strength variations in shaping orogenic plateaus, with application to Tibet. *Journal of Geophysical Research: Solid Earth* 113: B08407. https://doi.org/10.1029/2007jb005457.

Deng, Q., S. Chen, and X. Zhao. 1994. Tectonics, scismisity and dynamics of Longmenshan mountains and its adjacent regions. *Seismology and Geology* 16 (4): 389–403.

Densmore, A.L., M.A. Ellis, Y. Li, et al. 2007. Active tectonics of the Beichuan and Pengguan faults at the eastern margin of the Tibetan Plateau. *Tectonics* 26: TC4005. https://doi.org/10.1029/2006tc001987.

Di Toro, G., R. Han, T. Hirose, et al. 2011. Fault lubrication during earthquakes. *Nature* 471: 494–500.

Fu, B., P. Wang, P. Kong, et al. 2008. Preliminary study of coseismic fault gouge occurred in the slip zone of the Wenchuan Ms 8.0 earthquake and its tectonic implications. *Acta Petrologica Sinica* 24: 2237–2243. (In Chinese).

Fu, B., P. Shi, H. Guo, et al. 2011. Surface deformation related to the 2008 Wenchuan earthquake, and mountain building of the Longmen Shan, eastern Tibetan Plateau. *Journal of Asian Earth Sciences* 40: 805–824.

Fulton, P.M., E.E. Brodsky, Y. Kano, et al. 2013. Low coseismic friction on the Tohoku-Oki fault determined from temperature measurements. *Science* 342: 1214–1217.

Gong, Z., H.B. Li, L.J. Tang, et al. 2017. Real time drilling mud gas response to small-moderate earthquakes in Wenchuan earthquake Scientific Drilling Hole-1 in SW China. *Journal of Asian Earth Sciences* 138: 416–426.

Gratier, J.-P. 2011. Fault permeability and strength evolution related to fracturing and healing episodic processes (years to millennia): The role of pressure solution. *Oil & Gas Science and Technology-Revue d'IFP Energies Nouvelles* 66: 491–506.

He, X., H. Li, H. Wang, et al. 2018. Creeping along the Guanxian–Anxian fault of the 2008 Mw 7.9 Wenchuan earthquake in the Longmen Shan, China. *Tectonics* 37: 2124–2141.

Hirono, T., W. Lin, E.C. Yeh, et al. 2006. High magnetic susceptibility of fault gouge within Taiwan Chelungpu fault: Nondestructive continuous measurements of physical and chemical properties in fault rocks recovered from Hole B, TCDP. *Geophysical Research Letters* 33.

Hirono, T., K. Fujimoto, T. Yokoyama, et al. 2008. Clay mineral reactions caused by frictional heating during an earthquake: An example from the Taiwan Chelungpu fault. *Geophysical Research Letters* 35 (16): L16303. https://doi.org/10.1029/2008gl034476.

Hubbard, J., and J.H. Shaw. 2009. Uplift of the Longmen Shan and Tibetan plateau, and the 2008 Wenchuan (M = 7.9) earthquake. *Nature* 458: 194.

Kuo, L.W., S.R. Song, E.C. Yeh, et al. 2009. Clay mineral anomalies in the fault zone of the Chelungpu Fault, Taiwan, and their implications. *Geophysical Research Letters* 36.

Kuo, L.-W., H. Li, S.A. Smith, et al. 2014. Gouge graphitization and dynamic fault weakening during the 2008 Mw 7.9 Wenchuan earthquake. *Geology* 42: 47–50.

Kuo, L.-W., F. Di Felice, E. Spagnuolo, et al. 2017. Fault gouge graphitization as evidence of past seismic slip. *Geology* 45: 979–982.

Lei, J., D. Zhao, J. Su, et al. 2009. Fine seismic structure under the Longmenshan fault zone and the mechanism of the large Wenchuan earthquake. *Chinese Journal of Geophysics* 52 (2): 339–345. (In Chinese).

Li, H., P. Tapponnier, Y. Klinger, et al. 2010. Co-seismic surface rupture and normal faulting produced by the 2008 Ms 7.3 Ashikule earthquake, Xinjiang, China. City, p. 9300.

Li, Y., R. Zhou, S. Dong, et al. 2008. Surface rupture, thrusting and strike-slipping in the Wenchuan earthquake of Sichuan, China. *Journal of Chengdu University of Technology* 35 (4): 404–413. (In Chinese).

Li, H., H. Wang, Z. Xu, et al. 2013. Characteristics of the fault-related rocks, fault zones and the principal slip zone in the Wenchuan Earthquake Fault Scientific Drilling Project Hole-1 (WFSD-1). *Tectonophysics* 584: 23–42.

Li, H., Z. Sun, J. Pan, et al. 2014a. Field study of the 12 February 2014 Yutian Ms7.3 earthquake: A special surface rupture zone. *Acta Geoscientica Sinica* 3: 391–394. (In Chinese).

Li, H., Z. Xu, Y. Niu, et al. 2014b. Structural and physical property characterization in the Wenchuan earthquake Fault Scientific Drilling project—hole 1 (WFSD-1). *Tectonophysics* 619: 86–100.

Li, H., L. Xue, E.E. Brodsky, et al. 2015. Long-term temperature records following the Mw 7.9 Wenchuan (China) earthquake are consistent with low friction. *Geology* 43: 163–166.

Li, H., H. Wang, G. Yang, et al. 2016. Lithological and structural characterization of the Longmen Shan fault belt from the 3rd hole of the Wenchuan Earthquake Fault Scientific Drilling project (WFSD-3). *International Journal of Earth Sciences* 105: 2253–2272.

Li, H.B., Z.Q. Xu, W. Huan, et al. 2018. Fault behavior, physical properties and seismic activity of the Wenchuan earthquake fault zone: Evidences from the Wenchuan earthquake Fault Scientific Drilling project (WFSD). *Chinese Journal of Geophysics* 61: 1680–1697. (Chinese edition).

Lin, X., D. Dreger, H. Ge, et al. 2012. The spatial and temporal distribution of moment tensors of Wenchuan aftershocks. *Recent Developments in World Seismology* 6: 37. (In Chinese).

Lin, W., M. Conin, J.C. Moore, et al. 2013. Stress state in the largest displacement area of the 2011 Tohoku-Oki earthquake. *Science* 339: 687–690.

Liu, J., Z. Zhang, L. Wen, et al. 2008. The Ms 8.0 Wenchuan earthquake co-seismic rupture and its tectonic implications: An out of sequence thrusting event with slip partitioned on multiple faults. *Acta Geologica Sinica* 82 (12): 1707–1722. (In Chinese).

Liu, Y., T. Chen, F. Xie, et al. 2014. Analysis of fluid induced aftershocks following the 2008 Wenchuan Ms 8.0 earthquake. *Tectonophysics* 619: 149–158.

Liu-Zeng, J., Z. Zhang, L. Wen, et al. 2009. Co-seismic ruptures of the 12 May 2008, Ms 8.0 Wenchuan earthquake, Sichuan, East–west crustal shortening on oblique, parallel thrusts along the eastern edge of Tibet. *Earth and Planetary Science Letters* 286: 355–370.

Lockner, D., H. Naka, H. Tanaka, et al. 2000. Permeability and strength of core samples from the Nojima fault of the 1995 Kobe earthquake. Citeseer; City, pp. 147–152.

Logan, J.M., M. Friedman, N. Higgs, C. Dengo, and T. Shimamoto. 1979. Experimental studies of simulated gouge and their application to studies of natural fault zones. In *Proceedings of Conference VIII, Analysis of actual fault zones in bedrock* (Open File Rep. 79–1239), 305–343, Virginia, WA: United States Geological Survey.

Ma, K.-F., H. Tanaka, S.-R. Song, et al. 2006. Slip zone and energetics of a large earthquake from the Taiwan Chelungpu-fault Drilling Project. *Nature* 444: 473.

Ma, K.F., Y.Y. Lin, S.J. Lee, et al. 2012. Isotropic events observed with a borehole array in the Chelungpu fault zone, Taiwan. *Science* 337: 459–463.

Mishima, T., T. Hirono, W. Soh, et al. 2006. Thermal history estimation of the Taiwan Chelungpu fault using rock-magnetic methods. *Geophysical Research Letters* 33.

Mishima, T., T. Hirono, N. Nakamura, et al. 2009. Changes to magnetic minerals caused by frictional heating during the 1999 Taiwan Chi-Chi earthquake. *Earth, Planets and Space* 61: 797–801.

Niu, F., P.G. Silver, T.M. Daley, et al. 2008. Preseismic velocity changes observed from active source monitoring at the Parkfield SAFOD drill site. *Nature* 454: 204–208.

Royden, L.H., B.C. Burchfiel, R.W. King, et al. 1997. Surface deformation and lower crustal flow in eastern Tibet. *Science* 276: 788–790.

Shen, Z.K., J. Lü, M. Wang, et al. 2005. Contemporary crustal deformation around the southeast borderland of the Tibetan Plateau. *Journal of Geophysical Research: Solid Earth* 110.

Si, J., H. Li, L. Kuo, et al. 2014. Clay mineral anomalies in the Yingxiu–Beichuan fault zone from the WFSD-1 drilling core and its implication for the faulting mechanism during the 2008 Wenchuan earthquake (Mw 7.9). *Tectonophysics* 619: 171–178.

Sutherland, R., V.G. Toy, J. Townend, et al. 2012. Drilling reveals fluid control on architecture and rupture of the Alpine fault, New Zealand. *Geology* 40: 1143–1146.

Tang, L., G. Wang, J. Wang, et al. 2013. Responding features of fluids during drilling of the main fracture zone in WFSD-1 hole. *Acta Geoscientica Sinica* b (1): 95–102. (In Chinese).

Tanikawa, W., T. Mishima, T. Hirono, et al. 2007. High magnetic susceptibility produced in high-velocity frictional tests on core samples from the Chelungpu fault in Taiwan. *Geophysical Research Letters* 34.

Tanikawa, W., T. Mishima, T. Hirono, et al. 2008. High magnetic susceptibility produced by thermal decomposition of core samples from the Chelungpu fault in Taiwan. *Earth and Planetary Science Letters* 272: 372–381.

Tapponnier, P., Z.Q. Xu, F. Roger, B. Meyer, N. Arnaud, G. Wittlinger, and J.S. Yang. 2001. Oblique stepwise rise and growth of the Tibet Plateau. *Science* 294: 1671–1677. https://doi.org/10.1126/science.105978.

Togo, T., L. Yao, S. Ma, et al. 2016. High-velocity frictional strength of Longmenshan fault gouge and its comparison with an estimate of friction from the temperature anomaly in WFSD-1 drill hole. *Journal of Geophysical Research: Solid Earth* 121: 5328–5348.

Wang, C.Y., and M. Manga. 2010. Earthquake and water. Lecture Notes in Earth Sciences. Springer. https://doi.org/10.1007/978-3-642-00810-8.

Wang, C., H. Lou, Z. Yao, et al. 2010a. Crustal Thicknesses and Poisson's Ratios in Longmenshan Mountains and adjacent regions. *Quaternary Sciences* 30 (4): 652–661. (In Chinese).

Wang, H., H. Li, J. Pei, et al. 2010b. Structural and lithologic characteristics of the Wenchuan earthquake fault zone and its relationship with seismic activity. *Quaternary Sciences* 30 (4): 768–778. (In Chinese).

Wang, Q., D. Cui, X. Zhang, et al. 2010c. Studies on surface vertical deformation of the Longmenshan and the Wenchuan MS8.0 earthquake. *Recent Developments in World Seismology* 6: 11–12. (In Chinese).

Wang, H., H. Li, J. Si, et al. 2013. The relationship between the internal structure of the Wenchuan earthquake fault zone and the uplift of the Longmenshan. *Acta Petrologica Sinica* 29 (6): 2048–2060. (In Chinese).

Wang, H., H. Li, J. Si, et al. 2014. Internal structure of the Wenchuan earthquake fault zone, revealed by surface outcrop and WFSD-1 drilling core investigation. *Tectonophysics* 619: 101–114.

Wang, H., L.H. Bing, S.J. Liang, et al. 2015a. Progress in the study of the Wenchuan earthquake faulting. *Acta Geoscientica Sinica* 36 (3): 257–269. (In Chinese).

Wang, H., H. Li, C. Janssen, et al. 2015b. Multiple generations of pseudotachylite in the Wenchuan fault zone and their implications for coseismic weakening. *Journal of Structural Geology* 74: 159–171.

Xu, Z.Q., H.B. Li, and Z.L. Wu. 2008a. Wenchuan earthquake and scientific drilling. *Acta Geologica Sinica* 82: 1613–1622. (in Chinese).

Xu, Z., H. Li, and Z. Wu. 2008b. Wenchuan earthquake and scientific drilling. *Acta Geologica Sinica* 82 (12): 1613–1622. (In Chinese).

Xue, L., H.-B. Li, E.E. Brodsky, et al. 2013. Continuous permeability measurements record healing inside the Wenchuan earthquake fault zone. *Science* 340: 1555–1559.

Yang, G., H. Li, W. Zhang, et al. 2012c. Features of the Anxian-Guanxian fault zone in Longmenshan area of Sichuan Province: A case study of No.3 hole of Wenchuan earthquake Fault zone Scientific Drilling (WFSD-3). *Geological Bulletin of China* 31 (8): 1219–1232. (In Chinese).

Yang, T., J. Chen, H. Wang, et al. 2012a. Magnetic properties of fault rocks from the Yingxiu–Beichuan fault: constraints on temperature rise within the shallow slip zone during the 2008 Wenchuan earthquake and their implications. *Journal of Asian Earth Sciences* 50: 52–60.

Yang, T., J. Chen, H. Wang, et al. 2012b. Rock magnetic properties of fault rocks from the rupture of the 2008 Wenchuan earthquake, China and their implications: Preliminary results from the Zhaojiagou outcrop, Beichuan County (Sichuan). *Tectonophysics* 530: 331–341.

Yang, T., J. Chen, X. Yang, et al. 2013. Differences in magnetic properties of fragments and matrix of breccias from the rupture of the 2008 Wenchuan earthquake, China: Relationship to faulting. *Tectonophysics* 601: 112–124.

Zhang, L., and C. He. 2013. Frictional properties of natural gouges from Longmenshan fault zone ruptured during the Wenchuan Mw7. 9 earthquake. *Tectonophysics* 594: 149–164.

Zhang, W., H. Li, Y. Huang, et al. 2012. Lithologic characteristics and fault zone structure revealed by No. 2 hole cores of the Wenchuan earthquake Fault zone Scientific Drilling (WFSD-2). Geological Bulletin of China 31 (8): 1201–1218. (In Chinese).

Zhang, P., X. Xu, X. Wen, et al. 2008. Slip rates and recurrence intervals of the Longmen Shan active fault zone, and tectonic implications for the mechanism of the May 12 Wenchuan earthquake 2008, Sichuan, China. *Chinese Journal of Geophysics* 51 (4): 1066–1073. (In Chinese).

Zhang, L., Z. Sun, H. Li, et al. 2017a. Magnetic susceptibility of WFSD-2 borehole cores from the Longmenshan thrust belt and its implications for great seismic activity. *Chinese Journal of Geophysics* 60 (1): 225–239. (In Chinese).

Zhang, L., Z. Sun, H. Li, et al. 2017b. Rock record and magnetic response to large earthquakes within Wenchuan Earthquake Fault Scientific Drilling cores. *Geochemistry, Geophysics, Geosystems* 18: 1889–1906.

Zhao, G., M.J. Unsworth, Y. Zhan, et al. 2012. Crustal structure and rheology of the Longmenshan and Wenchuan Mw 7.9 earthquake epicentral area from magnetotelluric data. *Geology* 40: 1139–1142.

Zhou, Y, and C. He. 2009. The rheological structures of crust and mechanics of high-angle reverse fault slip for Wenchuan Ms8.0 earthquake. *Chinese Journal of Geophysics* 52 (2): 474–484. (In Chinese).

Zoback, M., S. Hickman, and W. Ellsworth. 2007. The role of fault zone drilling. *Geophysics* 4: 649–674.

Chapter 4
Coordinated Distributed Experiments (CDEs) Applied to Earthquake Forecast Test Sites

Zhongliang Wu, Yan Zhang and Jiawei Li

Abstract Field experiments for testing the hypotheses related to earthquake preparation and earthquake forecast have been facing dual challenges due to the nature of the study of earthquakes. On the one hand, physical laws derived from laboratory experiments, when applied to field, have the problems of scaling, which necessitate field experiments. On the other hand, due to the limitation of earthquake 'samples' and the complicated factors controlling the preparation of an earthquake, the tests of the physical hypotheses by field experiments have vague significance. Such challenges are not only in the field of earthquake studies. In ecology and environmental science, 'few samples, many factors' is also one of the difficulties blocking the test of scientific hypotheses. To tackle this problem, in those fields, 'Coordinated Distributed Experiments (CDEs)' was proposed as an operational tool for hypothesis testing. Such an idea also provides earthquake studies with a new vision. In connection to the top-level design of the China Seismic Experiment Site (CSES), in this chapter, we discuss the concept CDEs applied to the test sites of earthquake forecast. We propose that an 'earthquake rupture scenario' be used for the coordination.

Keywords Natural laboratory · Earthquake science · Coordinated Distributed Experiments (CDEs)

Z. Wu (✉)
Institute of Earthquake Forecasting, China Earthquake Administration, Beijing 100036, China
e-mail: wuzl@cea-igp.ac.cn

Y. Zhang · J. Li
Institute of Geophysics, China Earthquake Administration, Beijing 100081, China

J. Li
School of Earth and Space Sciences, Peking University, Beijing 100871, China

Y.-G. Li (ed.), *Earthquake and Disaster Risk: Decade Retrospective of the Wenchuan Earthquake*, https://doi.org/10.1007/978-981-13-8015-0_4

4.1 Natural Laboratories in Earthquake Science

Field experiments have been proposed for decades in earthquake science. Related to earthquake forecast, there were several field experiments conducted, such as the earthquake prediction experiments in the former Soviet Union (Semenov 1969), the Parkfield experiment in the USA (Bakun and Lindh 1985; Roeloffs and Langbein 1994; Roeloffs 2000), the TDP experiment in Turkey (Evans et al. 1987), the Tokai experiment in Japan (Davis and Somerville 1982; Mogi 2004),[1] and the PRENLAB[2] project in the Iceland, among others. On the other hand, however, in the view of physics, such 'experiments' are to much extent problematic due to the limitation of the precision of the measurement and the lack of controllable processes.

Such situation is facing a historic change. In recent years, innovative technologies have been reshaping the horizon of seismological, geodetic, and geological studies. One of the examples is the temporal variation of Earth structure. As early as in the 1960s, pre-earthquake variation of velocity of seismic waves was claimed and discussed (e.g., Semenov 1969), providing earthquake forecast with optimistic clues. However, due to the limitation on the precision of the field measurement, the scientific conclusions about the precursory structural variation have not been on a solid ground. Since the twenty-first century, emerging technologies such as waveform interferometry have enhanced significantly the capability of observing the co-seismic and post-seismic variations of structures, which potentially makes it feasible to constrain the pre-earthquake structural variation (e.g., Wegler et al. 2009; Chao and Peng 2009; Audet 2010). Such new opportunities are noticeable in the study of earthquake preparation and in turn reactivate the interests in the field experiments.

Accordingly, on 12 May, 2018, at the opening ceremony of the International Conference for the Decade Memory of the Wenchuan earthquake with the 4th International Conference on Continental Earthquakes (4th ICCE), it was officially announced that the China Seismic Experiment Site (CSES) be established in the Sichuan-Yunnan region. This natural laboratory, as a continuation and expansion of the West-Yunnan Earthquake Prediction Experiment Site since 1980 and the National Experiment Site for Earthquake Monitoring and Forecast since 2014, aims to make use of the cutting edge science and technology to deepen the understandings of the preparation and occurrence of continental earthquakes and the cause of seismic disasters. The discussion in this chapter is in connection with the top-level design of the CSES.

[1] Hoshiba (2006).

[2] Stefansson et al. (1998, 2001).

4.2 Challenges of the Natural Laboratories

Associated with the natural laboratories for earthquake science, for example, the being built CSES, what will be the most important challenge? Using the cliche of some international organizations 'opportunities and challenges': the main challenge is apparently that the 'opportunity' to 'meet' the 'target earthquake' is small. Indeed in the history of earthquake forecast experiments, for most of the test sites, the 'target earthquake' occurred either out of the range of the test area (such as the 1996 Lijiang earthquake which is near to, but just out of, the West-Yunnan Earthquake Prediction Experiment Site), or within the test area but after the test has formally closed (such as the 2004 Parkfield earthquake which occurred long after the predicted earthquake, 1988 ±4 years, and the planned duration of the experiment, 1984–1992, although observational facilities were still functioning). Ironically, the failure of the earthquake forecast test sites, which were originally designed for the test of short-term earthquake forecasts, was in fact due to the uncertainties of intermediate-term earthquake forecast.

Taking a larger area and longer duration of the test might be an operational countermeasure against the uncertainty of the intermediate-term earthquake forecast. However, the opportunity to 'meet' an earthquake is still problematic. In the decade summary of the Collaboratory for the Study of Earthquake Predictability (CSEP) project, it was pointed out that '*the dearth of large earthquakes in individual regions is a major limitation of evaluations*' (Schorlemmer et al. 2018).

Another important issue is the complicated factors controlling the process of the preparation of an earthquake, which necessitates and challenges the field experiments. In the above sentence, 'necessitate' means that field experiments are important as compared to laboratory experiments—just recall the 'heat flow paradox' (e.g., Lachenbruch et al. 1995; Mora and Place 1998); and 'challenge' means that field experiments, even if with good design, always have to face to the fact that more factors seem to be determining the preparation process of an earthquake, and actually most if not all of the factors cannot be controlled.

4.3 Coordinated Distributed Experiments (CDEs)

It is worth pointing out that the difficulties discussed in the above section are not only in the field of earthquake studies. In ecology and environmental science, for example, 'few samples, many factors' is also one of the difficulties blocking the test of scientific hypotheses. Comparing to ecology and environmental science which have the difficulty in obtaining the laws at the global scale from individual local studies, earthquake science faces the difficulty in obtaining the regularities of earthquake preparation and occurrence from the studies with the duration much shorter than an earthquake cycle. To some extent, the 'sampling' problem is mainly 'spatial' for ecology and environmental science, and mainly 'temporal' for earthquake

science. On the other hand, however, it is common for ecology/environmental science and earthquake science that the 'samples' are not sufficient, and there are many controlling parameters to be considered in the test of the hypotheses.

To tackle this problem, in the fields of ecology and environment science, the concept 'Coordinated Distributed Experiments (CDEs)' was proposed as an operational tool for hypothesis testing (Fraser et al. 2012). Similarly, in earthquake science, we may consider the use of the spirit of the CDEs, although the forms would be different.

The CDEs in ecology have the following features (Fraser et al. 2012): (1) hypothesis-driven experimental study; (2) multiple geographic locations; (3) standardized research design; (4) standardized data and coordinated data management; (5) intellectual property sharing; (6) synchronized data collection; (7) multiple investigative teams; and (8) low cost and low maintenance. In the above (1)–(5) are called 'defining attributes', and (6)–(8) 'probable characteristics'. It can be seen that almost none of the above-mentioned features are new to earthquake science. Earthquake science is even more advanced regarding 'standardized data and coordinated data management'.

In the perspective of the CDEs for earthquake science, there is a need of not only one or two but also several test sites with different tectonic settings. This is not a new idea either. In 1997, the International Association of Seismology and Physics of the Earth's Interior (IASPEI) passed the resolution[3] related to the test areas for earthquake prediction:

- **Recognizing** that research into earthquake prediction needs to be carried out over long time scales with extensive and detailed observation at substantial cost, and **aware** that many nations face serious threats to their populations with limited resources and skills,
- IASPEI **urges** the organization of additional multinational test areas in different tectonic settings where high-level research efforts are already in progress, for example, Kamchatka (plate-subduction), Iceland (plate spreading), Yunnan (intercontinental strike-slip), Gulf of Corinth (continental rifting), Beijing (intracontinental)
- and **recommends** that host countries welcome participants from all nations and in due course make the data available to the international research community in computer-accessible form.

Earlier, in 1991, IASPEI passed the resolution which stressed almost the same idea:

- **Recognizing** the importance of earthquake source and prediction research to better understanding of the causes of devastating earthquakes and to work toward predicting them,
- IASPEI **encourages** national organizations supporting earthquake research to give high priority to funding of work in the IASPEI-approved sites for international collaborative earthquake prediction research, which are: (1) North Anatolian strike-slip fault (Turkey), (2) Aleutian-Alaskan subduction zone (the USA), (3) deep

[3] http://iaspei.org/about/resolutions-statements, last access: July 31, 2018.

mine-induced seismicity (South Africa), and (4) intermediate intraplate earthquakes (Vrancea, Romania) in the framework of the circum-Pannonian Carpathian seismic belts.

But the resolutions did not specify how to 'approve' and how to conduct the field test. To some extent, it had already had the concept 'Distributed', but not yet the concept 'Coordinated' at that time. It turns out that for the natural laboratories of earthquake science, 'DEs' without 'C'[4] might be one of the problems at the early time of the field experiment.

4.4 Guidelines for the Coordination

The Collaboratory for the Study of Earthquake Predictability (CSEP) was one of the significant advancements in implementing the 'C' for the field experiments. In the CSEP project, several testing areas were selected with standardized data format and testing criteria. It was pointed out that '*Meaningful evaluations of hypotheses about the long-term behavior of large earthquakes may take decades or centuries in regional fault systems, necessitating global models for testing hypotheses such as characteristic earthquakes, segmentation, and quasi-periodic recurrences*' (Schorlemmer et al. 2018). The first phase of the CSEP (2007–2018) was mainly concentrating on the 'homogeneous' models of seismicity and deformation, with emphases on statistical seismology. And now, it is time to take more account of the tectonic settings and earthquake rupture processes.

For a certain segment of active fault or tectonic block boundary zone which would accommodate future earthquakes, an 'earthquake rupture scenario' plays the role of the 'coordination'. This 'earthquake rupture scenario' provides different versions of earthquake preparation model. Based on the 'earthquake rupture scenario', detection programs and monitoring systems are to be designed, with consensus-based guidelines of experiments.

The guidelines should include several issues: (1) evaluating the 'technical readiness level (TRL)' of researches to be integrated into the experiment; (2) technical standard (and communication protocol) of data and data products to be shared (and cited); (3) planning for the possible earthquakes within (and surrounding) the test area/s; and (4) planning of the experiments, based on the activity (and uncertainty) of earthquakes, considering the 'lifetime management' of the observation/monitoring system, to ensure the effectiveness of the experiment.

In the planning of the experiment, several questions need to be carefully answered:

Q1: how many earthquakes we are expecting in the test area within the next few years?

[4]Here we use the words of late Prof. Leon Knopoff who commented world seismicity as 'SO but not C' in which SO stands for self-organized and C criticality.

Q2: what is the characteristic time scale of a geodynamical phenomenon for an observational system to capture?
Q3: how long is needed for an observation system to be deployed, calibrated, and 'pre-heated' for getting the baseline/background information?
Q4: what is the key evidence to be observed to test/falsify a model which predicts that something should be 'in this way'?

In one word, the effective constraint of the long-term seismogenic model and the short-term models for earthquake preparation, the effective observation/monitoring of 'expected' phenomena, and the effective test of the forecast schemes are the objectives of such coordination.

4.5 Coordination for a Specific Scientific Problem

One of the advantages of the CDEs is that, by experiments run in parallel by several research teams in multiple locations around the globe, scientific hypotheses can be addressed and tested, which requires the research teams to identify general and specific research questions.

For example, in the predictive modeling of earthquake cycles (e.g., Barbot et al. 2012), estimation of fault slip rates (as well as their uncertainty) based on geology and geodesy (e.g., Bennett 2007; Zechar and Frankel 2009) is an important issue. Data assimilation (Werner et al. 2011) in earthquake science is just at its beginning, but will play an important role in obtaining 'correct' estimates of the fault slip rates, which will facilitate the approaches to physical/numerical earthquake forecast. Such a scientific issue is in need of investigation making use of the observation/research resources in the experiment site/s.

Associated with the earthquakes occurred in the test sites, controversies in earthquake science could be resolved by testing against the real situation of earthquakes and seismic disasters. For example, whether the probabilistic quantification of time-dependent seismic hazard, such as that used in the Uniform California Earthquake Rupture Forecast (UCERF, Field et al. 2014, 2017), useful? And comparing to the probabilistic approach, whether the neo-deterministic seismic hazard assessment (NDSHA) approach (e.g., Zuccolo et al. 2010; Nekrasova et al. 2014) does a better job? The earthquakes will test. However, to make the test effective, the criterion and scheme for the test have to be specified beforehand.

4.6 Concluding Remarks and Discussion

The establishment of the CSES is underway. What is the chance to 'meet' a strong earthquake in this experiment site? The exact answer is 'we do not know'. However, according to the Chinese earthquake catalog, since 1965, there were on average 14

earthquakes with $M_S \geq 6.0$, among which 3 with $M_S \geq 7.0$, for every decade in this region, which provides the planning of the experiment with a statistical background.

Associated with this experiment site, there are several outstanding scientific problems to be addressed, making this experiment attractive. One example is that, in this continental region, are there any kind of low-frequency tremors which have been widely observed and studied in the plate boundary regions (Schwartz and Rokosky 2007; Ide et al. 2007; Beroza and Ide 2011; Kano et al. 2018), and (if exist) what is the role of such tremors in the seismogenesis process of continental earthquakes? Another example is that, comparing to other faults such as the Anatolian fault and the San Andreas fault (e.g., Kaneko et al. 2013; Tong et al. 2015), the creeping state of faults in this continental region (such as the Xianshuihe fault, the Anninghe fault, the Zemuhe fault, and the Xiaojiang fault) are still in lack of thorough investigation.

In the top-level design of the experiment sites, there are many issues to be considered. However, the most important challenge of such experiments is still 'few samples, many factors'. Tackling this difficulty, we introduced the concept Coordinated Distributed Experiments (CDEs) from ecology and environmental science to earthquake science. We pointed out that these disciplines share some common languages in the design of the field experiments, although in ecology and environmental science the difficulty is mainly 'spatial', and in earthquake science the difficulty is mainly 'temporal.' In earthquake science, the experiment sites have long been 'Distributed', but one of the issues in need of more emphasizing is the 'Coordination'. We proposed to use an 'earthquake rupture scenario' as the basis of the 'coordination'. We suggested that there is a need for not only one but also several experiment sites. The China Seismic Experiment Site (CSES), as well as other existed (and being built) test sites, may play the role of pilot test site/s, with the missions of forming the guidelines for the Coordination.

Acknowledgements Thanks to Drs. Paramesh Banerjee and Li Li, President and Secretary-General of the Asian Seismological Commission (ASC), for invitation to the 12th ASC General Assembly in connection to the 4th ICCE, and to Prof. Yong-Gang Li for invitation to the current monograph.

References

Audet, P. 2010. Temporal variations in crustal scattering structure near Parkfield, California, using receiver functions. *Bulletin of the Seismological Society of America* 100: 1356–1362.

Bakun, W.H., and A.G. Lindh. 1985. The Parkfield, California, earthquake prediction experiment. *Science* 229: 619–624.

Barbot, S., N. Lapusta, and J.P. Avouac. 2012. Under the hood of the earthquake machine, toward predictive modeling of the Seismic Cycle. *Science* 336: 707–710. https://doi.org/10.1126/science.1218796.

Bennett, R.A. 2007. Instantaneous slip rates from geology and geodesy. *Geophysical Journal International* 169: 19–28.

Beroza, G.C., and S. Ide. 2011. Slow earthquake and non-volcanic tremor. *Annual Review of Earth and Planetary Sciences* 39: 271–296. https://doi.org/10.1146/annurev-earth-040809-152531.

Chao, K., and Z. Peng. 2009. Temporal changes of seismic velocity and anisotropy in the shallow crust induced by the 1999 October 22 M6.4 Chia-Yi, Taiwan earthquake. *Geophysical Journal International* 179: 1800–1816.

Davis, J.F., and P. Somerville. 1982. Comparison of earthquake prediction approaches in the Tokai area of Japan and in California. *Bulletin of the Seismological Society of America* 72: S367–S392.

Evans, R., D. Beamish, S. Crampin, and S.B. Ucer. 1987. The Turkish dilatancy project (TDP3), multidisciplinary studies of a potential earthquake source region. *Geophysical Journal of Royal Astronomical Society* 91: 265–286.

Field, E.H., T.H. Jordan, M.T. Page, K.R. Milner, B.E. Shaw, T.E. Dawson, G.P. Biasi, T. Parsons, J.L. Hardebeck, A.J. Michael, R.J. Weldon II, P.M. Powers, K.M. Johnson, Y.H. Zeng, K.R. Felzer, N. van der Elst, C. Madden, R. Arrowsmith, M.J. Werner, and W.R. Thatcher. 2017. A synoptic view of the third Uniform California Earthquake Rupture Forecast (UCERF3). *Seismological Research Letters* 88: 1259–1267. https://doi.org/10.1785/0220170045.

Field, E.H., R.J. Arrowsmith, G.P. Biasi, P. Bird, T.E. Dawson, K.R. Felzer, D.D. Jackson, K.M. Johnson, T.H. Jordan, C. Madden, A.J. Michael, K.R. Milner, M.T. Page, T. Parsons, P.M. Powers, B.E. Shaw, W.R. Thatcher, R.J. Weldon II, and Y.H. Zeng. 2014. Uniform California Earthquake Rupture Forecast, version 3 (UCERF3)—The time-independent model. *Bulletin of the Seismological Society of America* 104: 1122–1180. https://doi.org/10.1785/0120130164.

Fraser, L.H., H.A.L. Henry, C.N. Carlyle, S.R. White, C. Beierkuhnlein, J.F. Cahill Jr., B.B. Casper, E. Cleland, S.L. Collins, J.S. Dukes, A.K. Knapp, E. Lind, R. Long, Y. Luo, P.B. Reich, M.D. Smith, M. Sternberg, and R. Turkington. 2012. Coordinated distributed experiments, an emerging tool for testing global hypotheses in ecology and environmental science. *Frontier in Ecology and Environment Science* 11: 147–155.

Hoshiba, M. 2006. Current strategy for prediction of Tokai earthquake and its recent topics. http://cais.gsi.go.jp/UJNR/6th/orally/O04_UJNR_Hoshiba.pdf. Last access: 31 July 2018.

Ide, S., G.C. Beroza, D.R. Shelly, and T. Uchide. 2007. A scaling law for slow earthquakes. *Nature* 447: 76–79.

Kaneko, Y., Y. Fialko, D.T. Sandwell, X. Tong, and M. Furuya. 2013. Interseismic deformation and creep along the central section of the North Anatolian Fault (Turkey), InSAR observations and implications for rate-and-state friction properties. *Journal of Geophysical Research* 118: 316–331. https://doi.org/10.1029/2012JB009661.

Kano, M., N. Aso, T. Matsuzawa, S. Ide, S. Annoura, R. Arai, S. Baba, M. Bostock, K. Chao, K. Heki, S. Itaba, Y. Ito, N. Kamaya, T. Maeda, J. Maury, M. Nakamura, T. Nishimura, K. Obana, K. Ohta, N. Poiata, B. Rousset, H. Sugioka, R. Takagi, T. Takahashi, A. Takeo, Y. Tu, N. Uchida, Y. Yamashita, and K. Obara. 2018. Development of a slow earthquake database. *Seismological Research Letters* 89: 1566–1575. https://doi.org/10.1785/0220180021.

Lachenbruch, A.H., J.H. Sass, G.D. Clow, and R. Weldon. 1995. Heat flow at Cajon Pass, California. *Journal Geophysical Research* 100: 2005–2012.

Mogi, K. 2004. Two grave issues concerning the expected Tokai Earthquake. *Earth, Plants and Space* 56: li–lxvi. https://doi.org/10.1186/bf03353074.

Mora, P., and D. Place. 1998. Numerical simulation of earthquake faults with gouge: Toward a comprehensive explanation for the heat flow paradox. *Journal Geophysical Research* 103: 21067–21089. https://doi.org/10.1029/98JB01490.

Nekrasova, A., V. Kossobokov, A. Peresan, and A. Magrin. 2014. The comparison of the NDSHA, PSHA seismic hazard maps and real seismicity for the Italian territory. *Natural Hazards* 70: 629–641. https://doi.org/10.1007/s11069-013-0832-6.

Roeloffs, E. 2000. The Parkfield California earthquake experiment, an update in 2000. *Current Science* 79: 1226–1236.

Roeloffs, E., and L. Langbein. 1994. The earthquake prediction experiment at Parkfield, California. *Review of Geophysics* 32: 315–336.

Schorlemmer, D., M.J. Werner, W. Marzocchi, T.H. Jordan, Y. Ogata, D.D. Jackson, S. Mak, D.A. Rhoades, M.C. Hirata, N. Gerstenberger, M. Liukis, P.J. Maechling, A. Strader, M. Taroni, S. Wiemer, J.D. Zechar, and J. Zhuang. 2018. The Collaboratory for the Study of Earthquake Pre-

dictability: achievements and priorities. *Seismological Research Letters* 89: 1305–1313. https://doi.org/10.1785/0220180053.

Schwartz, S.Y., and J.M. Rokosky. 2007. Slow slip events and seismic tremor at circum-Pacific subduction zones. *Review of Geophysics* 45: RG3004. https://doi.org/10.1029/2006RG000208.

Semenov, A.M. 1969. Variations in the travel-time of transverse and longitudinal waves before violent earthquakes. *Izvestia Academy of Science. USSR Physics of Solid Earth* (Engl. Transl.) 4: 245–248.

Stefansson, R., F. Bergerat, M. Bonafede, R. Boovarsson, S. Crampin, K.L. Feigl, F. Roth, F. Sigmundsson, and R. Slunga. 2001. *PRENLAB-TWO—Final report*. Veourstofa Islands Report.

Stefansson, R., F. Bergerat, M. Bonafede, R. Boovarsson, S. Crampin, P. Einarsson, K.L. Feigl, A. Guomundsson, F. Roth, F. Sigmundsson, and R. Slunga.1998. *PRENLAB final report*. Reykjavik.

Tong, X., D.T. Sandwell, and B.R. Smith-Konter. 2015. An integral method to estimate the moment accumulation rate on the Creeping Section of the San Andreas Fault. *Geophysical Journal International* 203: 48–62. https://doi.org/10.1093/gji/ggv269.

Wegler, U., H. Nakahara, C. Sens-Schönfelder, M. Korn, and K. Shiomi. 2009. Sudden drop of seismic velocity after the 2004 Mw6.6 mid-Niigata earthquake, Japan, observed with passive image interferometry. *Journal of Geophysical Research: Solid Earth* 114: B06305. https://doi.org/10.1029/2008jb005869.

Werner, M.J., K. Ide, and D. Sornette. 2011. Earthquake forecasting based on data assimilation: sequential Monte Carlo methods for renewal point process. *Nonlinear Processes in Geophysics* 18: 49–70. https://doi.org/10.5194/npg-18-49-2011.

Zechar, J.D., and K.L. Frankel. 2009. Incorporating and reporting uncertainties in fault slip rates. *Journal Geophysical Research* 114: B12407. https://doi.org/10.1029/2009JB006325.

Zuccolo, E., F. Vaccari, A. Peresan, and G.F. Panza. 2010. Neo-deterministic and probabilistic seismic hazard assessments: A comparison over the Italian territory. *Pure and Applied Geophysics* 168: 69–83. https://doi.org/10.1007/s00024-010-0151-8.

Chapter 5
Annual Earthquake Potential Consultation: A Real Forward Prediction Test in China

Yongxian Zhang, Zhongliang Wu, Xiaotao Zhang and Gang Li

Abstract The Chinese seismologists have conducted the Annual Consultation on the Likelihood of Earthquakes in the Next Year as a real forward prediction test for over four decades since the 1970s. This approach has unique scientific and practical merits either as an active response to the social needs for mitigation of seismic disaster while the earthquake prediction remains to be a challenging problem scientifically. This chapter summarizes the National Annual Consultation from the 1970s to the present, its scientific outputs, methodology used for analysis, and in-depth philosophy guiding the Consultation and proposed further developments and improvements. Two case studies after the 2008 M8 Wenchuan earthquake were shown in this chapter.

Keywords National Annual Consultation · Earthquake forecast · Statistical seismology · Neural network · Fuzzy logic · Pattern recognition · *R* score

5.1 Background of Annual Consultation on Earthquake Potential in China

China is a country with serious earthquake disasters. After the foundation of the People's Republic of China in 1949, many large earthquakes occurred in China mainland and caused serious earthquake disasters, such as 1976 Tangshan $M7.8$ Earthquake and 2008 Wenchuan $M8.0$ earthquake. However, the 1966 Xingtai, Hebei $M7.2$ earthquake is a milestone for earthquake prediction in China due to its position of the first destructive earthquakes occurred in the densely populated Northern China in the twentieth century. The death toll of this earthquake is 8000 and the injured are 38,400 and this caused a stir to the society and actually triggered the beginning of the 'long-march' of Chinese seismologists to earthquake prediction, while the

Y. Zhang (✉) · X. Zhang · G. Li
China Earthquake Networks Center, Beijing 100045, China
e-mail: yxzhseis@sina.com

Z. Wu
Institute of Earthquake Forecasting, Earthquake Administration China, Beijing 100081, China
e-mail: wuzl@cea-igp.ac.cn

Y.-G. Li (ed.), *Earthquake and Disaster Risk: Decade Retrospective of the Wenchuan Earthquake*, https://doi.org/10.1007/978-981-13-8015-0_5

national long-term plan for earthquake prediction study can be traced back to 1956 in the National Twelve-year Plan for Development of Science and Technology (Wu et al. 2007). Shortly after the main shock of the Xingtai earthquake, sponsored by former Prime Minister Zhou Enlai, the State Committee for Science and Technology organized an extensive field investigation to the meizoseismal region, focusing on earthquake prediction study. Institutions and/or organizations involved in the investigation included the Chinese Academy of Sciences, the Ministry of Petroleum, the Ministry of Geology, the State Bureau of Surveying and Mapping, the State Bureau of Ocean, and some universities colleges, reflecting the insight of Chinese regarding earthquake prediction as a complex, comprehensive, and interdisciplinary problem. This insight plays an important role in the organization of the annual consultation meeting in the later time (Wu et al. 2007).

Based on the Central Working Group on Seismological Works established in 1969, the State Seismological Bureau (SSB) was founded in 1971, responsible for earthquake monitoring and prediction in China. SSB was renamed as China Seismological Bureau (CSB) in 1998, and the English translation changed to China Earthquake Administration (CEA) in 2002. The annual consultation was started in 1972 organized by SSB and was officially formalized in 1975. Since 1988 the annual consultation has been formally assigned as one of the official missions of the SSB. In 1998, Law of the People's Republic of China on Protecting Against and Mitigating Earthquake Disasters was enacted. Accordingly, the government issued the Regulations on Administration of Earthquake Prediction, aiming to regulate the procedure of the evaluation and publication of earthquake prediction, providing annual consultation with legislative authorization. In 1998, CEA organized an ad hoc Evaluation Committee, being independent of the working group for making the forecast prediction, responsible for the second round review of the forecast prediction conclusions produced by the consultation meeting (Wu et al. 2007).

In the early 1990s, some foreign seismologists were invited to participate in the meeting. American seismologist Francis Wu (1997) gave an introduction to the history and the state-of-the-art of the annual consultation in early stage of the annual consultation. However, only a few results of the annual consultation meetings have been published in the widely accessible academic journals. The scientific outputs related to the annual consultations were mostly published in Chinese by the Seismological Press in Beijing (in Chinese) (e.g., Center for Analysis and Prediction, CEA 2002, 2003; Comprehensive Evaluation Summary Group for Annual Earthquake Key Risk Area, CEA 2012, 2013, 2014), releasing public after three years because of the sensitivity and uncertainty of the present study of earthquake predictability. Twenty years have passed after Wu's observation of China's Annual Earthquake Consultation (Wu 1997), and the scientific intentions, forms, and procedures of the annual consultation have been updated to improve the prediction ability and fit the requirements from the government and public.

5.2 The Procedure of the Annual Consultation

Before 2010, the National Annual Consultation had been convened and held by SSB/CEA in January of each year, called 'National Consultative Meeting in Seismic Tendency' in Beijing, in which the geographic areas of possible seismic risks, areas for intensified monitoring, and areas where preparedness are to be heightened for the next one to two years were officially reviewed. This meeting was the culmination of a series of meetings at the provincial levels and meetings of the experts (from SSB research institutes) who analyzed the precursory observations. At these smaller preparatory meetings, the prediction data and opinions were evaluated in detail. The consensus reached at this meeting was then presented to the National Meeting and was further refined and reviewed by the staff of the Center of Analysis and Prediction (CAP), SSB, and by panels consisting of seismologists from various regions (Wu et al. 2007).

Since 2010, the meeting time of the National Annual Consultation has been moved to December of each year, and the output of the meeting has been reported to China Central Government at the 'Meeting of the State Council on Earthquake Prevention and Disaster Mitigation' held in January of each year. After this official meeting, the prediction results that have been officially reviewed are issued by the State Council to related provincial governments and local earthquake administrations for heightened preparedness for the forecasting year.

The approximate procedure of the complete Annual Consultation is described as follows.

5.2.1 Preparatory Meetings

Before the National Annual Consultation in December of each year, there are a series of preparatory meetings at levels of the disciplinary groups, provincial earthquake administrations/Institutes of CEA, tectonic region working groups, and expert groups from late September to late November. So the study of annual earthquake tendency is basically organized in a matrix, and some experts might attend most of the preparatory meetings.

5.2.1.1 Annual Consultations of Disciplinary Groups

Academically, the studies on annual earthquake prediction are divided into five subjects: seismology; geomagnetism and geo-electricity; ground deformation and gravity; underground fluid, geochemistry, and geothermal; and comprehensive analysis. For the former four subjects, four disciplinary earthquake monitoring systems were set up and operated by local earthquake administrations, and all the data are collected and processed by China Earthquake Networks Center (CENC), and quality of the

data was guaranteed by the Coordination Groups for Observation and Interpretation (CGOI) of each discipline organized by CEA. All these data are daily processed and analyzed by seismologists in departments of earthquake analysis and prediction in CENC and provincial earthquake administrations. These data are also used for scientific research by seismologists in institutions and colleges.

In late September of each year, four disciplinary meetings organized by CEA are firstly held for the Annual Consultation. The main task of these meetings is to determine earthquake anomalies which might be related to future earthquakes based on knowledge and experience nowadays. The confidence level, 'Long-term,' 'Medium term,' or 'Short-term, labels for each anomaly will be discussed and determined based on earthquake case studies (e.g., Zhang 1988, 1990a, 1990b, 1999, 2000; Chen 2002a, 2002b, 2003; Jiang 2014; Sun and Wu 2007; Huang et al. 2017) and expert experiences. The labeled anomalies are regarded as earthquake precursory anomalies and they imply the abnormal changes in different stage of the seismogenic process. Statistical analysis is applied not only to seismic activity, but also to the spatiotemporal distribution of precursor anomalies, broadening the scope of statistical seismology.

In spite of the experiential analyses, there are also some special domestic methods such as LURR (Load/Unload Response Ratio) (E.g., Yin 1987; Yin et al. 1995, 2006; Zhang et al. 2015), Geomagnetic low-point displacement (E.g., Ding 2008), etc. The international earthquake forecasting methods have also been applied to the annual forecasting, such as pattern informatics (Rundle et al. 2003; Holliday et al. 2006; Yu et al. 2016; Zhang et al. 2015, 2017).

Those areas with potential seismic risk in the coming year will also be worked out by each disciplinary group on their sides. The reports from these meetings are the important basis for the next preparatory Provincial Annual Consultation.

5.2.1.2 Annual Consultations of Geophysical Field Measurements

After the Wenchuan $M8.0$ earthquake, CEA organized large scale geophysical field measurements, such as deformation, gravity, geomagnetic, and geo-electric field, with organized quality-control system and strict standard for routine data processing. Special Annual Consultations of Geophysical Field Measurements are organized to discuss the relationship between the change of geophysical field and the forthcoming earthquakes (e.g., Chen et al. 1979, 2003; Zhu et al. 2009).

The geophysical measurements are helpful for earthquake location forecast. For example, analysis and prediction with recent mobile geomagnetic field measurements have shown positive prospect for location forecasting. Figure 5.1 shows an example of the forecasting and testing result by the mobile geomagnetic field measurements.[1] The outputs of these meetings supply important information for locating forecasting

[1] Presentation of earthquake prediction with mobile geomagnetic measurements by Gu Z.W. at the Annual Consultation of mobile geomagnetic measurements in 2013 (the document issued internally in CEA).

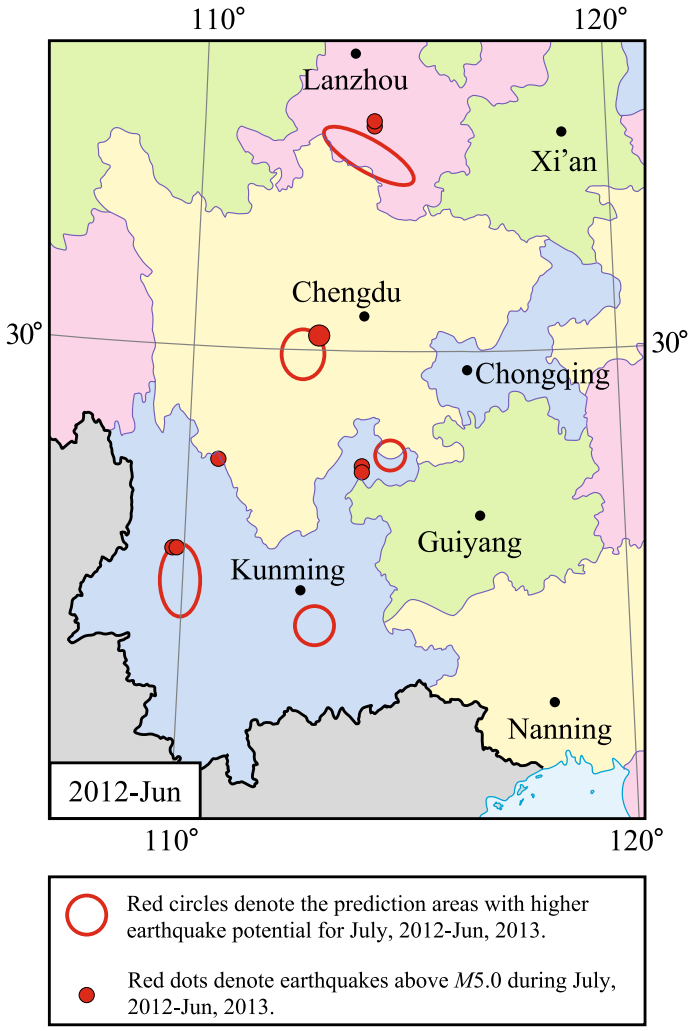

Fig. 5.1 Prediction and test map on the mobile geomagnetic field measurements. Red circles denote the prediction areas with higher earthquake potential for July 2012–Jun 2013. Red dots denote earthquakes above $M5.0$ during July 2012–Jun 2013

for the future earthquakes. Such consultations are often held in early October and the deadline to submit related reports is around late October.

5.2.1.3 Provincial/Institutional Annual Consultations

Based on the outputs of the disciplinary group meetings held in late September, Provincial/Institutional Annual Consultations are held successively in each provincial earthquake administration/institute around mid-October. The main task of the consultation is to determine the seismic potential area(s) for the next year in its administrative/researching area. The results of these meetings would be evaluated by Earthquake Prediction Review Committee of each province/institution and will be submitted to the local government. These results will be also submitted to CEA for the next preparatory meeting to determine the relative earthquake potential areas in each tectonic region. Detailed abstracts with conclusions and arguments are requested to submit online with the deadline of about Oct. 25. Electronic formal reports together with hard copies of each provincial earthquake administration/institution of about 100 pages are requested to submit to CEA before the National Annual Consultation (held in early December). These provincial/institutional reports are sealed and will be ranked by an expert group organized by CEA after the prediction period has passed. The excellent reports with confident observation data, rigorous logic, active innovation in earthquake prediction method, and higher prediction effects will be awarded in the National Annual Consultation of the next year.

5.2.1.4 Annual Consultation for Geographical Regions

The entire territory of continental China is divided into four geographical regions for study: the north- and northeast-China region; the northwest-China region (sometimes divided in Xinjiang Region and Gansu-Qinghai Region); the southwest-China region; and the east- and south-China region. When considering these regions, the surrounding areas of continental China, which are tectonically related, are also considered.

The main task of the Annual Consultation for Geographical Region is to determine the Annual Earthquake Key Risk Area in the coming year in this region. Although each province has determined its own Annual Earthquake Key Risk Area before this meeting, it is not a simple combination of the all Annual Earthquake Key Risk Area of them. Only those with more abundant and credible arguments and higher possibility of occurrence in the next year will be remained. And those Annual Earthquake Key Risk Areas standing on the provincial boundaries will be adjusted to a proper position according to earthquake case studies and expert experiences.

The outputs of these meetings supply the basic drafts of Annual Earthquake Key Risk Areas. The reports of Annual Consultations for these four Geographical Regions will be submitted to a summary group for drawing the outline of Annual Earthquake Key Risk Areas before the deadline of early November.

5.2.1.5 Workshop for Summarizing the Draft of the Annual Earthquake Key Risk Areas

After the Annual Consultations of Disciplinary Groups, Annual Consultations of Geophysical Field Measurements, Provincial/Institutional Annual Consultation, and Annual Consultation for Geographical Regions, all reports are collected together to China Earthquake Networks Center and a working group consisted of experts from provincial earthquake administrations will work out a draft of the Annual Earthquake Key Risk Areas before the end of November.

This is a key step before the National Annual Consultation because it gives a comprehensive national draft report on earthquake prediction for the next year. And this report with length of about several hundred pages (also called 'white book,' see examples in Sect. 5.3) gives very detailed arguments on the Annual Earthquake Key Risk Areas. The outcome of this workshop provides a target to review at the National Annual Consultation in early December.

5.2.1.6 National Annual Consultation

In early December, the National Annual Consultation is held in Beijing. There are about 120 participants including significant scientists and leaders from provincial earthquake administrations, Institutions of CEA and officials of CEA, together with invited scientists outside of CEA (e.g., Peking University, China University of Geosciences, China Academy of Sciences, etc.).

There are two rounds of meeting during the National Annual Consultation. The schedule of the first round of consultation includes opening ceremony, two major reports on earthquake tendency within future 3 years and 1 year, earthquake risk area arguments, specialist group meeting for updating earthquake potential region, comprehensive group workshop for summary of the national candidate Annual Earthquake Key Risk Area, and closing ceremony. Scientific reports on new development of earthquake monitoring and prediction will be presented by invited scientists during the period when the comprehensive group is working on the summary presentation. The director of CEA and leaders of the subordinate departments need to attend the opening and closing ceremonies. And the CEA director will give a speech on prospective earthquake monitoring and prediction. The first round consultation meeting finishes during two days.

After the closing ceremony, the second round of consultation will be held on the third day of the annual consultation meeting. An ad hoc Evaluation Committee (organized by CEA in 1998) will review the candidate Annual Earthquake Key Risk Areas produced by the first round consultation meeting. This committee consists of academicians from China Academy of Sciences, top scientists of CEA, and invited top scientists from outside universities and institutions. It is independent from the working group for making the forecast prediction. Only those candidate Annual Earthquake Key Risk Areas who pass the second review could be regarded as the confirmed as the Annual Earthquake Key Risk Areas and will be reported to China

Central Government at the 'Meeting of the State Council on Earthquake Prevention and Disaster Mitigation' held in January of each year. The premier of the State Council in charge of seismic hazards convenes this meeting and all Provincial Administrators need to attend in it. The Annual Earthquake Key Risk Areas are informed to the provincial governments for earthquake preparedness, and some engineering social countermeasures will be taken accordingly. CEA and the related provincial earthquake administrations will also strengthen the seismological monitoring in the regions which are expected to have higher probability of earthquakes, and working mechanisms on strengthening the analysis and consultation of the short-term prediction for these Annual Earthquake Key Risk Areas will also be set up. However, due to the social sensitivity and uncertainty of the present study of earthquake predictability, the annual earthquake prediction results especially the Annual Earthquake Key Risk Areas are only served for the governmental earthquake disaster preparedness but could not be released to the public.

During the two rounds of annual consultation, three problems are addressed and are proposed to be discussed with higher priorities:

(1) Is the present time in a seismically active or inactive period?
(2) What will be the overall level of seismic activity in the next year? Will there be any strong earthquakes with magnitude larger than $M7.0$ occurring in the whole Chinese mainland the next year, and will there be any earthquakes with magnitude larger than $M6.0$ occurring in the densely populated eastern China the next year?
(3) Which regions will have higher probability for earthquakes larger than $M6.0$ (in the western part) and or $M5.0$ (in the eastern part) in the coming year? It is evident that the answers to these questions, even if with very limited capability, are beneficial for the preparedness of society against earthquake disasters, especially for the annual financial budget allocation for earthquake emergency response (Wu et al. 2007).

In the comprehensive analysis which combines the information from different disciplines, Chinese seismologists prefer the combination of quantitative calculation and qualitative experience. Some of the calculation tools, such as fuzzy logic, pattern recognition, artificial neural networks, and expert system, are used for learning and predicting. On the other hand, however, experienced senior experts play an important role in the forming of the final conclusions, although the underlying physics of some of the experiences (i.e., the relation between the observation of experts and the conclusions they draw, and the relation between such logics and the process of earthquake preparation) are still not fully understood, even if by the experts themselves (Wu et al. 2007).

5.3 One Example of the Comprehensive Annual Prediction Draft Report

Here is the Comprehensive Annual Prediction Draft Report for 2013, an example of the Comprehensive Annual Prediction Draft Report (also called 'white book') submitted to the National Annual Consultation for review (Comprehensive Evaluation Summary Group for Annual Earthquake Key Risk Area, CEA, 2013). This report consists of the detailed abstract, eleven sections and one attachment. The detailed abstract mainly gives the characteristics of the seismicity and geophysical and geochemical in the past year, and the prediction results for the next year.

The first section 'introduction' describes the description of how this report was worked out, including the major issues which should be concerned in the prediction research of this year, the target and principle how to form the Annual Earthquake Key Risk Area, and the procedure how to summarize the last Annual Earthquake Key Risk Areas form the previous prepared meetings.

The second section 'General Seismicity in 2012' describes the actual seismic activity in 2012, and the spatial and temporal characteristics compared to the historical seismicity, including quiescence, activation, high frequency, earthquake belt, etc.

The third section 'Test for the Earthquake Prediction Map of 2012' provides the evaluation of the prediction ability for 2012 by quantitative R score method (Xu, 1989) and qualitative description.

The fourth section 'Analysis and Prediction for Earthquake Tendency in China Mainland' is for the estimation of the highest level in each tectonic or geographical region. In general, the following geographical regions are considered for study: the whole China mainland; the north- and northeast-China region; the northwest-China region (sometimes divided in Xinjiang Region and Gansu-Qinghai Region); the southwest-China region; and the east- and south-China region; the Capital region (38.5°–41°N, 113°–120°E) included in the east- and south-China region. South–North Seismic belt zone is also a considered region where a lot of large earthquakes including Wenchuan M8.0 occurred (e.g., Zhang et al. 2016). This belt zone is also the boundaries of active blocks, hence with the high activity of large earthquakes within it (Zhang et al. 2013, 2015).

The fifth section 'Earthquake Potential Areas in Southwest China' is for determination of earthquake potential areas of 2013 in Southwest China. Because there are many high earthquake potential areas in long term (such as historical seismic gaps, displacement deficit sections of active faults, areas with low b value, and areas with high strain energy accumulation), the Annual Earthquake Key Risk Areas must be those with medium-term signals such as significant changes of underground water level, water radon, geo-electricity, etc. Among those long-term earthquake potential areas, only when the incredible medium-term anomalies are detected around them, can they be elected as the annual earthquake potential areas.

The sixth section 'Annual Earthquake Key Risk Area in Gansu-Qinghai Region' is for determination of the key earthquake risk areas of 2013 in Gansu-Qinghai region.

The procedure to elect the Annual Earthquake Key Risk Areas from the long-term earthquake potential areas is as the same as the fifth section. So did the seventh section 'Annual Earthquake Key Risk Areas in Xinjiang Uygur Autonomous Region,' the eighth section 'Annual Earthquake Key Risk Areas in North- and Northeast-China Region,' and the ninth section 'Annual Earthquake Key Risk Area in East- and South-China Region.'

The tenth section 'Intensive Surveillance Region of Capital Area' is for analysis and prediction of the seismic level of the Capital Area of China in 2013. This area is also called Metropolitan Area of Beijing with range of (38.5°–41°N, 113°–120°E) which locates in Northern China (Zhang et al. 2013). Due to its high seismicity (Tangshan M7.8 Earthquake occurred within this area) and dense population, together with its complete historical earthquake catalogue of earthquake above M4.7 for about 200 years, it has been taken as one of the earthquake test sites in the mainland of China. Denser earthquake monitoring networks have been set up in this area. Abundant seismic, geological, geophysical, and geochemical data have been obtained, and the variation of seismic, geophysical, and geochemical parameters was recorded before several strong earthquakes and some moderate earthquakes (Zhang et al. 2013). All the information makes it possible to predict the seismic level and earthquake potential areas in medium- to short-term. So the Capital Area becomes an Intensive Surveillance Region in China, providing earthquake safeguard for the government and the public.

The eleventh section 'Preliminary Comprehensive Prediction of the Annual Earthquake Key Risk Areas in 2013' gives a brief conclusion for the Key Earthquake Potential Areas, Intensive Surveillance Regions of Capital Area, and Notable Regions.

The attachment provides the earthquake catalogue with domestic earthquakes above M5.0 and global earthquakes above M7.0 in 2012.

In the eleventh section, a prediction map of the key earthquake potential areas for 2013 is given, and we can have a test when the prediction window passed.

5.4 Test of the Annual Consultation by *R* Score

Figure 5.2 shows the prediction map for the Annual Earthquake Key Risk Areas of 2013 and earthquakes above M5.0 occurred in 2013. There were 11 Annual Earthquake Key Risk Areas for 2013 and four of them with earthquakes above M5.0 occurred in them (Fig. 5.2). There were 40 shallow earthquakes above M5.0 in China mainland in 2013, and 18 of them were independent ones (de-clustering ones) which occurred in the region with earthquake monitoring abilities. Seven out of the 18 independent earthquakes occurred in the four Annual Earthquake Key Risk Areas.

In order to evaluate the prediction ability of the Annual Consultation quantitatively, Xu (1989) proposed the R-score test based on the statistics of alarm-based forecast prediction.

R-score = (successful predictions/total number of earthquakes) − (false alarm area/total seismic area without earthquakes).

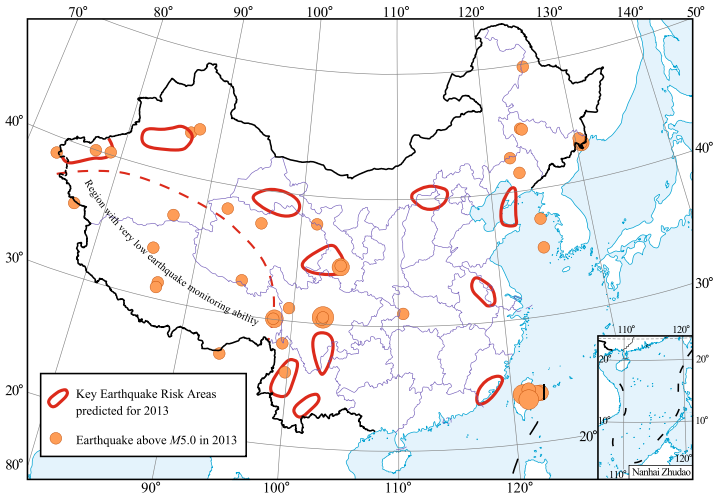

Fig. 5.2 Test of prediction map of key earthquake potential areas for 2013. Red circles denote the Key Earthquake Potential areas predicted for 2013; Orange dots denote earthquakes above $M5.0$ occurred in 2013; Red dash line denotes a boundary which divides China mainland into two regions, the left region is with very low earthquake monitoring ability compared with the right region

When all the predictions are successful, $R = 1$; When all the predictions are wrong, $R = -1$; for random prediction, $R = 0$ (Zhu et al. 1991; Shi et al. 2000).

Evaluation of the performance of the annual consultation meeting leads to objective conclusions on the capability of the estimation of annual seismic hazard in early period before 2000 (Shi et al. 2000; Zheng et al. 2000, 2002). Their evaluation for the early annual prediction maps shows that in average the R-value of the annual consultation is no more than 0.3 but still significantly outperforms random predictions (Shi et al. 2000; Zheng et al. 2000, 2002),, while this apparent success is largely dependent on the probabilistic estimation of background seismicity (Shi et al. 2004), implying that statistical seismology, largely based on the analysis of earthquake catalogues, has the potential for its application to the annual consultation.

After 2000, R-value of the Annual Consultation has become higher in average (Fig. 5.3), implying that the capacity of the Annual Prediction has been improved obviously. The highest R score is 0.73 in 2003, and the lowest R score is -0.08 in 2006. During 2000–2016, the average R score is 0.38. Wenchuan $M8.0$ earthquake occurred in 2008. Two years before this large earthquake, the seismicity of China mainland was very low, so the hit rate was lower and the false alarm rate was higher, hence the lower even negative R-value.

The test results of the annual consultation by R score for 27 years show that overall medium-term earthquake prediction is feasible even under limited monitoring ability and incomplete knowledge. However, it is still very difficult to give an accurate prediction, and the R-score test is not very strict for the magnitude prediction. In time period with very low seismicity, the capacity of the Annual Consultation is still

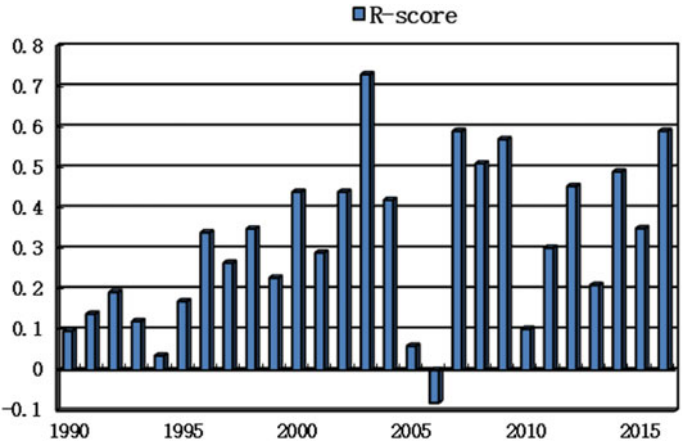

Fig. 5.3 *R*-value of the Annual Consultation during 1990–2016

very low, implying that our ability to tell the difference of medium-term anomaly from observed anomalies is still very low.

5.5 About the Annual Forecasting Before Wenchuan *M*8.0 Earthquake

Figure 5.4 shows the prediction map for the Annual Earthquake Key Risk Areas of 2008 and *earthquakes* above M_S 5.0 occurred in 2008. There are five key regions for 2008 and earthquakes above M_S 5.0 occurred in or very near the five key regions (with distance less than 50 km from the boundary). However, Wenchuan *M*8.0 and all aftershocks did not drop in any predicted regions. The *R* score for this year is 0.51, higher than the average value (0.3). However, the biggest earthquake Wenchuan M_S 8.0 missed. This means that *R*-score test is not the best evaluation in terms of disaster.

On the other hand, excluding deep earthquakes and those occurred in the Tibetan and nearby region with very low earthquake monitoring ability, there were total 19 major earthquakes with $M_S \geq 6.0$ occurred in the region with earthquake monitoring and forecasting ability during 2008–2016 (Table 5.1). It shows that 13 out of 19 earthquakes (68.4%) with $M_S \geq 6.0$ dropped in or very near the annual key earthquake potential areas predicted. Among the 19 major earthquakes, large earthquakes with $M_S \geq 7.0$ were not predicted, neither 2008 Wenchuan M_S 8.0 earthquake nor 2013 Lushan M_S 7.0 earthquake. However, among the rest 17 M_S 6.0–6.9 earthquakes, 13 were successfully predicted by annual consultation. The ratio of success of 76.5% is meaningful for disaster prevention.

Annual Consultation on Earthquake Potential is a kind of comprehensive subjective forecasting, mainly based on statistics, experience, and some simple models. In

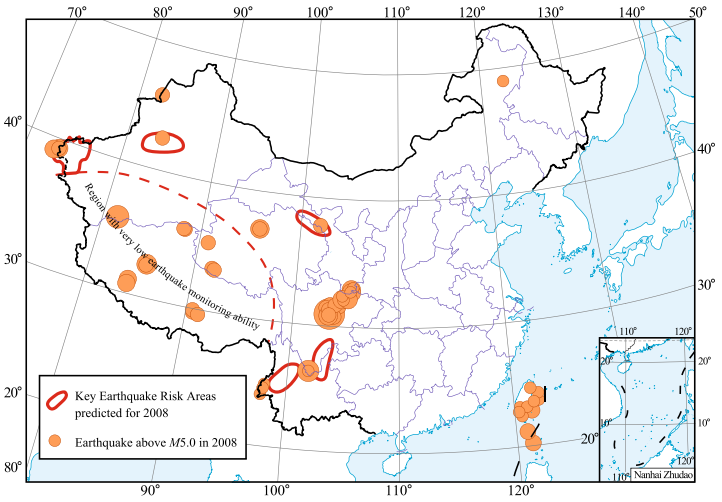

Fig. 5.4 Test of prediction map of key earthquake potential areas for 2008. (Red circles denote the key earthquake potential areas predicted for 2008; Orange dots denote earthquakes above $M5.0$ occurred in 2008; Red dash line denotes a boundary which divides China mainland into two regions, the left region is with very low earthquake monitoring ability compared with the right region, and no key earthquake areas could be drawn out)

China mainland, the average number of $M_S \geq 6.0$ for each year is about 4. But for $M_S \geq 7.0$ earthquake, the average number is once for 1.5 year. So earthquakes of MS6 are more experienced than those of $M_S \geq 7.0$, and the statistical forecasting relation for $M_S \geq 6.0$ earthquake is more robust and reliable than those for $M_S \geq 7.0$ earthquakes. In order to improve the forecasting ability for $M_S \geq 7.0$ earthquakes, physical forecasting model needs to be developed besides more experiences obtained.

5.6 Significance of the Annual Consultation

The Chinese seismologists have conducted the Annual Consultation on the Likelihood of Earthquakes in the Next Year as a real forward prediction test for nearly four decades since the 1970s. This approach has unique scientific and practical merits either as an active response to the social needs for mitigation of seismic disaster while the earthquake prediction remains to be a challenging problem scientifically.

Earthquake prediction is still an unsolved problem. The practice especially the Annual Consultation in China shows that it is possible to obtain some useful information about earthquake hazard based on the present (incomplete) knowledge and (incomplete) data. It is possible for us to draw some useful conclusions by a comprehensive consideration based on experiences and qualitative knowledge after having different kinds of observations.

Table 5.1 Test results of all earthquakes with $M_S \geq 6.0$ during 2009–2016 occurred in or not in the Annual Key Earthquake Potential Areas*

No.	Earthquake ($M_S \geq 6.0$)	Date (BJT)		In the forecasted key regions or not?
1	Wenchuan, Sichuan 8.0	2008-05-12	30.95°N, 103.40°E	No
2	Panzhihua, Sichuan 6.1	2008-08-30	20.20°N, 101.90°E	Very near (≤ 50 km)
3	Wuqia, Xinjiang 6.8	2008-10-05	39.50°N, 73.90°E	Yes
4	Haixi, Qinghai 6.3	2008-11-10	37.60°N, 95.90°E	No
5	Yaoan, Yunnan 6.0	2009-07-09	25.60°N, 101.10°E	Yes
6	Haixi, Qinghai 6.4	2009-08-28	37.60°N, 95.80°E	Yes
7	Yili, Xinjiang 6.0	2011-11-01	43.60°N, 82.40°E	Yes
8	Hetian, Xinjiang 6.0	2012-03-09	39.40°N, 81.30°E	No
9	Xinyuan, Xinjiang 6.6	2012-06-30	43.40°N, 84.80°E	Yes
10	Lushan, Sichuan 7.0	2013-04-20	30.30°N, 103.00°E	No
11	Minxian, Gansu 6.6	2013-07-20	34.50°N, 104.20°E	Yes
12	Yingjiang, Yunnan 6.1	2014-05-30	25.00°N, 97.80°E	No
13	Ludian, Yunnan 6.5	2014-08-03	27.10°N, 103.30°E	Yes
14	Jinggu, Yunnan 6.6	2014-10-07	23.40°N, 100.50°E	Very near(≤ 50 km)
15	Kangding, Sichuan 6.3	2014-11-22	30.30°N, 101.70°E	Yes
16	Pishan, Xinjiang 6.5	2015-07-03	37.60°N, 78.20°E	No
17	Minxian, Gansu 6.4	2016-01-21	37.70°N, 101.60°E	Yes
18	Aketao, Xinjiang 6.7	2016-11-25	39.27°N, 74.04°E	Yes
19	Hutubi, Xinjing 6.2	2016-12-08	43.83°N, 86.35°E	Yes

*(1) Earthquakes occurred in the region with very low earthquake monitoring ability are not listed. This region is as shown in Figs. 5.2 and 5.4 at the left part of the black bold arc line, and no key earthquake areas could be drawn out in this region;
(2) Deep earthquakes in Northeast China are not listed either;
(3) Only the major earthquakes in earthquake series are listed.

The practice of Chinese Earthquake Annual Consultation is in consistence with the recently developed ideas such as that of the CSEP (Collaboratory for the Study of Earthquake Predictability) project (http://scecdata.usc.edu/csep/project-documents/Jordan-CSEP-Luncheon.ppt/view) which is trying to turn the study of earthquake predictability from 'silver bullet approach' to 'brick-by-brick approach' (Wu et al. 2007).

In principle, earthquake prediction problem can be decomposed into three components: scientific, technique, and engineering. The scientific component deals with the physical predictability of earthquakes and the methods for feasible earthquake forecast prediction. The task of the technique component, in turn, is to make full use of the results of the scientific component (even if it is poor) to implement the forecast prediction scheme within the limits of the scientific results. Furthermore, the engineering component considers both the technical issues and the social issues to pursue

the global optimization of the social benefit. The philosophy of the annual consultation meeting is to make clear the difference between the scientific, technique, and engineering components, and seek for a global optimization in solving the problem of earthquake preparedness, so that seismologists may be able to make the maximum contribution to the society within the limit of the capacity of earthquake science (Wu et al. 2007).

Since recent years, it has been recognized that retrospective studies of earthquake cases, although being useful to provide heuristic clues for developing the forecast prediction schemes, is intrinsically problematic due to subjective selection of data (e.g., Mulargia 1997). The only remedy is real forward forecast prediction test (Wu et al. 2007). The unique scientific merit of the annual consultation meeting lies in that it is a real forward forecast prediction test, and most remarkably, it has been persistently conducted for over four decades.

5.7 Conclusion and Discussion

We briefly reviewed the annual consultation on the likelihood of earthquakes in continental China since the 1970s. The frames of the Summary Research Report on the national key earthquake potential areas in 2013 and 2014 were taken as two case studies. The failure forecast for Wenchuan M_S 8.0 earthquake was simply reviewed.

The real forward prediction test for over four decades since the 1970s has unique scientific and practical merits either as an active response to the social needs for mitigation of seismic disaster while the earthquake prediction remains to be a challenge problem scientifically. This chapter summarizes the National Annual Consultation from 1970s to the present, its scientific outputs, methodology used for analysis, and in-depth philosophy guiding the Consultation and proposed further developments and improvements.

In the perspective of statistical seismology, the long-time persistence, real forward forecast test, and combination of the information of different disciplines make this approach unique among the endeavors studying the predictability of earthquakes. Through wide discussions at the meeting, it is very helpful to raise new ideas as well as the scientific problems in earthquake prediction to be studied further.

However, some of the aspects in the Annual Consultation, such as the methodology for the identification of anomalies, the subjective effects of the panel discussion combining different kinds of information, and the interpretation and application of the output message from the Annual Consultation, still have a large space for improvement.

Communicating with international seismological communities is especially needed for the exchange of scientific ideas and research results and for the cooperation in applying the algorithms of statistical seismology and geodynamics to the annual consultation. More earthquake prediction theories, models, and methods need to be developed and more observation data need to be obtained to support earthquake simulation.

In any case, the Annual Consultation is one of the contributions of Chinese seismological community to the test of earthquake forecast schemes. There is much to be done in either the introduction or the improvement of this approach.

Acknowledgements We are grateful to China Earthquake Networks Center and China Earthquake Administration for supplying the Comprehensive Annual Prediction Draft Reports for many years. We also thank Prof. Jie Liu, Prof. Haikun Jiang and Mr. Long Jiang for the *R*-score evaluation calculation.

References

Center for Analysis and Prediction, CEA. 2002. *Study on the seismic tendency in China (for the year 2003)*. Beijing: Seismological Press. (In Chinese).

Center for Analysis and Prediction, CEA. 2003. *Study on the seismic tendency in China (for the year 2004)*. Beijing: Seismological Press. (In Chinese).

Chen, Q.F. (ed.). 2002a. *Earthquake cases in China (1992–1994)*. Beijing: Seismological Press. (In Chinese with English abstract).

Chen, Q.F. (ed.). 2002b. *Earthquake cases in China (1995–1996)*. Beijing: Seismological Press. (In Chinese with English abstract).

Chen, Q.F. (ed.). 2003. *Earthquake cases in China (1997–1999)*. Beijing: Seismological Press. (In Chinese with English abstract).

Chen, Y.T., H.D. Gu, and Z.X. Lu. 1979. Variations of gravity before and after Haicheng earthquake, 1975 and Tangshan earthquake. *Physics of Earth & Planetary Interiors* 18 (4): 330–338.

Chen, Y.T., Z.T. Wu, and L.L. Xie. 2003. Centennial national and institutional reports: Seismology and physics of the Earth's interior in China (Beijing). In *International handbook of earthquake and engineering seismology, Part B*, ed. W.H.K. Lee, H. Kanamori, P.C. Jennings, and C. Kisslinger, 1317–1321. Amsterdam: Academic Press.

Comprehensive Evaluation Summary Group for Annual Earthquake Key Risk Area, CEA. 2012. *Study on the seismic tendency in China (for the year 2013)*. Internal Report 2012. (In Chinese).

Comprehensive Evaluation Summary Group for Annual Earthquake Key Risk Area, CEA. 2013. *Study on the Seismic Tendency in China (for the year 2014)*. Internal Report 2013. (In Chinese).

Comprehensive Evaluation Summary Group for Annual Earthquake Key Risk Area, CEA. 2014. *Study on the seismic tendency in China (for the year 2015)*. Internal Report 2014. (In Chinese).

Ding, J.H. 2008. Geomagnetic low-point displacement phenomena and strong earthquake prediction research. *Chinese Journal of Radio Science* 23 (6): 1011–1017.

Holliday, J.R., J.B. Rundle, K.F. Tiampo, W. Klein, and A. Donnellan. 2006. Modification of the pattern informatics method for forecasting large earthquake events using complex eigenfactors. *Tectonophysics* 413: 87–91.

Huang, F.Q., M. Li, Y.C. Ma, Y.Y. Han, L. Tian, W. Yan, and X.F. Li. 2017. Studies on earthquake precursors in China: A review for recent 50 years. *Geodesy and Geodynamics*. http://dx.doi.org/10.1016/j.geog.2016.12.002.

Jiang, H.K. (ed.). 2014. *Earthquake cases in China (2003–2006)*. Beijing: Seismological Press. (In Chinese with English abstract).

Mulargia, F. 1997. Retrospective validation of the time association of precursors. *Geophysical Journal International* 131: 500–504.

Rundle, J.B., D.L. Turcotte, R. Shcherbakov, W. Klein, and C. Sammis. 2003. Statistical physics approach to understanding the multiscale dynamics of earthquake fault systems. *Reviews of Geophysics* 41: 1019. https://doi.org/10.1029/2003RG000135.

Shi, Y.L., J. Liu, and G.M. Zhang. 2000. The evaluation of Chinese annual earthquake prediction in the 1990s. *Journal of Graduate School, Academia Sinica* 17 (1): 63–69. (In Chinese with English abstract).

Shi, Y.J., Z.L. Wu, and L. Bai. 2004. Evaluation of annual prediction of seismicity tendency using Pearson test. *Journal of the Graduate School of the Chinese Academy of Sciences* 21 (2): 248–253. (In Chinese with English abstract).

Summary Group for the Annual Consultation, CEA. 2012. *Summary research report on the national key earthquake potential areas in 2013 (draft for review)*. Internal material of CEA.

Summary Group for the Annual Consultation, CEA. 2013. *Summary research report on the national key earthquake potential areas in 2014 (draft for review)*. Internal material of CEA.

Sun, Q.Z., and S.G. Wu. (ed.). 2007. *Development of the earthquake monitoring and prediction in China during 1966–2006*. Beijing: Seismological Press. (In Chinese).

Wu, F.T. 1997. The annual earthquake prediction conference in China (National Consultative Meeting on Seismic Tendency). *Pure and Applied Geophysics* 149: 249–264.

Wu, Z.L., J. Liu, C.Z. Zhu, C.S. Jiang, and F.Q. Huang. 2007. Annual consultation on the likelihood of earthquakes in continental China: Its scientific and practical merits. *Earthquake Research in China* 21: 365–371.

Xu, S.X. 1989. The evaluation of earthquake prediction ability. In *The practical research papers on earthquake prediction methods (Seismicity Section)*, ed. Department of Science, Technology and Monitoring, State Seismological Bureau, 586–589. Beijing: Seismo Press. (In Chinese).

Yin, X.C. (1987). A new approach to earthquake prediction. *Earthquake Research in China* 2(1): 1–7. (In Chinese with English abstract).

Yin, X.C., X.Z. Chen, Z.P. Song, and C. Yin. 1995. A new approach to earthquake prediction: the load/unload response ratio (LURR) theory. *Pure and Applied Geophysics* 145: 701–715.

Yin, X.C., L.P. Zhang, H.H. Zhang, C. Yin, Y.C. Wang, Y.X. Zhang, K.Y. Peng, H.T. Wang, Z.P. Song, H.Z. Yu, and J.C. Zhuang. 2006. LURR's 20 years and its perspective. *Pure and Applied Geophysics* 163: 2317–2341.

Yu, H.Z., R.F. Zhou, Q.Y. Zhu, X.T. Zhang, and Y.X. Zhang. 2016. Development of a combination approach for seismic hazard evaluation. *Pure and Applied Geophysics* 173(1): 221–233.

Zheng, Z.B., J. Liu, G.F. Li, J.D. Qian, and X.Q. Wang. 2000. Statistical simulation analysis of the correlation between the annual estimated key regions with a certain seismic risk and the earthquakes in China. *Acta Seismologica Sinica* 13 (5): 575–584.

Zhang, G.M., J. Liu, and Y.L. Shi. 2002. A scientific evaluation of annual earthquake prediction ability. *Acta Seismologica Sinica* 15 (5): 550–558.

Zhang, Y.X., F.W. Gao, J.J. Ping, and X.T. Zhang. 2013. A synthetic method for earthquake prediction by multidisciplinary data. *Natural Hazards* 69 (2): 1199–1209.

Zhang, Y.X., M.B. Yikilmaz, J.B. Rundle, X.C. Yin, Y. Liu, L.P. Zhang, and Z.J. Wang. 2015. Study of the potential earthquake risk in the western United States by the LURR method based on the seismic catalogue, fault geometry and focal mechanisms. *Pure and Applied Geophysics* 172 (8): 2265–2276.

Zhang, S.F., Z.L. Wu, and C.S. Jiang. 2016. Reducing false alarms of annual forecast in the central China north–south seismic belt by reverse tracing of precursors (RTP) using the pattern informatics (PI) 'Hotspots'. *Pure and Applied Geophysics*. https://doi.org/10.1007/s00024-016-1318-8.

Zhang, Y.X., C.Y. Xia, C. Song, X.T. Zhang, Y.J. Wu, and Y. Xue. 2017. Test of the predictability of the PI method for recent large earthquakes in and near the Tibetan Plateau. *Pure and Applied Geophysics*. https://doi.org/10.1007/s00024-017-1551-9.

Zhang Z.C. (ed.). 1988. *Earthquake cases in China (1966–1975)*. Beijing: Seismological Press. (In Chinese).

Zhang, Z.C. (ed.). 1990a. *Earthquake cases in China (1976–1980)*. Beijing: Seismological Press. (In Chinese).

Zhang, Z.C. (ed.). 1990b. *Earthquake cases in China (1981–1985)*. Beijing: Seismological Press. (In Chinese).

Zhang, Z.C. (ed.). 1999. *Earthquake Cases in China (1986–1988).* Beijing: Seismological Press. (In Chinese).

Zhang, Z.C. (ed.). 2000. *Earthquake cases in China (1989–1991).* Beijing: Seismological Press. (In Chinese).

Zhu, L.R., C.X. Zhu, S.Z. Hong, W.P. Qin, X.S. Zheng, and S.Q. Huang. 1991. Evaluation of earthquake prediction. In *Study on earthquake prediction method*, ed. Department of science, technology, and monitoring, state seismological Bureau, 35–45. Beijing: Seismological Press. (In Chinese).

Zhu, Y.Q., Y.M. Xu, Y.P. Lv, and T.M. Li. 2009. Relations between gravity variation of Longmenshan fault zone and Wenchuan Ms 8.0 earthquake. *Chinese Journal of Geophysics* 52 (10): 2538–2546.

Chapter 6
Structural Relationship Between the 2008 *M*8 Wenchuan and 2013 *M*7 Lushan Earthquakes Viewed by Fault-Zone Trapped Waves

Yong-Gang Li, Jin-Rong Su, Tian-Chang Chen and Peng Wu

Abstract We analyzed waveform data recorded at seismic network and temporal stations for aftershocks of the 2013 *M*7 Lushan earthquake and the 2008 *M*8 Wenchuan earthquake in both time and frequency. Prominent fault-zone trapped waves (FZTWs) with large amplitudes and long post-S coda durations are identified in seismograms at stations along the surface trace of the Xinkaidian fault (XF), but not at stations along the Dachuan-Shuangshi fault (DSF) to west and the Dayi fault (DF) to east within a thrust-folding region with multiple imbricated faults in Lushan area. Because the amplitude and dispersion of FZTWs are sensitive to the geometry and physical property of the fault-zone as well as the location of source and station relative to the fault zone, the recorded FZTWs infer a low-velocity waveguide existing along the XF. We interpret that this waveguide is formed by severely damaged rocks within the XF, which most likely ruptured at seismogenic depth in the 2013 *M*7 Lushan earthquake although the rupture did not reach the earth surface. 3D finite-difference simulations of these FZTWs show that seismic velocities within the XF rupture zone are reduced by ~40–50% from wall-rock velocities to form a remarkable low-velocity waveguide trapping seismic waves. We find that the FZTWs generated by Lushan aftershocks are also recorded at network stations located within Wenchuan rupture zones along the Yingxiu-Beichuan Fault (YBF) and Pengxian-Guanxian Fault (PGF) although there exists a ~45-km "seismic gap" between the Lushan and Wenchuan epicentral zones. Vice versa, FZTWs generated by Wenchuan aftershocks are recorded not only at stations within Wenchuan rupture zones but also at stations along the XF in Lushan area. Observations and finite-difference simulations show that a continuous waveguide extends along multiple faults of the south (LMSF) system. However, the

The original version of this chapter was revised: Incorrect figure has been replaced. The correction to this chapter is available at https://doi.org/10.1007/978-981-13-8015-0_10

Y.-G. Li (✉)
Department of Earth Sciences, University of Southern California, Los Angeles, CA 90089-0740, USA
e-mail: ygli@usc.edu

J.-R. Su · T.-C. Chen · P. Wu
Sichuan Earthquake Administration, Earthquake Administration China, Chengdu 610041, China
e-mail: sujr0816@163.com

Y.-G. Li (ed.), *Earthquake and Disaster Risk: Decade Retrospective of the Wenchuan Earthquake*, https://doi.org/10.1007/978-981-13-8015-0_6

waveguide effect (corresponding to the rock damage magnitude and velocity reduction) varies with the greater trapping efficiency along Wenchuan and Lushan rupture zones than the un-ruptured fault in the "seismic gap." Therefore, we consider that the 2008 $M8$ event and the 2013 $M7$ event consist of an earthquake sequence along the LMSF system, and the Lushan event is the largest aftershock of the Wenchuan earthquake.

Keywords Wenchuan earthquake · Lushan earthquake · South longmen shan fault system · Seismogenic fault · Rupture zone · Rock damage · Waveguide effect · Fault-zone trapped wave · Fault continuity and segmentation · Seismic gap · Earthquake sequence

6.1 Introduction

The April 20, 2013 M 7.0 Lushan earthquake was the most damaging earthquake since the 2008 M 8.0 Wenchuan earthquake and the 2010 $M7.1$ Yushu earthquake in China. The intensity map shows the maximum intensity of IX along a ~23-km-long and 11-km-wide northeast–southwest belt zone in the meizoseismal area along the south Longmen Shan fault (LMSF) (Han et al. 2014), consistent with rupture process inversion results (Chen et al. 2013a, b; Wang et al. 2013; Zhang et al. 2014). The LMSF system lies along the boundary between the Tibetan plateau and the Sichuan basin as a result of collision between these two crustal plates (Xu et al. 2008a) and consists of four major faults called the Wenchuan–Maowen fault (WMF), Yingxiu-Beichuan fault (YBF), Pengxian-Guanxian fault (PGF), and Dayi fault (DF) (Densmore et al. 2005). The $M7$ Lushan earthquake occurred ~80-km southwest of the epicenter of the 2008 $M8$ Wenchuan earthquake (Fig. 6.1). Although the YBF and PGF ruptured during the 2008 $M8$ Wenchuan earthquake with the unilateral rupture direction northeastward from Yingxiu to Qingchuan (Zhang et al. 2009), the Wenchuan shock increased the static stress on the southern fault segments of the LMSF, on which the 2013 $M7$ Lushan earthquake occurred (Chen et al. 2008; Parsons et al. 2008; Zhu and Miao 2015). The southern part of the LMSF system is composed of a series of imbricated reverse faults dipping to the northwest, including the Yanjing-Wulong fault (YWF), Dachuan-Shuangshi fault (DSF), Xinkaidian fault (XF) or called western Shangli fault (WSF), and the DF from the northwest to the southeast (Fig. 6.1). Lushan earthquake occurred at ~15-km depth just east of the DSF which was initially considered to rupture during the Lushan mainshock and to be the southwest extension of the PGF (Han et al. 2014).

Because no northeast-southwest striking surface rupture was reported after the 2013 Lushan earthquake, this event could not be obviously associated with any identified surficial geological faults in the epicentral area. Earthquake rupture studies show that the slip distribution of the Lushan event is dominated between 5- and 20-km-depth range, and the rupture does not reach the surface (Hao et al. 2013; Liu et al. 2013; Zhang et al. 2013a, b, 2014). Relocation of aftershocks using the double-difference relocation algorithm tomo-DD delineates a fault dipping to the

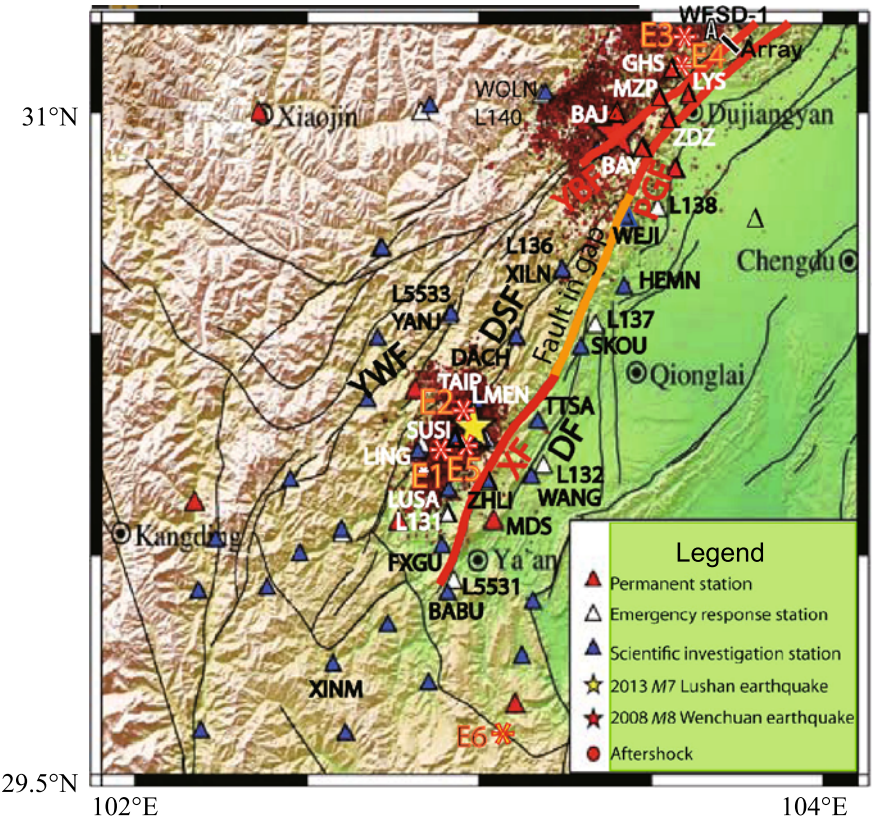

Fig. 6.1 Tectonic settings of the south Longmen Shan fault zone (adapted from Fang et al. 2015). The inset map shows the location of the study region in the Chinese mainland. Large stars indicate the epicenters of the 2008 *M*8.0 Wenchuan (red) and 2013 *M*7.0 Lushan (yellow) earthquakes as well as the 1970 M6.2 Dayi earthquake (brown). Red dots represent aftershocks of the Lushan and Wenchuan aftershocks. Black lines indicate the main faults. YWF: Yanjing-Wulong fault; DSF: Dachuan-Shuangshi fault; XF: Xinkaidian fault; DF: Dayi fault; PGF: Pengxian-Guanxian fault; YBF: Yingxiu-Beichuan fault. Red lines denote rupture zones along the YBF and PGF in the 2008 Wenchuan earthquake, and along the XF in the 2013 Lushan earthquake. Brown color line denotes the un-ruptured (developing) fault in a "seismic gap". Permanent seismic stations are shown as red triangles. Temporary seismic stations, deployed in the emergency response phase and the scientific investigation phase, are shown as white and blue triangles, respectively. Seismograms recorded at stations with names are used in this study. Small stars with names E1 to E5 are aftershocks occurring within Lushan and Wenchuan rupture zones, and E6 is a local earthquake far south of Lushan epicentral zone, waveforms from them are analyzed in this article. A black bar across the YBF denotes the linear seismic array deployed immediately after the 2008 M8 Wenchuan earthquake to record FZTWs generated by aftershocks in the early stage. The WFDS-1 is a scientific borehole drilled through the Wenchuan rupture zone along the YBF at shallow depth

northwest, and the dip angle of the principal slip plane is about 40° (Su et al. 2013; Han et al. 2014), close to that determined by waveform inversions using regional and teleseismic seismograms. These results reveal that the Lushan earthquake and aftershocks occurred between the DSF and the DF that are both active faults (Yang et al. 2005; Densmore et al. 2007). Based on aftershock distribution relative to the anticline, Xu et al. (2013) speculated that the Lushan earthquake occurred on a propagating blind thrust fault underneath a growing fold, while Zhang and Lei (2013) inferred that the Lushan earthquake probably occurred at the intersection of the detachment surface and the base of the southern part of the LMSF system. Xu and Xu (2014) found that the landslide density changes suddenly about 1 to 2-km northwest from the Xinkaidian fault (XF) or called the western Shangli fault (WSF), and the landslide density on the footwall is clearly lower than that of the hanging wall of the XF (WSF). Therefore, they infer that the seismogenic fault for the Lushan earthquake is neither the DSF nor the DF, rather probably the XF (or called WSF) located between these two faults. The XF shows an evident linear trace on the earth surface although the coseismic slip did not propagate upward to the ground during the 2013 Lushan earthquake. Aftermath, the precisely relocated aftershocks define a rupture that extends between approximately 5–20 km in depth and 55 km along the strike of the fault plane, with the most aftershocks confined along a northwest-dipping (at ~50°) blind thrust fault which upward extrapolation roughly aligns with the surface trace of the XF argued by Fang et al. (2015) rather than the DSF and the DF interpreted previously by Zhang and Lei (2013) and Su et al. (2013). The aftershock relocation results in conjunction with geologic investigations, focal mechanism solutions, and source rupture models support the hypothesis that the seismogenic structure of the 2013 Lushan earthquake is a blind thrust fault most likely connecting the XF although the rupture along it did not reach the ground surface. However, the genetic fault of the Lushan earthquake needs to be further confirmed.

After the 2013 M7.0 Lushan earthquake, another question whether this event is a strong aftershock of the 2008 M8.0 Wenchuan earthquake or an independent event was raised publicly. The hot debates focus on whether the Lushan quake ruptured one of the asperities which were left unbroken in the 2008 Wenchuan earthquake. Zhang et al. (2013a) argued that the Lushan event is an independent mainshock having its own aftershock sequence because the ruptures produced by the Wenchuan and Lushan events do not overlap each other and occurred on different faults. Du et al. (2013), Liu et al. (2013) held the same view that the Lushan earthquake is a new event because there is a ~45-km-long "seismic gap" between Wenchuan and Lushan epicentral zones. Pei et al. (2014), Fang et al. (2015) found that the weak and ductile materials in the upper crust between Wenchuan and Lushan rupture zones resulted in "seismic gap" in between and stop of the Lushan rupture in front of this gap.

On the other hand, Chen et al. (2013a, b), Wang et al. (2013) assumed that the 2013 M7 Lushan earthquake was the largest aftershock of the 2008 M8 Wenchuan earthquake in consideration of their close hypocentral locations, the similar thrusting mechanisms, and the ruptured area of the Lushan earthquake on the fault segments with increase in Column static stress caused by the 2008 Wenchuan mainshock (Jia

et al. 2014). Parsons and Segou (2014), and Wang et al. (2013) argued that the 2013 Lushan event was a delayed aftershock triggered by the 2008 Wenchuan mainshock. Zhu (2016) showed that the Wenchuan-Lushan earthquake sequence is well-satisfied statistical laws, namely the Gutenberg-Richter relation, modified Omori-Utsu law and Båth's law. Therefore, he concluded that the 2013 Lushan event was one of aftershocks of the 2008 Wenchuan mainshock. However, the question whether the 2013 $M7$ Lushan event is a strong aftershock of the 2008 $M8$ Wenchuan earthquake or an independent event remains.

A similar case was met in New Zealand's South Island. Approximately 6 months after the $M7.1$ Darfield earthquake occurred on the Greendale fault (GF) on September 4, 2010, the $M6.3$ Christchurch earthquake occurred on the Port Hills fault (PHF) on February 22, 2011, which epicenter is ~40-km east of the epicenter Darfield earthquake (Quigley et al. 2012). The close temporal coincidence of two major earthquakes on faults that are separated by distances of ~10–15 km between the GF and the PHF raises important questions about fault damage zone characteristics, fault geometries and crustal structure in the intervening areas as well as whether the $M6.3$ Christchurch earthquake is an aftershock of the $M7.1$ Darfield earthquake or an independent earthquake. However, the Christchurch earthquake and other earthquakes following the Darfield earthquake are forthwith referred to as aftershocks based on statistical merit (Shcherbakov et al. 2012). In order to evaluate GF-PHF "connectivity" with relevance for understanding fault evolution and earthquake potential in the area, Li et al. (2014a) used FZTWs to characterize the subsurface damage structure of rupture zones along the GF and the PGF, and the "seismic gap" between the two faults ruptured during the 2010 $M7.1$ Darfield and the 2011 $M6.3$ Christchurch earthquakes. Observations and finite-difference simulations of the FZTWs generated by Darfield aftershocks and Christchurch aftershocks illuminate a continuous low-velocity waveguide extended from the Darfield rupture zone along the GF through the "seismic gap" to the Christchurch rupture zone along the PHF. However, the waveguide effect varies along multiple faults with the greater trapping efficient along rupture zones of the GF and the PHF than that along the blind faults in the "seismic gap". Structurally, the results from FZTWs support that the $M6.3$ Christchurch earthquake is an aftershock of the $M7.1$ Darfield earthquake.

In our present study, we use FZTWs generated by aftershocks of the 2013 Lushan earthquake and recorded at seismic stations located along multiple faults of the south Longmen Shan fault system to identify the seismogenic fault of the 2013 $M7$ Lushan earthquake among multiple imbricated thrust faults in the complicated fold-faulting region. Because the FZTWs generated by Lushan aftershocks were also recorded at stations of Zipingpu dam seismic network located within rupture zones of the 2008 $M8$ Wenchuan earthquake, and vice versa the FZTWs generated by Wenchuan aftershocks were recorded at stations close to the XF in Lushan area. Therefore, we are able to investigate the fault continuity and segmentation of the south Longmenshan fault system using the recorded FZTWs. The variations of fault rock damage magnitudes and waveguide effects along multiple faults inferred by FZTWs help us better understand the structural relationship between the Lushan and Wenchuan events in an earthquake sequence on the LMSF system. This study

is also helpful for monitoring the fault evolution and earthquake potential in this earthquake-prone region.

6.2 The Data and FZTW Waveform Analysis

In order to provide invaluable data for scientific studies related to hazard, tectonics, and earthquake physics of the M_S 7.0 Lushan earthquake, multiple governmental and academic institutions deployed seismic instruments near the epicenter within the first few days after the mainshock to record aftershocks for improvement of earthquake detection and location capabilities (e.g., Fang et al. 2015; Su et al. 2013; Zhao et al. 2013; Zhen et al. 2013). A total of 50 temporary seismograph stations were deployed (Fig. 6.1). Both the permanent stations and portable stations enable detection and location of a complete earthquake catalog down to approximately M_L 0.8. Within a year after the M 7.0 Lushan earthquake on April 11, 2013, about 14,500 aftershocks with magnitudes M 0.5–5.6 occurred, including six $M \geq 5$ and fifty-four $M \geq 4$ events in a ~40-km-long belt epicentral zone.

We examined waveform data recorded for a part of aftershocks with magnitudes of M3.5–4.5 and with good signal-to-noise ratio recorded at stations named in Fig. 6.1. We identify fault-zone trapped waves (FZTWs) on the basis of extended coda waves with large amplitudes that follow the S-arrival on seismograms recorded at stations within the fault zone (e.g., Li and Leary 1990; Li et al. 1990, 1994, 2000, 2004). Generally, the coda length of the coherent guided waves generated by earthquakes increases with increasing hypocentral distance within the low-velocity fault zone between the earthquake source and the recording site (e.g., Li and Malin, 2008; Li et al. 2003, 2012, 2016). In addition, the difference between the P- and S-arrivals also increases with increasing hypocentral distances. Empirical studies have shown that the ratio of the post-S coda time to the time difference between the P- and S-arrivals $(t_C - t_S)/(t_S - t_P)$ is approximately higher than 1.2 for prominent guided waves well generated by aftershocks and well recorded at stations as both the source and receiver are located within the low-velocity fault zone (Li et al. 2014a, b, 2016). t_p and t_s are the P- and S-arrival times; $t_C - t_S$ is the post-S coda duration time in which the amplitudes of FZTWs are above twice those of the background signals in the late coda. In our president study, we use the ratio of post-S coda time to S–P arrival time difference $(t_C - t_S)/(t_S - t_P)$ higher than 1.0 to identify the trapped waves generated by aftershocks and recorded at stations located on or close to the low-velocity rupture zones along the seismogenic faults of the Lushan and Wenchuan earthquakes.

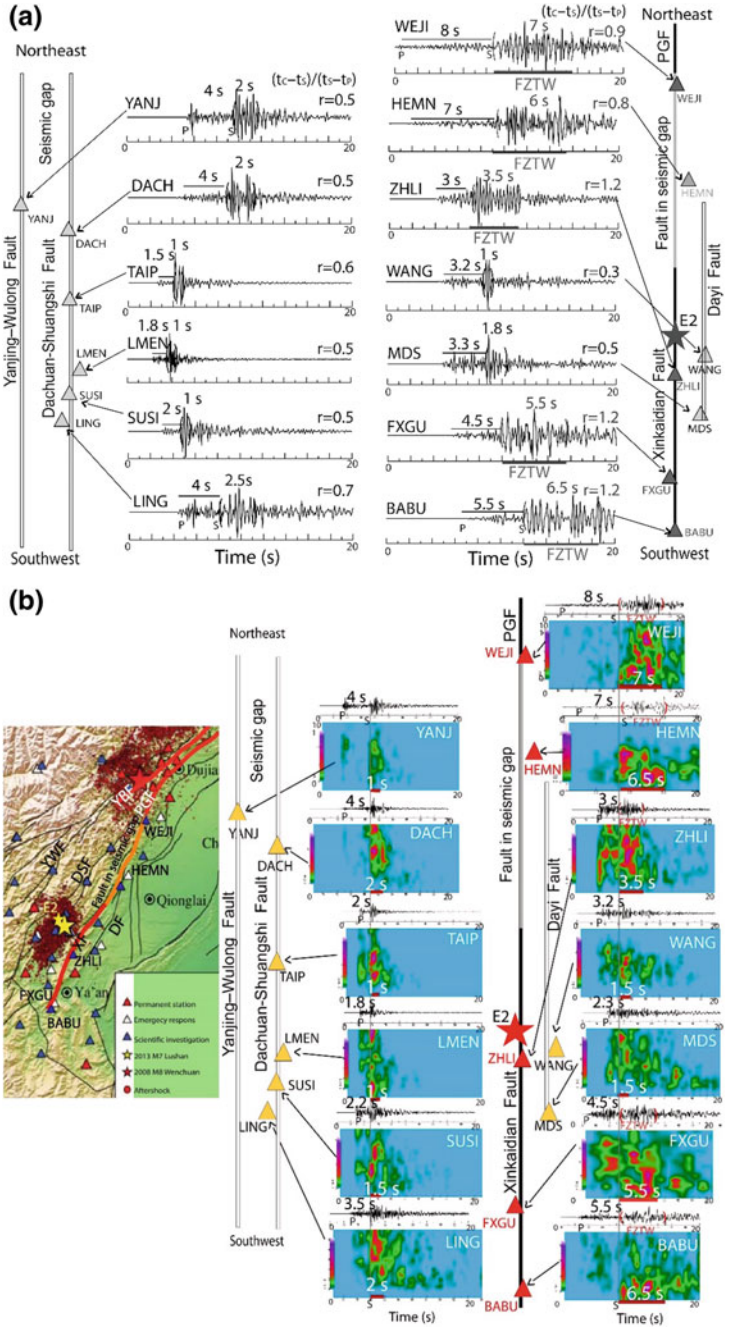
(a)
Northeast
Seismic gap
Yanjing–Wulong Fault
Dachuan-Shuangshi Fault
YANJ
DACH
TAIP
LMEN
SUSI
LING
Southwest
Time (s)
(tc−ts)/(ts−tp)
r=0.5
r=0.6
r=0.7
r=0.9
r=0.8
r=1.2
r=0.3
FZTW
WEJI
HEMN
ZHLI
WANG
MDS
FXGU
BABU
PGF
Fault in seismic gap
Dayi Fault
Xinkaidian Fault
E2
(b)
Dujia
TBF
PGF
WEJI
Ch
YMF
DSF
HEMN
Qionglai
DF
ZHLI
FXGU
Ya'an
BABU
Permanent station
Emergency respons
Scientific investigation
2013 M7 Lushan
2008 M8 Wenchuan
Aftershock

◀**Fig. 6.2** **a** Vertical-component seismograms recorded at thirteen seismic stations (triangles with their names) for aftershock E2 (star) occurring within Lushan rupture zone. Stations ZHLI, FXGU, and BABU are close to the surface trace of the XF (solid line) that ruptured in the 2013 $M7$ Lushan earthquake. Stations WEJI and HEMN are close to the un-ruptured fault (gray line) in the ~45-km-long "seismic gap" between Wenchuan and Lushan epicentral zones. Stations WANG and MDS are located along the DF (open line). Stations DACH, TAIP, LMEN, SUSI and LING are along the DSF while station YANJ is at the YWF (open lines). Assuming that the XF in Lushan area connects the un-ruptured fault in "seismic gap," which runs northward to connect the PGF in Wenchuan. Seismograms have been low-pass (<5 Hz) filtered. The measured post-S coda duration time, P-to-S time, and their ratio at each station are shown in the figure. **b** Spectral amplitudes of vertical-component seismograms (1–10 Hz) at thirteen stations for aftershock E2 (small star in the map). Spectral contours are normalized with respect to the maximum amplitude among them between 0 and 1 (colored from green to red). P-to-S time and post-S coda duration time measured at each station are plotted in the figure. Prominent FZTWs with large amplitudes and long post-S coda durations (within red brackets and marked by red bars) with respect to P-to-S times are observed in seismograms and spectral amplitudes at stations ZHLI, FXGU, BABU, HEMN, and WEJI (labeled in map to left) along the XF and the un-ruptured fault segment in "seismic gap," but much shorter post-S coda durations with respect to P-to-S times at other stations

6.2.1 The FZTWs Generated by Aftershocks Occurring Within Lushan Rupture Zone

First, we examine the data recorded at stations deployed in the epicentral region of the 2013 $M7$ Lushan earthquake and in the ~45-km-long "seismic gap" between Wenchuan and Lushan epicentral zones for Lushan aftershocks. For example, Fig. 6.2a shows seismograms and normalized spectral energy recorded at thirteen stations for a $M3.8$ aftershock (labeled by E2 in Fig. 6.1) occurring at 16-km depth with its epicenter close to the Lushan earthquake epicenter (latitude: 30.30°N, longitude: 102.99°E, depth: 14–16 km) between surface traces of the DSF and XF. The time, location, and magnitude of this aftershock (E2) are shown in Tables 6.1 and 6.2. We observe prominent FZTWs characterized by large amplitudes and long post-S coda durations (3.5, 5.5, and 6.5 s) with respect to P-to-S times (3.0, 4.5, and 5.5 s) at stations ZHLI, FZGU, and BABU located close to the surface trace of the XF (or called WLF). The ratios of $(t_C - t_S)/(t_S - t_P)$ at three stations are ~1.2, showing that FZTWs were well generated by aftershock E2 and well recorded at these stations. We interpret that there is a remarkable low-velocity waveguide along the XF within which both aftershock and stations are located. The data recorded at stations HEMN and WEJI, located near the un-ruptured fault (brown line in Fig. 6.1) in "seismic gap" between Lushan and Wenchuan epicentral zones, show 6 and 7 s post-S coda durations with respect to the P-to-S times 7.0 and 8.0 s. The ratios of $(t_C - t_S)/(t_S - t_P)$ at two stations are ~0.8–0.9, suggesting that the FZTWs generated by Lushan aftershock E2 occurring on the XF propagated to two stations along an un-ruptured fault in "gap" but with degradation. The post-S coda durations, P-to-S times and their ratios at these stations for Lushan aftershock E2 are shown in Table 6.1.

In contrast, stations WANG and MDS located close to the DF show much shorter post-S coda durations (1.0 and 1.8 s) with respect to P-to-S times (3.2 and 3.3 s) for

Table 6.1 Time, location, and magnitude of aftershocks, and measurements at stations in Lushan area and seismic gap

No.	Date	Time	Lat.	Long.	Depth	M_D	Post-S Coda Duration(s)	P-to-S time (s)	$(t_C - t_S)/(t_S - t_P)$ ratio
	(yy/mm/dd)	(hh:mm:ss)	(°)	(°)	(km)		WEJ(138)/HEMN/SKOU(137)/TTSA/ZHLI/FXGU(L131)/BADU(L5531)		
E1	2013/05/04	19:29:48	30.286	102.894	21	3.7	7.0/–/7.0/–/–/3.8/6.0	9.0/–/7.5/–/–/3.8/6.0	0.8/–/0.9/–/–/1.0/1.0
E2	2013/08/18	12:55:27	30.320	102.998	16	3.8	7.0/6.0/–/–/3.5/5.5/6.5	8.0/7.0/–/–/3.0/4.5/5.5	0.9/0.8/–/–/1.2/1.2/1.2
E3	2014/04/02	14:04:42	31.173	103.599	18	4.2	– /–/10/12/–/16/17	– /–/10/12/–/16/17	– /–/1.0/1.0/–/1.0/1.0
E4	2014/06/11	22:46:42	31.257	103.594	18	3.7	– /8.0/–/–/14/13/16	– /10/–/–/15/16/18	– /0.8/–/–/0.9/0.8/0.9
E5	2014/06/23	19:57:48	30.302	102.997	16	3.7	– /–/–/2.3/4.0/6.0/–	– /–/–/2.3/2.8/5.0/–	– /–/–/1.0/1.4/1.2/–
E6	2014/07/11	19:56:42	29.638	103.094	25	4.0	– /6.0/–/–/4.0/2.0/2.0	– /14/–/–/8.0/7.0/5.5	– /0.4/–/–/0.5/0.3/0.4_

Table 6.2 Time, location, and magnitude of aftershocks, and measurements at stations of Zipingpu dam network

No	Date	Time	Lat.	Long.	Depth	M_D	Post-S Coda duration (s)	P-to-S time(s)	$(t_C - t_S)/(t_S - t_P)$ ratio
	(yy/mm/dd)	(hh:mm:ss)	(°)	(°)	(km)		BAY/ZDZ/MZP/LYS		
E1	2013/05/04	19:29:48	30.286	102.894	21	3.7	8.0/11/10/–	10/11/12/–	0.8/1.0/0.9/–
E2	2013/08/18	02:55:27	30.320	102.998	16	3.8	– /–/–/–	– /–/–/–	– /–/–/–
E3	2014/04/02	14:04:42	31.173	103.599	18	4.2	5.5/3.6/3.8/3.8	4.2/2.7/2.5/2.4	1.3/1.3/1.6/1.6
E4	2014/06/11	22:46:42	31.257	103.594	18	3.7	4.0/4.0/4.0/–	4.0/3.2/2.5/–	1.0/1.2/1.6/–
E5	2014/06/23	19:57:48	30.302	102.997	16	3.7	10/11/13/13	11/12/13/13	0.9/0.9/1.0/1.0
E6	2014/07/11	19:56:42	29.638	103.094	25	4.0	6.0/4.0/2.0/2.0	8.0/8.0/9.0/4.0	0.2/0.4/0.5/0.2

aftershock E2. The ratios of $(t_C - t_S)/(t_S - t_P)$ at two stations are 0.3–0.5, showing that FZTWs generated by aftershock E2 were not recorded at these two stations along the DF. Similarly, seismograms recorded at stations DACH, TAIP, LMEN, SUSI, LING, and YANJ located close to the DSF or YWF show 1 to 2.5-s post-S coda durations with respect to 1.5–4.0 s P-to-S times. The ratios of $(t_C - t_S)/(t_S - t_P)$ at five stations are 0.5–0.7, showing that the FZTWs generated by aftershock E2 were also not well recorded at stations along the DSF and YWF. These observations suggest that there is lack of low-velocity waveguides between aftershock E2 and these stations located along either the DF or the DSF.

Our observations of prominent FZTWs at stations close to the surface trace of the XF but not at stations close to the DF, DSF, and YWF infer that a remarkable low-velocity waveguide exists along the XF within which fault rocks were severely damaged during dynamic rupture in the 2013 $M7$ Lushan earthquake. Therefore, we interpret that the XF is most likely a seismogenic fault of the $M7$ Lushan earthquake among multiple imbricated thrust faults in Lushan area. Our interpretation is consistent with the speculation of Xu et al. (2013), Xu and Xu (2014) that the Lushan earthquake was spawned by a blind-thrust fault beneath the western Shangli fault (WSF), called Xinkaidian Fault (XF) here, which is located between the DF and DSF inferred by aftershock distribution relative to the anticline and the spatial distribution pattern of landslides. Based on the relocation of Lushan aftershocks, Fang et al. (2015) claim that the 2013 Lushan event occurred on a northwest-dipping deep blind fault which upward extrapolation to the ground surface aligns with the surface trace of the XF. Although the slip did not reach the ground surface in the 2013 $M7$ mainshock, the top portion of the pre-existing XF might be experienced minor damage due to strong shaking to provide a conduit with moderate low velocities to guide FZTWs generated by aftershock E2 at seismogenic depth to stations close to its surface trace.

In this example, we observe that post-S coda durations of FZTWs recorded at stations ZHLI, FXGU, and BABU along the XF increase from 3.5 s to 6.5 s with hypocentral distances increasing from 23 to 42 km (corresponding to P-to-S times of 3.0 s to 5.5 s registered at these stations) from aftershock E2. This observation suggests that the low-velocity waveguide extends ~40-km along the XF between the hypocenter of aftershock E2 at 16-km depth and station BABU at the surface. On the other hand, the $(t_C - t_S)/(t_S - t_P)$ ratios of FZTWs recorded at stations HEMN and WEJI are 0.8–0.9, suggesting that the un-ruptured fault in "seismic gap" has weaker waveguide effect than the XF does. In the following examples, we study if the waveguide extends continuously along the XF ruptured in the 2013 Lushan earthquake through this un-ruptured fault in "seismic gap" to the PGF ruptured in the 2008 Wenchuan earthquake. The most recent 1970 M_S 6.2 Dayi Earthquake occurred within the "seismic gap" between Wenchuan and Lushan rupture zones (Fig. 6.1), which is supposed to have released, at least in part, the accumulated strain in this area (Yang et al. 2005; Su et al. 2013; Pei et al. 2014).

Figure 6.3 exhibits seismograms and normalized spectral energy at seven temporary stations deployed in the 2013 Lushan epicentral area and six permanent stations of Zipingpu dam seismic network in the southern epicentral zone of the 2008

Wenchuan earthquake for an aftershock E5 in Fig. 6.1 occurring at 16-km depth nearly south of the 2013 *M*7 Lushan epicenter. We observe prominent FZTWs characterized by long post-S coda durations (2.2, 4.0, and 6.0 s) with respect to the P-to-S times (2.2, 2.8, and 5.0 s) at stations TTSA, ZHLI, and FXGU close to the surface trace of the XF. The ratios of $(t_C - t_S)/(t_S - t_P)$ at three stations are 1.0, 1.4, and 1.2, showing that FZTWs were well generated by aftershock E5 and recorded at these stations because of both the source and receivers located within the low-velocity waveguide along the XF. Station TTSA located near the north end of XF rupture zone. In contrast, the measured $(t_C - t_S)/(t_S - t_P)$ ratios for seismograms recorded at stations TAIP, LMEN, LUSA, and MDS located along the DSF and DF are 0.6–0.7, showing that the FZTWs generated by Lushan aftershock E5 were not observed clearly at these stations. These observations infer that the low-velocity waveguide formed by severely damaged rocks extends along the XF rather than the DSF and DF. Therefore, the XF among multiple imbricated faults in this thrust-folding region is most likely a seismogenic fault ruptured in the 2013 *M*7 Lushan earthquake.

We further examine the data recorded at stations of Zipingpu dam seismic network approximately 80-km northeast of the 2013 *M*7 Lushan earthquake (refer to Fig. 6.1). The network stations are installed with FBS-3B sensors with 0.05–40 Hz frequency band. The 24-bit EDAS seismographs work continuously at 100 samples per second. All these stations are located on outcrops of hard rock at the ground surface. Stations MZP and LYS are close to the escarpments of 5–7 m along the south YBF in Shenxigou valley, which were produced by the 2008 *M*8 earthquake (Xu et al. 2009; Zhang et al. 2010). Station BAJ is near the southernmost part of the YBF where no obvious slips were found at the surface after the 2008 Wenchuan mainshock. Stations BAY and ZDZ are located on the hanging wall close to the surface rupture of the PGF. Station GHS is located on the hanging wall of the YBF and ~6-km northwest of its surface rupture. Rupture zones along the YBF and PGF connect at depth (Densmore et al. 2007; Zhu and Miao, 2015; Li et al. 2012, 2014b).

We observe the FZTWs generated by Lushan aftershock E5 occurring on the XF at stations BAY, ZDZ, MZP, and LYS located within southern Wenchuan rupture zones along the YBF and PGF (Fig. 6.3). The ratios of $(t_C - t_S)/(t_S - t_P)$ are 0.9–1.0 measured from 10 to 13-s post-S coda durations and 11–13 s P-to-S times at four stations, showing that the FZTWs generated by E5 propagated from the Lushan rupture zone along the XF, through un-ruptured faults in the ~45-km "seismic gap" to Wenchuan rupture zones along the YBF and PGF although they were degraded when they passed the "gap." Because the post-S coda durations of these FZTWs generated by aftershock E5 increase with their travel distances to stations along the Lushan and Wenchuan rupture zones, we suggest that a roughly continuous low-velocity waveguide extends from the XF to the YBF/PGF, but the waveguide effect varies along multiple faults with weaker trapping efficiency along the un-ruptured fault (having less damage magnitude of fault rocks) in the "seismic gap." In contrast, seismograms recorded at station GHS and BAJ show much shorter post-S coda durations (4–5 s) with respect to the P-to-S times (10–15 s) for this aftershock. The corresponding $(t_C - t_S)/(t_S - t_P)$ ratio is 0.3–0.4, indicating that FZTWs are not recorded at these two stations located away from Wenchuan surface ruptures.

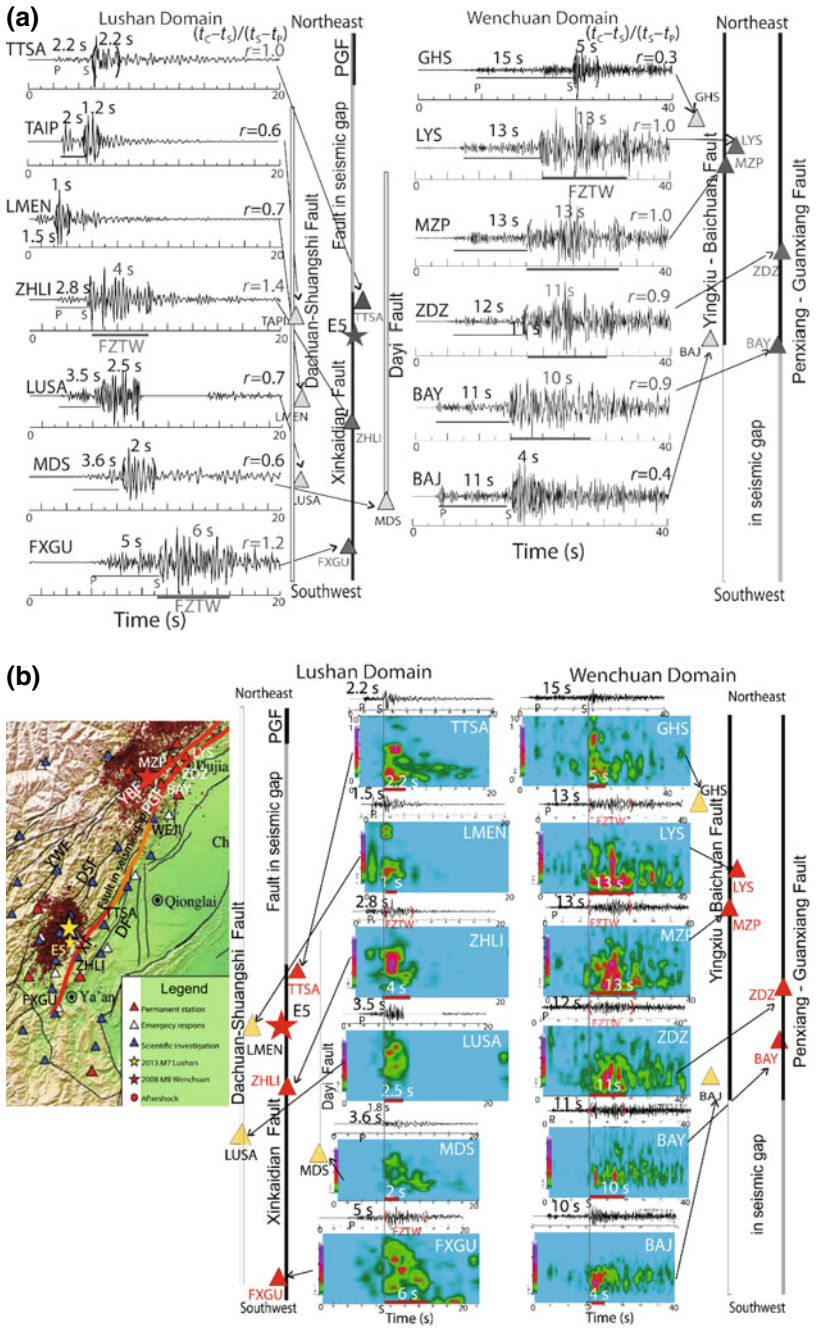
(a)
Lushan Domain
Northeast
Wenchuan Domain
Northeast
TTSA
TAIP
LMEN
ZHLI
LUSA
MDS
FXGU
GHS
LYS
MZP
ZDZ
BAY
BAJ
FZTW
PGF
Fault in seismic gap
Dachuan-Shuangshi Fault
Xinkaidian Fault
Dayi Fault
E5
Yingxiu - Baichuan Fault
Penxiang - Guanxiang Fault
in seismic gap
Southwest
Southwest
Time (s)
Time (s)
(b)
Lushan Domain
Wenchuan Domain
Northeast
Northeast
Qingjia
Qionglai
Ya'an
Legend
Permanent station
Emergecy respons
Scientific investigation
2013 M7 Lushan
2008 M8 Wenchuan
Aftershock
Southwest
Southwest
Time (s)
Time (s)

◀**Fig. 6.3** **a** Vertical-component seismograms recorded at seven stations (triangles) deployed in Lushan domain, and six permanent stations in Wenchuan domain for Lushan aftershock E5 (star) occurring on the XF. Prominent FZTWs with large amplitudes and long post-S coda durations with respect to P-to-S times are observed at stations ZHLI, FXGU, and TTSA close to the XF (solid line), but short post-S coda durations with respect to P-to-S times at stations TAIP, LMEN, LUSA, and MDS located along the DSF and the DF (open lines). FZTWs are also observed at stations MZP, LYS, ZDZ, and BAY of Zipingpu dam seismic network close to surface ruptures along the YBF and the PGF (solid lines), but not at stations GHS and BAJ away from Wenchuan surface ruptures. The un-ruptured fault segment (gray line) in the ~45-km-long "seismic gap" is marked by a gray line. Other notations are same as in Fig. 6.2a. **b** Normalized spectral amplitudes of vertical-component seismograms at six stations in Lushan domain and six stations in Wenchuan domain for Lushan aftershock E5 (small star in the map). Prominent FZTWs with large amplitudes and long post-S coda durations (within red brackets and marked by red bars) with respect to P-to-S times are observed in seismograms and spectral amplitudes at stations ZHLI, FXGU, and TTSA along the XF (solid line), but much shorter post-S coda durations with respect to P-to-S times at stations along the DSF and DF (open lines) in Lushan domain. In Wenchuan domain, FZTWs generated by Lushan aftershock E5 arrive at stations MZP, LYN, ZDZ, and BAY close to the ruptured YBF and the PGF (solid lines), but not at stations GHS and BAJ located west of the YBF. Other notations are same as in Fig. 6.2b

In the next example, we analyze the data recorded at six seismic stations located in Lushan epicentral area and in the 'seismic gap," and six stations located in southern Wenchuan rupture zones for Lushan aftershock E1 occurring at 21-km depth and ~4-km southwest of the Lushan $M7$ epicenter (Fig. 6.4). The post-S coda durations are measured to be 3.2 s and 6.0 s with respect to P-to-S times 3.8 and 6.0 s at stations L131 and L5531 located close to the surface trace of the XF. The ratios of $(t_C - t_S)/(t_S - t_P)$ at two stations are ~1.0, smaller than the ratio (1.2) registered at the co-located stations FXGU and BABU for aftershock E2 occurring at 16-km depth, suggesting that the low-velocity waveguide along the XF rupture zone probably diminishes below 16-km. In contrast, short post-S coda durations (2.0–6.0 s) with respect to the P-to-S times (4.2–8.0 s) are registered at station L136 along the DSF, station L5533 on the YWF and station L132 along the DF for Lushan aftershock E1. The $(t_C - t_S)/(t_S - t_P)$ ratios at three stations are 0.4–0.6, suggesting that there are no remarkable low-velocity waveguides on the DF, DSF, and YWF because they did not rupture in the 2013 $M7$ Lushan earthquake. Therefore, we interpret that they are unlike to be the seismogenic causal fault for the 2013 $M7$ Lushan earthquake. The $(t_C - t_S)/(t_S - t_P)$ of FZTWs recorded at station L137 close to the un-ruptured fault in the "seismic gap" is measured to be 0.9, larger than ratios (0.4–0.6) at stations L5533, L136, and L132 located close to the YWF, DSF, and DF, but smaller than the ratio (1.0) at stations L131 and L5531 close to the XF. The FZTWs generated by E1 are well recorded at station L137 but not at station L136, suggesting that the low-velocity waveguide on the XF connects to the un-ruptured fault (marked by a brown line on the map in Fig. 6.1) rather than the DSF in the "seismic gap" between Lushan and Wenchuan rupture zones.

In south Wenchuan rupture zones, we observe 8 to 11-s post-S coda durations of FZTWs with respect to 10–11 s P-to-S times are registered at stations L138,

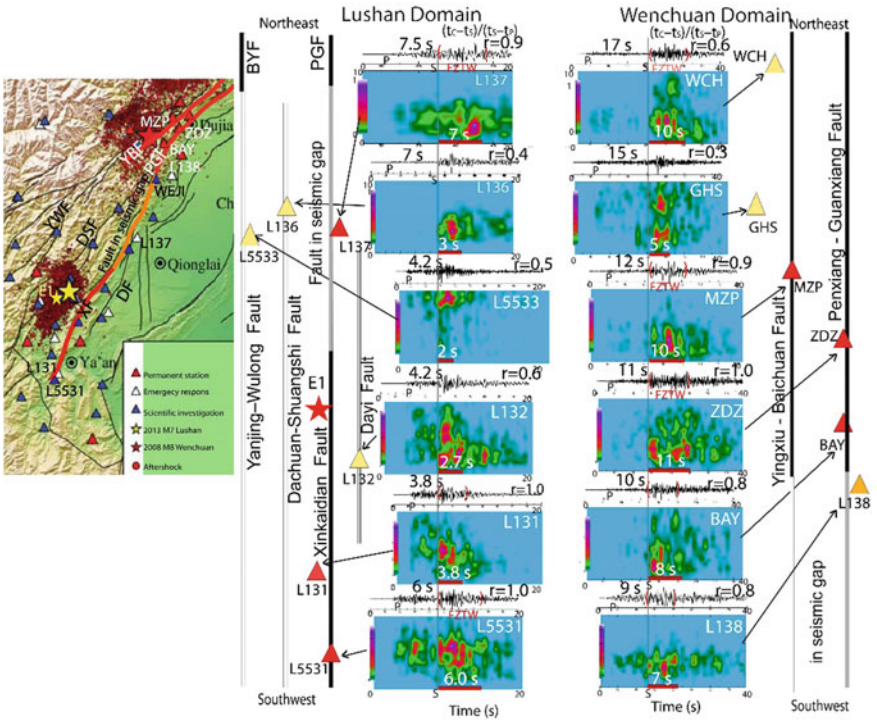

Fig. 6.4 Vertical-component seismograms and normalized spectral amplitudes at twelve seismic stations in Lushan region, "seismic gap" and Wenchuan region for Lushan aftershock E1 (small star in the map) occurring at depth of 21 km with its epicenter between the XF and DSF. FZTWs (marked by red brackets and bars) are observed at stations L131, L5531, and L137 located close to the surface trace of the XF and the un-ruptured fault (marked by a brown line) in the "gap". In contrast, the FZTWs generated by E1 are not obvious at stations L136 on the DSF, L5533 on the YWF, and L132 close to the DF, respectively. However, the FZTWs generated by Lushan aftershock E1 arrived at stations MZP, ZDZ, BAY, and L138 (labeled in the map to left) located within Wenchuan rupture zones along the YBF and the PGF, but did not arrive at station GHS located away from the YBF. Other notations are same as in Fig. 6.3

BAY, ZDZ, and MZP for Lushan aftershock E1. The ratios of $(t_C - t_S)/(t_S - t_P)$ of FZTWs registered at three stations for this deep event are 0.9–1.0. In contrast, the $(t_C - t_S)/(t_S - t_P)$ ratios are 0.3–0.6 registered at stations GHS and WCH located away from Wenchuan rupture zones. These observations further suggest that the low-velocity waveguide extends continuously from Lushan rupture zone on the XF through the un-ruptured fault in "seismic gap" to Wenchuan rupture zones on the PGF and YGF at depth above ~16 km. However, the waveguide shows the stronger trapping effect on ruptured faults either in the 2008 $M8$ Wenchuan or in the 2013 $M7$ Lushan earthquake than the un-ruptured fault in the "seismic gap." We tentatively interpret that this un-ruptured fault is possibly a developing fault, within which rocks experienced damage during the 1970 M_S 6.2 Dayi earthquake occurred only 46 years

ago, that is supposed to have released, at least in part, the accumulated strain in this area (Yang et al. 2005; Su et al. 2013; Pei et al. 2014). In addition, this developing fault might experience strong shaking during the 2008 Ms 8.0 Wenchuan and the 2013 M_S 7.0 Lushan earthquakes (Fig. 6.4).

6.2.2 *The FZTWs Generated by Aftershocks Occurring Within Wenchuan Rupture Zone*

In this section, we examine the data recorded for aftershocks occurring within south Wenchuan rupture zones. Figure 6.5 exhibits seismograms and normalized spectral energy recorded at six stations of Zipingpu dam seismic network and at eleven stations in the Lushan epicentral area as well as "seismic gap" for an aftershock E3 occurring at 18-km depth within Wenchuan rupture zones. Prominent FZTWs with long post-S coda durations (3.6–5.5 s) with respect to P-to-S times (2.4–4.2 s) are observed at stations MZP, LYS, ZDZ, and BAY located within south Wenchuan rupture zones along the YBF and PGF. The corresponding $(t_C - t_S)/(t_S - t_P)$ ratios are 1.0–1.6, showing that FZTWs were well generated and well recorded because both E3 and stations were located within Wenchuan rupture zones. In contrast, seismograms recorded at station GHS and BAJ located away from rupture zones for this aftershock show lower $(t_C - t_S)/(t_S - t_P)$ ratios of ~0.7.

These observations are consistent with our previous observations at the same stations for early aftershocks of the 2008 M8 Wenchuan earthquake (Li et al. 2012, 2014b; and refer to Appendix in this chapter). However, the $(t_C - t_S)/(t_S - t_P)$ ratios (1.0–1.6) for FZTWs generated by aftershocks E3 in 2014 are smaller than the average ratios (1.3–2.1) registered at the same stations for Wenchuan aftershocks in 2008, suggesting that the fault healing has occurred on the ruptured YBF and PGF since the 2008 M8 Wenchuan mainshock.

We also note that the $(t_C - t_S)/(t_S - t_P)$ ratios of FZTWs generated by E3 and recorded at these stations in 2014 are larger than the ratios (1.0–1.2) of FZTWs generated by aftershocks occurred within Lushan rupture zone and recorded at stations close to the XF. It might be because (1) Wenchuan rupture zones reached the ground surface while the Lushan rupture did not reach the surface so that Wenchuan rupture zones form an entire waveguide extending from the depth to the surface but the top portion of the waveguide on the XF has the weaker trapping effect; (2) the damage magnitude of fault rocks within the XF caused by the M7 Lushan earthquake is smaller than those within the YBF and the PGF caused by the M8 Wenchuan earthquake although Wenchuan rupture zones have been partially healed since 2008.

On the other hand, we observed wave trains characterized by long post-S coda durations (10–17 s) with the $(t_C - t_S)/(t_S - t_P)$ ratios of ~1. 0 at stations SKOU and TTSA along the un-ruptured fault in "seismic gap," and stations FXGU and BABU along the ruptured XF in Lushan area for aftershock E3 occurring within south Wenchuan rupture zone. In contrast, seismograms recorded at station YANJ on the

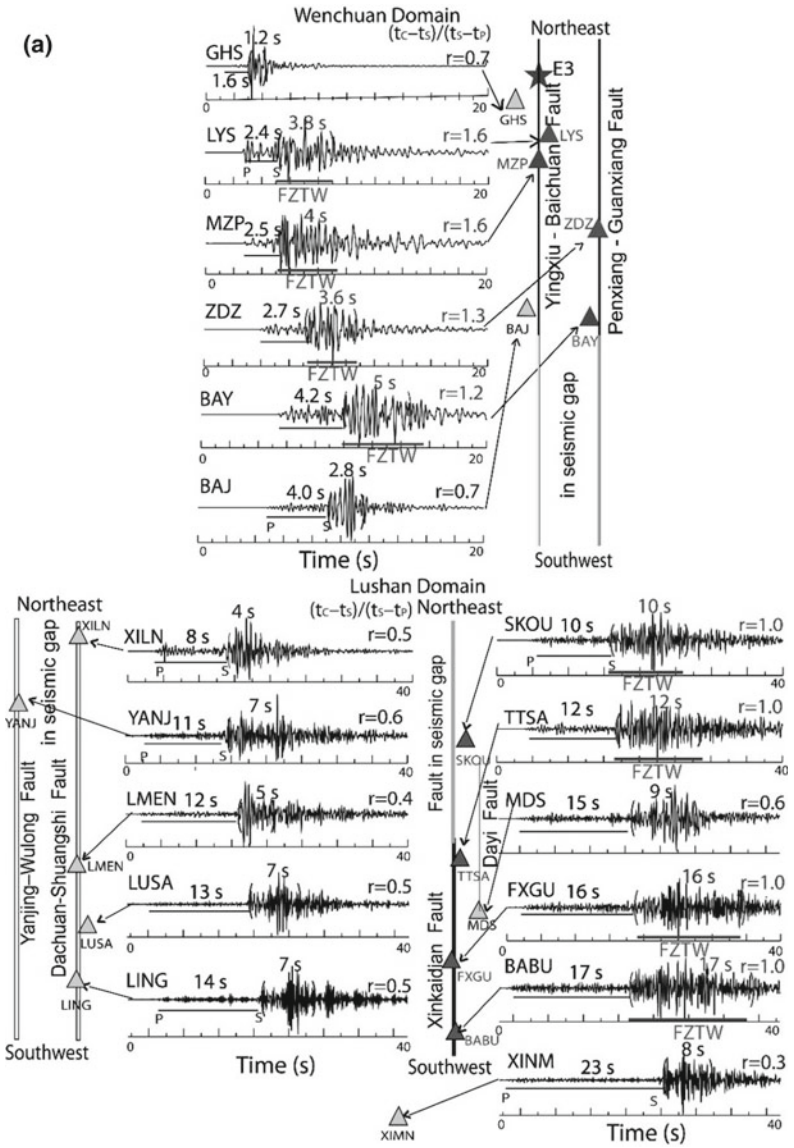

Fig. 6.5 **a** Seismograms and **b** spectral amplitudes recorded at six permanent network stations in south Wenchuan Domain and eleven temporary seismic stations deployed in Lushan Domain for aftershock E3 (small star in the map) occurring within Wenchuan rupture zone. P-to-S time and post-S coda duration time measured at each station are plotted in the figure. Prominent FZTWs (within red brackets and marked by red bars) are observed at stations along the waveguide extending from Wenchuan rupture zones on the YBF and PGF through the un-ruptured fault (denoted by a brown line) in "seismic gap" to Lushan rupture zone on the XF. Other notations are same as in Fig. 6.3

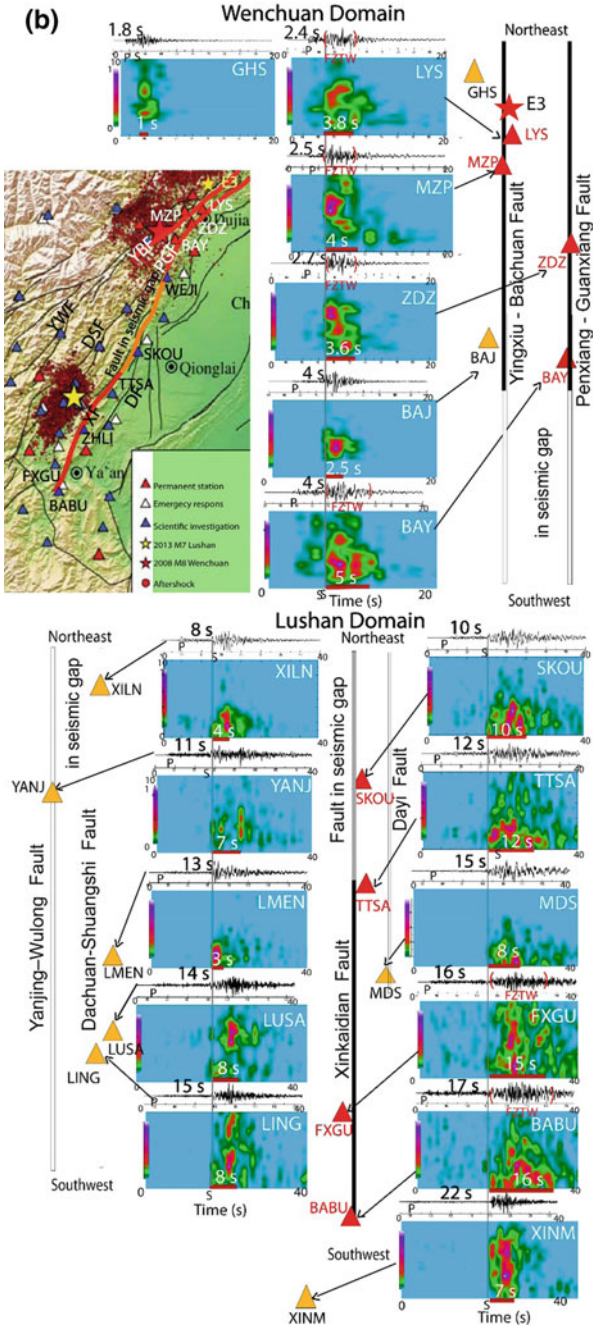

Fig. 6.5 (continued)

YWF, stations XILM, LMEN, LUSA, and LING along the DSF, station MDZ near the DF and station XINM far south of Lushan epicentral zone show shorter post-S coda durations (4–10 s) with much smaller $(t_C - t_S)/(t_S - t_P)$ ratios of 0.3–0.6 for aftershock E3, further illuminating that the XF rather than the YWF, DSF, and DF ruptured and was a genetic fault during the 2013 $M7$ Lushan earthquake. Furthermore, seismograms recorded at station XILN (co-located with station L136) located on the surface trace of the DSF in the "seismic gap" show very short post-S coda duration (4 s) with $(t_C - t_S)/(t_S - t_P)$ ratio of 0.5 as compared for to 10-s duration registered with the ratio of 1.0 at station SKOU located close to the north extension of the XF while their travel distances are similar.

These observations of FZTWs infer that the low-velocity waveguide extends continuously at depth along the YBF and PGF in Wenchuan area, through the un-ruptured fault (or called a developing fault marked by the brown color line in Fig. 6.1) rather than the DSF in "seismic gap" and to the XF in Lushan area. While, the waveguide in the "seismic gap" between Wenchuan and Lushan rupture zones shows weaker trapping effect than those along rupture zones because the fault within the "gap" did not slip during both Wenchuan and Lushan earthquakes. However, it might be a developing fault and experienced minor damage due to strong shaking by the 2008 $M8$ Wenchuan and 2013 $M7$ Lushan earthquakes.

FZTWs shown in Fig. 6.6 further characterize the waveguide along multiple faults of the south Longmenshan fault system. Prominent FZTWs with the $(t_C - t_S)/(t_S - t_P)$ ratios of 1.0–1.6 are registered at stations MZP, ZDZ, and BAY of Zipingpu dam seismic network along the YBF and the PGF for aftershock E4 occurring within southern Wenchuan rupture zone. In contrast, the ratio of $(t_C - t_S)/(t_S - t_P)$ registered at stations GHS and BAJ away from Wenchuan rupture zones is ~0.6. The FZTWs generated by E4 were also recorded at stations ZHLI, FXGU, and BABU close to the surface trace of the XF, and at station HEMN located close to the un-ruptured (developing) fault in "seismic gap." The $(t_C - t_S)/(t_S - t_P)$ ratios registered at these stations are 0.8–0.9. In contrast, much smaller $(t_C - t_S)/(t_S - t_P)$ ratios of 0.2–0.5 are registered at stations LMEN, SUSI, LUSA, and LING located along with the DSF, station MDS along the DF, and station XINM far south of Lushan epicentral region. These observations further confirm that a low-velocity waveguide continuously extends along multiple faults of the south Longmenshan fault system, including the YBF and the PGF that ruptured in the 2008 $M8$ Wenchuan earthquake, the XF ruptured in the 2013 $M7$ Lushan earthquake, and the un-ruptured fault in the "seismic gap" between Wenchuan and Lushan rupture zones. However, the waveguide effect of the un-ruptured fault in the "gap" is weaker than that of ruptured faults.

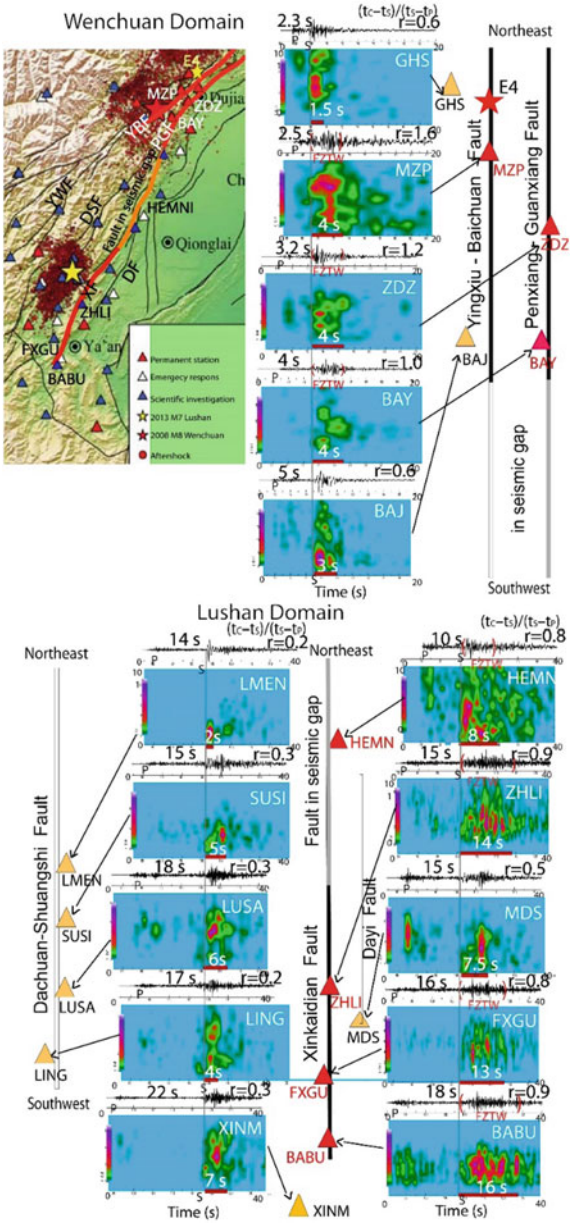

Fig. 6.6 Vertical-component seismograms and normalized spectral amplitudes at eleven seismic stations in Lushan region and "seismic gap," and five stations of Zipingpu dam seismic network for Lushan aftershock E4 (small star in the map) occurring at 18-km depth within southern Wenchuan rupture zone. FZTWs (marked by red brackets and bars) are observed at stations MZP, ZDZ, and BAY along the ruptured YBF and PGF in Wenchuan domain, station HEMN close to the un-ruptured fault (marked by a brown line) in "seismic gap," and stations ZHLI, FXGU, and BABU along the ruptured XF in Lushan domain. FZTWs are not obvious at stations located along the DSF and the DF. Other notations are same as in Fig. 6.5

6.2.3 The Data Recorded for Local Earthquakes Away from Rupture Zones

For comparison with the data from aftershocks occurring within rupture zones of either the 2013 $M7$ Lushan earthquake or the 2008 $M8$ Wenchuan earthquake, we examine seismograms and spectral amplitudes recorded at the same stations for earthquakes occurring away from rupture zones. For example, Fig. 6.7 shows waveforms and spectral contours at eighteen stations for a $M4$ local earthquake occurring ~40-km south of Lushan epicentral zone. There are no clear FZTWs identified in seismograms recorded at all stations for earthquake E6. We observe short post-S coda durations with respect to P-to-S times. The $(t_C - t_S)/(t_S - t_P)$ ratios registered at these stations are 0.2–0.5. Even at stations BABU, FXGU, ZHLI along the XF, the post-S coda durations are 2–4 s with respect to P-to-S times of 5.5–8 s, corresponding to the $(t_C - t_S)/(t_S - t_P)$ ratio of 0.3–0.5. At Zipingpu dam seismic network stations along the ruptured YBF and PBF, the $(t_C - t_S)/(t_S - t_P)$ ratios are 0.2–0.5, corresponding to post-S coda durations of 6–9 s with respect to P-to-S times of 14–18 s. These observations show that FZTWs were not generated by this local earthquake away from rupture zone, and therefore no clear FZTWs were recorded at stations located either within or away from Lushan and Wenchuan rupture zones.

6.3 Subsurface Damage Structures Inferred from FZTWs

We have shown waveform data recorded at seismic stations located in Lushan and Wenchuan areas for five aftershocks (E1–E5) and a local earthquake E6 in both time and frequency. In summary, Fig. 6.8 exhibits the post-S coda durations and P-to-S times as well as $(t_C - t_S)/(t_S - t_P)$ ratios measured at those stations for six events.

The measurements shown in Fig. 6.8 have the following characterizations:

(1) The $(t_C - t_S)/(t_S - t_P)$ ratios at stations close to the XF are 1.0–1.4 for Lushan aftershocks E1, E2, and E5, showing that FZTWs were well generated and recorded when both aftershocks and recording stations located within the low-velocity waveguide along the XF. In contrast, the ratios are 0.3–0.7 at stations along the DF, DSF, and YWF for the same aftershocks, suggesting that there are no effective waveguides between these aftershocks and stations. We interpret that the XF most likely ruptured in the 2013 $M7$ Lushan earthquake, within which rocks were severely damaged to form a remarkable low-velocity waveguide to trap seismic waves generated by aftershocks occurring within it. Therefore, the XF is plausible to be a genetic fault of the 2013 Lushan quake rather than the DF, DSF, and YWF within a thrust-folding region with multiple imbricated faults in Lushan area, consistent the previous speculations and interpretations by Xu et al. (2013), Fang et al. (2015).

(2) The ratios for FZTWs generated and recorded within Wenchuan rupture zones along the YBF and PGF are up to 1.6, larger than those for FZTWs generated

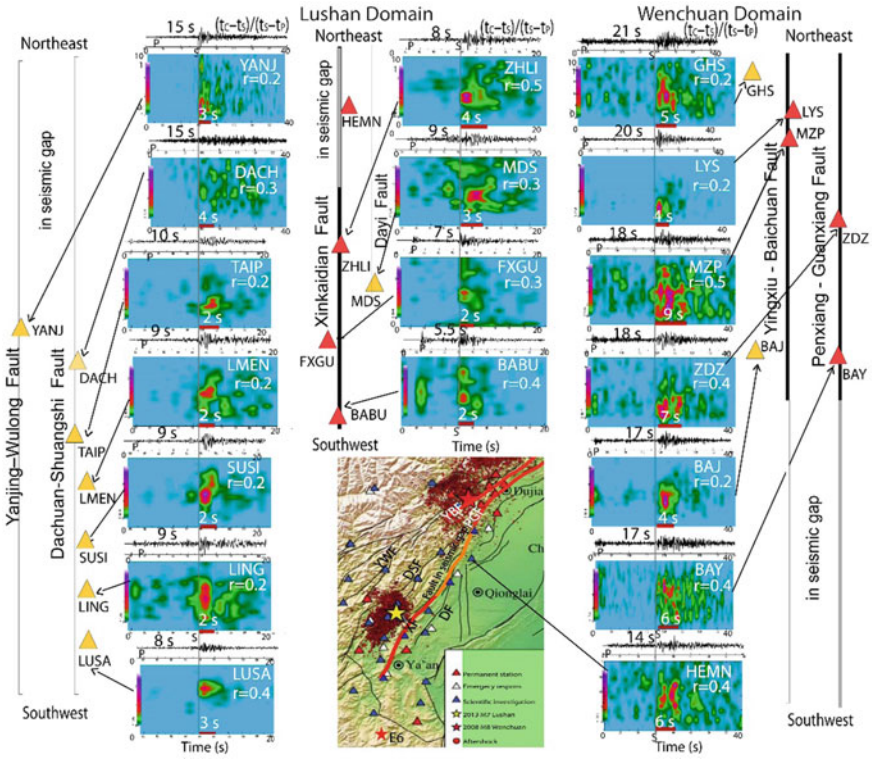

Fig. 6.7 Vertical-component seismograms and normalized spectral amplitudes at eighteen seismic stations in Wenchuan-Lushan areas for a local earthquake E6 (small star in the map) occurring far south of Lushan epicentral zone. The measured post-S coda duration time, P-to-S time, and their ration ratio at each station are shown in the figure. The $(t_C - t_S)/(t_S - t_P)$ ratios registered at all stations either within or away from Wenchuan and Lushan rupture zones are $\leq$0.5, showing no clear FZTWs generated by this local earthquake out of rupture. Other notations are same as in Fig. 6.4

and recorded within Lushan rupture zone along the XF, suggesting that the low-velocity waveguide of Wenchuan rupture zones has stronger trapping effect than that of the XF.

It might be because the rupture zone on the XF did not reach the ground surface so that the FZTWs could be degraded in the near-surface layer. Alternatively, the fault rocks of the YBF and PGF were much severely damaged (larger velocity reduction) during the 2008 $M8$ Wenchuan earthquake than the fault rocks of the XF damaged during the 2013 $M7$ Lushan earthquake. Li et al. (2012, 2014b; also see Appendix in this chapter) show the severe damage of fault rocks within the YBF and the PGF inferred by FZTWs at the same stations in the early stage after the 2008 Wenchuan earthquake. The $(t_C - t_S)/(t_S - t_P)$ ratios of the FZTWs generated by those aftershocks are up to 2.1 (see Appendix in this chapter). Although the damage magnitude decreases with time due to post-

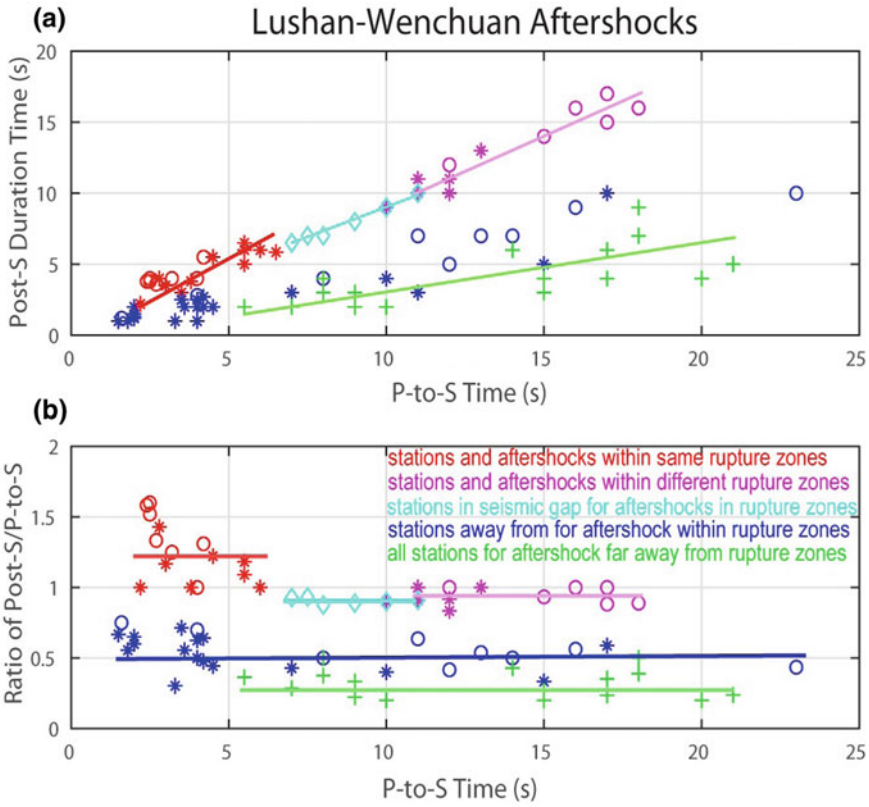

Fig. 6.8 **a** Post-S coda durations versus P-to-S times measured at stations in study area for five aftershocks and a local earthquake (see Fig. 6.1 for their locations). Red asterisks: measurements at stations close to the XF in Lushan region for aftershocks E1, E2, and E5 occurring within Lushan rupture zone. Red circles: measurements at Zipingpu dam seismic network stations close to surface ruptures of the YBF and the PGF for aftershocks E3 and E4 occurring within Wenchuan rupture zones. Pink asterisks: measurements at stations close to the YBF and the PGF in Wenchuan region for aftershocks E1, E2, and E5 occurring within Lushan rupture zone. Pink circles: measurements at stations close to the XF in Lushan region for aftershocks E3 and E4 occurring within Wenchuan rupture zones. Blue asterisks (circles): measurements at stations along with other faults DF, DSF, and YWF in Lushan region and stations away from YBF and PGF in Wenchuan region for aftershocks E1, E3, and E5 (E3 and E4). Cyan diamonds: measurements at stations located along the un-ruptured (developing) fault (marked by a brown line) in "seismic gap" for aftershocks E1–E5. Green crosses: measurements at all stations in this study for local an earthquake E6 located far south of Lushan epicentral zone. Color lines are the least-square fit to the corresponding measurements. **b** Ratios of $(t_C - t_S)/(t_S - t_P)$ versus P-to-S times for the measurements in (**a**), using the same symbols and colors. The horizontal color line denotes the average $(t_C - t_S)/(t_S - t_P)$ ratio for the corresponding data

seismic healing, seismic velocity reduction within Wenchuan rupture zones in 2013 was still larger than that within the XF which ruptured during the $M7$ Lushan earthquake.

(3) The $(t_C - t_S)/(t_S - t_P)$ ratios are 0.8–1.0 registered at stations located along the XF in Lushan area for aftershocks E3 and E4 occurring within southern Wenchuan rupture zone, and vice versa at stations along the YBF and the PGF in south Wenchuan rupture zones for aftershocks E1, E2, and E5 occurring within Lushan rupture zone. It is because when the FZTWs generated aftershocks occurring within Lushan or Wenchuan rupture zones traveled through the un-ruptured fault with the weaker trapping effect in the "seismic gap," the $(t_C - t_S)/(t_S - t_P)$ ratios decreased from 1.0–1.6 to 0.8–1.0. However, these ratios are still higher than those registered at stations located away rupture zones, suggesting that there exists a moderate waveguide along a developing fault (marked by a brown line in Fig. 6.1) in the "seismic gap" to connect Wenchuan and Lushan rupture zones although this developing fault in-between them did not rupture in the 2008 $M8$ Wenchuan and 2013 $M7$ Lushan earthquakes. Furthermore, the FZTWs generated by aftershocks occurring within rupture zones and recorded at stations along this un-ruptured (developing) fault show $(t_C - t_S)/(t_S - t_P)$ ratios of ~0.9 while the $(t_C - t_S)/(t_S - t_P)$ ratios registered at stations along YWF and DSF for the same aftershocks are less than 0.5, confirming that the low-velocity waveguide extends from the YBF/PGF through this developing fault rather than the DSF and YWF to the XF.

(4) In contrast, the $(t_C - t_S)/(t_S - t_P)$ ratios registered at all stations either close to or away from Lushan and Wenchuan rupture zones for a local earthquake E6 occurring far south of Lushan epicentral region are 0.2–0.4, showing no FZTWs generated by E6 and recorded at all stations in Lushan and Wenchuan areas. This example supports our observations of FZTWs well generated and recorded as both the aftershock and station located within Lushan and Wenchuan rupture zones (refer to the data in Figs. 6.2, 6.3, 6.4, 6.5, 6.6) are due to the waveguide effect of low-velocity fault zones at depth rather than the site affect or near-surface geological structure.

6.4 Simulation of FZTWs Generated by Lushan Aftershocks

In this section, we demonstrate the preliminary synthetic FZTWs generated by Lushan aftershocks in terms of fault-zone structural model schemed in Fig. 6.9a. Seismic velocities of surrounding rocks are based on layered crustal model beneath the Longmen Shan thrust belt (refer to Table 2 in Xu et al. 2013). We assume a 200-m-wide low-velocity fault core zone with velocity reductions varying along multiple fault zones and depth. We use a 3-D finite-difference code to propagate the complete wave-field through an elastic media with a free surface boundary and spatially

variable anelastic damping (an approximate Q) (Vidale et al. 1985; Graves 1996). This computer code has been used in our previous investigation of rock damage within southern Wenchuan rupture zone along the YBF and PGF using FZTWs generated by aftershocks recorded at stations of Zipingpu dam seismic network (Li et al. 2012, 2014b). When the grid spacing is 50 m and the minimum velocity is 1.0 km/s, the maximum frequency of the synthetic seismograms is 4 Hz in modeling. In order to reduce the computer memory in modeling, we decrease the number of element grids along y-axis only for the distance between the aftershock and seismic station. The synthetic seismic waves are derived from a double-couple source (according to the mainshock focal mechanisms) with radiation patterns included within low-velocity rupture zone.

Figure 6.9b shows synthetic waveforms using the model in Fig. 6.9a to match seismograms recorded at three stations ZHLI, BADU, and LING for Lushan aftershock E2 that occurred on the XF at 16-km-depth with epicenter ~18-km north of station ZHLI. Synthetic FZTWs show large amplitudes and long post-S coda durations arrive at stations ZHLI and BADU located close to the surface trace of the XF. The post-S coda durations of synthetic FZTWs increase from ~3.5 to ~6 s as travel distances within rupture zone along the XF increase from ~25 km (between E2 and ZHLI) to ~45 km (between E2 and BADU). Synthetic waveforms are comparable with seismograms recorded at these two stations for aftershock E2. Measured post-S coda durations, P-to-S times and their ratios are shown in Tables 6.1 and 6.2. In contrast, much short post-S coda duration (~2.0 s) is registered at station LING located at the similar hypocentral distance as station ZHLI, but away from the low-velocity rupture zone along the XF. Synthetic and observed seismograms show that the $(t_C - t_S)/(t_S - t_P)$ ratios are 1.2 at stations ZHLI and BABU close to the surface trace of the XF, but 0.5 at station LING away from the XF.

We then simulate FZTWs recorded at stations located along the PGF within southern Wenchuan rupture zones for aftershocks occurring within Lushan rupture zone along the XF. In the forward modeling, we test two end-member models first (see Fig. 6.10a). One end-member test model is a half-space with the free surface, including a continuous lateral-uniform waveguide along multiple faults (the XF, the fault in "seismic gap," the PGF-YBF) of the south Longmen Shan fault system within which seismic velocities are consistently reduced by 50%. Lushan aftershock E5 is located at 16-km depth within the rupture zone along the XF. Station ZDZ is located at the surface within Wenchuan rupture zones along the PGF-YBF, ~80 km from Lushan aftershock. In another end-member test model, the low-velocity waveguide is discontinuous. There is no fault zone within the "seismic gap" between Wenchuan and Lushan rupture zones.

For the first end-member test model with a uniform lateral-uniform low-velocity waveguide along multiple faults (the top model in Fig. 6.10a), very long post-S coda duration (20 s) with the $(t_C - t_S)/(t_S - t_P)$ ratio of ~1.5 is registered at station ZDZ located within Wenchuan rupture zone along the PGF for aftershock E5 occurring within Lushan rupture zone along the XF (Fig. 6.10b). The FZTWs are well generated and well recorded in this case. However, the synthetic FZTWs show too long post-S coda duration to match observed post-S coda duration of 12 s at station ZDZ for aftershock E5. It is because the fault in "seismic gap" is assigned by the same

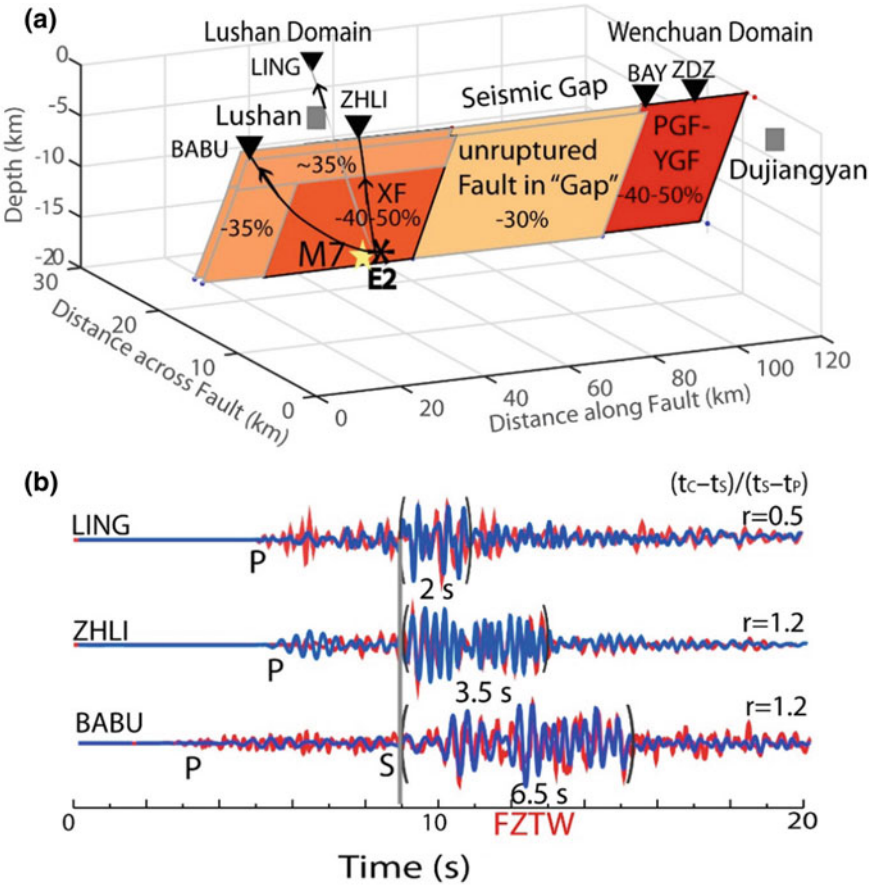

Fig. 6.9 **a** 3-D volume shows schematic geometry of the Xinkaidian fault (XF), the un-ruptured fault in "seismic gap" and the Pengxian-Guanxian fault (PGF) at the surface and subsurface fault planes dipping northwestward at 50° along the south Longmen Shan fault system. The PGF connects the Yingxiu-Beichuan (YBF, not shown in the figure) at depth. The XF and the PGF-YBF (red planes) were ruptured during the 2013 $M7$ Lushan and the 2008 $M8$ Wenchuan earthquakes, respectively, within which seismic velocities are reduced by ~40–50%. Wenchuan rupture zones along the PGF-YBF reached the surface. Lushan rupture along the XF did not reach the surface. Seismic velocities within the shallow portion of the XF above 3-km depth are reduced by ~35%. The un-ruptured fault with ~30% seismic velocity reduction in "seismic gap" connects the XF to south and the PGF to north. Black lines with arrows denote raypaths from aftershocks E2 (asterisk) to stations ZHLI, BABU, and LING at the surface. **b** Observed (red lines) and synthetic (blue lines) seismograms at stations ZHLI and BADU located close to the surface trace of the XF, and station LING 2-km away from the XF for Lushan aftershock E2 at 16-km depth. FZTWs with large amplitudes (within brackets) and post-S coda durations of 3.5 s at station ZHLI and ~6.5 s at station BADU, but 2 s at station LING. The $(t_C - t_S)/(t_S - t_P)$ ratios at three stations are shown in figure

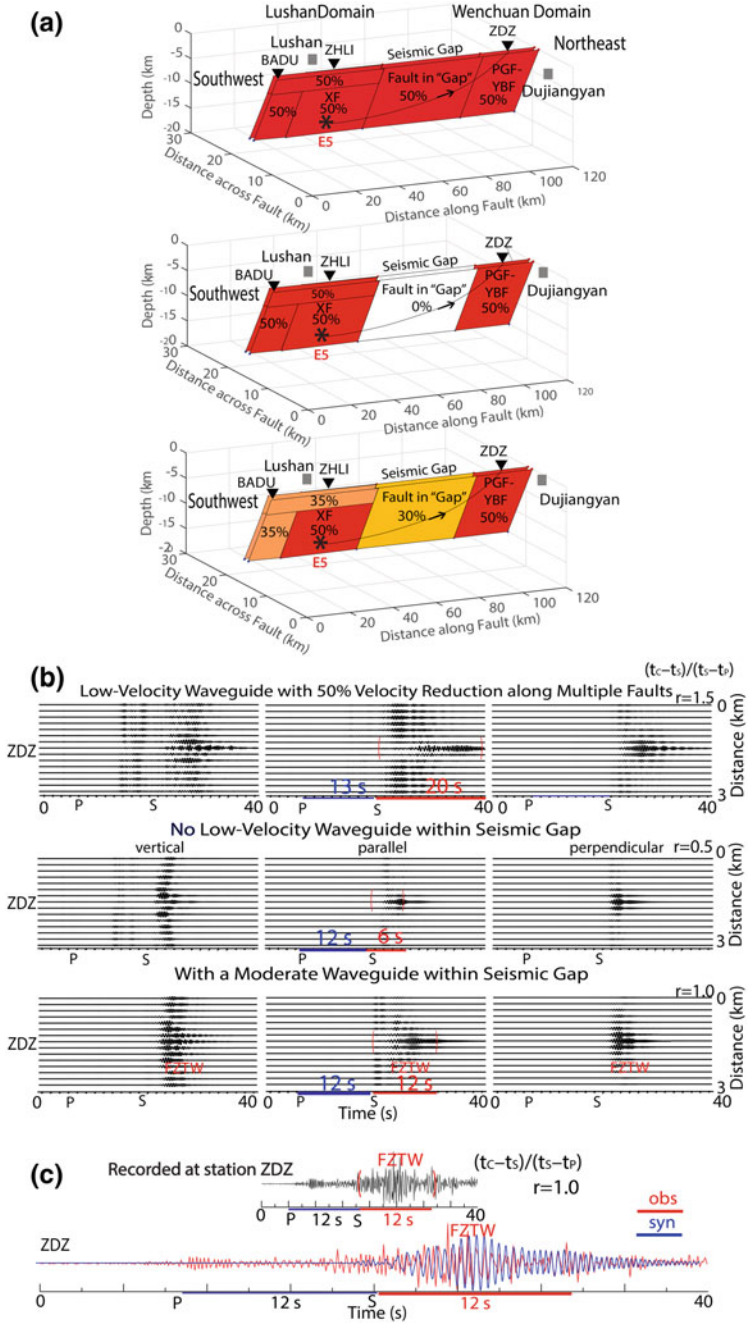
(a)
LushanDomain
Wenchuan Domain
Lushan
ZHLI
BADU
Seismic Gap
ZDZ
Northeast
Southwest
50%
XF
50%
50%
Fault in "Gap"
50%
PGF-
YBF
50%
Dujiangyan
ES
Depth (km
Distance across Fault (km)
Distance along Fault (km)
0%
35%
30%
(b)
Low-Velocity Waveguide with 50% Velocity Reduction along Multiple Faults
(tc−ts)/(ts−tp)
r=1.5
ZDZ
13 s
20 s
Distance (km)
No Low-Velocity Waveguide within Seismic Gap
vertical
parallel
perpendicular
r=0.5
12 s
6 s
With a Moderate Waveguide within Seismic Gap
r=1.0
FZTW
12 s
Time (s)
(c)
Recorded at station ZDZ
FZTW
(tc−ts)/(ts−tp)
r=1.0
obs
syn
ZDZ
P
S
12 s
Time (s)

◀**Fig. 6.10** **a** from top to bottom: the first end-member test model including a lateral-uniform low-velocity waveguide, within which seismic velocities are reduced by 50% from wall-rock velocities, along multiple faults of the south Longmenshan fault (LMSF) system including the XF, the fault in "seismic gap" and the PGF-YBF. A double-couple source is located at the hypocenter of Lushan aftershock E5 at 16-km depth within rupture zone of the XF. Station ZDZ is located at the surface within Wenchuan rupture zone of the PGF-YBF with its epicentral distance of ~80-km from E5. In the second end-member test model, Lushan and Wenchuan rupture zones are separated by a ~40-km-long "seismic gap." There is no low-velocity waveguide within the "gap." Other notations are same as in the first test model. The best-fit mode includes a developing fault with 30% velocity reduction within "seismic gap" to connect Lushan rupture zone on the XF and Wenchuan rupture zone on the PGF-PGF with 40–50% velocity reductions. **b** from top to bottom: three-component synthetic seismograms for Lushan aftershock E5 using three models in (**a**). The seismic profile along a linear array perpendicularly crosses the PGF which is located in the middle of the profile. The trace spacing in seismic profile is 200 m. Station ZDZ is located within the rupture zone along the PGF. Post-S coda durations, P-to-S times, and $(t_C - t_S)/(t_S - t_P)$ ratios for three models are shown in the figure. **c** Synthetic and recorded seismograms at station ZDZ for Lushan aftershock E5, using the best-fit model in (**a**)

velocity reduction as rupture zones along the XF and PGF in this end-member model. In fact, the fault in the 'seismic gap" did not rupture either in the 2008 $M8$ Wenchuan earthquake or in the 2013 $M7$ Lushan earthquake so that rock damage magnitude (velocity reduction) within it should be less than those within Wenchuan and Lushan rupture zones.

For the second end-member test model without a low-velocity waveguide in ~40-km-long "seismic gap" between Wenchuan and Lushan rupture zones (the middle model in Fig. 6.10a), the synthetic FZTWs generated by Lushan aftershock E5 are disrupted within "gap" so that the $(t_C - t_S)/(t_S - t_P)$ ratio is only 0.5 registered at station ZDZ located within Wenchuan rupture zone. The post-S coda duration is 6 s, too shorter to match 12-s post-S coda duration observed at ZDZ for E5 (Fig. 6.10b).

In a trial-and-error modeling procedure, we finally add a fault zone with 30% velocity reduction within "seismic gap" to make the low-velocity waveguide extends continuously from the XF to PGF (the bottom model in Fig. 6.10a). However, the waveguide trapping efficiency of this fault within the "gap" is weaker than that of Wenchuan and Lushan rupture zones. The synthetic FZTWs derived from this best-fit model show 12-s post-S coda duration with the $(t_C - t_S)/(t_S - t_P)$ ratio of 1.0 (Fig. 6.10b), in general agreeable with the FZTWs recorded at station ZDZ located within Wenchuan rupture zone for aftershock E5 occurring within Lushan rupture zone (Fig. 6.10c).

The results from forward modeling are not uniquely constrained because there are trade-offs among model parameters. We find that the S-wave velocity reduction and Q-value within rupture zones are more sensitive than other model parameters to the post-S coda duration and amplitude of FZTWs at higher frequencies. The width of the damage zone at shallower depth is more sensitive than the width at a deeper level to observations of FZTWs at surface stations located within rupture zones. Although the layer depths and velocities of surrounding rocks are constrained based on the velocity model for the Longmen Shan thrust belt (Xu et al. 2013), variations in surrounding-

rock velocities and layer depths affect the arrival times of P and S-waves. As a result of the limited available constraints, we permit a ~3- to 5-km variation in hypocentral distances used in our model in allowance for the possible lateral heterogeneity of rock damage along multiple faults and for aftershock location errors. Nevertheless, the finite-difference simulations provide a first-order estimate of the overall velocity structure of the south LMSF system, including Wenchuan and Lushan rupture zones and the developing fault in "seismic gap" at seismogenic depths. In order to obtain a more realistic model for multiple faults of the south LMSF, we shall make a systemic modeling of FZTWs generated using more aftershocks occurring at various depths and epicentral distances, and recorded at more stations along the LMSF system.

6.5 Conclusion and Discussion

The fault-zone trapped waves (FZTWs) observed at the south Longmanshan fault (LMSF) help us to learn more about the structural, physical, and mechanical relationship between 2008 $M8.0$ and 2013 $M7.0$ earthquakes.

I. The prominent FZTWs recorded at stations close to the pre-existing surface trace of the XF but not at stations along the nearby Dayi fault (DF), Dachuan-Shuangshi fault (DSF), and Yanjing-Wulong fault (YWF) for aftershocks occurring nearby the hypocenter of the 2013 $M7$ Lushan earthquake show that a remarkable low-velocity waveguide exits along the XF between these aftershocks and seismic stations close to the XF surface trace. We interpret that rocks within the XF rather than the DF, DSF, and YWF were severely damaged during dynamic rupture in the 2013 $M7$ strike to form this low-velocity waveguide, and therefore, the XF is most likely the genetic fault of the 2013 Lushan earthquake among multiple imbricated faults within a thrust-folding region although no surface rupture was mapped in the epicentral area after this earthquake. Our interpretation inferred by FZTWs is consistent with the results from surface structural geology, fault plan solutions, and aftershock relocations for the 2013 $M7$ Lushan earthquake, revealing that the seismogenic structure of this earthquake is a blind thrust fault connecting the XF at seismogenic depth although the rupture did not reach the surface (Han et al. 2014; Xu et al. 2013; Fang et al. 2015). Xu and Xu (2014) found that the landslide density on the footwall is clearly lower than that of the hanging wall of the XF or called the western Shangli fault (WSF). They infer that the seismogenic fault for the 2013 Lushan earthquake is neither the DSF nor the DF, rather probably the XF (or called WSF), which is an evident linear trace on the earth surface although the coseismic slip did not propagate upward to the ground.

II. The FZTWs generated by Lushan aftershocks were also recorded at Zipingpu dam seismic network stations within southern Wenchuan region, suggesting that the low-velocity waveguide extends continuously from Lushan rupture zone on the XF along a developing but un-ruptured fault within ~45-km-long "seismic

gap" to Wenchuan rupture zones on the PGF and YBF. Vice versa, the FZTWs generated by aftershocks occurring on the YGF and PGF were recorded at stations close to the trace of the XF, further confirming that there exists a waveguide in "seismic gap" to connect Wenchuan and Lushan rupture zones although this waveguide has weaker trapping effect than Lushan and Wenchuan rupture zones because it did not rupture either in the 2008 $M8$ Wenchuan earthquake or in the 2013 $M7$ Lushan earthquake so that rocks within it were less damaged than those within the YBF, PGF, and XF. Moreover, we observe FZTWs at stations located close to this developing fault (marked by a brown line on the map in Fig. 6.1) but not at stations along the DSF, the YWF and the DF in "seismic gap," further suggesting that this developing fault in "seismic gap" connects Lushan rupture and Wenchuan ruptures to make a continuous low-velocity waveguide along multiple faults of the south Longmen Shan fault (LMSF) system. We speculate that this developing fault in the "gap" may be a northward extension of the XF or called WSF on which the 1970 $M6.2$ Dayi earthquake occurred.

III. We have developed models of subsurface rock damage structure along multiple faults of the south LMSF. The preliminary finite-difference simulations of recorded FZTWs provide a first-order estimate of the overall structure of the low-velocity zone along the XF ruptured in the 2013 $M7$ Lushan earthquake, the PGF/YBF ruptured in the 2008 $M8$ Wenchuan earthquake, and the un-ruptured fault in the 45-km-long "seismic gap" in-between. Modeling results confirm a continuous low-velocity waveguide along the south LMSF although the magnitude of rock damage within it varies along multiple faults. In a structural viewpoint, the 2008 Wenchuan earthquake and the 2013 Lushan earthquake consisting of a sequence of major earthquakes occurred on the same LMSF. Therefore, we suppose that the 2013 event to be the largest aftershock of the 2008 mainshock. A similar situation was met in the 2010 $M7.1$ Darfield and the 2011 $M6.3$ Christchurch earthquakes in South Island, New Zealand. Fault-zone trapped waves have been used to characterize the continuity of the low-velocity waveguide along the Greendale fault that ruptured in the 2010 $M7.1$ earthquake, the Port Hills fault that ruptured in the 2011 $M6.3$ earthquake, and the un-ruptured faults in a ~15-km-long "slip gap" between two rupture zones (Li et al. 2014a). Structurally, the 2010 $M7.1$ Darfield earthquake and the 2011 $M6.3$ Christchurch earthquake consist of a sequence of earthquakes occurring on the same fault system.

IV. The waveguide effect of the southern rupture zones along the YBF and the PGF has been investigated in our previous study using FZTWs generated by Wenchuan aftershocks and recorded at stations of Zipingpu dam seismic network and a dense temporary seismic array deployed across the YBF immediately after the 2008 Wenchuan earthquake (refer to Appendix in this chapter). The features of FZTWs recorded at same seismic network stations for Wenchuan aftershocks in 2008 and 2013 are similar, but the $(t_C - t_S)/(t_S - t_P)$ ratios decreased from 1.3–2.1 in 2008 to 1.0–1.6 in 2014, suggesting that the fault rocks within Wenchuan rupture zones had been partially healed with time, but was not back to the background level of rock damage magnitude yet.

Three strong historical earthquakes with magnitude larger than $M6.0$ occurred at the southern Longmen Shan fault: Tianquan earthquake in 1327, Baoxing-Kangding $M6.0$ earthquake on June 12, 1941 and Dayi $M6.2$ earthquake on February 2, 1970 (Yang et al. 2005; Su et al. 2013; Pei et al. 2014). Dong et al. (2017) suggest that the faults within the "seismic gap" could be capable of generating $M6.0$–7.0 earthquakes, but that the likelihood of such an occurrence in the near future is not very high, according to the most recent geological and geophysical findings on image interpretation, trench excavation, radiocarbon and optically stimulated luminescence dating, and paleoseismological comparisons with historical earthquakes, including the most recent 1970 $M6.2$ Dayi earthquake within the "gap." Our study using FZTWs to evaluate fault connectivity and segmentation along the south LMSF system helps us understanding fault evolution and earthquake potential in the region. Because the 2013 $M7$ Lushan earthquake only ruptured a small fault segment, increased seismic hazards in its adjacent regions, particularly in the "seismic gap," should be noticeable (Zhang et al. 2014). Our investigation infers that the XF-PGF connectivity may increase to a state where combined XF-PGF ruptures are a possibility for even a larger earthquake.

Acknowledgements We thank Sichuan Earthquake Administration for usage of the data recorded at the Sichuan Province Seismic Network and portable stations deployed immediately after the 2013 Lushan earthquake. We also thank the Department of Earth Sciences in University of Southern California for usage of computer facilities to analyze the data.

Appendix: FZTWs Generated by Wenchuan Aftershocks in 2008

We carried out a systematic analysis of fault-zone trapped waves using the data recorded at eight stations of Zipingpu reservoir seismic network (ZDSN) for ~1500 aftershocks in the first year after the $M8$ Wenchuan earthquake on May 12, 2008 (Li 2008, 2010; Li et al. 2012, 2014b). Part of these aftershocks was re-located using double-difference (D–D) method.

For example, Fig. 6.11 shows seismograms recorded at network stations MZP and GHS for three Wenchuan aftershocks occurring within the rupture zone at depths of ~10–11 km and epicentral distances of 6, 14 and 25 km, respectively, from station MZP. We observed prominent FZTWs with large amplitudes and long durations at station MZP located close to the surface rupture of the YBF near Yingxiu Town. The measured post-S coda durations of FZTW increase from ~2.8 s, ~4.2 s to ~6.1 s as hypocentral distances of these aftershocks increase from ~12 km, ~18 km, to ~27 km (showed by a move-out of FZTW wavetrain length with travel distance). The $(t_C - t_S)/(t_S - t_P)$ ratios are 1.7–2.1 at station MZP for three aftershocks, showing that FZTWS were well generated and well recorded as both the source and receiver located within the low-velocity waveguide along the YBF. In contrast, much shorter post-S

durations (~1.3–1.8 s) with flat changes with hypocentral distance registered at station GHS located away from the YBF rupture for the same aftershocks. The $(t_C - t_S)/(t_S - t_P)$ ratios at station GHS are 0.5–0.9, showing that FZTWS generated by these aftershocks were not well recorded at the off-waveguide station. These observations suggest that the rupture zone on the YBF extends down to the depth of at least ~10 km. We also note that the $(t_C - t_S)/(t_S - t_P)$ ratios (1.7–2.1) for FZTWs generated by these aftershocks in the early stage after the 2008 $M8$ Wenchuan mainshock are larger than the ratios (1.0–1.6 shown in Tables 6.1 and 6.2) registered at the same station MZP for aftershocks E3 and E4 in 2014. This shows that Wenchuan rupture zone along the YBF had a greater waveguide effect in the earlier stage after the 2008 $M8$ earthquake. Then, the waveguide effect decreased as fault healed (seismic velocity reduction decreased within the rupture zone) gradually with time.

In the following example, Fig. 6.12 shows seismograms recorded at stations MZP, LYS, and GHS of the ZDSN for three Wenchuan aftershocks occurring at different depths and epicentral distances. Prominent FZTWs with large amplitudes and long post-S coda durations were observed at stations MZP and LYS close to the surface rupture along the YBF for aftershocks (events 08022311 and 08022248) occurring within the Wenchuan rupture zone at depths of ~20 and ~14-km depth, and epicentral distances of ~20 and ~35-km northeast of station MZP, respectively. We measured ~7 and ~10-s post-S durations at station MZP for the two aftershocks, showing the longer post-S coda duration of FZTWs over a longer travel distance within the low-velocity rupture zone. The corresponding $(t_C - t_S)/(t_S - t_P)$ ratios at station MZP closest to the YBF are 1.6 and 1.7, showing that FZTWS were well generated by these two aftershocks and well recorded at station MZP because both the source and recorder were located within the low-velocity waveguide along the Wenchuan rupture zone. We have similar observations at station LYS close to the surface rupture of the YBF. The corresponding $(t_C - t_S)/(t_S - t_P)$ ratios are 1.3 and 1.5.

In contrast, much shorter S-waves (~2 s) at station GHS located away from the rupture zone for these two aftershocks. The $(t_C - t_S)/(t_S - t_P)$ ratios are 0.4–0.5, showing that FZTWS were not recorded at the off-waveguide station even though the FZTWs were generated by aftershocks within the rupture zone. We further measured 0.5–0.7 of $(t_C - t_S)/(t_S - t_P)$ ratios at these three stations located for an aftershock (event 08022335) occurring ~8 km away from the YBF at ~15-km depth and ~15-km epicentral distance from station MZP, showing that FZTWs were not well generated and recorded for this aftershock away from the low-velocity rupture zone. Our observations of FZTWs illuminate a remarkable low-velocity waveguide formed by severely damaged fault rocks within the YBF that ruptured in the 2008 $M8$ Wenchuan earthquake.

The FZTWs recorded at stations of ZDSN for aftershocks E3 and E4 that occurred within Wenchuan rupture zones in 2014 (see Sect. 6.2.2 of this chapter) are similar to those recorded at the same stations for the aftershocks occurring at the similar locations within Wenchuan rupture zones in 2008. However, the average $(t_C - t_S)/(t_S - t_P)$ ratios (1.3–2.1) for FZTWs generated by the earlier aftershocks in 2008 are larger than the ratios (1.0–1.6) of FZTWs recorded at the same stations for aftershocks E3 and E4 in 2014, further infer that the damage magnitude of fault rocks within

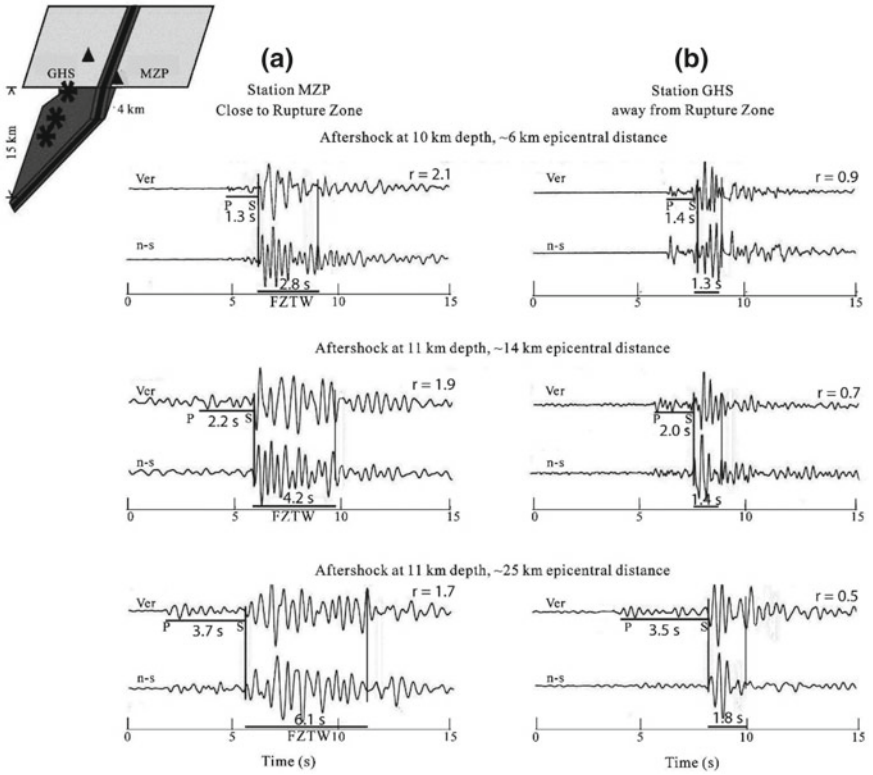

Fig. 6.11 Top left: The schematic diagram shows locations of network stations MZP and GHS (triangles) and three Wenchuan aftershocks (stars) in 2008 with respect to the rupture zone along the south YBF which dips to NW with a high angle at shallow depth and a low angle at deep portion. **a** and **b** Vertical and north-south components of seismograms recorded at stations MZP and GHS for three on-fault aftershocks occurring at ~10-to 11-km depths with approximate 6-, 14-, and 25-km epicentral distances (from top to bottom). Aftershock depths and epicentral distances are plotted in headlines. Prominent FZTWs with large amplitudes and long post-S coda durations were recorded at station MZP close to the YBF surface rupture, but much shorter post-S durations registered at station GHS located away from the YBF. Seismograms have been <3 Hz filtered. Post-S durations of FZTWs are measured on average in two components, marked by two vertical lines within which amplitudes of FZTWs are above twice the level of background noise. The post-S coda duration, P-to-S time, and their ratio at each station are plotted for each aftershock

Wenchuan rupture zones decreases with time because the post-seismic fault healing has occurred since the 2008 $M8$ mainshock.

We had examined ~350 Wenchuan aftershocks recorded at ZDSN stations in 2008 and divided them into two groups (Li et al. 2012, 2014b). Aftershocks in the first group show prominent FZTWs with large amplitudes and long post-S coda durations at ZDSN network stations located close to surface ruptures of Wenchuan earthquake, but not at stations away from rupture zones. Aftershocks in the second group do not

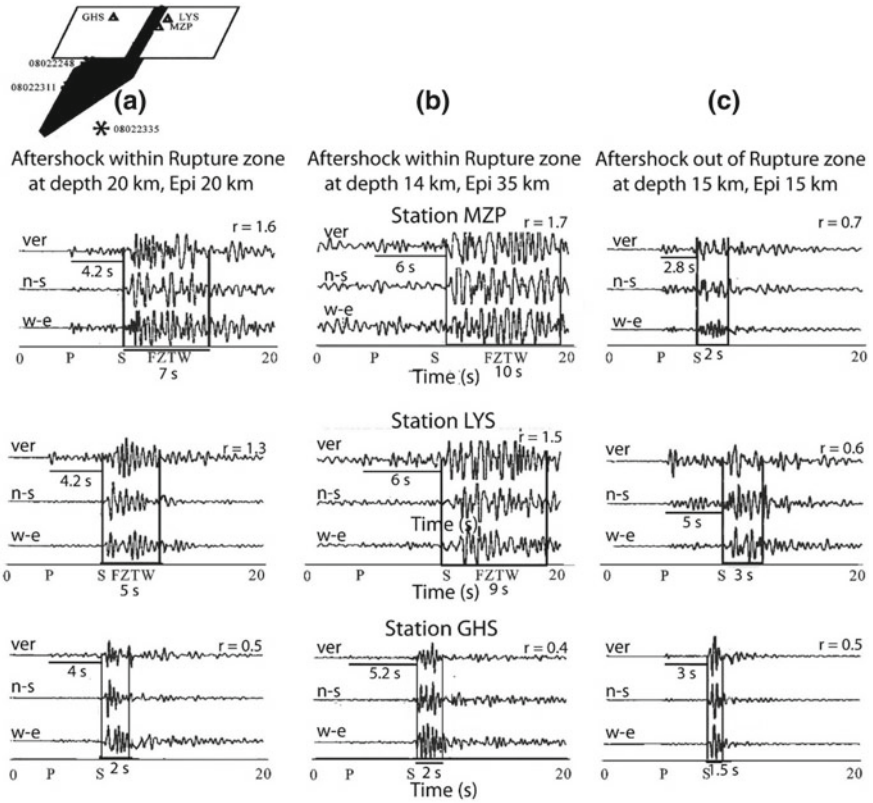

Fig. 6.12 Top left: The schematic diagram shows locations of network stations MZP, LYS, and GHS (triangles) and three Wenchuan aftershocks (stars) with respect to the rupture zone along the YBF. **a–c** Low-pass (<3 Hz) filtered three-component seismograms recorded at stations (top) MZP, (middle) LYS, and (bottom) GHS for the three aftershocks. From left to right: a $M2.8$ aftershock and a $M1.9$ aftershock occurring within the YBF rupture zone northeast of station MZP, and a $M2.3$ off-fault aftershock southeast of station MZP. Aftershock ID numbers, depths and epicentral distances are plotted in the figure. The post-S coda duration, P-to-S time, and their ratio at each station are plotted for each aftershock. Prominent FZTWs were recorded at stations MZP and LYS closet to Wenchuan rupture zone along the YBF for aftershocks within the rupture zone, but no clear FZTWs registered at station GHS for three aftershocks within or away from the rupture zone

show clear FZTWs at all network stations. We identify aftershocks in the first group based on criteria: the $(t_C - t_S)/(t_S - t_P)$ ratios of recorded FZTWs is larger than 1.2. We interpret that these aftershocks in the first group occurred within or very close to the low-velocity waveguides formed by highly damaged rupture zones of the 2008 $M8$ Wenchuan earthquake. In contrast, aftershocks in the second group, showing brief S-waves with short post-S wavetrains dominate in seismograms recorded at all stations because they occurred out of the rupture zone and did not generate FZTWs well. Locations of aftershocks in the first group generating prominent FZTWs delineate the

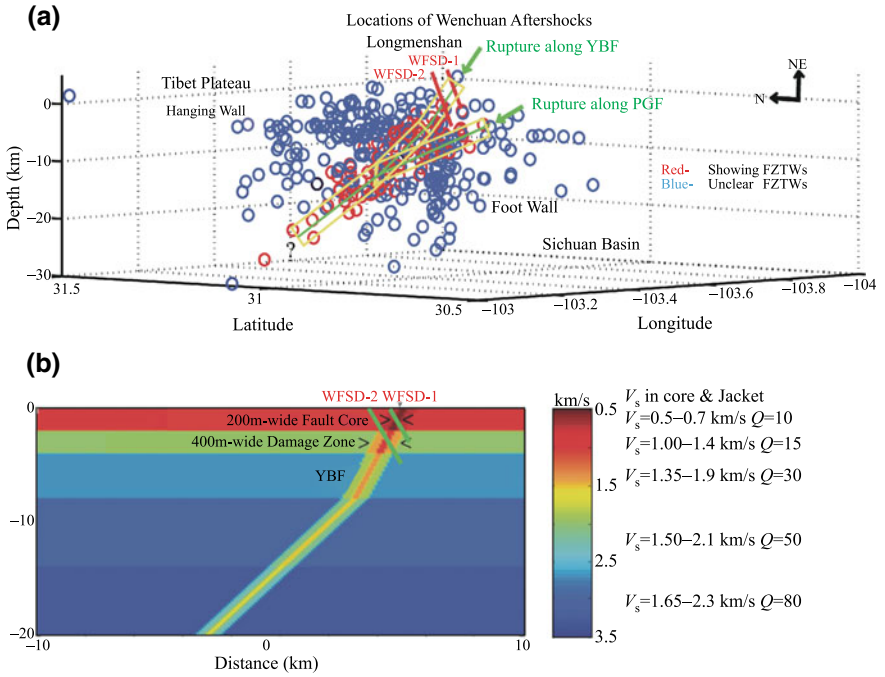

Fig. 6.13 **a** Locations of ~350 Wenchuan aftershocks (circles) which waveforms have been examined. Red circles denote aftershocks in group 1 showing clear FZTWs. Blue circles denote aftershocks in group 2 without clear FZTWs. Yellow bands are interpreted as being damage zones based on locations of those aftershocks generating prominent FZTWs, which indicate the principal slip planes of Wenchuan earthquake along the YBF and PGF dipping at different angles at shallow depth. Two red bars denote two CAGS scientific boreholes WFSD-1 and WFSD-2 drilling through the YBF (Xu et al. 2008b). **b** Vertical section of velocity and Q model across the YBF used in 3-D finite-difference simulations of observed FZTWs. A 200-m-wide (in horizontal) fault core zone composed by severely damaged rocks is sandwiched by the 400-m-wide (in horizontal) jacket with moderate damage rocks. Velocities within the damage zone are reduced by 25–50% from wall-rock velocities with the maximum reduction within the fault core at shallow depth. The fault dips at 75° above 4 km and 45° below. Shear velocities and Q values within the fault core and damaged jacket at different depths are shown at right to the model. Two green bars denote CAGS boreholes WFSD-1 and WFSD-2 drilled to depths of 1201 and 2284-m, respectively

low-velocity waveguides formed by severely damaged fault rocks within the YBF and PGF (Fig. 6.13a), in general agreeable with the geometry of reverse-thrusting south Longmenshan fault system in the geological model (Zhang et al. 2009). Locations of aftershocks in group 1 show that Wenchuan rupture zone was bifurcated along the YBF and PGF, and merged at depth between approximate 10 and 15 km, consistent with the geometry of these two faults in the geological map (Fig. 6.13a).

Based on the geological mapping of surface ruptures along the Longman-Shan fault in the 2008 $M8$ Wenchuan earthquake (e.g., Zhang et al. 2008), the information from cores of fault-zone drilling at the south YBF after Wenchuan earthquake (Xu

et al. 2008b), and the geometry of low-velocity waveguides along rupture zones at depth inferred by locations of Wenchuan aftershocks generating prominent FZTWs (Fig. 6.13a), we constructed a primary model for rupture zone across the dipping YBF (Fig. 6.13b). The near-surface width of the low-velocity rupture zone along the south YBF is constrained by the geological mapping (Xu et al. 2009), core analysis of fault-zone drilling (Xu et al. 2008b), and the FZTWs recorded at a linear seismic array deployed across the YGF (Li 2008, 2010; Li et al. 2009). The depth extension of the low-velocity rupture zone along the south YBF at depth is constrained by the coseismic slip model of the 2008 Wenchuan earthquake derived from joint inversion of interferometric synthetic aperture radar, GPS, and field data (Chen et al. 2008; Tong et al. 2010; Xu et al. 2010). Velocities of surrounding rocks in our model are constrained by Sichuan Province velocity model (An et al. 2010) and results from low-frequency 3D wave propagation modeling of the 2008 M8 Wenchuan earthquake (Chavez et al. 2010). The structural model in Fig. 6.13b is depth dependent and includes a 200-m-wide rupture zone sandwiched in the 400-m-wide damage zone (jacket). In simulation, a double-couple source is placed against one edge of the fault core zone. The velocities within the fault core are reduced by 35–55% from wall-rock velocities with the maximum reduction within the fault core at shallow depth. This structure most effectively traps 1–10-Hz seismic waves.

In order to better understand the mechanical, physical and chemical characteristics of the Longmen Shan Fault (LSF) ruptured in the 2008 M8 earthquake, five scientific boreholes were drilled near the surface rupture along the LSF by Chinese Academe of Geological Science (CAGS) (Xu et al. 2008b; refer to Chap. 3 in this book). Boreholes WFSD-1 and WFSD-2 were drilled through the YBF where nearly ~4.3-m vertical slip found at the surface in the 2008 M8 Wenchuan earthquake (see Fig. 6.13b). The fault scarp with sleek surface caused by one rock mass sliding over another is seen clearly at this site (Fig. 6.14). Figure 6.14 shows a severely fractured zone with the apparent thickness of ~183 m across the 1201-m-deep CAGS borehole WFSD-1. Lithologic profile of cores indicates that fault breccia and gouges consist of Triassic sedimentary rocks. Cataclasites mostly with dark to light-gray color are present in the Pengguan massif and abundant near the boundary with an incohesive fault zone in the Triassic sedimentary rocks. Fragments of cataclasites are contained in the wide fault zone from 586- to 759-m depth, within which fault breccia and gouges are included (Li et al. 2013 refer to the details in Chap. 3 of this book). The subsurface damage zone along the rupture zone on the YBF is composed of many subsidiary faults as also shown in the ~190-m-wide outcrop at the hanging wall of the YBF, consistent with the width of rupture zone of the YBF at shallow depth shown in our primary model (Fig. 6.13b) inferred by FZTWs generated by Wenchuan aftershocks in 2008 (Fig. 6.13a).

In the following examples, we show synthetic FZTWs using the structural model in Fig. 6.13b to fit observed FZTWs for Wenchuan aftershocks occurring in 2008. The details of simulations of these FZTWs have been discussed in our previous papers (Li et al. 2012, 2014b). Figure 6.15a shows 3-D finite-difference synthetic seismograms to fit the seismic profile recorded at the cross-fault dense array for a M2.1 aftershock occurring within the YBF rupture zone at depth of 10 and ~30 km from the array in

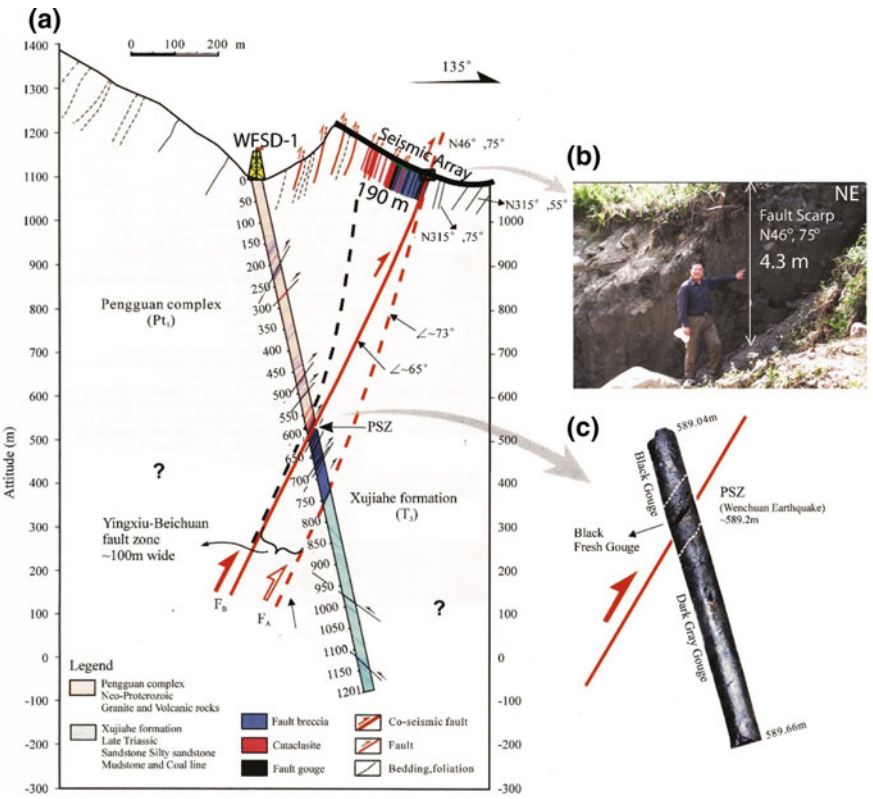

Fig. 6.14 (Courtesy of Li et al. 2013; Li et al. 2014b). **a** Geologic cross-section across the drilling site of ~1200-m-deep borehole WFSD-1 and coseismic surface rupture zone of the 2008 *M*8 Wenchuan earthquake (adapted from HB Li et al. 2013). The width of the YBF (consisting of fault gouge, breccia, and cataclasite) is ~190 m at the outcrop. The surface rupture zone strikes N46°E and dips 75°NW at the fault outcrop. FA and FB: the possible co-seismic slip of the 2008 Wenchuan earthquake from the observed fault scarp at the surface to the top and bottom of the fracture zone in WFSD-1 cores, respectively. The YBF core zone is about 100 m wide shown in the WFSD-1 rock cores, consistent with the ~190 m width of the fault zone at the outcrop. The dip angle of the YBF is about 68°–73° at the depth of 760 m. **b** The sleek surface on the nearly-vertical fault scarp sliding of ~4.3 m between the hanging wall and footwall along the south YBF at this site where a dense linear seismic array of 16 seismographs (black line in the left figure) was deployed across the surface rupture to record FZTWs generated by aftershocks in 2008. The lead author Y.G. Li of this chapter stands in the front of the fault scarp. **c** The core taken from WFSD-1 shows black to dark-gray gouges and the principal slip zone (PSZ) at the depth of 589.2 m

2008, using the model in Fig. 6.13b. Prominent FZTWs with large amplitudes and long post-S coda durations appear at stations within the ~200-m-wide low-velocity rupture core-zone. The $(t_C - t_S)/(t_S - t_P)$ ratios of ~1.1 at stations within the rupture zone.

We then simulated seismograms recorded at ZDSN network stations for Wenchuan aftershocks occurring within the rupture zone in 2008. For example, Fig. 6.15b shows 3-D finite-difference synthetic waveforms using the model (Fig. 6.13b) to fit observed seismograms at stations BAJ, MZP, LYS, and ZDZ for a $M2.3$ on-fault aftershock occurring at 7-km-depth within the rupture zones long the YBF southwest of these stations in 2008. FZTWs with large amplitudes, long post-S coda durations, and the $(t_C - t_S)/(t_S - t_P)$ ratios of 1.3–1.4 appear at stations MZD and LYS located close to the surface ruptures along the south YBF. Seismograms recorded at station BAJ near the geological fault trace of the southern YBF segment without surface rupture found in the 2008 Wenchuan earthquake show the $(t_C - t_S)/(t_S - t_P)$ ratio of 0.7. Furthermore, seismograms recorded at station ZDZ located close to the surface rupture along the PGF for this shallow aftershock occurring at 7-km depth on the YBF show the $(t_C - t_S)/(t_S - t_P)$ ratio is 0.8, suggesting that two ruptured faults YBF and PGF connect at depth below at least 7 km. If two low-velocity rupture zones along the YBF and PGF are connected at the depth above 7 km, the $(t_C - t_S)/(t_S - t_P)$ ratio registed at station ZDZ close to the PGF is expected to be similar to that registered at station MZD and LYS 0.8 close to the YBF. In general, synthetic seismograms match the features of observed seismograms.

Finally, Fig. 6.16a exhibits 3-D finite-difference synthetic seismograms to fit observations at network stations GHS and MDZ for other two Wenchuan aftershocks in 2008 (events 08022248 and 08022311) occurring within the Wenchuan rupture zone at depths of 14 and 25 km; their epicentral distances to station MZD are approximately ~32 and ~20 km, respectively. The hypocentral distances between the two aftershocks and stations are similar (~32–35 km). Fault-zone trapped waves with large amplitudes and long post-S durations arrived at station MZD located close to the surface rupture of the YBF. In contrast, brief S-waves arrived at station GHS ~6-km NW of the YBF. The measured $(t_C - t_S)/(t_S - t_P)$ ratios are 1.5–1.7 at station MZP for the two aftershocks occurring within the Wenchuan rupture zone, while the $(t_C - t_S)/(t_S - t_P)$ ratios are 0.5 at station GHS for the same aftershocks. We interpret that the FZTWs were well generated and well recorded when both the source and receiver were located within the low-velocity waveguide formed by severely damaged rocks along the YBF/PGF ruptured in the 2008 $M8$ Wenchuan earthquake. Figure 6.16b exhibits synthetic and observed seismograms for aftershock (08022248) at ZDSN station LYS close to the surface rupture of the YBF and station BAJ near the YBF beyond the southernmost surface rupture caused by the 2008 $M8$ mainshock. The $(t_C - t_S)/(t_S - t_P)$ ratios are 1.7 at station LYS, but 1.0 at station BAJ, further suggesting that the Wenchuan rupture zone along the YBF likely diminished when it approached southward to station BAJ site during dynamic rupture in the 2008 $M8$ mainshock.

In these examples of simulations of FZTWs generated by Wenchuan early aftershocks in 2008, we demonstrate a good fit between the synthetic and observed seismograms at Zipingpu dam seismic network stations. Our primary model (in Fig. 6.13b) is in general able to characterize the subsurface rock damage structure along the south

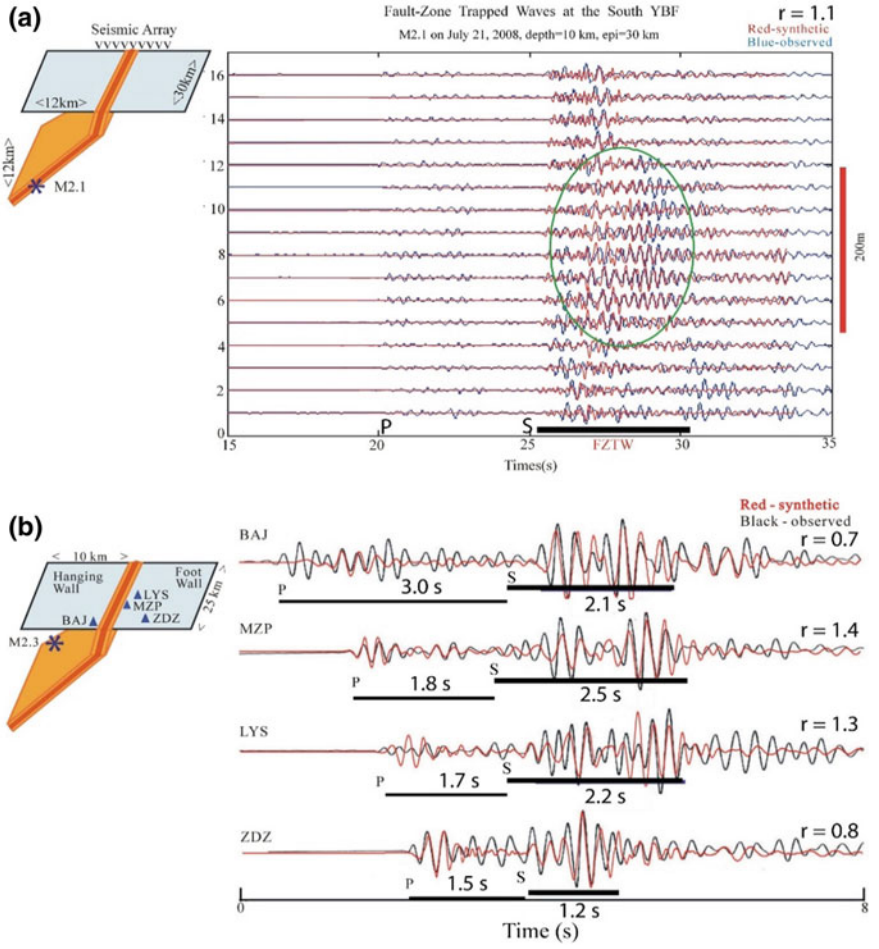

Fig. 6.15 **a** Top left: Schematic diagram shows the geometry of YBF rupture zone, the aftershock location, and the cross-fault array. 3-D finite-difference synthetic seismograms (red lines) using the best-fit model parameters in Fig. 6.13b to fit seismograms (blue lines) recorded at the 16-station linear array across the YBF for a $M2.1$ on-fault aftershock occurring at depth of ~10 and ~30 km NE of the array. Seismograms have been low-pass (<3 Hz) filtered. FZTWs with large amplitudes and long wave trains (in a green circle) appear at stations within the 200-m-wide fault core (marked by the vertical red bar at right). The horizontal bar denotes the duration of FZTWs, in which amplitude envelopes of FZTWs are above twice the level of the background noise coda. The $(t_C - t_S)/(t_S - t_P)$ ratio is 1.1. **b** Top left: Schematic diagram shows the fault geometry and locations of four network stations LYS, MZP, ZDZ and BAJ and a $M2.3$ aftershock occurring at 7-km depth within the fault-zone. Model parameters are shown in Fig. 6.13b. Vertical-component synthetic (red) and observed (black) seismograms recorded at four network stations for this on-fault aftershock. The post-S coda durations are denoted by horizontal bars. Seismograms have been <3 Hz filtered and plotted in trace-normalization. Post-S coda durations, P-to-S times and their ratios at these stations are shown in the figure

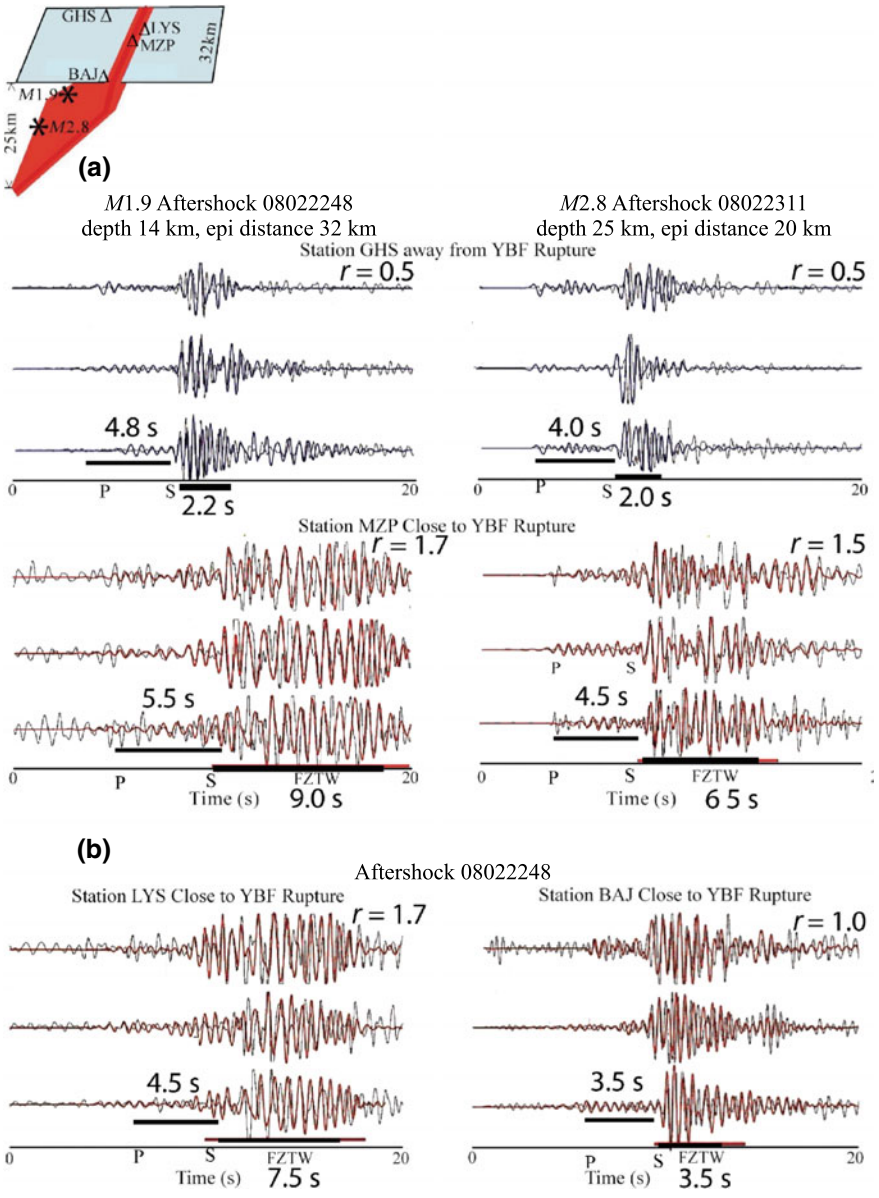
GHS Δ
LYS
MZP
BAJ
32km
25km
M1.9
M2.8
(a)
M1.9 Aftershock 08022248
depth 14 km, epi distance 32 km
M2.8 Aftershock 08022311
depth 25 km, epi distance 20 km
Station GHS away from YBF Rupture
r = 0.5
r = 0.5
4.8 s
4.0 s
0
P
S
2.2 s
2.0 s
20
Station MZP Close to YBF Rupture
r = 1.7
r = 1.5
5.5 s
4.5 s
FZTW
Time (s)
9.0 s
6.5 s
(b)
Aftershock 08022248
Station LYS Close to YBF Rupture
Station BAJ Close to YBF Rupture
r = 1.7
r = 1.0
4.5 s
3.5 s
7.5 s
3.5 s

◀**Fig. 6.16** **a** top left: The schematic diagram shows the fault geometry and locations of Zipingpu dam seismic network (ZDSN) stations MZP, LYS, BAJ, and GHS for two aftershocks (event 08022248 and 08022311) occurring within Wenchuan rupture zones in 2008. The magnitudes, focal depths and epicentral distances of these two aftershocks as well as post-S coda durations, P-to-S times and $(t_C - t_S)/(t_S - t_P)$ ratios are shown in the figure. 3-D finite-difference synthetic seismograms were computed using the model in Fig. 6.13b. Synthetic waveforms (red color) in general match seismograms (gray color) with prominent FZTWs recorded at station MZP close to the surface rupture of the YBF. At station GHS away from the YBF, synthetic waveforms (black color) also match seismograms (gray color) showing brief S-waves but without FZTWs. **b** Synthetic and observed seismograms at network stations LYS and BAJ for aftershock (event 08022248). FZTWs recorded at station LYS closer to the surface rupture along the YBF show larger The $(t_C - t_S)/(t_S - t_P)$ ratio (1.7) than the ratio (1.0) at BAJ station site where there were no surface ruptures along the YBF

YBF which ruptured in the 2008 Wenchuan $M8$ earthquake. Based on this preliminary fault-zone structural model, we develop a model including multiple faults of the southern LMSF system to simulate the FZTWs generated by Lushan aftershocks and recorded at stations located within Lushan and Wenchuan rupture zones in this chapter.

References

An, M.J., M. Feng, and C.X. Long. 2010. Deep ruptures around the hypocenter of the 12 May 2008 Wenchuan earthquake deduced from aftershock observations. *Tectonophysics* 491: 96–104.

Chavez, M., E. Cabrera, R. Madariaga, H. Chen, N. Perea, D. Emerson, A. Salazar, M. Ashworth, C.H. Moulinec, X. Li, M. Wu, and G. Zhao (2010). Low-frequency 3D wave propagation modeling of the 12 May 2008 Mw 7.9 Wenchuan earthquake. *Bull. Seism. Soc. Am. 100* (5B): 2561–2573. https://doi.org/10.1785/0120090240.

Chen Y.T., Z.X. Yang, Y. Zhang, C. Liu. 2013a. A brief talk on the 20 April 2013 Lushan M_W 6.7 earthquake. *Acta Sismologica Sinica 35* (3): 285–295.

Chen, Y.T., Z.X. Yang, Y. Zhang, and C. Liu. 2013. From 2008 Wenchuan earthquake to 2013 Lushan earthquake. *Scientia Sinica Terrae* 43: 1064–1072.

Chen, Y.T., L.S. Xu, Y. Zhang, H.L. Du, W.P. Feng, and C. Li. 2008. *Report on the source characteristics of the 12 May 2008 M8 Webcguan Earthquake: Preliminary results from investigation*. Institution of Geophysics, Beijing: China Earthq. Adm.

Densmore, A.L., Y. Li, M.A. Ellis, and R. Zhou. 2005. Active tectonics and erosional unloading at the eastern margin of the Tibetan Plateau. *Journal of Mountain Science* 2 (2): 146–154.

Densmore, A.L., M.A. Ellis, Y. Li, R. Zhou, G.S. Hancock, and N. Richardson. 2007. Active tectonics of the Beichuan and Pengguan faults at the eastern margin of the Tibetan Plateau. *Tectonics* 26 (TC4005): 1–17. https://doi.org/10.1029/2006TC001987.

Dong, S.P., Z.J. Han, and Y.F. An. 2017. Paleoseismological events in the "seismic gap" between the 2008 Wenchuan and the 2013 Lushan earthquakes and implications for future seismic potential. *Journal of Asian Earth Sciences* 135: 1–15.

Du, F., F. Long, X. Ruan, G. Yi, Y. Gong, M. Zhao, Z. Zhang, H. Qiao, Z. Wang, and J. Wu. 2013. The M7.0 Lushan earthquake and the relationship with the M8.0 Wenchuan earthquake in Sichuan. *Chinese Journal of Geophysics*56(5): 1772–1783. http://doi.org/10.6038/cjg20130535 (in Chinese with abstract in English).

Fang L.H., J.P. Wu, W.L. Wang, W.K. Du, J.R. Su, C.Z. Wang, T. Yang, and Y. Cai. 2015. Aftershock observation and analysis of the 2013 Ms 7.0 Lushan earthquake. *Seismological Research Letters*86(4). https://doi.org/10.1785/0220140186.

Graves, R.W. 1996. Simulating seismic wave propagation in 3D elastic media using staggered-grid finite differences. *Bulletin of the Seismological Society of America* 86: 1091–1106.

Han L.B., X.F. Zheng, C.S. Jiang, S.D. Ni, H.J. Zhang, and F. Long. 2014. Focal mechanisms of the 2013 Mw 6.6 Lushan, China earthquake and high-resolution aftershock relocations. *Seismological Research Letters* 85(1): 8–14. https://doi.org/10.1785/0220130083.

Hao, J., C. Ji, W. Wang, and Z. Yao. 2013. Rupture history of the 2013 Mw 6.6 Lushan earthquake constrained with local strong motion and teleseismic body and surface waves. *Geophysical Research Letters* 40(20): 5371–5376. https://doi.org/10.1002/2013gl056876.

Jia, K., S. Zhou, J. Zhuang, and C. Jiang. 2014. Possibility of the independence between the 2013 Lushan earthquake and the 2008 Wenchuan earthquake on Longmen Shan fault, Sichuan, China. *Seismological Research Letters* 85 (1): 60–67. https://doi.org/10.1785/0220130115.

Li, H.B., H. Huang, Z.Q. Xu, J.L. Si, J.L. Pei, T.F. Li, Y. Huang, S.R. Song, L.W. Kuo, Z.M. Sun, M.L. Chevalier, and D.L. Liu. 2013. Characteristics of the fault-related rocks, fault zones and the principal slip zone in the Wenchuan Earthquake Fault Scientific Drilling Project Hole-1 (WFSD-1). *Tectonophysics* 584: 23–42.

Li, S.L., X.L. Lai, Z.X. Yao, and Q. Yang. 2009. Fault zone structures of northern and southern portions of the main central fault generated by the 2008 Wenchuan earthquake using fault zone trapped waves. *Earthquake Science* 22 (4): 417–424.

Li, Y.G. 2008. Seismic study of the San Andreas fault in California and the Longmen-Shan fault ruptured in the 2008 M8 Wenchuan earthquake in China. *Academic Perspectives* 4: 4–25. ISSN 1936-1246.

Li, Y.G. 2010. Fault zone trapped waves at the Thrusting Longmen-shan fault of *M* 8.0 Wenchuan earthquake: 3-D finite difference investigation on trapping efficiency. Abstract, 2010 Western Pacific Geophysical Meeting, Taipei.

Li, Y.G., and P.C. Leary. 1990. Fault-zone trapped seismic waves. *Bulletin of the Seismological Society of America* 80: 1245–1271.

Li, Y.G. and P.E. Malin. 2008. San Andreas Fault damage at SAFOD viewed with fault-guided waves. *Geophysical Research Letters* 35: L08304. https://doi.org/10.1029/2007GL032924.

Li, Y.G., J.E. Vidale, and K. Aki. 2000. Depth-dependent structure of the Landers fault zone using fault zone trapped waves generated by aftershocks. *Journal of Geophysical Research* 105: 6237–6254.

Li, Y.G., J.E. Vidale, and S.E. Cochran. 2004. Low-velocity damaged structure of the San Andreas fault at Parkfield from fault-zone trapped waves. *Geophysical Research Letters* 31: L12S06.

Li, Y.G., J.E. Vidale, D. Oglesby, S.M. Day, and E. Cochran. 2003. Multiple-fault rupture of the M7.1 Hector Mine, California, earthquake from fault-zone trapped waves. *Journal of Geophysical Research* 108, ESE 11: 1–25.

Li, Y.G., K. Aki, D. Adams, A. Hasemi, and W. H. K. Lee. 1994. Seismic guided waves trapped in the fault zone of the Landers, California, earthquake of 1992. *Journal of Geophysical Research* 99(11): 705–722.

Li, Y.G., R.D. Catchings, and M. R. Goldman. 2016. Subsurface fault damage zone of the 2014 Mw 6.0 South Napa, California, earthquake viewed from fault-zone trapped waves. *Bulletin of the Seismological Society of America* 106. https://doi.org/10.1785/0120160039.

Li, Y.G., P.C. Leary, K. Aki, and P.E. Malin. 1990. Seismic trapped modes in the Oroville and San Andreas fault zones. *Science* 249: 763–766.

Li, Y.G., G. De Pascale, M. Quigley, and D. Gravely. 2014a. Fault damage zones of the M7.1 Darfield and M6.3 Christchurch earthquakes characterized by fault-zone trapped waves. *Tectonophysics*. https://doi.org/10.1016/j.tecto.2014.01.029.

Li, Y.G., Z.Q. Xu, and H.B. Li. 2014b. Rock damage structure of the south Longmen-Shan fault in the 2008 M8 Wenchuan earthquake viewed with fault-zone trapped waves and scientific drilling. *Acta Geological Sinica (English Edition)* 88 (2): 444–467.

Li, Y.G., J.R. Su, and T.C. Chen (2012). Fault-zone trapped waves at a dip fault: Documentation of rock damage on the thrusting Longmen-Shan fault ruptured in the 2008 M8 Wenchuan earthquake. In *Imaging, Modeling and Assimilation in Seismology*, 151–198, ed. Y.G. Li. Higher Education Press in Beijing and De Gruyter in Boston.

Liu, J., G.X. Yi, Z.W. Zhang, Z. Guan, X. Ruan, F. Long, and F. Du. 2013. Introduction to the Lushan, Sichuan M7.0 earthquake on 20 April 2013. *Chinese Journal of Geophysics* 56 (4): 1404–1407. https://doi.org/10.6038/cjg20130434. (in Chinese).

Liu R.F., Y.T. Chen, L.Y. Zou, H.F. Chen, and J.H. Liang. 2013. Determination of parameters for the 20 April 2013 Lushan M_W6.7(M_S7.0) earthquake in Sichuan Province. *Acta Seismologica Sinica* 35(5): 652–660.

Parsons, T., and M. Segou. 2014. Stress, distance, magnitude, and clustering influences on the success or failure of an aftershock forecast: the 2013 Mw 6.6 Lushan earthquake and other examples. *Seismological Research Letters* 85(1). http://doi.org/10.1785/0220130100.

Parsons, T., C. Ji, and E. Kirby. 2008. Stress changes from the 2008 Wenchuan earthquake and increased hazard in the Sichuan basin. *Nature* 454: 509–510.

Pei, S., H. Zhang, J. Su, and Z. Cui. 2014. Ductile gap between the Wenchuan and Lushan earthquakes revealed from the two dimensional Pg seismic tomography, Scientific Reports 4. https://doi.org/10.1038/srep06489.

Quigley, M., R. Van Dissen, N. Litchfield, P. Villamor, D. Barrel, T. Stahl, E. Bilderback, and D. Noble. 2012. Surface rupture during the 2010 Mw7 Darfield (Canterbury) earthquake; implications for fault rupture dynamics and seismic hazard analysis. *Geology* 40 (1): 55–58.

Shcherbakova,R., M. Nguyena, and M. Quigley. 2012. Statistical analysis of the 2010 MW7.1 Darfield Earthquake aftershock sequence. *New Zealand Journal of Geology and Geophysics* 55(3): 305–311.

Su, J.R., Y. Zheng, J.S. Yang, T.C. Chen, and P. Wu. 2013. Accurate locating of the Lushan, Sichuan M 7.0 earthquake on 20 April 2013 and its aftershocks and analysis of the seismogenic structure. *Chinese Journal of Geophysics* 56(8): 2636–2644. https://doi.org/10.6038/cjg20130813.

Tong, X.P., D.T. Sandwell, and Y. Fialko. 2010. Coseismic slip model of the 2008 Wenchuan earthquake derived from joint inversion of interferometric synthetic aperture, radar, GPS, and field data. *Journal Geophysical Research* 115: B04314. https://doi.org/10.1029/2009JB006625.

Vidale, J.E., D.V. Helmberger, and R.W. Clayton. 1985. Finite-difference seismo-grams for SH waves. *Bulletin of the Seismological Society of America* 75: 1765–1782.

Wang, W.M., J.L. Hao, and Z.X. Yao. 2013. Preliminary result for rupture process of Apr. 20, 2013, Lushan earthquake, Sichuan, China. *Chinese Journal of Geophysics* 56: 1412–1417. https://doi.org/10.6038/cjg20130436. (in Chinese with English abstract).

Xu, C., and X. Xu. 2014. The spatial distribution pattern of landslides triggered by the 20 April 2013 Lushan earthquake of China and its implication to identification of the seismogenic fault. *Chinese Science Bulletin* 59 (13): 1416–1424. https://doi.org/10.1007/s11434-014-0202-0.

Xu, C.J., Y. Liu, and Y.M. Wen. 2010. Coseismic slip distribution of the 2008 Mw 7.9 Wenchuan earthquake from joint inversion of GPS and InSAR data. *Bulletin of the Seismological Society of America* 100: 2736–2749. https://doi.org/10.1785/0120090253.

Xu, X.X., Y.G. Wen, G. Chen, Y. Klinger, J. Hubbard, and J. Shaw. 2009. Coseismic reverse- and oblique-slip, surface faulting generated by the 2008 Mw 7.9 Wenchuan earthquake. *The China Geological* 37(6): 515–518.

Xu, X.W., X.Z. Wen, and Z.J. Han et al. 2013. Lushan Ms 7.0 earthquake: a blind reserve-fault earthquake. *Chinese Science Bulletin* 58. http://dx.doi.org/10.1007/s11434-013-5999-4.

Xu, Z.Q., S.C. Ji, H.B. Li, L.W. Hou, X.F. Fu, and Z.H. Cai. 2008a. Uplift of the Longmenshan range and the Wenchuan earthquake. *Episodes* 31: 291–301.

Xu, Z.Q., H.B. Li, and Z.L. Wu. 2008b. Wenchuan earthquake and scientific drilling. *Acta Geologica Sinica (Chinese edition)* 82 (12): 1613–1622.

Yang, Z.X., F. Waldhauser, Y.T. Chen, and P.G. Richards. 2005. Double-difference relocation of earthquakes in central-western China, 1992–1999. *Journal of Seismology* 9: 241–264.

Zhang, G.W., and J.S. Lei. 2013. Relocations of Lushan, Sichuan strong earthquake (Ms) 7.0 and its aftershocks. *Chinese Journal of Geophysics* 56: 1764–1771. https://doi.org/10.6038/cjg20130534. (in Chinese with English abstract).

Zhang, P.Z., X.Z. Wen, X.W. Xu, W.J. Gan, M. Wang, Z.K. Shen, Q.L. Wang, Y. Huang, Y. Zheng, X.J. Li, Z.Q. Zhang, S.L. Ma, Y.K. Ran, Q.Y. Liu, Z.F. Ding, and J.P. Wu. 2009. Tectonic model of the great Wenchuan earthquake of May 12, 2008, Sichuan, China. *Chinese Science Bulletin* 54 (7): 944–953. (in Chinese).

Zhang, Y., S. Dong, C. Hou, et al. 2013a. Seismogenic structure of the April 20, 2013, Lushan Ms 7 earthquake in Sichuan. *Acta Geologica Sinica* 87 (3): 633–645.

Zhang Y., L.S. Xu, and Y.T. Chen. 2013b. Rupture process of the Lushan 4.20 earthquake and preliminary analysis on the disaster-causing mechanism. *Chinese Journal of Geophysics* 56(4): 1408–1411. https://doi.org/10.6038/cjg20130435 (in Chinese with English abstract).

Zhang, Y., R. Wang, Y.T. Chen, L. Xu, F. Du, M. Jin, H. Tu, and T. Dahm. 2014. Kinematic rupture model and hypocenter relocation of the 2013 Mw 6.6 Lushan earthquake constrained by strong-Motion and teleseismic data. *Seismological Research Letters* 85(1): 15–22. https://doi.org/10.1785/0220130126.

Zhao, B., Y. Gao, Z.B. Huang, X. Jiang, and D.H. Li. 2013. Double difference relocation, focal mechanism and stress inversion of Lushan Ms 7.0 earthquake sequence. *Chinese Journal of Geophysics* 56: 3385–3395. https://doi.org/10.6038/cjg20131014. (in Chinese with English abstract).

Zhang, P.-Z., X.-W. Xu, X.-Z. Wen, and R.K. Rang. 2008. Slip rates and recurrence intervals of the Longmen Shan active fault zone and tectonics implications for the mechanism of the May 12 Wenchuan earthquake, 2008, Sichuan, China (in Chinese with English abstract). *Chinese Journal of Geophysics* 51: 1066–1073.

Zhang, P.-Z., X.-Z. Wen, Z.-K. Shen, and J.-H. Chen. 2010. Oblique, high-angle, listric-reverse faulting and associated development of strain: The Wenchuan earthquake of May 12, 2008, Sichuan, China. *Annual Reviews of Earth and Planetary Sciences* 38: 353–382. https://doi.org/10.1146/annurev-earth-040809-152602.

Zhen, X.F., Y. Luo, L.B. Han, and Y.L. Shi. 2013. The Lushan Ms 7.0 earthquake on 20 April 2013: A high-angle thrust event. *Chinese Journal of Geophysics* 56 (4): 1418–1424. https://doi.org/10.6038/cjg20130437. (in Chinese with English abstract).

Zhu, S., and M. Miao. 2015. How did the 2013 Lushan earthquake (Ms = 7.0) trigger its aftershocks? Insights from static Coulomb stress change calculations. *Pure and Applied Geophysics* http://doi.org/10.1007/s00024-015-1064-3.

Zhu, S. 2016. Is the 2013 Lushan earthquake (Mw = 6.6) a strong aftershock of the2008 Wenchuan, China mainshock (Mw = 7.9)? *Journal of Geodynamics* 99: 16–26.

Chapter 7
Analyzing Earthquake Events in the Vicinity of Wenchuan Using ETAS Models

Annie Chu

Abstract This chapter applies the spatial–temporal epidemic-type aftershock sequence (ETAS) model of Ogata to regional seismicity of surrounding Wenchuan, China. Events between 1973 and 2017 with magnitude 4.0 or above are included for analysis according to the model. The Preliminary Determination of Epicenters (PDE) data used in this study are in a rectangular space window between 98°E and 108°E in longitude and between 26°N and 36°N in latitude. The space window includes the Wenchuan event of May 12, 2008 (epicenter located at 31.021°N, 103.367°E) approximately in the center of the rectangle. We implement five different models, a homogeneous model and four inhomogeneous models, and we compare them in model diagnostics and predicted intensity rate based on MLEs (maximum likelihood estimates), with calculation details provided and emphasized. Additionally, the data in 45 years between 1973 and 2017 are partitioned into two catalogs, before and after the Wenchuan event, and models are built for each catalog for comparison. We have discovered that the seismic activities appear distinct before and after the Wenchuan event, and we describe the difference using the ETAS model with its background rates, triggering parameters and predicted intensity rate. We also implement simulation to provide standard error and confidence interval for each triggering parameter of the best model found among the five models.

Keywords Branching-point processes · Earthquake forecasting · Epidemic-type aftershock sequence (ETAS) model · Space-time point process models · Maximum likelihood estimation · EM algorithm · Wenchuan earthquake

A. Chu (✉)
Department of Mathematics, Woodbury University, 7500 N. Glenoaks Boulevard, Burbank, CA 91504, USA
e-mail: aannchu@gmail.com

Y.-G. Li (ed.), *Earthquake and Disaster Risk: Decade Retrospective of the Wenchuan Earthquake*, https://doi.org/10.1007/978-981-13-8015-0_7

7.1 Introduction

To study the regional seismicity using data analysis and statistical models, this chapter applies the epidemic-type aftershock sequence (ETAS) model of Ogata (1998) to the regional data of Wenchuan and its vicinity. The ETAS model is a spatial–temporal Hawke's model to describe the intensity rate of seismicity as the sum of background rate and triggering function. The ETAS model is commonly used for modern seismic analysis on regional data in Japan (Ogata) and Southern California (Veen 2006) and on global data (Chu et al. 2011). It has been used for study of the Wenchuan earthquake on similar rectangular regions, using different time windows of 1970/01/01–2008/05/12 (Jiang and Zhuang 2010) and 1973–2013 (Guo et al. 2015). In this chapter, we provide a robust inhomogeneous model to fit the data to ETAS model. The expectation–maximization (EM) algorithm adopted from Veen and Schoenberg (2008) is modified to seek for the maximum likelihood estimates (MLEs). In order to find an optimal model computationally, MLEs of the parameters are obtained using computer software iteratively. The earthquake catalog data in PDE Web site are chosen for data analysis due to its relative completeness over years. A larger time window of 1973–2017 is used in this chapter.

This chapter is organized as follows. Section 7.2 presents information of the Wenchuan's vicinity for our computation, and the dataset used for analysis. Section 7.3 introduces the ETAS methods with an emphasis on the computer software used for implementation of inhomogeneous models. Comparison with the background rate is discussed in this section. Section 7.4 presents the result of homogeneous and inhomogeneous modeling. Section 7.5 provides simulation using the parameters obtained in Sect. 7.4 and standard errors of the triggering parameters. Section 7.6 concludes the chapter.

7.2 The Study Region and Data

We use the data of PDE in the time window of 45 years from 1973/01/01 to 2017/12/31 in this study. The data analyzed are in the rectangular space window [98°E, 108°E] in longitude by [26°N, 36°N] in latitude. The space window includes the location of the Wenchuan earthquake (31.021°N, 103.367°E), recorded 7.9 in centroid moment magnitude and 8.0 in surface magnitude by the PDE database (Preliminary Determination of Epicenters, USGS 2017), approximately in the center of the rectangular window. We have obtained the data, including 2015 events with magnitudes $\geq$4.0, 250 events with magnitudes $\geq$5.0, and 25 events with magnitude $\geq$6.0. The online PDE database is in fact incomplete for events with magnitude <4.0; the magnitude types of those events are different: Some are moment magnitude some are surface magnitude, etc. The PDE data contain only 338 events with magnitude in the interval between 3.0 and 4.0. Therefore, we exclude events with magnitude <4.0 in data analysis. Moreover, there are six events with relatively small magnitude $\leq$4.3 and at

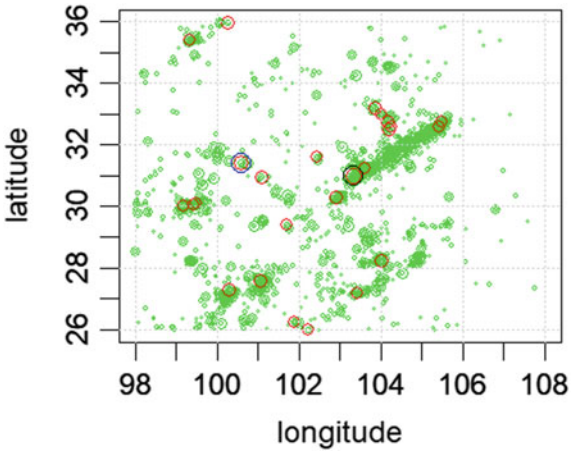

Fig. 7.1 Events in the space window = [98°E, 108°E] by [26°N, 36°N] and time window 1973/01/01 to 2017/12/31. Small green circles indicate events of magnitude 4.0–4.9; large green circles indicate events of magnitude 5.0–5.9. Red circles indicate events of magnitude 6.0–6.9. There are two events of magnitude ≥7.0: The large black circle on (31.021°N, 103.367°E) indicates the M7.9 Wenchuan earthquake event in 2008, and the large blue circle indicates the M7.4 Luhuo earthquake in 1973

depth >70 km in the PDE online database. To be consistent with global zone data analysis of Chu et al. (2011), we do not use these six deep events and include only shallow events at depth ≤70 km in this chapter. The Wenchuan event occurred at the depth of 19 km. In time window 1973/01/01–2017/12/31, there are only two events with magnitude ≥7: the 2008 Wenchuan event with moment magnitude 7.9 and the Luhuo event with surface wave magnitude 7.4 occurring on 1973/02/06.

The events of magnitudes ≥4.0 are plotted in Fig. 7.1. We observe that numerous events appear clustered along the stripe of the Longmenshan fault between the Wenchuan mainshock epicenter (at 31.021°N, 103.367°E) and the northeast end of the Wenchuan aftershock zone (approximately at 106°E, 33.5°N). However, most of the larger events with magnitudes ≥6.0 are scattered in Fig. 7.1, and only four of them are located close to the Longmenshan fault. We also observe that the clusters occur around the Longmenshan fault region and around the bottom-left of the study area, but there are not obvious clusters close to the boundary of area, and this minimizes the bias that may be caused by boundary effect in data modeling.

Grouping the data by 0.1 increment in magnitude, we calculate the number of events in each interval of magnitude. In Fig. 7.2, the survivor function is plotted with $\log_{10}(n)$ versus magnitude, where n denotes the number of events in intervals magnitude ≥4.0 (2009 events), magnitude ≥4.1(1868 events), magnitude ≥4.2(1669 events), etc. The survivor function shows the relation $\log_{10}(n)$ versus magnitude is roughly linear, and it leads to the data's capability to be modeled by the ETAS model.

The region belongs to the active continent (zone 1) of the four major tectonic zones in Bird's tectonic plate model PB2002 (Birds 2003). Zone 1 includes conti-

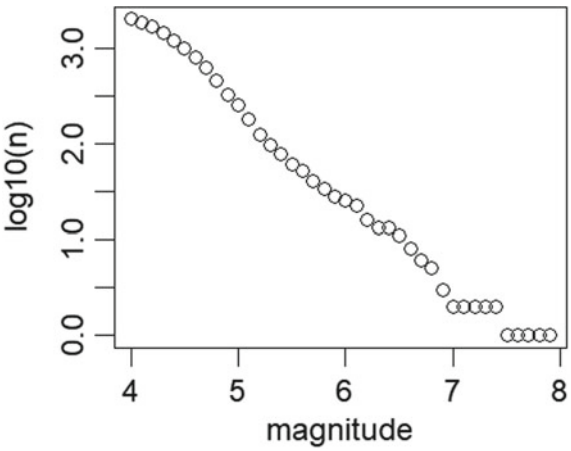

Fig. 7.2 Survival function of the events. $\log_{10}(n)$ is plotted versus event magnitude where n is the cumulative number of events. The function is roughly linear, showing near completeness of the seismic catalog

nental parts of all orogens of PB2002 model, plus continental plate boundaries of PB2002) calculated by Chu et al. (2011). Orogens are part of zone 1 based on Bird's plate boundary model, and it indicates regions of mountain formation or at least topographic roughening. Such regions are difficult to define plates because there is too much seismic, geologic, and geodetic evidence for distributed anelastic deformation (Birds 2003).

This work examines both the estimated Gutenberg–Richter branching ratio 2.6 of zone 1, and the estimated Gutenberg–Richter branching ratio 2.3 provided by Veen (2006) for Southern California earthquake data analysis. The Gutenberg–Richter branching ratio is needed to compute the initial values for the iterated EM algorithm computation, and these two values both lead to the same MLEs in this chapter.

7.3 Model and Method

The model used for data analysis in this chapter is the spatial–temporal ETAS model described in Ogata (1998). Since the rectangular region analyzed is in zone 1 of Bird's tectonic zone (Bird 2003) and one of the three Ogata's models, model (2.3), appears to fit slightly better for this zone with an only small difference compared to Ogata's model (2.4) (Chu 2018), we choose this particular model for data fitting in this chapter.

The ETAS model is a type of Hawkes point process model and is also known as branching or self-exciting point process. For such a process with only event time considered, conditional intensity rate at time t, given history information H_t of all events prior to time t, has the form:

$$\lambda(t|H_t) = \mu(x, y) + \sum_{i:t_i<t} g(t - t_i, m_i) \tag{7.1}$$

Ogata's model (2.3) (1998) extends the temporal ETAS model (7.1) to describe the space-time-magnitude distribution of earthquake occurrences by introducing circular or elliptical spatial functions into the triggering function:

$$\lambda(t|H_t) = \mu(x, y) + \sum_{i:t_i<t} g(t - t_i, x - x_i, y - y_i, m_i) \tag{7.2}$$

where $\mu(x, y) > 0$ denotes the background rate, which may depend on location. A simple case of such model treats $\mu(x, y)$ as constant. Background events are the events treated as always existing and not being triggered by previous events. The second term $\sum_{i:t_i<t} g(t - t_i, x - x_i, y - y_i, m_i)$ is the model's triggering part, and it is considered intensity that is triggered by previous events. The nonnegative function $g(t - t_i, x - x_i, y - y_i, m_i)$ is the triggering function dictating the aftershock activity rate associated with a prior event with time t_i, location (x_i, y_i) and magnitude m_i. Models such as (7.1) are called epidemic by Ogata (1988). In other words, an earthquake can produce aftershock, and the aftershocks produce their aftershocks, and so on.

An example of triggering functions is the time-magnitude ETAS model of Ogata's model (2.3) (1988), which has magnitude-dependent triggering function with the term $K_0/(t - t_i + c)^p$ describing the temporal distribution of aftershocks and is known as the modified Omori–Utsu law (Utsu et al. 1995):

$$g(t - t_i, x - x_i, y - y_i, m_i) = K_0(t - t_i + c)^{-p} \frac{e^{\alpha(m_i - M_0)}}{\left((x - x_i)^2 + (y - y_i)^2 + d\right)^q} \tag{7.3}$$

where the parameter α describes the influence of magnitude, the smaller α value indicates more swarm-type seismic activity, and the larger α value indicates the seismic activity being more clustered. The normalizing constant $K_0 > 0$ governs the expected number of direct aftershocks triggered by earthquake i; m_i denotes the magnitude of earthquake i. Events with magnitude less than the lower cutoff $M_0 = 4$ are excluded. Parameters c and p are related to the temporal decay of aftershock activity. c indicates temporal decay in clustering as an event moves further from the mainshock. The parameter p governs the temporal distribution of aftershocks. The smaller p value corresponds to the longer temporal decay while the larger p value indicates the shorter range decay. Similarly, parameters d and q are related to the temporal decay of aftershock activity. d indicates spatial decay in clustering as an event moves further from the mainshock. The parameter q governs the spatial distribution of aftershocks. The smaller q value corresponds to the longer range decay while the larger q value indicates the shorter range decay (Chu et al. 2011).

The spatial background rate $\mu(x, y)$ may be treated as homogeneous or inhomogeneous depending on modeling preference and computational feasibility. In this

chapter, we adopt both homogeneous and inhomogeneous models. Many researchers have used various methods to manage the computation of inhomogeneous background rate of the model. For example, Ogata (2011) uses Delaunay tessellation, and Veen and Schoenberg (2008) use manual selection of irregular polygons according to geographic features. The method of adopting irregular polygon requires manual dissection of polygons and might be subjective. In this chapter, we demonstrate a simple implementation of rectangular grids to implement the spatial inhomogeneity part instead of manual selection of polygons. It has the advantage of computation simplicity and not being subjective to polygon determination. Once the rectangle is determined, lines may be drawn arbitrarily in both vertical and horizontal directions. In each rectangular grid, the background rate is assumed homogeneous. If the complete region is partitioned into 100 square regions with each direction portioned into 10 segments, we have 100 grids and the complete rectangular region is considered inhomogeneous in space. The number 100 is chosen only for easy understanding and simple computation. The software has the capability to adjust for other possible grid partitions. In the process of model building, we use four variations of square grid partitions and show that model fitting is improved when number of square grids is large enough. Using the values of log-likelihood, we determine the best models among these five models. Including the homogeneous model, we will compare such partitions of five different models. Their abbreviated names are used as follows throughout this chapter:

1. Homogeneous models M_{H}. $\mu(x, y)$ are a constant over the entire region.
2. Inhomogeneous model M_{I25} with 25 grids, each grid is 2° in longitude by 2° in latitude. $\mu(x, y)$ is a constant within one grid. There are 25 parameters of $\mu(x, y)$ to be computed.
3. Inhomogeneous model M_{I100} with 100 grids, each grid is 1° in longitude by 1° in latitude. $\mu(x, y)$ is a constant within one grid. There are 100 parameters of $\mu(x, y)$ to be computed.
4. Inhomogeneous model M_{I400} with 400 grids, each grid is 0.5° in longitude by 0.5° in latitude. $\mu(x, y)$ is a constant within one grid. There are 400 parameters of $\mu(x, y)$ to be computed.
5. Inhomogeneous model M_{I1600} with 1600 grids, each grid is 0.25° in longitude by 0.25° in latitude. $\mu(x, y)$ is a constant within one grid. There are 1600 parameters of $\mu(x, y)$ to be computed.

The Akaike's information criterion (AIC; Akaike 1974) is widely used and convenient statistically for model comparison. We apply the Akaike's information criterion (AIC) to evaluate each model for model diagnosis. Smaller values of AIC indicate better-fit models. Here,

$$\mathrm{AIC} = -2\max(\log - \text{likelihood}) + 2(\text{number of adjusted parameters}).$$

7.4 Results

Table 7.1 shows the ETAS modeling results from MLEs of homogeneous background rate of M_{H} and triggering parameters of the five models. We observe that there is no pronounced discrepancy among the estimates of triggering parameters for these models. M_{I100} appears to have the best fit among all models, according to AIC. Unsurprisingly, M_{I400} and M_{I1600} are indeed over-fitting models since the catalog's sample size is 2009, and it is close to 2 × (number of adjusted parameters). The number of adjusted parameters differs by models: M_{H} contains seven parameters (one background rate and six triggering parameters); M_{I25} contains 31 parameters (25 background rate and six triggering parameters); M_{I100} contains 106 parameters (100 background rate and six triggering parameters), etc. According to their AIC values, M_{H} and M_{I25} do not fit as well as M_{I100}, M_{I400} and M_{I1600}.

The background rates of all five models M_{H}, M_{I25}, M_{I100}, M_{I400} and M_{I1600} are displayed in Fig. 7.3. In all of the inhomogeneous models, unsurprisingly, grids with more events, especially clusters, have larger background rates than those grids having sparse events. The highest background rates occur around the bottom-left part of Longmenshan fault, where the 2008 Wenchuan $M7.9$ earthquake occurred.

Predicted intensity rate is calculated according to Eq. (7.2) for all five models. Figure 7.4a and b shows the predicted intensity rate λ of models M_{H} and M_{I25}. Grids with more events have higher predicted intensity rate. The intensity rate λ of models M_{I100}, M_{I400}, and M_{I1600} appears alike to the predicted intensity rate λ of M_{H} and M_{I25} (omitted in figure), but they are not identical. We compute the difference $\lambda_{\mathrm{I25}} - \lambda_{\mathrm{H}}$

Table 7.1 ETAS MLE results obtained using the homogeneous model M_{H} and inhomogeneous models M_{I25}, M_{I100}, M_{I400}, and M_{I1600}

Homogeneous	Model M_{H}	$(\alpha, c, d, K_0, p, q, \mu) = (1.028, 0.0789, 0.0149, 1.488\mathrm{E}{-4}, 1.246, 2.160, 2.666\mathrm{E}{-4})$ Log-likelihood = −5719; AIC = 11,440
Inhomogeneous	Model M_{I25}	$(\alpha, c, d, K_0, p, q) = (1.047, 0.0704, 0.0152, 1.308\mathrm{E}{-4}, 1.246, 2.184)$ Log-likelihood = −1583; AIC = 3215
	Model M_{I100}	$(\alpha, c, d, K_0, p, q) = (1.047, 0.0826, 0.0149, 1.349\mathrm{E}{-4}, 1.270, 2.184)$ Log-likelihood = −254; AIC = 707
	Model M_{I400}	$(\alpha, c, d, K_0, p, q) = (1.066, 0.0752, 0.0154, 1.207\mathrm{E}{-4}, 1.270, 2.207)$ Log-likelihood = −32; AIC = 863
	Model M_{I1600}	$(\alpha, c, d, K_0, p, q) = (1.066, 0.0808, 0.0160, 1.084\mathrm{E}{-4}, 1.293, 2.254)$ Log-likelihood = 1138; AIC = 924

Each model's log-likelihood and AIC are given. Computation tolerance is 0.001. Smaller AIC indicates better fit. We can see from AIC that M_{I100} fits better than other models. The models M_{I400}, and M_{I1600} are not better due to large number of parameters, and the penalty is applied in AIC

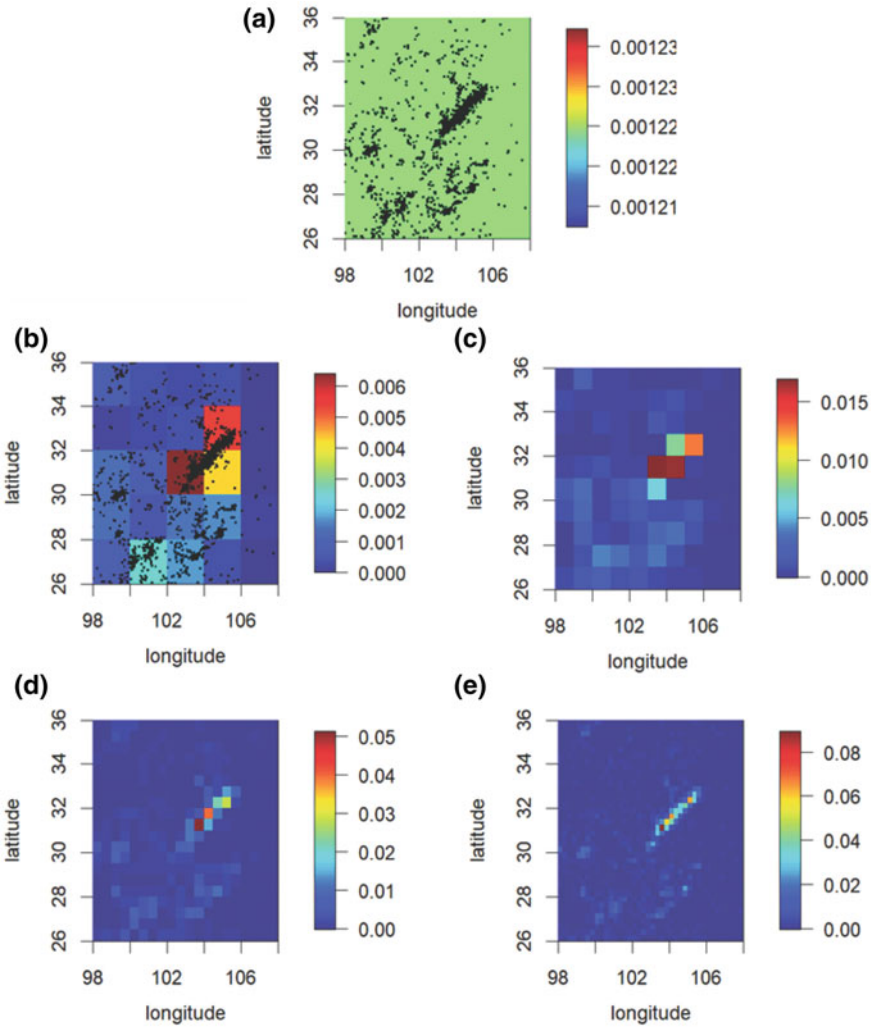

Fig. 7.3 **a** Homogeneous background rate of model M_{H} displayed with events. Constant background rate $\mu = 2.666E{-}4$. **b** Inhomogeneous background rate of M_{I25} displayed with events. Grids with higher background intensity rates are the three neighborhood grids of the Wenchuan event, which is part of the Longmenshan fault seismic cluster. The grid including the Wenchuan event has the highest background intensity rate. **c** Inhomogeneous background rate of M_{I100}, **d** M_{I400} and **e** M_{I1600} displayed with events. Events are not displayed for clarity of the grids. Difference between the clustered regions and sparse regions is larger when number of grids increases

and demonstrate it in Fig. 7.4c. λ_{I25} is greater than λ_H over the complete rectangular region. In area with sparse events, the difference is more pronounced. In area with clustered events, the difference is relatively smaller. Similar phenomenon appears in Fig. 7.4c–f, which respectively show the differences $\lambda_{I25} - \lambda_H$, $\lambda_{I100} - \lambda_{I25}$, $\lambda_{I400} - \lambda_{I100}$ and $\lambda_{I1600} - \lambda_{I400}$. We have observed that $\lambda_{I1600} > \lambda_{I400} > \lambda_{I100} > \lambda_{I25} > \lambda_H$. The predicted intensity rate is larger when a inhomogeneous model with more grids is used. The difference between two models with larger number of grids, for example, M_{I400} and M_{I1600}, tends to be larger than difference between two models with fewer grids, for example, M_{I25} and M_H. In summary, by observing the predicted intensity rate, the homogeneous model and models with few grids appear to underestimate the intensity rate. Models with large number of background grids appear to overestimate the intensity rate.

It is informative to compare the seismic activities before and after the Wenchuan event. We partition the data into two sub-catalogs: 1973/01/01–2008/05/08 excluding the Wenchuan event (we will call this time window TW_I) and 2008/05/08 excluding the Wenchuan event (we will call this time window TW_{II}). The time windows TW_I and TW_{II} have catalog sizes 690 and 1318, respectively. If we view the 45-year time window from 1973 to 2017 without partitioning it into TW_I and TW_{II}, it is not possible to observe the difference. TW_I is much larger than TW_{II}, but it has much lesser events. The seismic activities before and after Wenchuan event along Longmenshan fault are noticeably different. Events appear clustered in the southwest area in TW_I. It is unsurprising to learn that these two time windows produce distinct α values as shown in Table 7.2, which summarizes the result of ETAS model fitting of catalogs in TW_I and TW_{II}.

The triggering parameters except α are similar between the two time windows. However, α has its value varying between the two time windows, and the values have noticeable difference from the α values of models over the complete time window of 1973–2017, roughly around 1.03–1.07. α is about 1.28 in TW_I and about 1.47 in TW_{II}, indicating that the seismicity is closer to swarm type in TW_I, but is more clustered in TW_{II}. As described in Sect. 7.3, ETAS models give the parameter MLEs and they have physical meanings. Besides the abovementioned parameter α that is related to seismicity types, the parameters c and p are related to how an event is affected by previous events in time. c of $TW_I > c$ of TW_{II} and it indicates that in TW_I, temporal decay is larger and more gradual in time as an event moves away from the mainshock, and in TW_{II}, temporal decay is relatively smaller. However, their difference is small. p of $TW_I < p$ of TW_{II} indicates that TW_I has longer and gradual time decay and TW_{II} has shorter and sharper time decay, which coincide with the conclusion drawn by the c values. Their difference is also small. Similarly, the parameters d and q are related to how an event is affected by previous events in space. d of $TW_I > d$ of TW_{II} indicates that in TW_I, spatial decay is larger and gradual as an event moves further from the mainshock, and in TW_{II}, spatial decay is relatively smaller. Their difference is also small. q of $TW_I < q$ of TW_{II} indicates that TW_I has longer and gradual spatial decay and TW_{II} has shorter and sharper spatial decay, which coincide with the conclusion drawn by the d values. In summary, events in TW_{II} tend to have shorter influence temporally and spatially. The parameter K_0

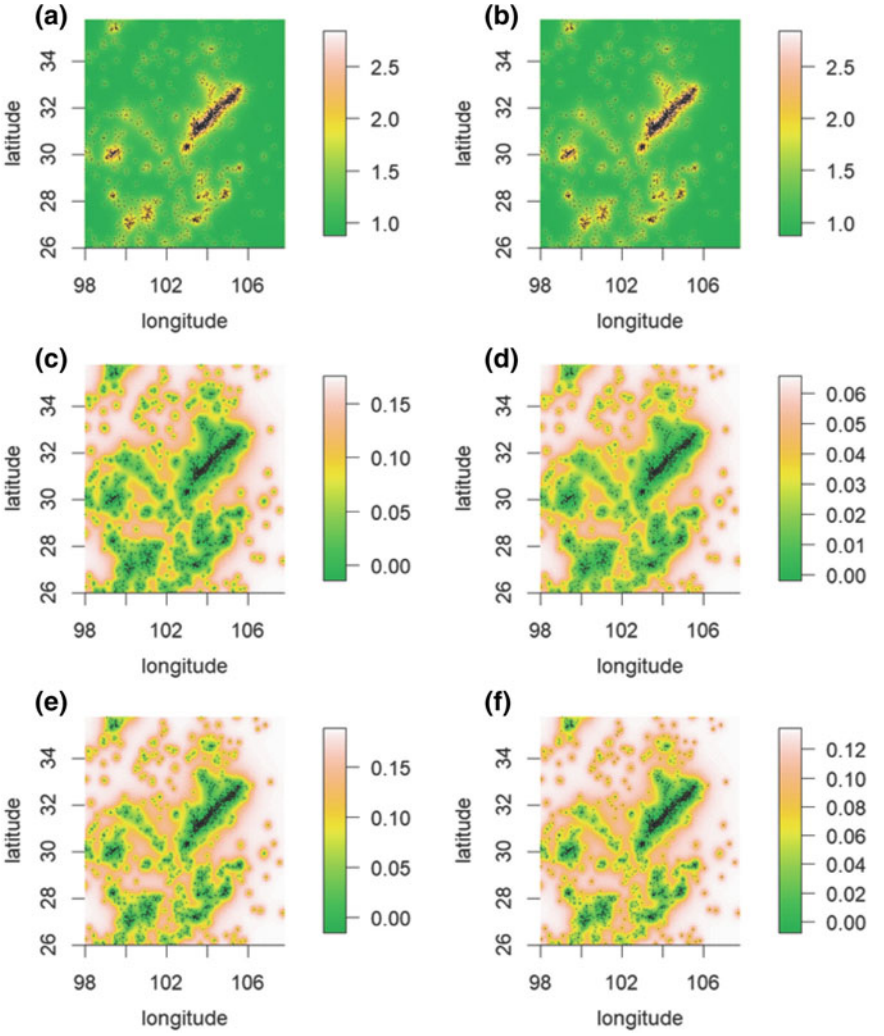

Fig. 7.4 Predicted intensity **a** λ_H using the homogeneous model M_H and **b** λ_{I25} using the inhomogeneous model M_{I25}, respectively, displayed with events. **c** $\lambda_{I25} - \lambda_H$, difference in predicted intensity between M_H and M_{I25}. **d** $\lambda_{I100} - \lambda_{I25}$, difference in predicted intensity between M_{I25} and M_{I100}. The difference is much less than the difference $\lambda_{I100} - \lambda_H$. **e** $\lambda_{I400} - \lambda_{I100}$, difference in predicted intensity between M_{I400} and M_{I100}. $\lambda_{I400} > \lambda_{I100}$ over the entire rectangular region. The difference is more pronounced for area with clustered events and more pronounced for area with sparse events. **f** $\lambda_{I1600} - \lambda_{I400}$, difference in predicted intensity between M_{I100} and M_{I400}. $\lambda_{I1600} > \lambda_{I400}$ over the entire rectangular region. The difference is less pronounced for area with clustered events and more pronounced for area with sparse events

Table 7.2 ETAS MLE result of triggering parameters obtained using M_{I} and M_{II}. Both models have their α much larger than the original time window (1973–2017)

M_{I}	$(\alpha, c, d, K_0, p, q) = (1.277, 0.0935, 0.0197, 7.869\mathrm{E}{-5}, 1.246, 2.184)$
M_{II}	$(\alpha, c, d, K_0, p, q) = (1.468, 0.0811, 0.0152, 8.210\mathrm{E}{-5}, 1.293, 2.324)$

governs the expected number of direct aftershocks triggered by earthquake i. Larger K_0 in $\mathrm{TW_{II}}$ indicates that the expected number of direct aftershocks is slightly larger according to the ETAS model. The physical meaning of seismicity explained by the triggering parameters also coincides with background rate. The plots of events in Fig. 7.5a, indeed, show that in $\mathrm{TW_I}$, the seismicity is mostly swarmed with moderate clusters around the bottom-left corner. In contrast, the seismicity in $\mathrm{TW_{II}}$ is noticeably clustered along the Longmenshan fault in Fig. 7.5b.

Table 7.3 shows the number of events roughly by years, with the first two rows indicating the number of events in 2008, before and after Wenchuan earthquake. The difference is tremendous. In 2008, there are only six events before the Wenchuan earthquake but 794 events after the Wenchuan earthquake. Among the 2009 shallow events from 1973 to 2017, 794 events within approximately eight months after the Wenchuan earthquake account for 39.5% of the seismic activity during 45 years. These events may dominate the estimation of parameter MLEs, especially the parameter, that are sensitive to change in data, such as α and K_0.

It might be artificial to use year as grouping criterion; therefore, we provide the magnitude on time plot to depict the region's seismicity from 1973 to 2017 in Fig. 7.6a. It is noted that $\mathrm{TW_I}$ has 12,889 days (approximately 35.3 years and 78% of the 45-year window) and 690 events (approximately 34% of the complete 45-year time window), while $\mathrm{TW_{II}}$ has 3505 days (approximately 9.6 years and 21% of the 45-year window) and 1318 events (approximately 66% of the complete 45-year time

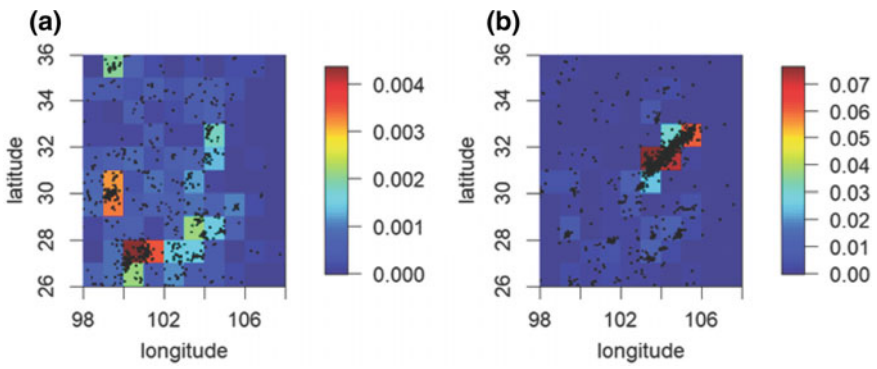

Fig. 7.5 **a** Catalog of 609 events in $\mathrm{TW_I}$ modeled using M_{I100}. Inhomogeneous background rate is plotted with the events. **b** Catalog of 1318 events in $\mathrm{TW_{II}}$ modeled using M_{I100}. Inhomogeneous background rate is plotted with the events

Table 7.3 Number of events by year in TW_{II}

Time window	Number of events with magnitude ≥4.0
2008/01/01–2008/05/08 (before and excluding Wenchuan event)	6
2008/05/08–2008/12/31 (after and excluding Wenchuan event)	794
2009/01/01–2009/12/31	46
2010/01/01–2010/12/31	34
2011/01/01–2011/12/31	44
2012/01/01–2012/12/31	41
2013/01/01–2013/12/31	132
2014/01/01–2014/12/31	79
2015/01/01–2015/12/31	45
2016/01/01–2016/12/31	103
2017/01/01–2017/12/31	48

window). We observe that the number of events shows a very noticeable variation. Right after the Wenchuan event, the density of events is much larger than other intervals for about eight months and this might be related to the clustered events along the Longmenshan fault.

We separate these two time windows and depict their seismicity. The events in TW_I are displayed in Fig. 7.7a, where larger events are shown by larger circles. The seismicity appears clustered moderately in the southwest area, but not along the Longmenshan fault. The seismicity of TW_{II} is displayed in Fig. 7.7b. Seismic clusters shown in Fig. 7.7a and b are not resembled indeed. To observe how the Wenchuan earthquake might have produced aftershocks, Fig. 7.7c shows 794 events from 2008/05/08 to 2008/12/31, excluding the Wenchuan earthquake. The events from 2009/01/01 to 2012/12/31 are shown in Fig. 7.7d while the events from 2013/01/01 to 2017/12/31 are shown in Fig. 7.7e. They all appear to be different in distribution of events in space. We can see that the Wenchuan earthquake appears to have tremendously influence the region's seismicity within a few months. The effect appears to last within approximately for more than four years. After four years, the cluster along Longmenshan fault is no longer pronounced as shown in Fig. 7.7e.

One might be curious if the Wenchuan event's seismicity is similar to later three large events: $M6.6$ Lushan event occurring on 2013/04/20, the $M6.2$ Ludian event occurring on 2014/08/03, and the $M6.5$ Jiuzhaigou event occurring on 2017/08/08. These events happened after the Wenchuan event, and they happened during the later time of TW_{II}. They are part of the data analysis for all of the 45 years (1973–2017) and also part of TW_{II} (2013/01/01 to 2017/12/31, which is a very short period to analyze). They do not seem to create significant clusters. The clusters after 2008/05/08 appear mostly related to the Wenchuan event. To see that the Lushan, Ludian, and Jiuzhaigou events' aftershocks are relatively more sparse than the aftershocks of the Wenchuan

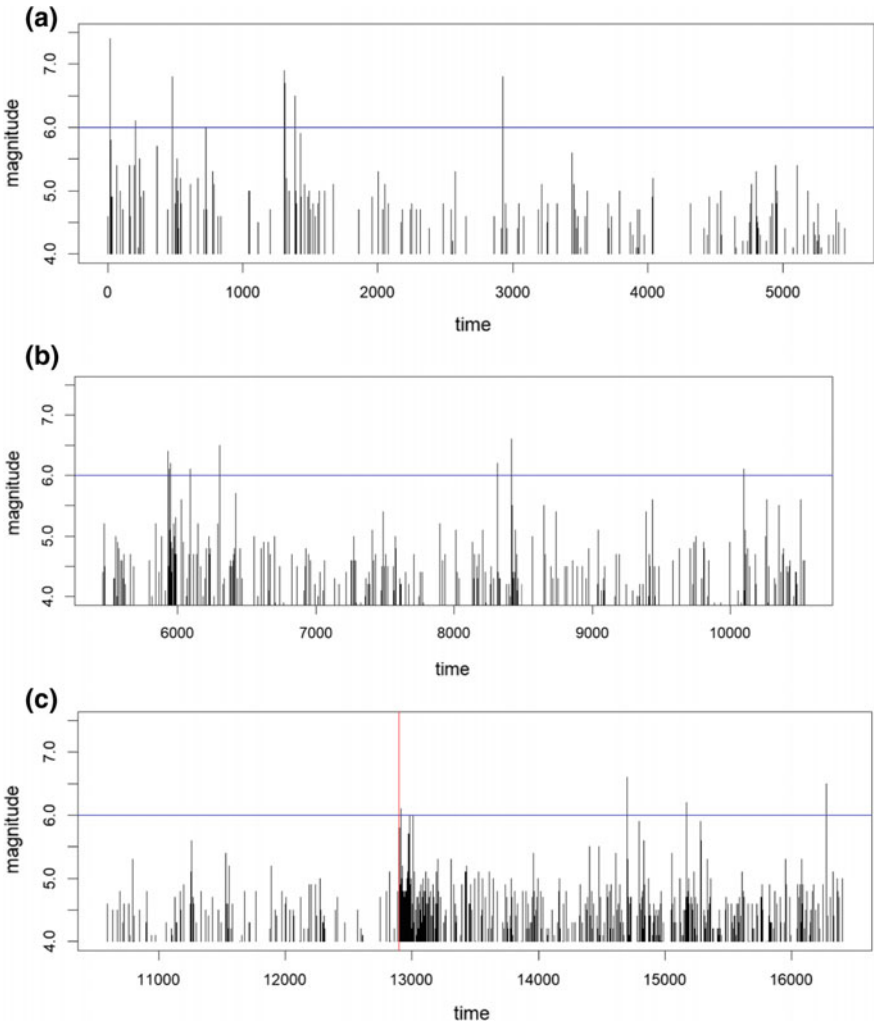

Fig. 7.6 Plot of magnitude versus time. The horizontal axis indicates time in day, and the vertical axis indicates magnitude. The time interval is 45 years from 1973/01/01 to 2017/12/15, and time = 16,403 is the occurrence time of the last event. **a** Time window from 1973/01/01 to 1987/12/31 (15 years). **b** 1988/01/01–2002/12/31 (15 years). **c** 2003/01/01–2017/12/31 (15 years), which contains the Wenchuan event. The three large events in the same figure as the 2008 M7.9 Wenchuan (marked by red vertical line) events are Lushan, Ludian, and Jiuzhaigou events. The Wenchuan event appears to have noticeably more aftershocks with magnitude $\geq$4.0 than the other three events

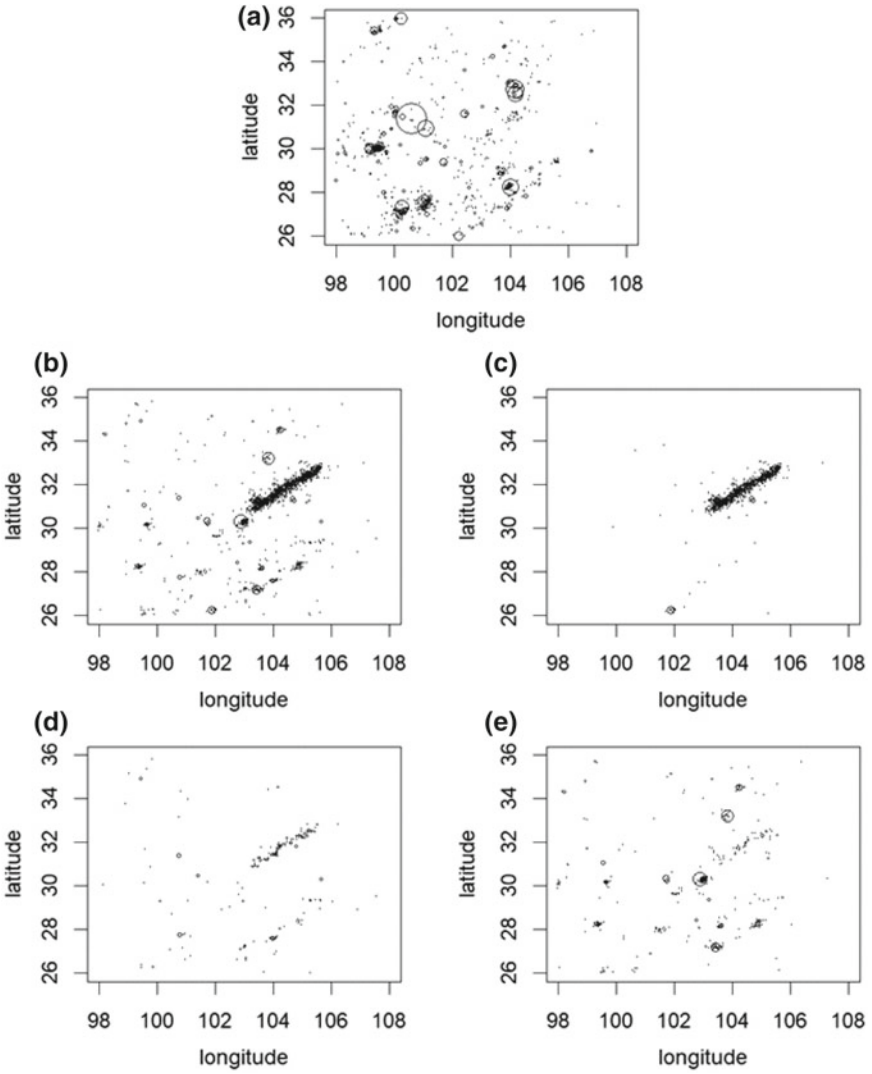

Fig. 7.7 **a** Events in TW_I. The largest event is the Luhuo earthquake. The Wenchuan earthquake is not displayed in this figure. **b** Events in TW_{II} from 2008/05/08 to 2017/12/31. There are 1318 events. Clustered events along the Longmenshan fault is shown clearly. The Wenchuan earthquake is not displayed in this figure. **c** Events in part of TW_{II} from 2008/05/08 to 2008/12/31. There are 794 events. Clustered events along the Longmenshan fault is shown clearly. The Wenchuan even is not displayed in this figure. **d** Events in part of TW_{II} from 2009/01/01 to 2012/12/31. There are 165 events. Clustered events are obvious along the Longmenshan fault. **e** Events in part of TW_{II} from 2013/01/01 to 2017/12/31. There are 359 events. Clustered events are not as pronounced as in the time window from 2008/05/08 to 2012/12/31. There are only three events with magnitude $\geq$6.0: Lushan event occurring at 30.308°N, 102.888°E on 2013/04/20, with magnitude 6.6, and it is close to the Wenchuan earthquake epicenter, the Ludian event occurring at 27.1891°N, 103.4086°E on 2014/08/03 with magnitude 6.2, and the Jiuzhaigou event occurring at 33.1926°N, 103.8552°E on 2017/08/08, with magnitude 6.5

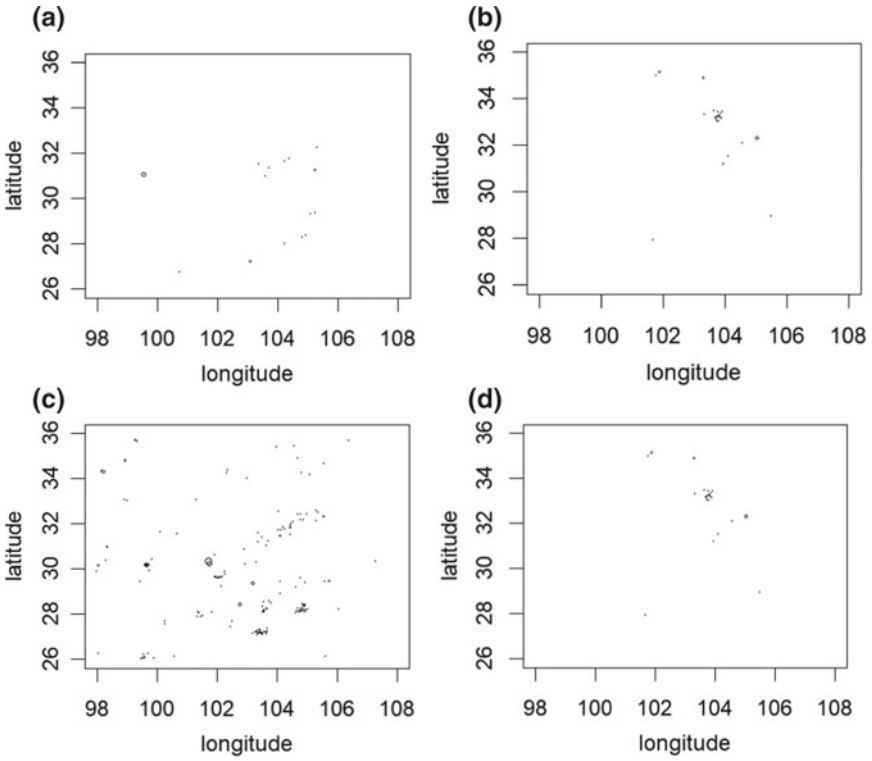

Fig. 7.8 Plots show the seismicity for **a** TW_{III}, **b** TW_{IV}, **c** TW_{V}, and **d** TW_{VI}

event, we will define time windows and describe their seismicity, TW_{III}: 2013/01/01 to 2014/04/20 before Lushan event (excluding Lushan quake), TW_{IV}: 2014/04/20 to 2014/08/03 after Lushan event before Ludian event (excluding Lushan and Ludian quakes), TW_{V}: 2017/08/08 after Ludian event before Jiuzhaigou event (excluding Ludian and Ludian quakes), and TW_{VI}: 2017/08/08 to 2017/12/31 after Jiuzhaigou event (excluding Jiuzhaigou quake). Figures 7.8 and 7.9 provide spatial and time plots made for these time windows, and we can see that the aftershock patterns of the later three large events do not act similar to the Wenchuan event, although data might be too few to conclude for Jiuzhaigou event (2017/08/08). Wenchuan event's aftershocks also appear differently from the Luhuo event in 1973. Although it is commonly observed that numerous aftershocks occur after a large event, the Wenchuan event appears to have more aftershocks with magnitude $\geq$4.0 according to Fig. 7.6.

We also provide the data of Southern California for a comparison. Figure 7.10 shows the seismic data of Southern California in rectangular region [112°W, 124°W] in longitude by [30°N, 38°N] in latitude, from 1973/01/01 to 2015/12/31. The survivor plot in Fig. 7.11 shows that the data are complete for magnitude $\geq$3.0, and we

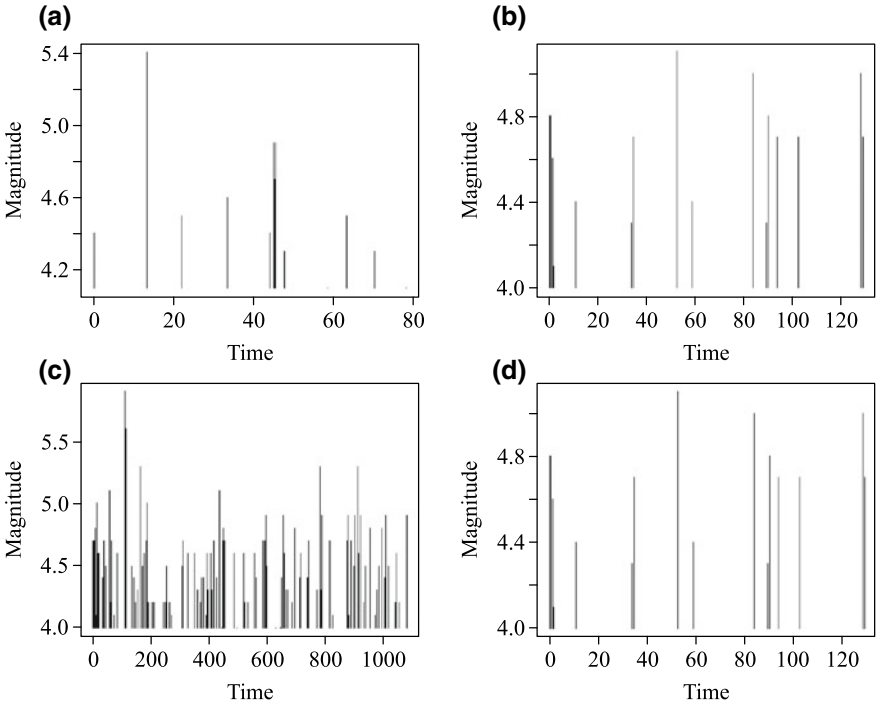

Fig. 7.9 Plots of magnitude versus time for **a** TW_{III}, **b** TW_{IV}, **c** TW_{V}, and **d** TW_{VI}

include all data with magnitude ≥3.0 in Fig. 7.10. We can observe that not all the large events with magnitude ≥6.0 have similar foreshock and aftershock patterns. Some large events are more clustered, and some have longer decay than others. Those similar on aftershocks with magnitude ≥4.0 may appear differently on aftershocks with magnitude <4.0. Since the Wenchuan region is not complete for magnitude interval between 3.0 and 4.0, it is difficult to compare Wenchuan event's aftershocks below 4.0 with other large event's aftershocks below 4.0. However, the Wenchuan event has noticeably more aftershocks with magnitude ≥4.0 than Southern California's Landers, Hector Mine, and Baja California events as shown in Fig. 7.11. Before the Wenchuan event, foreshocks are observed. Before the foreshocks, a period of time shows serenity. In Fig. 7.6, we also see that there are lesser events before the Wenchuan event—a quiet period of time and few foreshocks for about 500 days. In contrast, three large events after 2008 do not show the same foreshock and aftershock patterns.

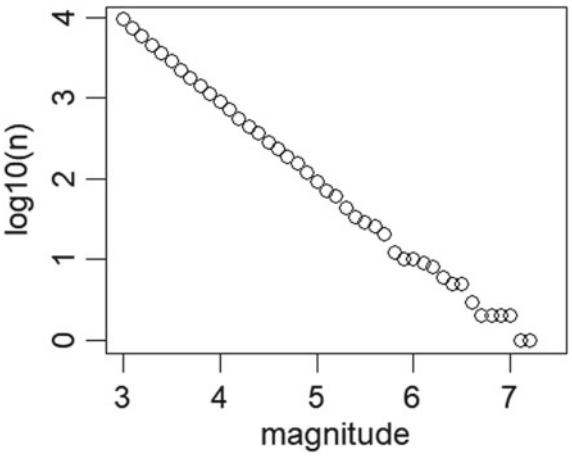

Fig. 7.10 Survivor curve of Southern California earthquake data with minimum magnitude cutoff 3.0, from 1973/01/01 to 2015/12/31, in rectangular space $[-124, -112]$ in longitude by [30, 38] in latitude. There are 11,684 events. The plot of $\log_{10}(n)$ on magnitude is linear, and this shows near completeness of catalog with minimum magnitude cutoff 3.0

7.5 Simulation

In this section, we demonstrate simulation using the estimated parameters by ETAS model. Simulation provides the benefit of calculating standard errors of the parameters. The inhomogeneous model M_{I100} is used for our simulation demonstration. The simulation process consists of two stages: generation of background events and triggered events. For each simulated catalog, the data of 2009 events in 1973/01/01 to 2017/12/31 are used to stochastically determine which events are included in the simulated catalog as background events. The background events are kept in the simulated catalog, and their aftershocks are generated. Each background event will have a number of aftershocks. There are four variables to simulate for each aftershock event in a simulated catalog: longitude, latitude, time, and magnitude. The simulation mechanisms of the four variables are described below:

- The time of an event is uniformly generated within the time window.
- Longitude (x) and latitude (y) are uniformly generated spatially. For an inhomogeneous model, they are generated within a grid.
- Magnitude of the i-th event is generated by:

$$m_i = m_{\mathrm{GR}} - \ln(1 - r(1 - \exp(-\beta(M_{\mathrm{GR}} - m_{\mathrm{GR}}))))/\beta$$

where β denotes the Gutenberg–Richter branching ratio described in Sect. 7.2. r is a uniform random number, $0 < r < 1$. M_{GR} and m_{GR} denote Gutenberg–Richter's maximum and minimum magnitudes, respectively. Such limits are applied because an exponential distribution of earthquake magnitudes would make extremely strong earthquakes more likely than they actually occur. Therefore, a truncated exponential distribution is used, which sets a specified maximum for simulated earthquake events (Veen and Schoenberg 2008). In our study, they are set to be $m_{\mathrm{GR}} = 4.0$ and $M_{\mathrm{GR}} = 10.0$.

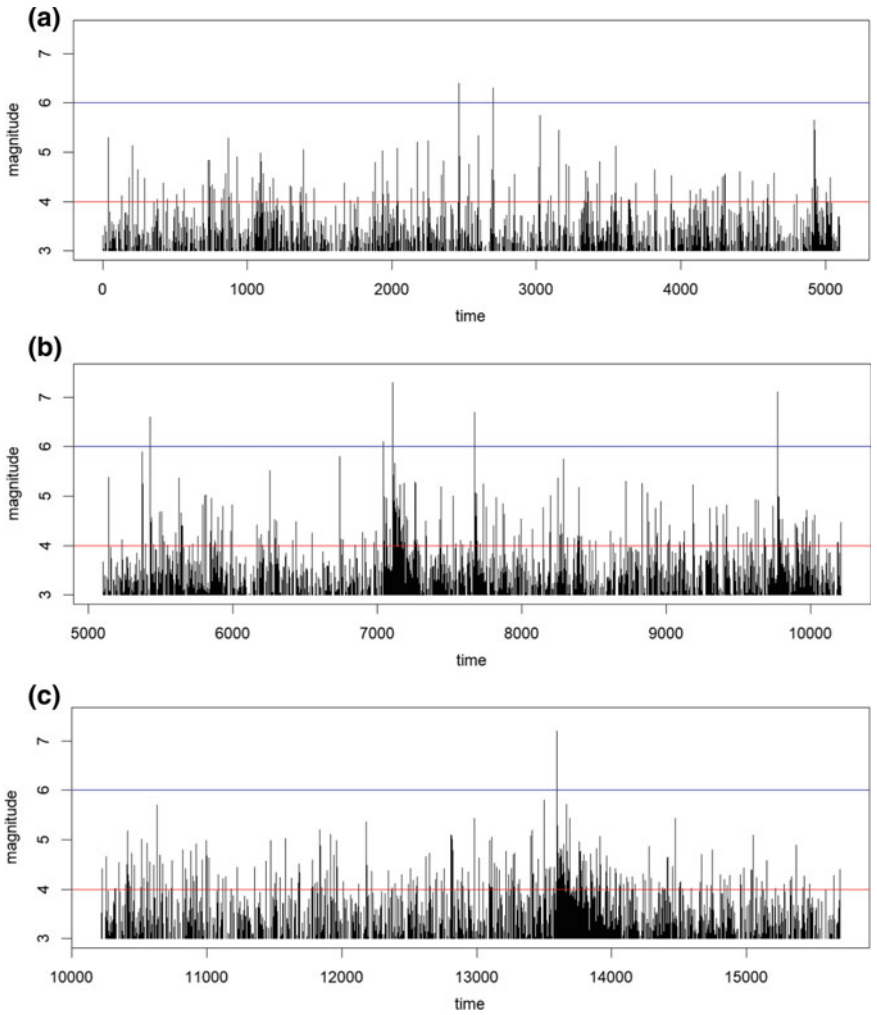

Fig. 7.11 Plots of magnitude versus time for Southern California earthquake data of 11,684 events over 43 years. **a** Time window from 1973/01/01 to 1986/12/31 (14 years). **b** 1987/01/01–2000/12/31 (14 years). **c** 2001/01/01–2015/12/31 (15 years). We observe that the patterns of foreshocks and aftershocks differ for large events with magnitude $\geq$6.0: Some appear to have lots of foreshocks below magnitude 3.0 but not above 4.0. Some have almost no foreshocks with magnitude 3.0. Some large events have many more aftershocks $\geq$4.0 than other events. The event at time approximately $=$ 7300 days is the M7.3 Landers event (1992/06/28). The event at time approximately close to 10,000 days is the M7.2 Hector Mine event (1999/10/16). The event at time between time 13,000 and 14,000 is the M7.1 Baja California event (2010/04/04). Both the Landers and Baja California events appear to have numerous aftershocks, but the later one has more aftershocks with magnitude between 3.0 and 4.0, over longer period of time

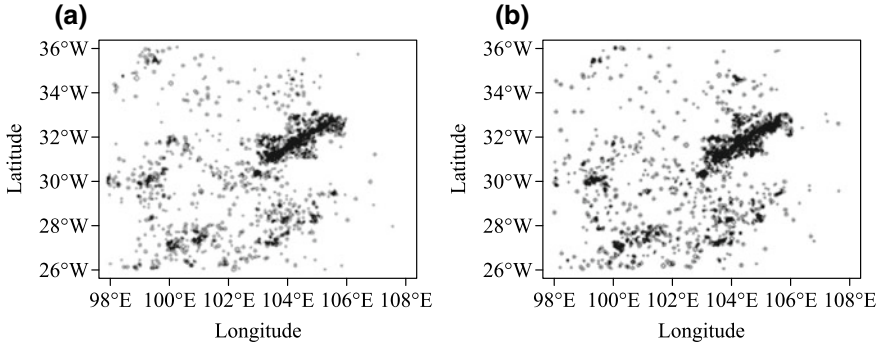

Fig. 7.12 **a** and **b** are two examples of simulation using model M_{I100}. All 30 simulated catalogs have their spatial distributions similar to these two examples

A thinning process is implemented in event generation. The expected number of first-generation events is calculated using the parameters $(\alpha, c, d, K_0, p, q)$:

$$G_i(\theta) = \int_0^{\infty}\int_{-\infty}^{\infty}\int_{-\infty}^{\infty} g(t-t_i, x-x_i, y-y_i, m_i)\mathrm{d}x\mathrm{d}y\mathrm{d}t = \pi K_0 \frac{c^{-\omega}}{\omega}\frac{d^{-\rho}}{\rho} e^{\alpha(m_i - M_0)} \tag{7.4}$$

Using 30 simulated catalogs, we have computed the standard error for each triggering parameter. Most of the simulated catalogs have catalog size between 1700 and 2400. Figure 7.12 shows examples of simulation using MLEs of M_{I100}. Two examples of time versus magnitude plot are displayed in Fig. 7.13. All simulated catalogs are similar to these two examples and have magnitude cutoff $M_0 = 4.0$. The standard errors and 95% confidence intervals of M_{I100}'s triggering parameters are given below.

$$\begin{aligned}
\widehat{\text{SE}}_{\alpha} &= 0.114,\ 95\%\,\text{CI}_{\alpha} = (0.819,\ 1.274)\\
\widehat{\text{SE}}_{c} &= 0.000134, 95\%\,\text{CI}_{c} = (0.823,\ 0.829)\\
\widehat{\text{SE}}_{d} &= 0.000116, 95\%\,\text{CI}_{d} = (0.0147,\ 0.0151)\\
\widehat{\text{SE}}_{K_0} &= 1.81E{-}05, 95\%\,\text{CI}_{K_0}(9.88E{-}05,\ 1.17E{-}04)\\
\widehat{\text{SE}}_{p} &= 0.00485, 95\%\,\text{CI}_{p} = (1.26,\ 1.28)\\
\widehat{\text{SE}}_{q} &= 0.00831, 95\%\,\text{CI}_{q} = (2.17, 2.20)
\end{aligned}$$

The parameters c, d, p, and q appear to have small standard errors with respect to their estimates. These parameters are indeed those that have smaller variations among model fitting in not only Wenchuan data, but also in Southern California and global data. In contrast, the parameters α and K_0 have larger standard errors with respect to their estimates. K_0 is a parameter that has large variation with respect to its

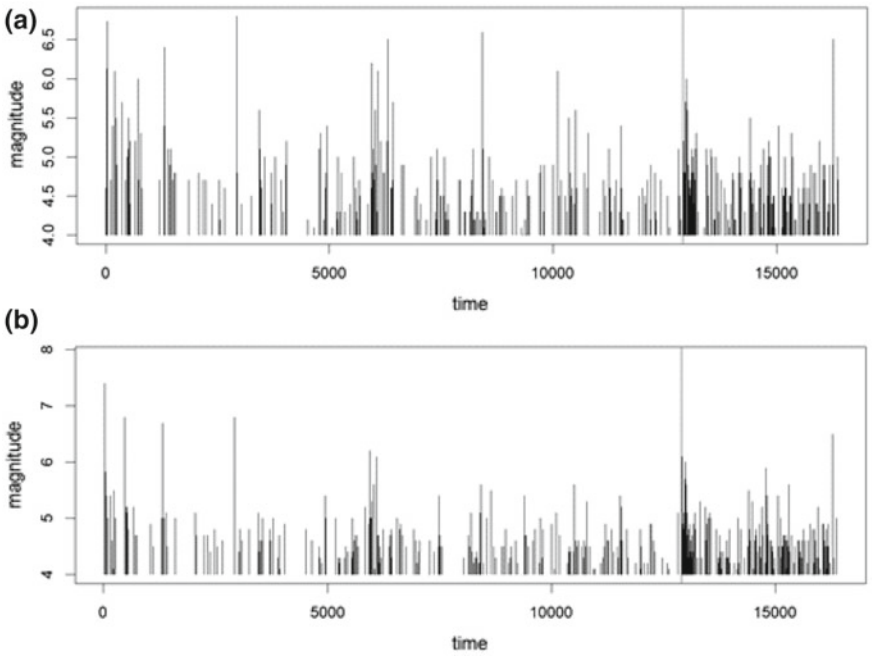

Fig. 7.13 **a** and **b** Plots of magnitude versus time for simulated examples of Fig. 7.12, using model M_{I100}. The highest vertical line indicates the time of the 2008 M**7.9** Wenchuan earthquake

estimate due to the flatness of convergence plane of maximum likelihood estimation (Veen and Schoenberg 2008). α is a parameter that is relatively difficult to estimate and may suffer the scenario of divergence in estimation (Chu 2018), which has worse convergence than parameter K_0. α is more sensitive to data than K_0. The aftershocks within months after the Wenchuan earthquake account for about 39.5% of the 2009 events and might play a crucial role for the calculation of α.

We also have obtained the standard errors and confidence interval for some of the background rates. The summary statistics of 30 standard errors of background rates $\mu(x, y)$ are: minimum $= 0$, $Q_1 = 0.000120$, median $= 0.000479$, mean $= 0.000949$, $Q_3 = 0.00143$, and maximum $= 0.00479$. The minimum is 0 because there are grids with no events. Figure 7.14 depicts the distribution of the background rates. The background rate grids with highest standard errors at the histogram's right tail come from the grids of the middle part of Longmenshan fault (approximately 31.5°N, 104.5°E) and the bottom area of the region. Simulated catalogs have larger variation in these sub-regions due to these regions' larger variation of seismicity. The grids with more points tend to have larger standard errors. Some of the grids have their standard errors being 0 due to lacking any event.

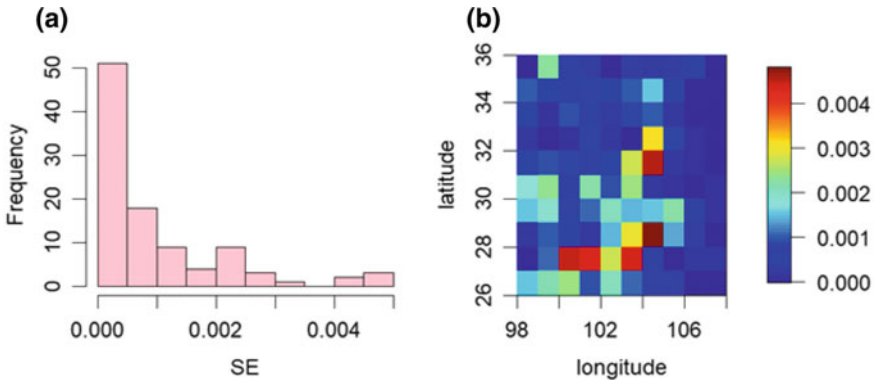

Fig. 7.14 **a** Histogram showing the distribution of standard errors. Most grids have standard errors 0 or close to 0 due to their sparseness. **b** Graph to show the standard errors of background rate $\mu(x, y)$

7.6 Conclusion

We have demonstrated estimation of inhomogeneous background rate with ETAS model, using simple rectangular grids and shown that among the models we tested, the inhomogeneous model M_{I100} fits better than the other four models. It is reasonable to understand that the homogeneous model M_{H} lacks adequacy to explain the seismic data of Wenchuan region, and models with numerous background rate parameters like M_{I400} and M_{I1600} are not optimal due to over-fitting the catalog of 2009 events. It should also be remarked that all the models triggering parameters' MLEs are similar comparing to triggering parameters of Southern California data and global data of the same zone 1. ETAS parameter MLEs can help us build predicted intensity rate like Fig. 7.4a and b. It makes possibility to visualize the region and sub-regions' intensity rates. We have also discovered that the seismic activity of Wenchuan vicinity changes over the 45 years from 1973 to 2017, and the seismicity appears noticeably different in scatter plots and model's MLEs. Additionally, as we have observed from the events of Wenchuan, Lushan, Ludian, and Jiuzhaigou, as well as Southern California's large earthquakes, foreshocks and aftershock pattern may be noticeably different and incompleteness of data is an important factor to consider.

To conclude the chapter, we raise four questions for our future study:

- It should be noted that the model M_{I100} is chosen for computation convenience, and a more optimal model may exist around 100 grids between 25 and 400 grids. Non-square grid partitions may also be implemented. Such grid partition may be also compared with other types of inhomogeneous approach, for example, irregular polygons along the Longmenshan fault, to identify an optimal model that may be easily generated by our software.
- It is observed that the time constants c and p have very small standard errors. Such phenomenon appears not only in analysis presented in this chapter, but also

in ETAS models' maximum likelihood estimation in general. While computation can be cumbersome, time-consuming, and unstable for ETAS MLE computation, we seek for solutions to attain more stable computation. Two questions are raised: Can we compute the time constants c and p by estimating the time model first, and then we use the estimated c and p as fixed values in the time-space model? Will such alternation make the computation for α, K_0, d and q more stable?

- Our sub-catalogs of TW_I and TW_{II} have tremendous difference in seismicity. The seismicity within TW_{II} varies approximately every four to five years. It is worthwhile for further study if the serenity along Longmenshan before the Wenchuan event (Fig. 7.6) is related to the Wenchuan earthquake. In general, we should be aware that when different time window intervals are applied to the same region, we might obtain different MLE results to explain the region's seismicity differently since some parameters such as α and K_0 are sensitive to small variation of data. Such procedure is worthwhile to consider for seismic research.
- It is noted that the PDE catalog is incomplete for magnitude <4.0. By applying simulation, we can extend our work to simulate catalogs with lower magnitude cutoff, e.g., $M_0 = 3.0$ or lower to investigate how seismicity modeling may be improved. As previously mentioned in this chapter, some triggering parameters such as c, d, p and q are stable in estimation, and their standard errors are small compared to parameters α and K_0. Simulation can help us understand how they are sensitive to data, improve our estimation for their MLEs, and find ways to eliminate bias. Simulations along with estimated ETAS parameters may also help us understand the missing data issue of incomplete magnitude <4.0.

Acknowledgements I am grateful to Dr. Yong-Gang Li, the editor-in-chief of this special volume, for his warm invitation and helpful suggestions to make this chapter possible.

References

Akaike, H. 1974. A new look at the statistical model identification. *IEEE Trans. Autom. Control*, AC-19, 716–723.

Bird, P. 2003. An updated digital model of plate boundaries. *Geochem. Geophys. Geosyst.* 4 (3): 1027. https://doi.org/10.1029/2001GC000252.

Chu, A., F.P. Scheoenberg, P. Bird, D.D. Jackson, and Y.Y. Kagan. 2011. Comparison of ETAS parameter estimates across different global tectonic zones. *Bull. Seismol. Soc. Am.* 101 (5): 2323–2339.

Chu, A. 2018. Comparisons of ETAS models on global tectonic zones with computing implementation. In *Chapter 4 of Fault-zone guided wave, ground motion, landslides and earthquake forecast*, ed. Y.-G. Li, 136–159. Beijing: Higher Education Press.

Guo, Y., J. Zhuang, and S. Zhou. 2015. An improved space-time ETAS model for inverting the rupture geometry from seismicity triggering. *J. Geophys. Res.: Solid Earth*, 120 (5): 3309–3323, https://doi.org/10.1002/2015jb011979.

Jiang, C.S., and J.C. Zhuang. 2010. Evaluation of background seismicity and potential source zones of strong earthquake in the Sichuan-Yunan region bae on the space-time ETAS model. *Chin. J. Geophys. (in Chinese)*, 53 (2): 305–317. 10.3969/j.issn. 0001-5733. 2010.02.008.

Ogata, Y. 1988. Statistical models for earthquake occurrences and residual analysis for point processes. *J. Am. Stat. Assoc.* 83: 9–27.

Ogata, Y. 1998. Space-time point process models for earthquake occurrences. *Ann. Inst. Stat. Math.* 50: 379–402.

Ogata, Y. 2011. Significant improvements of the space-time ETAS model for forecasting of accurate baseline seismicity. *Earth Planets Space* 63: 217–229.

Utsu, T., Y. Ogata, and R.S. Matsu'ura. 1995. The centenary of the Omori formula for a decay law of aftershock activity. *J. Phys. Earth* 43: 1–33.

Veen, A. 2006. Some methods of assessing and estimating point processes models for earthquake occurrences. Ph.D. thesis, University of California, Los Angeles.

Veen, A., and F.P. Schoenberg. 2005. Assessing spatial point process models for California earthquakes using weighted K-functions: analysis of California earthquakes. In *Case studies in spatial point process models*, ed. A. Baddeley, P. Gregori, J. Mateu, R. Stoica, and D. Stoyan, 293–306. NY: Springer.

Veen, A., and F. Schoenberg. 2008. Estimation of space-time branching process models in seismology using an EM-type algorithm. *J. Am. Stat. Assoc.* 103 (482): 614–624.

Chapter 8
Full-3D Seismic Tomography for Structure of the Critical Zone

Wei Wang, Po Chen, En-Jui Lee and Dawei Mu

Abstract Recent advances in full-3D seismic tomography (F3DT), in which the starting model and the inverted model perturbations are 3D in space and the sensitivity (Fréchet) kernels are computed using purely numerical solutions of 3D (visco) elastodynamic equations, have opened up new possibilities for imaging the structures of the near surface where mechanical properties of materials play important roles in various geotechnical engineering applications. In this study, we have successfully applied F3DT to image the near-surface structure under a granitic ridge in the Blair Wallis watershed, southeastern Wyoming. The seismic data used in our tomography consist of both 2D active-source seismic refraction data and 3D ambient-noise Green's functions obtained from a minimally invasive "large-N" seismic survey using a square array of 400 autonomous geophones. Lateral variations of our 3D velocity model show strong correlations with surface topography. Depth variations of our velocity model may give clues about the depth interval within which chemical weathering plays a significant role. With the calibration of borehole casing depths and saprolite refusal depths, our F3DT technique can be a highly effective tool for investigating the structure of the near surface.

Keywords Full-3D tomography · Galerkin method · Finite difference method · Surface wave · Head wave · Turning wave · Ambient-noise · Refraction · Joint inverse

W. Wang (✉) · P. Chen
Department of Geology and Geophysics, University of Wyoming, 82071 Laramie, WY, USA
e-mail: pseudopochen@gmail.com

E.-J. Lee
Department of Earth Sciences, Cheng Kong University, Taiwan, China

D. Mu
National Center for Supercomputing Applications, Urbana, USA

Y.-G. Li (ed.), *Earthquake and Disaster Risk: Decade Retrospective of the Wenchuan Earthquake*, https://doi.org/10.1007/978-981-13-8015-0_8

8.1 Introduction

The critical zone is the outermost layer of the solid earth that extends from the deepest reach of the groundwater chemical reactions to the top of the vegetation canopy (Anderson et al. 2007; Brantley et al. 2007). It is a highly dynamic layer that hosts a wide variety of physical, chemical, hydrological, and biological processes. These processes and the interactions among them create and transform the environment that sustains agriculture and most terrestrial life. In order to understand these processes and to build predictive quantitative models that can accurately describe them require us to characterize the structure of the critical zone across its full depth range from the soil at the surface to the saprolite, regolith, and fractured bedrock which may extend to depths of tens to hundreds of meters. Drilling and coring are expensive and provide measurements of the deep critical zone (DCZ) at only a spot, but unable to represent the whole area. This issue happens especially in areas with strong lateral heterogeneities where geostatistical interpolation may fail to provide an adequate representation. Geophysical imaging techniques (GITs) are minimally invasive and relatively inexpensive to provide indirect estimates of physical properties over large areas quickly. Thus, GITs are highly useful complements to drilling/coring, especially when they can be calibrated with direct measurements, and they can provide crucial guidance of site-selecting for excavation and sampling efforts (Riebe and Chorover 2013).

A variety of GITs have been applied to image the DCZ while each of them has its own strengths and limitations (Parsekian et al. 2015). In practice, by combining results from multiple types of GITs, we can potentially obtain a more robust interpretation. It has been shown that images of subsurface seismic velocities (i.e., physical quantities related to density and elastic moduli) obtained from seismic refraction surveys (SRS) using ray-theoretic travel-time tomography (RTT) correlate well with the degree of weathering in the DCZ and can be used to delineate the weathering interfaces (WI) (or reaction zone, depending upon the observation scale) separating soil, weathered bedrock and fresh crystalline bedrock (e.g., Hunter et al. 1984; Dasios et al. 1999; Befus et al. 2011; Holbrook et al. 2014). The architecture of the WI is an important indicator of the balance between the rates of weathering and erosion, and often controls the flow and storage of subsurface fluids (e.g., Buss et al. 2013; Drake et al. 2009; Brantley et al. 2011; Holbrook et al. 2014). It is, therefore, critical to image not only the overall geometry but also the internal structure of the WI. The resolution of the images obtained from SRS using first-arrival RTT is typically in the order of tens of meters, which is comparable to or even larger than the thicknesses of some WI (Brantley et al. 2011).

The resolution of conventional first-arrival RTT is inherently limited by two factors: (1) the underlying seismic ray theory (SRT) is a high-frequency approximation of the elastodynamic equations, which limits the resolution to the size of the first Fresnel zone ($\sim \sqrt{D\lambda}$, D: source-receiver distance; λ: dominant wavelength); (2) only the travel-time of the first-arriving P-wave is utilized in the inversion and all the rest of waveform data, which carry a tremendous amount of information about the

DCZ structure, are discarded; (3) the refraction ray paths become nearly horizontal in the DCZ with almost no crossing paths so that the lateral structural constraints are very poor; (4) conventional ray-theoretic first-arrival refraction tomography has difficulties dealing with velocity reversals (i.e., a low-velocity layer underlies a high-velocity layer).

In the past decade, advances in computing technology have opened up new possibilities for seismic tomography. The latest tomography technique is full-3D waveform tomography (F3DT) (e.g., Tarantola 1988; Tromp et al. 2005; Chen et al. 2007a, b; Tape et al. 2009; Chen 2011; Liu and Gu 2012; Fichtner 2011; Lee et al. 2014a, b, Chen and Lee 2015), which inverts the complete seismic waveform recordings for 3D subsurface structures by solving the 3D elastodynamic equations. F3DT is capable of improving the resolution of seismic velocity images to (sub)meter-scale using the same waveform data collected in conventional SRS. F3DT is based on purely numerical solutions of the 3D elastodynamic equations. It eliminates the high-frequency approximation in SRT and allows us to treat many types of waves (e.g., refraction, reflection, and surface waves) in a unified framework. Since different types of waves have different structural sampling patterns, by integrating them in a unified inversion, we can effectively improve both lateral and vertical resolutions. Because F3DT can invert the waveforms, all data points in seismogram can be utilized. The theoretical resolution limit of F3DT is about half of the dominant wavelength. By F3DT, we can provide high-resolution, three-dimensional seismic velocity images that will lead to a better understanding of the DCZ weathering processes.

8.2 Data Sets

In the past few years, the geophysics team of the Wyoming Center for Environmental Hydrology and Geophysics (WyCEHG), which was funded by the NSF Research Infrastructure Improvement (RII) Track-1 award, has collected a large amount of geophysical, hydrological, and borehole data at multiple critical zone observatories across the country. We have used primarily SRS and ambient-noise seismic data collected by WyCEHG in our F3DT inversions. Other types of geophysical and borehole data will be used to (1) cross-validate our F3DT images and (2) reduce the non-uniqueness of our F3DT inversions using independent constraints from borehole measurements.

8.2.1 Seismic Refraction Data

Seismic refraction data were acquired using 4-6 interconnected 24-channel Geometrics Geode systems and 40 Hz vertical component geophones spaced at 1 m (for lines passing boreholes) and 2.5 m (for other lines) (Fig. 8.1). A 12-pound steel sledgehammer produced seismic waves by striking a 20-cm-long, 20-cm-wide, and 2-cm

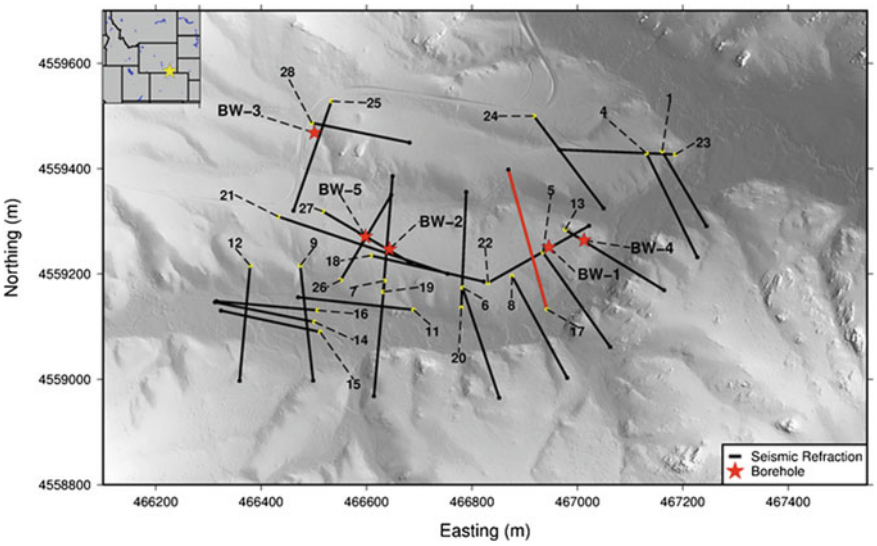

Fig. 8.1 Geophysical survey lines across the Blair Wallis area in Laramie Range, Wyoming. Black lines: survey lines with both seismic refraction and electrical resistivity data; red line: Line 17 used in our preliminary F3DT inversion; red stars: locations of borehole data. Background grayscale shows local topography

thick stainless steel plate on the ground. Shot spacing was 10 m. Recorded signals from eight shots at each shot location were stacked to reduce uncorrelated noise and increase SNR. A straightened tape was used to ensure that all the geophones were in-line. Topographic relief along the lines was measured using a tape measure and inclinometer. The estimated accuracy of the surveyed positions was within ± 0.2 m, which is sufficiently accurate for F3DT and other geophysical imaging techniques. Examples of a shot gather are shown in Fig. 8.2. The dominant frequency of the recorded seismograms is about 40 Hz. In general, the SNR is sufficiently high between 15 and 80 Hz (Fig. 8.3).

8.2.2 Passive-Source Seismic Ambient-Noise Data

Over the last two summers, we have deployed 400 vertical component seismic 10 Hz Zland nodes nine times in 200 by 200 m sized squares. Each deployment recorded the ambient wavefield at a 500 Hz sampling rate for 3–4 days. Three different critical zone environments are sampled by the three array deployments in each of these critical zone study sites: the southern Sierra batholith, the Laramie Range (Fig. 8.4), and the Medicine Bow Mountains. The total size of these seismic recordings is 2.7 TB and currently resides on our disk storage. In addition, at these nine array sites we

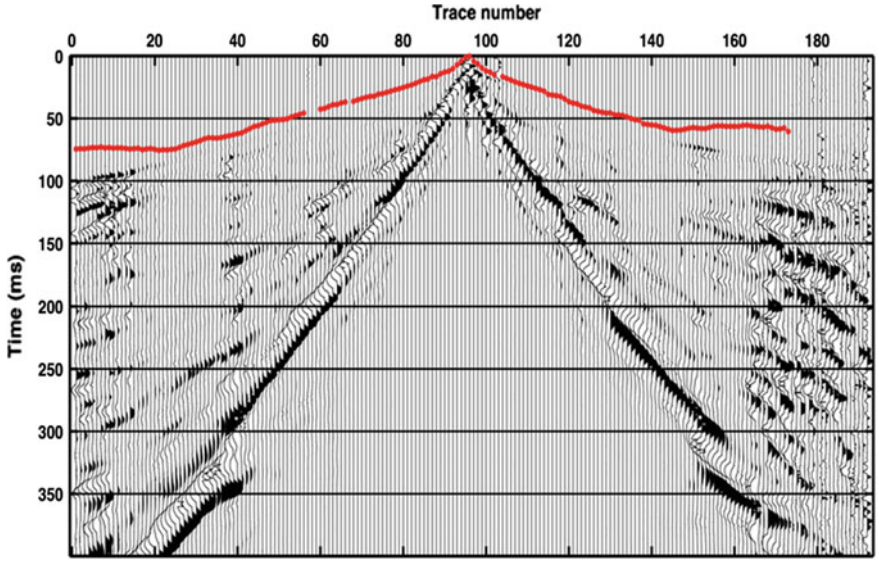

Fig. 8.2 Examples of seismic refraction data from Line 26 crossing borehole 5 on Fig. 8.1. This line has a spread of 192 m with 1 m inter-geophone spacing. Sledgehammer shots are placed at every 5 m. Total recording time is 0.4 s. Red dots show manually picked first-arrival travel-times

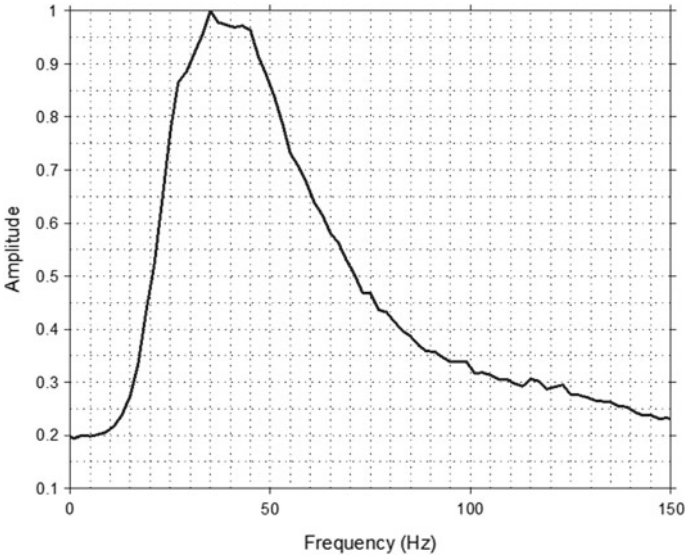

Fig. 8.3 Normalized stacked amplitude spectrum of all observed seismograms on line 17 (Fig. 8.1)

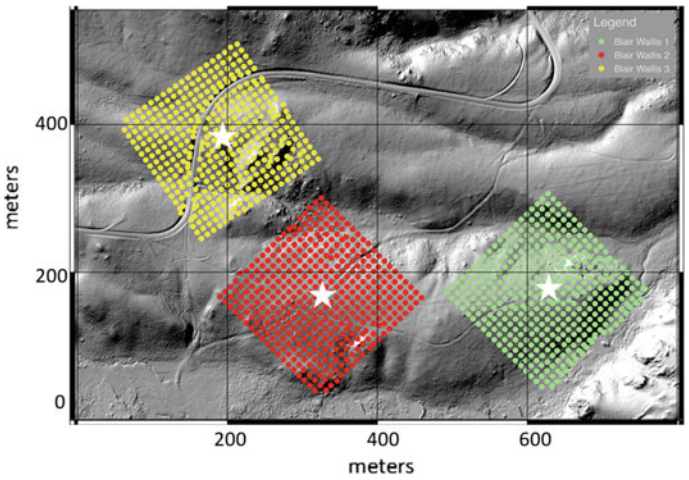

Fig. 8.4 Three arrays deployed in the Blair Wallis watershed during the summer of 2015. Green, red, and yellow dots show locations of the Blair Wallis 1, 2, and 3 nodal arrays, respectively. Stars indicate the locations of borehole wells, of which the three arrays were centered for ground truthing. Each array is roughly 200 m by 200 m. Each receiver recorded the ambient-noise field continuously for 3–4 days

have complementary geophysical data: P-wave refraction, electrical resistivity, and ground penetrating radar.

The recorded ambient-noise data were processed following a sequence of operations that are often called "seismic interferometry" (e.g., Bensen et al. 2007), which typically involves three steps: single-receiver processing, inter-receiver cross-correlation, and temporal stacking. The final results after processing are often called "ambient-noise Green's function" (ANGF), which are approximations of the response of the subsurface material recorded at one receiver as if there were an impulse excitation at the other receiver (i.e., the Green's function).

The computational cost for obtaining the ANGFs depends upon the total number of receivers and the total recording time. For the ambient-noise data set collected in our studies, it took 13 days of uninterrupted computing time on a single state-of-the-art 4-core desktop computer to process the noise data recorded by one array of 400 receivers and our existing ambient-noise data set has three such arrays. To speed up the seismic interferometry process, we have developed a scalable parallel algorithm for seismic interferometry (pSIN) (Chen et al. 2016). Past parallelization of the seismic interferometry algorithm suffers from heavy I/O overhead and cannot scale. The same noise recording must be read from and write to disk many times during the entire calculation due to the limited memory size per core. In our pSIN code, we have minimized the I/O burden by redesigning the entire seismic interferometry algorithm. The noise recordings of the entire array are read only once at the beginning of the execution, and all ANGFs are written to disk at the end of the calculation. Computational cost, inter-process communication overhead, memory usage, and I/O

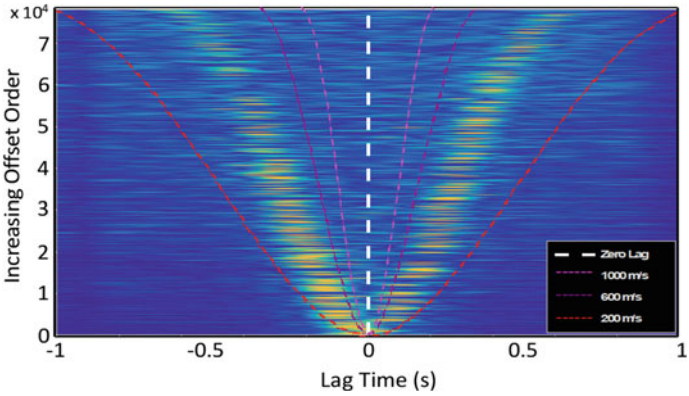

Fig. 8.5 Two sided, nominally 80,000 Blair Wallis correlation pairs that are ordered by increasing interstation offset. The yellow-green band is the energy envelope of the Rg wave in this 64 Hz frequency band that is propagating at about 350 m/s. There are 20 different frequency bands from which lag times are measured, which correspond to the maximum envelope peak. Those lag times are the input to the group velocity map inversions

overhead are well balanced among all cores. On the Yellowstone supercomputer at the NCAR-Wyoming Supercomputing Center, we achieved nearly linear scalability from 80 cores to over 3000 cores and reduced the processing time of one 400-receiver array from over 13 days on a single 4-core desktop to about 52 min on 2112 CPU cores on the Yellowstone supercomputer. Examples of the ANGFs for one of the three 400-receiver arrays are shown in Fig. 8.5.

8.2.3 Electrical Resistivity Data

In addition to the seismic data, electrical resistivity data were also collected along the lines shown in Fig. 8.1. All electrical resistivity data were collected using 56 stainless steel electrodes and the Advanced Geosciences (AGI) Super Sting R8 instruments. The geophysics team used a combination of the dipole-dipole and Wenner arrays setup in the field. Occasionally, the pole-dipole setup was used to improve the signal-to-noise ratio. The bedrock underlying the Blair Wallis watershed is Sherman Granite with high resistivity. So the geophysics teams used 2–3 electrodes at each location and applied salt water to reduce contact resistances. On average, our resistivity data set contained ~2500 data points. All of the resistivity data were inverted using the AGI Earth Imager 2D software with a smoothness constraint.

8.3 Methodology

F3DT is in essence an iterative numerical optimization algorithm, by which we search for an optimal subsurface seismic structure model that can minimize the waveform discrepancies between model-predicted (i.e., synthetic) seismograms and observed seismograms. The seismic structure model is usually represented using (visco) elastic parameters, such as elastic moduli, density, and seismic velocities (Vp and Vs). These parameters are 3D continuous functions of the space coordinate and can in general be discretized using a 3D spatial mesh. During optimization, we search for the optimal discrete representation of the structural parameters. To initiate the iterative optimization algorithm, we need a "starting model," an initial estimate of the discretized structure model, which does NOT have to be very close to the optimal structure model that is to be found. Synthetic seismograms can then be computed using the starting model by solving the elastodynamic equations using a numerical method, such as the finite difference, finite element, spectral element, and discontinuous Galerkin methods. The discrepancies between synthetic and observed waveforms can be used to make corrections to the starting model. These corrections are often called "perturbations." The mathematical instrument that converts waveform discrepancies to model perturbations is known as the "sensitivity (Fréchet) kernel," which in essence is the derivative of the waveform discrepancy with respect to the structure model, evaluated at the structure model used for computing the synthetic seismograms. After applying the perturbations to the starting model, an updated structure model is obtained, which can then be used for computing updated synthetic seismograms, computing updated sensitivity kernels, and making new corrections to the updated structure model. The entire procedure is repeated until no more corrections can be made.

8.3.1 Discontinuous Galerkin (DG) Solution of Elastodynamic Equations

The DG method is particularly suitable for solving elastodynamic equations in a complex geological model, such as the highly heterogeneous critical zone. The DG method is a combination of ideas from the spectral element and finite volume methods. Like the spectral-element method, the solution of DG method inside each element is approximated using a set of orthogonal basis functions, which leads to diagonal mass matrices. The advantage of the DG scheme over the spectral-element scheme is that the DG solution is allowed to be discontinuous across element boundaries. The discontinuities are treated using well-established ideas of numerical flux functions from the high-order finite volume framework (Toro and Titarev 2002). The DG method allows arbitrary unstructured meshes for the model and easy control of accuracy without compromising simulation stability. Unstructured tetrahedral mesh often provides the highest flexibility when meshing geological structures with complex geometries (e.g., Baker 1989; de Cougny and Shephard 1999; Xing et al. 2009).

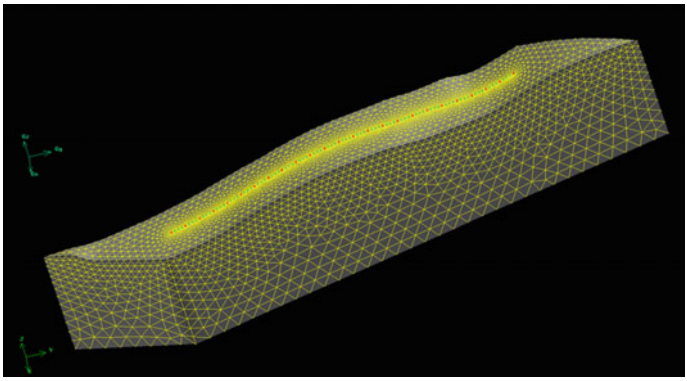

Fig. 8.6 A perspective view of the tetrahedral mesh used in our DG simulations. The top surface of the mesh conforms to local topography derived from DEM data. Locations of the seismic shots and geophones are indicated using red dots and green dots, respectively. Element size increases gradually with both depth and the distance from the survey line

Conventional finite element schemes often lose accuracy on such meshes in comparison with structured hexahedron or rectangle grids (e.g., Baker 2005). Numerical convergence studies have shown that the DG scheme retains very high-order accuracy on unstructured tetrahedral meshes (e.g., Dumbser and Käser 2006), thereby providing a good combination of geometrical flexibility and computational accuracy.

For our F3DT inversion of Line 17 (Fig. 8.1), we constructed a 3D tetrahedral mesh with element sizes adapting to both spatial variations of seismic velocities and also the desired resolution (Fig. 8.6). The 2D starting model obtained from RTT refraction tomography was extended in the other horizontal dimension and interpolated onto our 3D tetrahedral mesh. The seismic velocities at shallower depths are much lower than those at larger depths, and the wavelengths at shallower depths are therefore much shorter. So at shallower depths, we used tetrahedral elements with much smaller sizes (~0.75 m at the ground surface) than those at larger depths (~10 m at about 150 m depth) (Fig. 8.6). To improve the resolution of the seismic velocity model just below the refraction survey line, the tetrahedral mesh was further refined on and around the vertical plane containing the survey line. As the seismic velocity model was updated from iteration to iteration, the tetrahedral mesh can be updated accordingly to adapt to the changing velocity model. If any sharp geological interfaces, e.g., the sharp boundary at the base of the weathering interface, spontaneously emerge during the iterative F3DT inversion, the tetrahedral mesh can be easily modified to adapt to such changes in the structure model.

8.3.2 Waveform Misfits

The discrepancies between synthetic and observed waveforms must be quantified before being used to compute model perturbations. There are a variety of techniques for quantifying waveform differences, such as a subtraction in the time or frequency domain or subtraction of the logarithms of the waveforms, and F3DT is capable of inverting any types of misfits. The information about subsurface structure is distributed unevenly in time on a seismogram and also highly unevenly between the phase and the amplitude. In fact, the majority of seismic tomography work in the past few decades was based upon the travel-time (a type of phase data) of a handful of seismic arrivals (time-localized wave packets, such as P-, S-, and surface waves). On the contrary, the waveform data (a type of amplitude data) of the entire seismogram are highly nonlinear with respect to seismic velocity models, which introduces many spurious local minima into the objective function and an iterative optimization algorithm can easily get stuck into local minima without converging into a useful velocity model. To capture the rich information in waveforms without introducing significant nonlinearity into our optimization process, we quantify waveform discrepancies using frequency-dependent phase and amplitude misfits extracted from synthetic and observed waveforms that are localized in the time-frequency domain (Lee and Chen 2013).

Our waveform misfit quantification technique can be applied to any segment of the seismogram. Figure 8.7 shows an example of a surface wave from Line 17 (Fig. 8.1). For this particular example, the Rayleigh wave on the synthetic and observed seismograms can be isolated in the time domain through windowing operations using a cosine-taper window. The frequency-dependent phase and amplitude differences can be represented as weighted summations of B-spline functions, and the optimal weights can be found by minimizing the energy of waveform differences in the time domain using the Levenberg-Marquardt algorithm. Figure 8.7d shows the frequency-normalized optimized phase difference as a function of frequency, which is called the "frequency-dependent phase-delay time" and can be roughly considered as frequency-dependent "travel-time" differences between the windowed synthetic and observed waveforms. In our preliminary F3DT inversion, this technique was applied on a hand-selected waveform subset mainly composed of P/P-coda waves (i.e., each time window is around the first-break on a seismogram) and surface waves (i.e., each time window is around the wave with the largest amplitude on a seismogram). And the frequency-dependent phase-delay time measurements were used to compute the perturbations (corrections) to the seismic velocity models.

8.3.3 Sensitivity Kernels

Intuitively, the sensitivity (Fréchet) kernels tell us how to change our structure model in order to reduce the discrepancies between synthetic and observed waveforms quan-

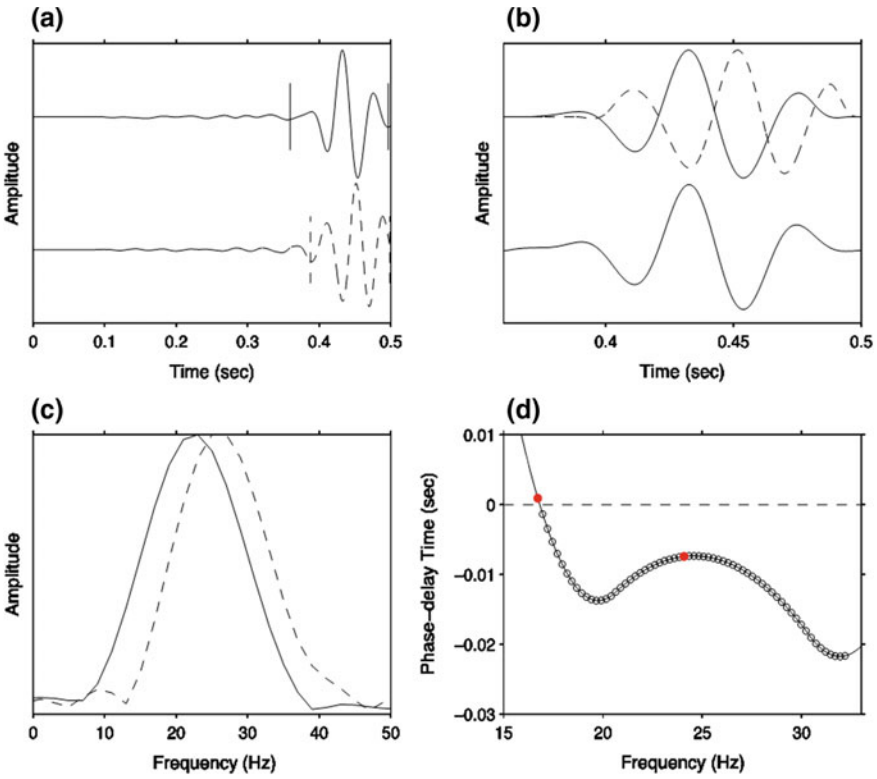

Fig. 8.7 **a** Observed (solid line) and synthetic (dashed) seismograms; **b** the top traces show the observed waveform (solid line) and the synthetic waveform (dashed); the bottom traces show the perfect fit between the observed and synthetic waveforms after correcting the synthetic waveform with the frequency-dependent phase and amplitude misfit measurements; **c** the amplitude spectrums of the observed (solid line) and synthetic (dashed) waveforms; **d** frequency-dependent phase-delay time misfits between observed and synthetic waveforms

tified using a specific misfit measure. They play a central role in converting waveform misfit measurements into corrections to the model. As the structure model changes from one iteration to another, the model corrections and therefore the kernels need to be re-computed in each iteration. In practice, it is the construction of the kernels that consumes most of the computational resources in a typical F3DT inversion.

The sensitivity kernels for the waveform misfit measurements with respect to structure parameters (e.g., seismic velocities, elastic moduli, Lamé parameters) can be computed using either the scattering-integral method (F3DT-SI) (Zhao et al. 2005; Chen et al. 2007b; Chen and Lee 2015) or the adjoint-wavefield method (F3DT-AW) (e.g., Tarantola 1988; Tromp et al. 2005; Liu and Tromp 2006). Both methods are physically equivalent, but have very different computational requirements (Chen et al. 2007a). For the source-receiver configurations of our critical zone seismic data set, in which the number of receivers is much larger than the number of seismic

sources, the adjoint-wavefield method is computationally more efficient (Chen et al. 2007a) and we adopted it in our F3DT inversion.

The adjoint method requires two wave-propagation simulations per seismic source: one forward simulation that propagates seismic waves from the seismic source to all receivers and one adjoint simulation that propagates waves from virtual sources composed of the misfit-weighted adjoint sources positioned at the receiver locations back to the seismic source. The DG method that we have adopted in solving the elastodynamic equations uses the velocity-stress formulation in which the stress fields, as functions of 3D space and time, are explicitly constructed. We converted those stress fields to strain fields by applying the elastic constitutive relation (Zhao et al. 2006). The adjoint kernel can then be constructed through a combination of tensor operations and temporal correlation between the forward and adjoint strain fields within each tetrahedral element. In the following section, we show examples of the adjoint kernels computed for a collection of carefully chosen seismic velocity models and seismic arrivals to validate our computer code for constructing the kernels.

8.3.3.1 Half-Space Example

This example follows that in Zhao et al. (2005). The reference structure model is a uniform half-space model with P-velocity 6.5 km/s, S-velocity 3.5 km/s, and density 3000 kg/m^3. Both the source and the receiver are buried at a depth of 24 km below the free-surface, and the source-receiver distance is 32.2 km. The source-time function has a Gaussian form $s(t) = \exp\left[-a(t - b/2)^2\right]$ where $a = 60$ and $b = 0.65$, which gives synthetic seismograms with a dominant frequency of about 2 Hz. We consider two types of source mechanisms: an explosive (isotropic) source and a double-couple source with strike 90°, dip 45°, and rake 45°. The sensitivity kernel depends upon the type of misfit measurements used for quantifying the discrepancies between synthetic and observed waveforms. The type of misfit measurements determines the specific form of the seismogram perturbation kernel, which is the Fréchet derivative of the misfit measurement with respect to the synthetic waveform (Chen et al. 2007a). In this example, we use the broadband cross-correlation delay-time, i.e., the time shift between an isolated waveform on the observed displacement seismogram and the corresponding waveform on the reference synthetic displacement seismogram estimated by maximizing the cross-correlation between the two waveforms. For this example, the synthetic displacement on the X-component is much larger than that on the other two components and there are only three major arrivals: the direct P-wave and the free-surface reflected pP-wave and the free-surface converted pS-wave. The direct P- and pP-waves should have strong sensitivity to the P-velocity, and the pS should be sensitivity to P-velocity on its up-going leg and be sensitive to S-velocity on its down-going leg.

Figure 8.8 displays the sensitivity kernels of the broadband cross-correlation delay-time measured on the three different types of waves with respect to P- and S-velocity models. The kernels show the counterintuitive "banana-doughnut" behavior

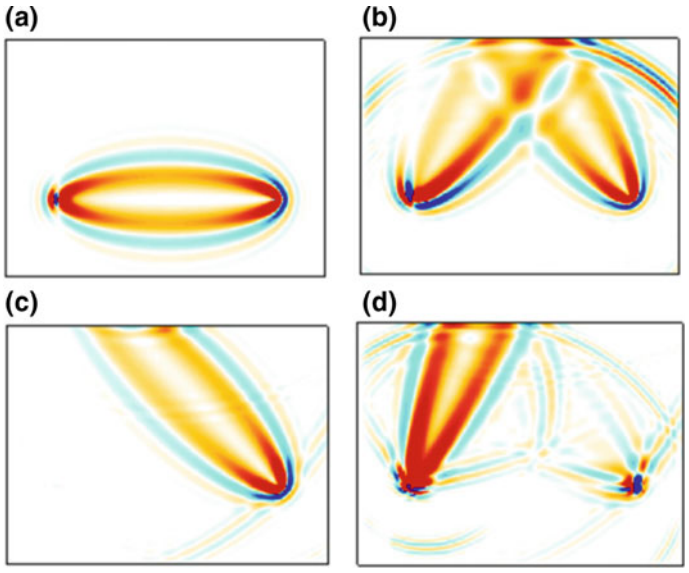

Fig. 8.8 Kernel examples for the half-space structure model with the explosive source on the right side and the receiver on the left side of the modeling volume. **a** Kernel for direct P-wave. **b** Kernel for free-surface-reflected pP-wave. **c** P-velocity kernel for free-surface-converted pS-wave. **d** S-velocity kernel for free-surface-converted pS-wave

with vanishing sensitivity on the ray paths (Marquering et al. 1999; Dahlen et al. 2000; Hung et al. 2000; Zhao et al. 2000). The exact shape of the sensitivity kernels depends upon several factors. For a fixed forward wavefield from the source, changing the source-time function used for computing the receiver-side Green's tensors (RGT) can change the shape of the kernel. The kernel shown in Fig. 8.9a was computed using the RGT whose source-time function was given by the 6th-order low-pass Butterworth filter with the corner at 1.5 Hz and the kernels shown in Fig. 8.9b, c were computed using the RGT whose source-time function was given by the 4th-order low-pass Butterworth filter with the corner at 3.5 Hz. The kernel in Fig. 8.9a has a wider first Fresnel zone than those in Fig. 8.9b, c because of a longer dominant wavelength. Whether the measurement is made on displacement (Fig. 8.9a, b) or the velocity seismogram (Fig. 8.9c) can have effects on the shape and the strength of the sidebands of the kernels.

For the double-couple source buried in the uniform half-space structure model, the source emits both P- and S-waves and there should be six arrivals at the receiver: the direct P- and S-waves, the free-surface reflected pP- and sS-waves, and the free-surface converted pS- and sP-waves. The kernel for the broadband cross-correlation delay-time and amplitude anomaly measured on the direct S-wave on the Y-component with respect to S-velocity are shown in Fig. 8.10. The spatial distribution of the sensitivity for delay-time is mostly similar to that of the direct P-wave shown in Figs. 8.8 and 8.9. The width of the first Fresnel zone is narrower than the

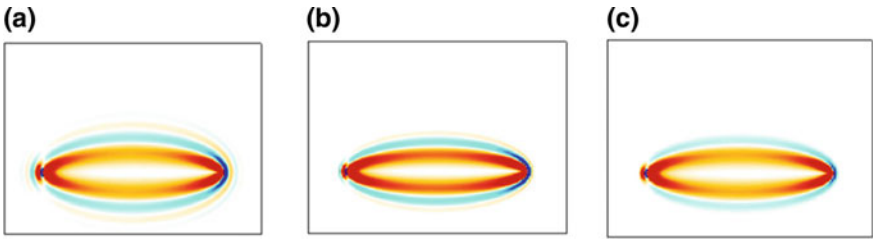

Fig. 8.9 Comparison of sensitivity kernels for the broadband cross-correlation delay-time measured for direct P-wave on the velocity seismogram (left and center) and the displacement seismogram (right), filtered using the low-pass Butterworth filter with corner frequency at 1.5 Hz (left) and 3.5 Hz (center and right)

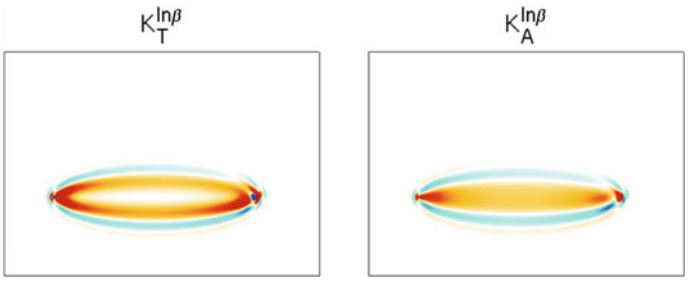

Fig. 8.10 Kernel examples for the broadband cross-correlation delay-time (left) and amplitude anomaly (right) with respect to S-velocity for the direct S-wave on the Y-component synthetic velocity seismogram generated by a double-couple source buried in the uniform half-space structure model

kernels shown in Figs. 8.8 and 8.9 due to the smaller wavelength of the direct S wave than that of the direct P-wave. We can also observe that unlike the kernels for the explosive source, the kernels shown in Fig. 8.10 are not symmetric with respect to the source-receiver path, which is due to the S-wave radiation pattern from the double-couple source mechanism used in computing the forward strain fields.

8.3.3.2 Layer-Over-Half-Space Example

This example follows that in Zhang et al. (2007). For the top layer, the P-velocity is 5207 m/s, the S-velocity is 3189 m/s, and the density is 2950 kg/m^3 and for the half-space, the P-velocity is 9058 m/s, the S-velocity is 5307 m/s, and the density is 3992 kg/m^3. The top layer has a thickness of 21.4 km, and both the explosive source and the receiver are buried inside of the top layer. The source is at depth 18 km and the receiver is at depth 6.4 km and the horizontal source-receiver distance is 88 km. The source-time function has the same Gaussian form as that used in the half-space example with $a = 20$ and $b = 2$, which gives synthetic seismograms with a dominant frequency of around 0.5 Hz. The misfit measurement type is the broadband cross-

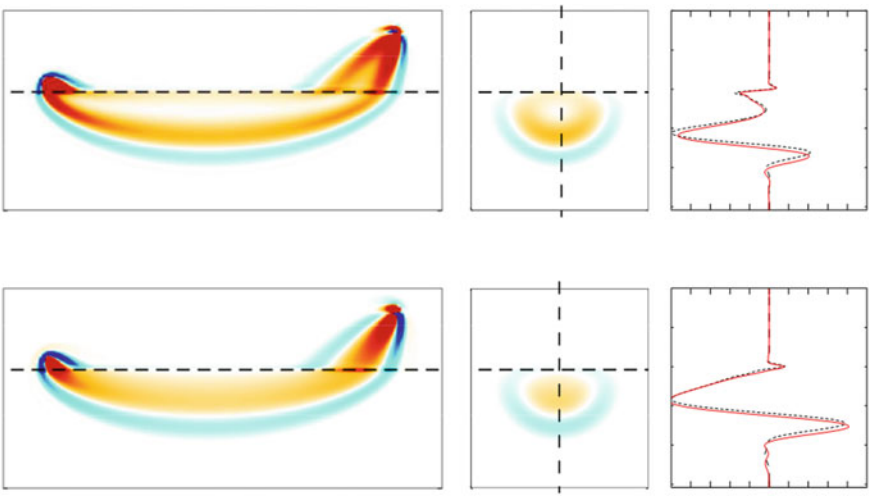

Fig. 8.11 Kernels for the broadband cross-correlation delay-time (top row) and amplitude anomaly (bottom row) with respect to P-velocity for the head wave on the vertical component velocity seismogram. Left column: cross-sections on the source-receiver plane perpendicular to the y-axis; center column: cross-sections mid-way between source and receiver and perpendicular to the x-axis; right column: sensitivity along the vertical dash lines in the center column for the "layer-over-half-space" model (black dash lines) and the "layer-over-gradient" model (red solid lines)

correlation delay-time and amplitude anomaly, and the kernels are computed for the head wave on the vertical component seismogram with respect to P-velocity.

Figure 8.11 shows the sensitivity kernels for the head wave broadband cross-correlation delay-time and amplitude anomaly misfits with respect to P-velocity. As pointed out in Zhang et al. (2007), the strongest sensitivity is located mostly on only the lower side of the refracted ray path below the velocity interface, and the delay-time kernel can be characterized as a "split-banana-doughnut" kernel.

The layer-over-half-space structure model can be easily modified to introduce a velocity gradient in the half-space. We can call the modified structure model "layer-over-gradient." Here, we increase both P- and S-velocity linearly with depth at a rate of 0.02 km/s/km. The sensitivity kernels for the broadband cross-correlation delay-time and amplitude anomaly misfits are highly similar to those for the layer-over-half-space model shown in Fig. 8.11, except that the sensitivity has extended slightly to larger depths. For such a dispersive head wave, we can compute the sensitivity kernels for the frequency-dependent phase-delay time with respect to P-velocity. Figure 8.12 shows the kernels for frequency-dependent phase-delay time measured at 1.0 and 2.0 Hz. At higher frequencies, the width of the first Fresnel zone is narrower and the sensitivity is compressed more toward the velocity interface. The sidebands in the kernels are due to the narrow-band nature of the frequency-dependent phase-delay misfit.

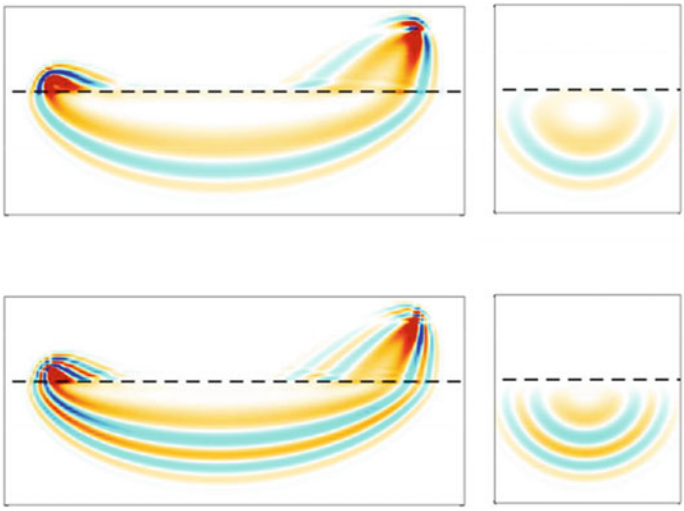

Fig. 8.12 Kernels for the frequency-dependent phase-delay time with respect to P-velocity for the head wave in the "layer-over-gradient" model at 1.0 Hz (top row) and 2.0 Hz (bottom row)

8.3.3.3 Critical Zone Example

Examples of the adjoint kernels for frequency-dependent phase-delay time measured on P/P-coda waves and surface waves used in our F3DT inversion for the critical zone structure at the Blair Wallis area are shown in Figs. 8.13 and 8.14. We have examined many kernels computed in F3DT inversion, and we summarize major features of those kernels as below, which are also consistent with what we expect from 3D wave physics.

1. The spatial sampling patterns of P/P-coda wave kernels are highly different from those of surface wave kernels. The cross-sectional views of P/P-coda kernels show the typical "banana-doughnut" shape with diminishing sensitivities along the ray paths as discussed in Marquering et al. (1999) and Dahlen et al. (2000).
2. The sensitivities of surface wave kernels are concentrated close to the ground surface. At lower frequencies, the kernel has a wider Fresnel zone and higher sensitivities at larger depths than the kernel at higher frequencies.
3. These two types of waves are sensitivity to different structureal parameters. The kernels for P/P-coda waves show much stronger sensitivities to P-velocity than to S-velocity. In general, the sensitivities to S-velocity (not plotted in Fig. 8.13) is less than one-tenth of their sensitivities to P-velocity. The surface wave kernels show stronger sensitivities to S-velocity than to P-velocity in general.
4. The intensity of the sensitivity kernels is highly variable through space. For P/P-coda wave kernels, amplitudes of the sensitivities at source and receiver locations are much larger than those between the source and receiver locations. For surface

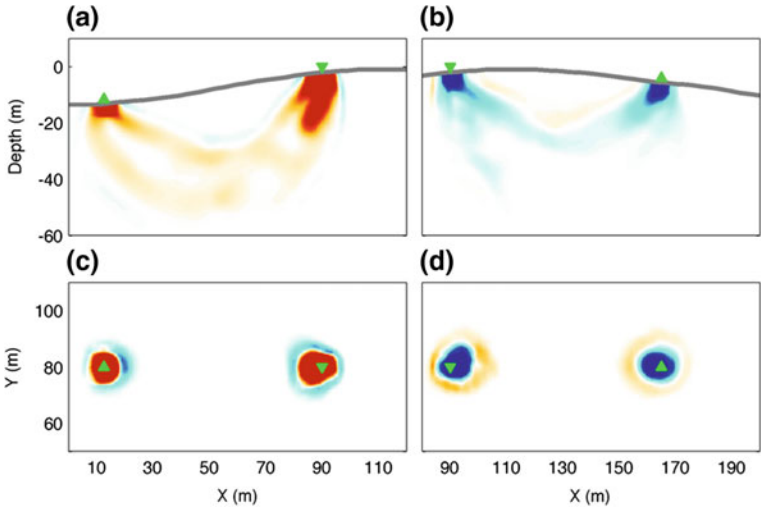

Fig. 8.13 Example adjoint kernels for P/P-coda waves for two source-receiver paths on opposite sides of the ridge top. **a** and **b** cross-sectional views perpendicular to the vertical plane containing the source and receiver; **c** and **d** map views at 15 m depth below the topography. Warm and cool colors are negative and positive perturbation to P-velocity. Green reverse triangle: source location; green triangle: receiver location; gray line: topography. These are misfit-weighted Fréchet kernels. The sign of the kernel depends upon the sign of the misfit measurement

waves, the kernel intensity decreases rapidly with depth. The intensity of both types of kernels shows significant spatial variations caused by 3D heterogeneities.

8.4 F3DT Results and Discussion

In our F3DT inversion of Line 17 (Fig. 8.1), there were 24 shots along the survey line, and therefore, 48 wave-propagation simulations were needed to construct the adjoint kernels for each iteration. We have carried out 12 iterations using P/P-coda waves and 9 iterations using surface waves. As the structure model improves gradually through the iterations, synthetic seismograms computed using the updated structure model are capable of fitting more waveforms on the observed seismograms and the total number of waveforms amenable to F3DT inversion increases gradually through iterations. The latest P-velocity (Vp) and S-velocity (Vs) model as well as the derived Vp/Vs model are shown in Fig. 8.15.

In this F3DT experiment, our Vp starting model (Fig. 8.15a) was constructed using first-arrival RTT. The observed travel-time was picked manually. The velocity inversion grid comprised 241 × 181 grid points covering the 240 m × 90 m modeling region with horizontal and vertical grid spacing of 1 and 0.5 m, respectively. We used the ray bending implementation of Koulakov et al. (2010). The mis-

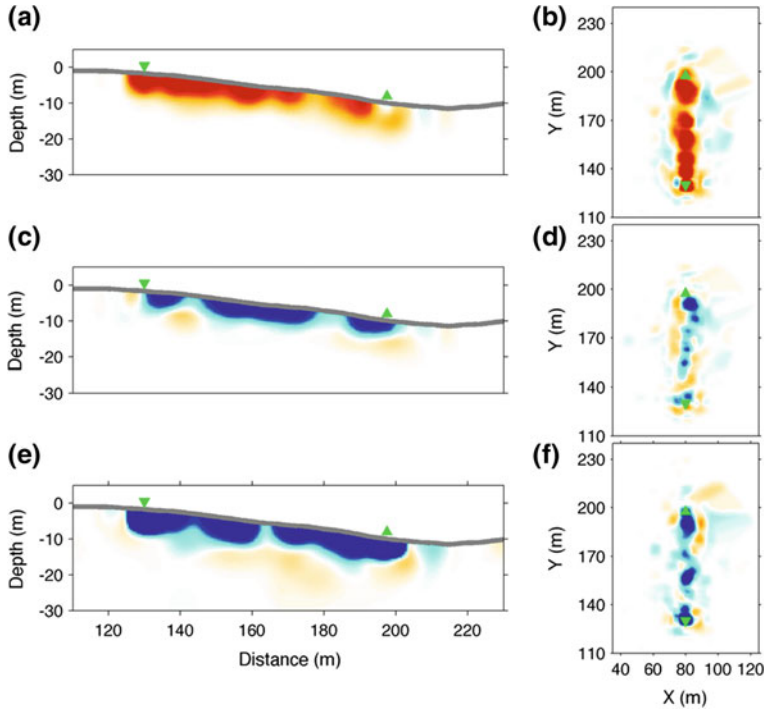

Fig. 8.14 Examples of adjoint kernels for a surface wave along the hill slope. **a**, **c**, and **e** cross-sectional views perpendicular to the source-receiver plane; **b**, **d** and **f** map views at 2 m below topography. **a** and **b** kernel for phase-delay time measured at 16 Hz; **c** and **d** kernel for phase-delay time measured at 24 Hz; **e** and **f** misfit-weighted summation of adjoint kernels for phase-delay time measured at multiple frequencies. Warm and cool colors are negative and positive perturbation to S-velocity. These are misfit-weighted Fréchet kernels. The sign of the kernel depends upon the sign of the misfit measurement. For the kernel at 16 Hz in (**a** and **b**), the misfit is positive (Fig. 8.7d) and the kernel is mostly red. For the kernel at 24 Hz in (**c** and **d**), the misfit is negative (Fig. 8.7d) and the kernel is mostly blue

fits between model-predicted and observed first-arrival travel-time were minimized using the LSQR algorithm (Paige and Saunders 1982). After 10 iterations, the RMS travel-time misfit reduced to about 1.6 ms. Our Vs starting model was obtained by scaling our Vp starting model using a constant factor.

8.4.1 Three-Dimensional Structure of the Weathering Interface

As shown in Fig. 8.15, the velocity images constructed using F3DT (Fig. 8.15b) show many small-scale structural features that do not exist in the image obtained

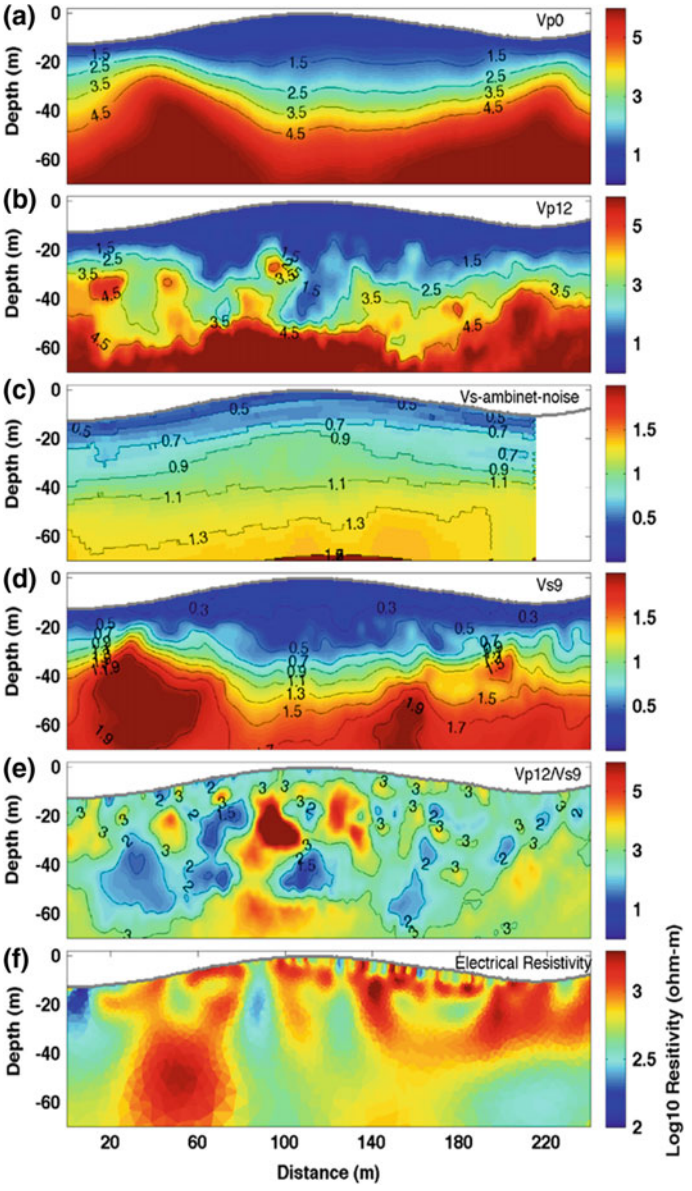

Fig. 8.15 Seismic velocity and electrical resistivity models for Line 17. **a** Vp model from first-arrival RTT; **b** Vp model from our preliminary F3DT using P/P-coda waves after 12 iterations; **c** Vs model from ambient-noise simple-imaging; **d** Vs model from our F3DT using surface waves after 9 iterations; **e** Vp/Vs ratio model computed from (**b**) and (**d**); **f** electrical resistivity model. Black circles on (**e**) and (**f**) indicate major structural features that are anti-correlated (see text). For seismic velocity models, cool colors represent lower velocity values and warm colors represent higher velocity values, which is different from the convention used in large-scale seismic tomography but consistent with past critical zone seismic tomography studies. For the electrical resistivity image, cool colors represent low resistivity and warm colors represent high resistivity and color scale is in log10

from RTT (Fig. 8.15a). The resolution provided by F3DT allows us to investigate the 3D internal structures of the WI in the DCZ using waveform data gathered in conventional SRS. Previous studies based on geochemistry (i.e., element concentration as a function of depth), outcrop observations and drilling (i.e., rock fragment/corestone size as a function of depth) at the Shale Hill critical zone observatory (CZO), and the Luquillo CZO (Brantley et al. 2011; Buss et al. 2013) have led to the construction of a conceptual model for the WI that transforms fresh crystalline bedrock into saprolite. Our F3DT velocity image (Fig. 8.15b) is remarkably consistent with this conceptual model and its structural implications. For example, chemical weathering is a key factor in transforming bedrock into regolith, and the depth distribution of element concentration curves (Brantley and Lebedeva 2011; Brantley et al. 2011) shows a sharp chemical boundary at the base of the weathering interface where the concentration of major silicates and carbonates drops from their normal level in bedrock to nearly zero over a depth interval of about one meter. In Fig. 8.15b, at about 50 m beneath the ridge top there exists a sharp velocity gradient where P-velocity (Vp) decreases from 4.5 km/s to about 1.5 km/s within a depth interval of ~5 m. Unlike RTT, which typically produces smoothed images of the real structure, F3DT is capable of resolving sharp structural discontinuities and this capability was documented previously in our F3DT studies in Southern California, where we found sharp gradients in our F3DT images that match major strike-slip and dip-slip faults in that region (Lee et al. 2014a; Chen and Lee 2015; Lee and Chen 2016).

A structural consequence of the chemical weathering model is that the sizes of the bedrock fragments or corestones should generally decrease toward the surface (Brantley and Lebedeva 2011; Brantley et al. 2011). In Fig. 8.15b, within around 20–40 m depth range, high-velocity parcels (Vp > 4 km/s) with onionskin-like shells are dispersed inside low-velocity layers. These high-velocity parcels might be large corestones surrounded by regolith. At larger depths (40–60 m), sizes of corestones are larger and the regolith gaps between them are smaller and our F3DT image cannot resolve those smaller regolith gaps yet. The conceptual model of the WI is based dominantly on one-dimensional downward fluid flow in porous media. In reality, lateral flow can significantly alter the structure of the WI and thereby the balance between weathering and erosion rates. We plan to apply F3DT to the seismic waveform data collected at three CZOs located in regions with very different composition, climate and erosional regimes. Once completed, our new F3DT velocity models will allow critical zone researchers to take into account the effects of lateral flow and construct new conceptual models. In addition, the evolution of the weathering interface (reaction zone) is complex; hence, comparisons between the different CZO's using the same F3DT technique will permit more reliable inferences regarding how the CZO evolves under climate, tectonic, and anthropogenic forcing and responds to external stresses (e.g., droughts).

8.4.2 *Characterizing Water Flow and Storage Using Seismic Velocities*

S-velocity (Vs) is not sensitive to the saturation of the porous material, whereas Vp increases with saturation (e.g., Scholz et al. 1973; O'Connell and Budiansky 1974; Toksoz et al. 1976; Moos and Zoback 1983; Zhao et al. 1996; Zimmer et al. 2002). By estimating both Vp and Vs or their ratio Vp/Vs, one can detect and characterize subsurface water effectively. The Poisson's ratio, which can be calculated from Vp/Vs, is a parameter that measures the compressibility of the material and any increases of water, air or, unconsolidated material in the subsurface will increase the Poisson's ratio from around 0.25 in hard rock to values potentially larger than 0.45 (e.g., Barton 2006).

F3DT can utilize any waves that have sensitivity to Vs, including pure and mixed mode waves, multiply scattered waves and the surface wave, to construct Vs images. In our very preliminary F3DT study of Line 17, we used only a subset of surface waves to obtain the Vs image shown in Fig. 8.15d. Other types of waves sensitive to Vs can be included into the F3DT inversion without difficulty and will likely improve the resolution of our Vs image, especially at larger depths. Since the S-wave wavelength is usually smaller than the P-wave wavelength at the same frequency and the theoretical resolution limit of F3DT only depends upon the wavelength, our final S-velocity image after including all available data will potentially reach a better resolution than our P-velocity image.

Even at the resolution already reached in our current F3DT study, our image of the Vp/Vs ratio (Fig. 8.15e) shows a truly remarkable anti-correlation (i.e., a high Vp/Vs value corresponds to high saturation and a low-resistivity value) with the electrical resistivity image (ERI) (Fig. 8.15f), which is highly sensitive to water saturation.

(1) There exist two low-resistivity (blue) zones on both sides of the ridge top in the ERI (Fig. 8.15f), which might indicate the existence of two potential water channels. The low-resistivity zone on the left side of the ridge top has even lower resistivity than the one on the right. We observe a similar pattern in our Vp/Vs image (Fig. 8.15e), and there exist two zones with high Vp/Vs values on both sides of the ridge top at about the same horizontal distances and depths as the two low-resistivity zones in Fig. 8.15f. The high Vp/Vs zone on the left side of the ridge top has higher Vp/Vs value than the one on the right.
(2) At a larger scale, the high-resistivity zone from horizontal distance of ~20 m to ~70 m on the x-axis in Fig. 8.15f is anti-correlated with the low Vp/Vs zone at about the same horizontal distance and depth ranges in our Vp/Vs image in Fig. 8.15e.
(3) The high-resistivity zone extending from horizontal distance of ~140 m to ~230 m on the x-axis in Fig. 8.15f anti-correlates with the low Vp/Vs zone with a similar shape in our Vp/Vs image (Fig. 8.15e).

The resolution of our seismic images obtained from F3DT suggests that it is feasible to estimate the 3D spatial distributions of crack density, porosity, and its

water saturation levels by applying crack theory (e.g., O'Connell and Budiansky 1974; Zhao and Mizuno 1999; Takei 2002) to the Vp, Vs, and Poisson's ratio (or Vp/Vs) models obtained from our F3DT inversion. The crack theory provides a set of equations relating Vp, Vs, and Poisson's ratio to crack density and water saturation, and the porosity theory of Picket (1963) can be used to estimate porosity from seismic velocity. The crack theory has been successfully applied before to estimate fluid distributions in the source volumes of large earthquakes (e.g., Zhao et al. 1996; Zhao and Mizuno 1999; Mishra and Zhao 2003).

8.5 Future Work on Critical Zone Hydrological Properties

The western USA has a semi-arid climate characterized by dry hot summers and cool wet winters. Wyoming, as a headwater state in the West, drains to three river basins in the continental USA: Columbia River to the Pacific Northwest, Colorado River to the Gulf of California, and Missouri-Mississippi River to the Gulf of Mexico. Physiographically, Wyoming consists of mountains and high plains, or intermountain basins, with a mean elevation ~2 km amsl. The mountains lie approximately perpendicular to the prevailing westerlies, providing a barrier for air currents moving in from the Pacific. Air rises above the mountains and drops much of its moisture there, thus most of the state's intermountain basins lie in the rain shadows. Mountain precipitation is approximately 2 ~ 3 times the basin average, and these mountains are nicknamed, aptly, as "Water Towers of the West." In Wyoming, maximum precipitation occurs in winter and spring in the form of snowfalls, hydrology of the state is thus snowmelt-driven: Mountain snowmelt is partitioned into streamflow and groundwater, which constitute Wyoming's water resources. However, for these mountain catchments, snowmelt partitioning into groundwater is poorly understood due to sparse and often non-existent subsurface characterization and monitoring data. Because these watersheds typically have thin soils underlain by bedrocks, most conceptual hydrological models assume negligible groundwater storage, giving rise to the nickname "Teflon basin." This paradigm, which assumes bedrock is impervious to flow, is being challenged, as increasing evidence suggests that groundwater can play an active role in mountain hydrological processes.

The Laramie Range lies on the eastern edge of the Colorado Plateau and is considered a northern extension of the Colorado Front Range. It is approximately 225 km long and 40–70 km wide and was created by Laramide Orogeny at ~70 Ma. Elevation varies from 2.4 to 3.1 km amsl while surrounding basin floors lie at an elevation of 1.8–2.1 km amsl. Geology of the Range consists of a thin mantle of weathered granitic soil (saprolite) overlying fractured granite bedrock, both derived from the Precambrian Sherman batholith. In many areas, fractured granite forms exposed outcrops without soil cover, while vegetation, where it exists, is dominated by dryland grasses, shrubs, and trees. During the late Cretaceous time, numerous thrust faults formed along the eastern flank of the Range in response to tectonic movements. Along its western flank, no thrust faults have been identified although post-Miocene

extensional faults are superimposed throughout the region. The granite bedrock in the Range is highly fractured, to the extent that the northern portion of the range may have rotated southward. The highly fractured bedrock is confirmed by geologic mapping studies in the region that have identified numerous lineaments on or near the land surface. Despite the progress made in hydrological observations at Blair Wallis, understanding of much of the actual processes remains incomplete, especially at locations away from boreholes. As a result, there is a lack of quantification in elucidating subsurface flow processes including recharge, discharge, and their variability. During the period of hydrological data collection, extensive geophysical characterization was carried out to investigate bedrock depth, thickness, and fracture distribution (e.g., Flinchum et al. 2018a, b; Wang et al. 2019a, b). Flinchum et al. (2018b) and Wang et al. (2019b), in particular, showed that 3D seismic velocity models obtained through tomography can be used to construct 3D models of subsurface hydrological properties, such as water content and porosity, using physics-based petrophysical models (Dvorkin and Nur 1996; Nur et al. 1998; Helgerud 2001; Bachrach and Avseth 2008; Holbrook et al. 2014; Pasquet et al. 2016). Such porosities were found to be highly consistent with direct porosity measurements made on core samples extracted from boreholes. Considering that hydrological techniques for characterizing subsurface properties, such as slug tests, flowmeter tests, and pumping tests, rely upon the availability of boreholes and are only applicable to obtain property distribution in the vicinity of the boreholes, 3D seismic velocity tomograms are therefore particularly useful for quantifying subsurface hydrological properties in areas away from wellbores. When calibrated against borehole measurements, seismic tomography can be an effective tool for quantifying subsurface hydrological properties.

One possible extension of our previous work is to quantify 3D and temporal distribution of porosity and water content in saprolite and fractured granite at Blair Wallis through joint inversions of time-lapse seismic refraction data and hydrological measurements (water-level fluctuations) obtained at borehole locations. The temporal variations can be obtained by collecting 3D, seismic refraction data at carefully chosen time intervals before, during, and after the snowmelt peak in April–June. The seismic sources and the geophones used in the surveys will be located at the same positions to minimize uncertainties in the inverted temporal variations of hydrological properties due to changes in seismic source-receiver geometries.

In order to obtain spatiotemporal mappings of subsurface hydrological properties, we can follow a two-step approach. In the first step, we will invert the entire seismic data set obtained for all time intervals for a time-averaged 3D P- and S-wave velocity models of the Blair Wallis subsurface. A time-averaged 3D porosity model will be obtained from both the P- and S-velocity models following the approaches of Flinchum et al. (2018b) and Wang et al. (2019b). A time-averaged, 3D water saturation model will be derived from the inverted 3D P-velocity model following the approach of Flinchum et al. (2018b).

In the second step, the time-averaged, 3D models obtained from the first step will be used as the starting sample in a stochastic inversion for time-dependent models based on Bayesian inference and Markov Chain Monte-Carlo (MCMC) sampling for which both hydrological and seismic measurements will be used to condition

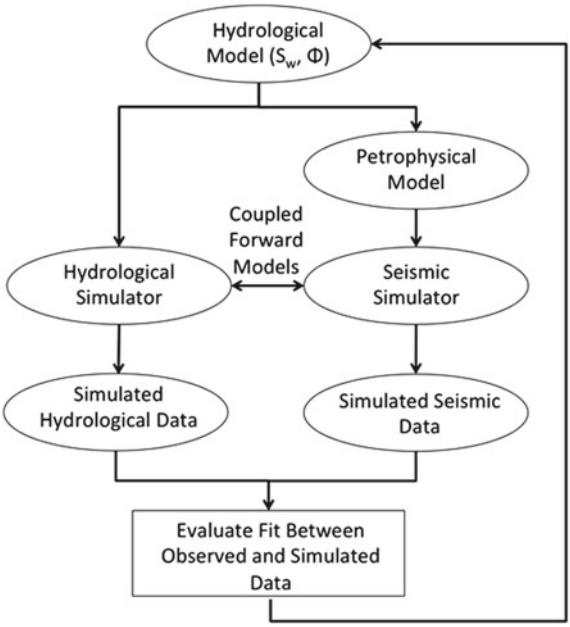

Fig. 8.16 Flow chart for joint inversion of time-lapse, 3D seismic data, and hydrological measurements using MCMC based upon Bayesian inference and the MH sampling algorithm. The petrophysical model maps the hydrological model to P- and S-velocity models used by the seismic simulator to generate simulated seismic data, which are then compared with actual observed seismic data gathered during each time interval. The same hydrological model is also fed into the hydrological simulator, and the simulated hydrological data are compared with actual hydrological observations in the boreholes. The value of the posterior PDF is calculated based upon the fit between observed and simulated data, as well as the prior distribution. The new candidate sample of the hydrological models is either accepted or rejected based upon the MH algorithm, and the entire process is iterated until convergence

the inversion. A flow chart depicting the proposed hydrogeophysical joint inversion technique is shown in Fig. 8.16. The hydrological property models for the different time intervals, as well as the associated uncertainty estimates, will be derived independently using the observed seismic and hydrological data gathered during each time interval. The prior distribution of the hydrological property models can be constructed based upon both the 3D characterization of the subsurface architecture obtained in the first step and the results documented in our previous works (Wang et al. 2019a, b). The posterior probability density function (PDF) of the hydrological property models of water saturation and porosity will be sampled using the Metropolis–Hastings (MH) algorithm, which is an efficient MCMC sampling strategy and has proved to be effective in several parameter estimation applications in hydrology (e.g., Kuczera and Parent 1998; Bates and Campbell 2001; Vrugt et al. 2003; Feyen et al. 2007; Blasone et al. 2008).

The MH sampling strategy evolves by drawing a new sample of the hydrological property models from a candidate-generating density function and decides whether to replace the previous sample with the new candidate sample by comparing the value of the posterior PDF at the new candidate sample against the value at the previous sample. We will be experimenting with different types of candidate-generating density functions, and in particular, we will compare candidate-generating functions based upon random walks and those based upon maximum a posteriori (MAP) estimates. MCMC is a computationally intensive approach for nonlinear parameter estimation, and the computational efficiency of the hydrological and seismic simulators is of paramount importance to the feasibility of the proposed stochastic inversion workflow. To improve the computational efficiency of the entire workflow, we will explore the possibility of combining linearized forward models that are much cheaper to evaluate with the fully nonlinear forward simulator based upon the discontinuous Galerkin PDE solver.

The expected results of the proposed research will include time-dependent, fully 3D, hydrological property models of water saturation and porosity of the Blair Wallis subsurface constrained by time-lapse, 3D seismic data, and hydrological observations in the existing boreholes. It will be a monumental achievement both in the field of hydrology and also in the field of geophysics. More importantly, the methodology developed during the proposed research will open up new possibilities in the rapidly emerging new field of hydrogeophysics.

8.6 Conclusion

The critical zone plays a central role in supporting agriculture and the majority of terrestrial life. To understand the complex physical, chemical, hydrological, and biological processes that create and transform the critical zone, we need to characterize its structure, especially at depths where the weathering engine transforms fresh bedrock into regolith. Prior studies at multiple critical zone observatories based on results from geochemistry, drilling/coring, and surface observations have allowed critical zone researchers to construct first-order conceptual models that account for downward fluid flow. A verifiable structural implication of this conceptual model is that in granitic terrains the corestone size generally decreases toward the ground surface. Conventional ray-theoretic travel-time tomography does not have the spatial resolution to resolve small-scale structures of the weathering interface. F3DT uses the same seismic data collected in conventional seismic surveys and provides much higher spatial resolution, which will allow us to validate the conceptual model at spatial scales ranging from pedon (meter) to catchment and landscape (kilometer). Such spatial scales might be too large for drilling/coring efforts to be practical. F3DT provides high-resolution 3D images of the weathering interface, which will allow the critical zone research community to incorporate higher-order effects, such as effects of lateral fluid flow, into the conceptual model.

Weathering is closely related to hydrology in the critical zone. Water interacting with mineral grains in rocks causes chemical weathering that can increase permeability, which in turn enhances fluid flow and accelerates chemical weathering. On the other hand, it is also possible that permeability is decreased due to clay formation. F3DT provides high-resolution 3D images of P-velocity, S-velocity, and Poisson's ratio, which are highly sensitive to subsurface water content and allow us to systematically image critical zone crack density, saturation and porosity by using the crack theory and its modern improvements. By systematically estimating critical zone water pathways and storage potentials, we can help to provide quantitative constraints for water resource management and also insights into the link between weathering and hydrology.

The critical zone is not a static layer, but evolves through time. For critical zones in the quasi-stationary state (Lichtner 1988; Brantley et al. 2007), regolith experiences little erosion and the concentration-depth profile retains its shape and moves downward with time at the weathering advance rate (Brantley et al. 2007). Regolith at the surface may become depleted of weathering-mobilized nutrients. For critical zones in the steady state, the erosion rate is balanced by weathering advance rate and the concentration-depth profile remains constant with time (Brantley et al. 2007). Such systems can provide ecosystems with a constant supply of weathering-derived nutrients. If the erosion rate is larger than the weathering advance rate, the regolith layer can become thinner with time (Carson and Kirkby 1972; Stallard and Edmond 1983). In the near future, we will carry out F3DT using data sets covering critical zones located in different climate, composition, and tectonic regimes. Comparisons among these critical zones using the same F3DT imaging technique will allow us to better understand the evolution of the weathering interface (reaction zone) under different climate, tectonic, and anthropogenic forcing and how they react to external stresses such as droughts or floods.

References

Anderson, S.P., F. von Blanckenburg, and A.F. White. 2007. Physical and chemical controls on the critical zone. *Elements* 3 (5): 315–319.

Bachrach, R., and P. Avseth. 2008. Rock physics modeling of unconsolidated sands: Accounting for nonuniform contacts and heterogeneous stress fields in the effective media approximation with applications to hydrocarbon exploration. Geophysics 73(6): E197–E209.

Baker, T.J. 1989. Automatic mesh generation for complex three-dimensional regions using a constrained Delaunay triangulation. *Engineering with Computers* 5 (3): 161–175.

Baker, T.J. 2005. Mesh generation: Art or science. Progress in Aerospace Sciences 41(1): 29–63.

Barton, N. 2006. *Rock quality, seismic velocity, attenuation and anisotropy*, 729. London, UK: Taylor & Francis Group.

Bates, B.C., and E.P. Campbell. 2001. A markov chain Monte carlo scheme for parameter estimation and inference in conceptual rainfall- runoff modeling. *Water Resource Research* 37 (4): 937–947.

Befus, K.M., A.F. Sheehan, M. Leopold, S.P. Anderson, and R.S. Anderson. 2011. Seismic constraints on critical zone architecture, Boulder Creek watershed, Front Range, Colorado. *Vadose Zone Journal* 10 (4): 1342. https://doi.org/10.2136/vzj2010.0108er.

Bensen, G.D., M.H. Ritzwoller, M.P. Barmin, A.L. Levshin, F. Lin, M.P. Moschetti, N.M. Shapiro, and Y. Yang. 2007. Processing seismic ambient noise data to obtain reliable broad-band surface wave dispersion measurements. *Geophysical Journal International* 169 (3): 1239–1260.

Blasone, R.S., H. Madsen, and D. Rosbjerg. 2008. Uncertainty assessment of integrated distributed hydrological models using glue with markov chain Monte carlo sampling. *Journal of Hydrology* 353 (1–2): 18–32.

Brantley, S.L., and M. Lebedeva. 2011. Learning to read the chemistry of regolith to understand the critical zone. Annual Review of Earth and Planetary Sciences 39: 387–416.

Brantley, S.L., M.B. Goldhaber, and K.V. Ragnarsdottir. 2007. Crossing disciplines and scales to understand the critical zone. *Elements* 3 (5): 307–314.

Brantley, S.L., H. Buss, M. Lebedeva, R.C. Fletcher, and L. Ma. 2011. Investigating the complex interface where bedrock transforms to regolith. *Applied Geochemistry* 26 (Supplement): S12–S15. https://doi.org/10.1016/j.apgeochem.2011.03.017.

Buss, H.L., S.L. Brantley, F.N Scatena, E.A. Bazilievskaya, A. Blum, M. Schulz, R. Jiménez, A.F. White, G. Rother, and D. Cole. 2013. Probing the deep critical zone beneath the Luquillo Experimental Forest, Puerto Rico. *Earth Surface Processes and Landforms* 38: 1170–1186. https://doi.org/10.1002/esp.3409.

Carson, M.A., and M.J. Kirkby. 1972. *Hillslope form and process*, 475. London: Cambridge University Press.

Chen, P. 2011. Full-wave seismic data assimilation: Theoretical background and recent advances. *Pure and Applied Geophysics* 168 (10): 1527–1552.

Chen, P., and E-J. Lee. 2015. *Full-3D seismic waveform inversion—Theory, software and practice*, 513. Springer.

Chen, P., T. Jordan, and L. Zhao. 2007a. Full three-dimensional tomography: A comparison between the scattering-integral and adjoint-wavefield methods. *Geophysical Journal International* 170 (1): 175–181.

Chen, P., N.J. Taylor, K.G. Dueker, L.S. Keifer, A.K. Wilson, C.L. McGuffy, C.G. Novitsky, A.J. Spears, and W.S. Holbrook. 2016. A scalable, Parallel algorithm for Seismic Interferometry of large-N ambient-noise data. *Computers & Geosciences* 93: 88–95.

Chen, P., L. Zhao, and T. Jordan. 2007b. Full 3D tomography for the crustal structure of the Los Angeles region. *Bulletin of the Seismological Society of America* 97 (4): 1094–1120.

Dahlen, F., S. Hung, and G. Nolet. 2000. Fréchet kernels for finite-frequency traveltimes-I. Theory. *Geophysical Journal International* 141: 157–174.

Dasios, A., C. McCann, T.R. Astin, D.M. McCann, and P. Fenning. 1999. Seismic imaging of the shallow subsurface, shear-wave case histories. *Geophysical Prospecting* 47: 565–591.

de Cougny, H., and M.S. Shephard. 1999. Parallel refinement and coarsening of tetrahedral meshes. *International Journal for Numerical Methods in Engineering* 46 (7): 1101–1125.

Drake, H., E. Tullborg, and A.B. MacKenzie. 2009. Detecting the near-surface redox front in crystalline bedrock using fracture mineral distribution, geochemistry and U-series disequilibrium. *Applied Geochemistry* 24: 1023–1039.

Dumbser, M., and M. Käser. 2006. An arbitrary high-order discontinuous Galerkin method for elastic waves on unstructured meshes—II. The three-dimensional isotropic case. *Geophysical Journal International* 167(1): 319–336. https://doi.org/10.1111/j.1365-246x.2006.03120.x.

Dvorkin, J., and A. Nur. 1996. Elasticity of high-porosity sandstones, theory for two North Sea datasets. *Geophysics* 61: 1363–1370.

Feyen, L., J.A. Vrugt, B.O. Nuallain, J. van der Knijff, and A. De Roo. 2007. Parameter optimisation and uncertainty assessment for large- scale streamflow simulation with the lisflood model. *Journal of Hydrology* 332: 276–289.

Fichtner, A. 2011. *Full seismic waveform modeling and inversion*. Berlin: Springer/Heidelberg.

Flinchum, B.A., W.S. Holbrook, D. Rempe, S. Moon, C.S. Riebe, B.J. Carr, and M.P. Peters. 2018a. Critical zone structure under a granite ridge inferred from drilling and three-dimensional seismic refraction data. *Journal of Geophysical Research, Earth Surface* 123 (6): 1317–1343. https://doi.org/10.1029/2017JF004280.

Flinchum, B.A., W.S. Holbrook, D. Grana, A. Parsekian, B.J. Carr, J. Hayes, and J. Jiao. 2018b. Estimating the water holding capacity of the critical zone using near-surface geophysics. *Hydrological Processes*. https://doi.org/10.1002/hyp.13260.

Helgerud, M.B. 2001. *Wave speeds in gas hydrates and sediments containing gas hydrate: A laboratory and modeling study*. Ph.D. Thesis, Stanford University, Stanford, California.

Holbrook, W.S., C.S. Riebe, M. Elwaseif, J.L. Hayes, K. Basler-Reeder, D.L. Harry, A. Malazian, A. Dosseto, P.C. Hartsough, and J.W. Hopmans. 2014. Geophysical constraints on deep weathering and water storage potential in the Southern Sierra Critical Zone Observatory. *Earth Surface Processes and Landforms* 39 (3): 366–380. https://doi.org/10.1002/esp.3502.

Hung, S.H., F.A. Dahlen., and G. Nolet. 2000. Fréchet kernels for finite-frequency traveltimeséII. Examples. Geophysical Journal International 141(1): 175–203.

Hunter, J.A., S.E. Pullan, R.A. Burns, R.M. Gagne, and R.L. Good. 1984. Shallow seismic reflection mapping of the overburden–bedrock interface with the engineering seismograph; some simple techniques. *Geophysics* 49: 1381–1385. https://doi.org/10.1190/1.1441766.

Koulakov, I., T. Stupina, and H. Kopp. 2010. Creating realistic models based on combined forward modeling and tomographic inversion of seismic profiling data. *Geophysics* 75 (3): B115–B136.

Kuczera, G., and E. Parent. 1998. Monte carlo assessment of parameter uncertainty in conceptual catchment models: The metropolis algorithm. *Journal of Hydrology* 211 (1–4): 69–85.

Lee, E.J., and P. Chen. 2013. Automating seismic waveform analysis for full 3-D waveform inversions. *Geophysical Journal International* 194 (1): 572–589.

Lee, E.J., and P. Chen. 2016. Improved basin structures in Southern California obtained through full 3D seismic waveform tomography (F3DT). *Seismological Research Letters*.

Lee, E.J., P. Chen, T.H. Jordan, P.B. Maechling, M.A. Denolle, and G.C. Beroza. 2014a. Full 3D tomography for crustal structure in southern California based on the scattering integral and the adjoint wavefield methods. *Journal of Geophysical Research: Solid Earth* 119 (8): 6421–6451.

Lee, E.J., P. Chen, and T.H. Jordan. 2014b. Testing waveform predictions of 3D velocity models against two recent Los Angeles earthquakes. *Seismological Research Letters* 85 (6). https://doi.org/10.1785/0220140093.

Lichtner, P.C. 1988. The quasi-stationary state approximation to coupled mass transport and fluid-rock interaction in a porous medium. *Geochimica et Cosmochimica Acta* 52: 143–165.

Liu, Q., and J. Tromp. 2006. Finite-frequency kernels based on adjoint methods. *Bulletin of the Seismological Society of America* 96 (6): 2383–2397.

Liu, Q., and Y.J. Gu. 2012. Seismic imaging: From classical to adjoint tomography. *Tectonophysics*. https://doi.org/10.1016/j.tecto.2012.07.006.

Marquering, H., F.A. Dahlen., and G. Nolet. 1999. Three-dimensional sensitivity kernels for finite-frequency traveltimes: The banana-doughnut paradox. Geophysical Journal International 137(3): 805–815.

Mishra, O.P., and D. Zhao. 2003. Crack density, saturation rate and porosity at the 2001 Bhuj, India, earthquake hypocenter: A fluid-driven earthquake? *Earth and Planetary Science Letters* 212 (3): 393–405.

Moos, D., and M.D. Zoback. 1983. In situ studies of velocity in the fractured crystalline rocks. *Journal Geophysical Research* 88: 2345–2358.

Nur, A., G. Mavko, J. Dvorkin, and D. Galmudi. 1998. Critical porosity: A key to relating physical properties to porosity in rocks. *The Leading Edge* 17 (3): 357–362. https://doi.org/10.1190/1.1437977.

O'Connell, R.J., and B. Budiansky. 1974. Seismic velocities in dry and saturated cracked solids. *Journal Geophysical Research* 79: 5412–5426.

Paige, C.C., and M.A. Saunders. 1982. LSQR: An algorithm for sparse linear equations and sparse least squares. *Association for Computing Machinery ACM Transactions on Mathematical Software* 8: 43–71.

Parsekian, A.D., K. Singha, B.J. Minsley, W.S. Holbrook, and L. Slater. 2015. Multiscale geophysical imaging of the critical zone. *Reviews of Geophysics* 53: 1–26. https://doi.org/10.1002/2014RG000465.

Pasquet, S., W.S. Holbrook, B.J. Carr, and K.W.W. Sims. 2016. Geophysical ima- ging of shallow degassing in a Yellowstone hydrothermal system. *Geophysical Research Letters* 43: 12027–12035. https://doi.org/10.1002/2016GL071306.

Pickett, G.R. 1963. Acoustic character logs and their applications in formation evaluation. *Journal of Petroleum Technology* 15: 650–667.

Riebe, C.S., and J. Chorover. 2013. *Report on drilling, sampling, and imaging the depths of the critical zone, an NSF workshop*.

Scholz, C.H., L.R. Sykes, and Y.P. Aggarwal. 1973. Earthquake prediction: A physical basis. *Science* 181: 803–809.

Stallard, R.F., and J.M. Edmond. 1983. Geochemistry of the Amazon 2: The influence of geology and weathering environment on the dissolved-load. *Journal of Geophysical Research—Oceans and Atmospheres* 88: 9671–9688.

Takei, Y. 2002. Effects of pore geometry on Vp/Vs: From equilibrium geometry to crack. *Journal of Geophysical Research* 107. https://doi.org/10.1029/2001jb000522.

Tarantola, A. 1988. Theoretical background for the inversion of seismic waveforms, including elasticity and attenuation. *Pure and Applied Geophysics* 128 (1/2): 365–399.

Tape, C., Q. Liu, A. Maggi, and J. Tromp. 2009. Adjoint tomography of the Southern California crust. *Science* 325 (5943): 988–992. https://doi.org/10.1126/science.1175298.

Toksoz, M.N., C.H. Cheng, and A. Timur. 1976. Velocities of seismic waves in porous rocks. *Geophysics* 41: 621–645.

Toro, E.F., and V.A. Titarev. 2002. Solution of the generalized Riemann problem for advection-reaction equations. *Proceedings of the Royal Society of London* 458: 271–281.

Tromp, J., C. Tape, and Q. Liu. 2005. Seismic tomography, adjoint methods, time reversal and banana-doughnut kernels. *Geophysical Journal International* 160: 195–216.

Vrugt, J.A., H.V. Gupta, W. Bouten, and S. Sorooshian. 2003. A shuffled complex evolution metropolis algorithm for optimization and uncertainty assessment of hydrologic model parameters. *Water Resources Research* 39 (8): 1.1–1.16.

Wang, W., P. Chen, I. Keifer, K. Dueker, E. Lee, D. Mu, J. Jiao, Y. Zhang, and B. Carr. 2019a. Weathering front under a granite ridge revealed through full-3D seismic ambient-noise tomography. *Earth and Planetary Science Letters*. (in press).

Wang, W., Chen, P., Keifer, I., Dueker, K., Lee, E., Mu, D., Jiao, J., Zhang, Y., and Carr, B. 2019b. *Critical zone structure and saprolite water storage capacity under a granite terrain obtained from full-3D seismic ambient-noise tomography*. (under review).

Xing, H., W. Yu, and J. Zhang. 2009. *II. 3D mesh generation in geocomputing*. Lecture Notes in Earth Sciences, vol. 119, 27–64. Berlin, Heidelberg: Springer. https://doi.org/10.1007/978-3-540-85879-9_2.

Zhang, Z., Y. Shen., and L. Zhao. 2007. Finite-frequency sensitivity kernels for head waves. Geophysical Journal International 171(2): 847–856.

Zhao, D., H. Kanamori, H. Negishi, and D. Wiens. 1996. Tomography of the source area of the 1995 Kobe earthquake: Evidence for fluids at the hypocenter? *Science* 274 (5294): 1891.

Zhao, D., and T. Mizuno. 1999. Crack density and saturation rate in the 1995 Kobe earthquake region. *Geophysical Research Letters* 26: 3213–3216.

Zhao, L., T.H. Jordan., and C.H. Chapman. 2000. Three-dimensional Fréchet differential kernels for seismicdelay times. Geophysical Journal International 141(3): 558–576.

Zhao, L., P. Chen, and T.H. Jordan. 2006. Strain Green's tensors, reciprocity, and their applications to seismic source and structure studies. Bulletin of the Seismological Society of America 96(5): 1753–1763.

Zhao, L., T. Jordan, K. Olsen, and P. Chen. 2005. Frechet kernels for imaging regional earth structure based on three-dimensional reference models. *Bulletin of the Seismological Society of America* 95 (6): 2066–2080. https://doi.org/10.1785/0120050081.

Zimmer, M., M. Prasad, and G. Mavko. 2002. Pressure and porosity influences on Vp/Vs ratio in unconsolidated sands. *The Leading Edge* 21.

Chapter 9
Self-correcting Estimate of Earthquake Death Toll Based on Field Reports: The April 25, 2015, Nepal, Earthquake

Tengfei Ma, Zhongliang Wu and Yingchun Li

Abstract Uncertainty in the estimate of earthquake death toll is one of the most important concerns in the rescue and relief actions after a disastrous earthquake. Such uncertainty was especially evident after the April 25, 2015, Nepal, great earthquake, after which the estimate had to be modified for many times. The modification is basically based on the revision of earthquake parameters and intensity parameters. In this paper, using a simple model, we discuss a self-correcting method for the estimate of earthquake death toll. The method is based on the modeling of the field reports of found fatalities from the news media. We applied the estimate and its ongoing updating to the situation of the Nepalese earthquake. As an improvement of the previous model, we discussed the role of the very early reports and used the model by eliminating the very early data. The result shows that this 'dynamic' estimate can act as a complement of other 'static' estimates.

Keywords The 2015 Nepal earthquake · Earthquake fatality estimate · Rescue and relief · Reports from the field

9.1 Introduction

Saving life is the most critical concern of earthquake emergency and rescue. A correct estimate of the earthquake fatalities helps much to the deploying and adjusting of the task forces for rescue and relief actions. Previous works on the estimate of earthquake death toll mainly focused on the relation with the magnitude of an

T. Ma
Institute of Geophysics, China Earthquake Administration, Beijing 100081, China

ChinaRe, Beijing 100081, China

Z. Wu (✉)
Institute of Earthquake Forecasting, China Earthquake Administration, Beijing 100081, China
e-mail: wuzl@cea-igp.ac.cn

Y. Li
Jiangsu Earthquake Agency, Nanjing, China

Y.-G. Li (ed.), *Earthquake and Disaster Risk: Decade Retrospective of the Wenchuan Earthquake*, https://doi.org/10.1007/978-981-13-8015-0_9

earthquake or intensity distribution, with the consideration of exposures and vulnerability (Ashkenazi et al. 2005; Badal et al. 2005; Gutiérrez et al. 2005; Jaiswal and Wald 2010a, b; Koshimura et al. 2006; Lamontagne 2008; Lomnitz 1970; Ohta et al. 1993; Samardjieva and Badal 2002; Samardjieva and Oike 1992; Spence et al. 2011; Tsai et al. 2001; Wyss 2005). Several public, governmental, or commercial agencies, such as the U.S. Geological Survey (USA), the China Earthquake Administration (China), and the WAPMERR (World Agency for Planetary Monitoring and Earthquake Risk Reduction) agency (Switzerland), provide such (open or internal) information service shortly after an earthquake.

For the real earthquake cases, many factors such as site condition, heterogeneity of intensity distribution, status of infrastructure and economy, and capability of local community for emergency response all contribute to the uncertainty of such database-based estimate. After the great earthquake in Nepal on April 25, 2015, the estimate had to be modified for many times with more information coming in. In such modification, the basic rational is the variation of the parameters in the database. A question is whether it is possible to develop a self-correcting method for the ongoing updating of the estimate, using the feedback from the field.

9.2 The Model and Its Variation

Studies on previous earthquakes found that the temporal variation of fatalities reported after an earthquake and/or an earthquake-generated tsunami has regularity as described by a simple model and/or its variation (Gao and Jia 2005; Li et al. 2011; Liu and Wu 2005; Liu et al. 2005; Wu et al. 2009; Yang et al. 2011; Zhao et al. 2008). The simplest model gives that the reported number of deaths at time t, $N(t)$ can be represented by

$$N(t) = N_0[1-\exp(-\alpha t)] \tag{9.1}$$

In which N_0 and α are constants. Such a relationship can be understood by taking the time derivative of both sides:

$$\mathrm{d}N/\mathrm{d}t = \alpha(N_0-N) \tag{9.2}$$

In which term $\mathrm{d}N/\mathrm{d}t$ on the left-hand side is the rate of discovering dead bodies, and term $(N_0 - N)$ on the right-hand side is the dead bodies that remain undiscovered. The constant N_0 is the final death toll, which is of the most importance in the estimate. Proportional relation between the two quantities, $\mathrm{d}N/\mathrm{d}t$ and $(N_0 - N)$, is a natural outcome in rescue operation, that the more bodies of deaths remained to be discovered, the higher the probability for the rescue team to discover them. The coefficient α reflects the efficiency of the rescue practice. Earthquake cases show that $\log(\alpha)$ is reversely proportional to the surface wave magnitude of the earthquake under consideration, with regional dependence (Zhao et al. 2008). This provides an

opportunity to conduct a 'dynamic' estimate of the final death toll and update the estimate with new data coming in.

9.3 The Nepal Earthquake, the Loss Estimate, and the Modification

The U.S. Geological Survey (USGS) launched the Prompt Assessment of Global Earthquakes for Response (PAGER) system in 2007, which estimate fatality and economic loss impact following significant earthquakes worldwide and provide useful, actionable information for the response communities (Jaiswal and Wald 2010a, b). After the occurrence of the *M*7.8 Nepal earthquake on April 25, 2015, the PAGER system released successively seven versions of fatalities and economic losses estimate (Marano, 2015, personal communication, see Fig. 9.1 and Table 9.1). The revisions were basically based on the modified earthquake parameters and the 'ground truth' information of intensity. The latest estimate of the PAGER system was created about 9 days after the earthquake, stating that there would be probably 1000–10,000 fatalities in total. In the same day, news reports gave that the found deaths accounted 7,000. As stated by Wyss (2015, personal communication), poor information provided from the local agencies prevented from an accurate estimate of the losses.

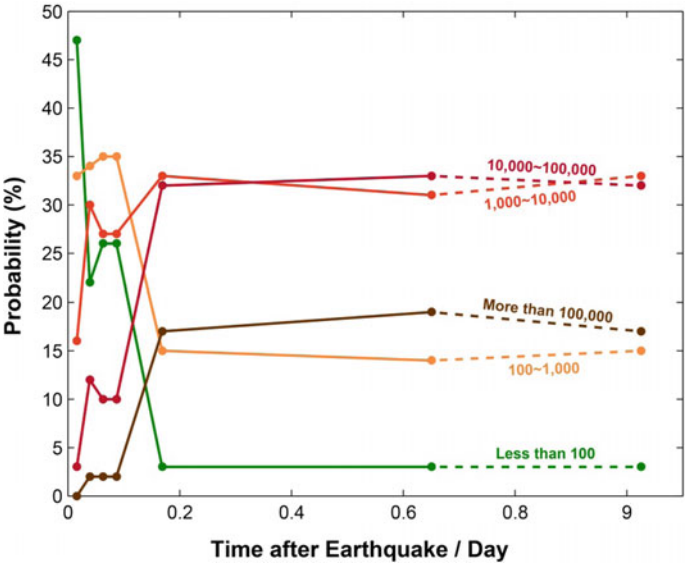

Fig. 9.1 Temporal variation of probabilities of the earthquake death toll, estimated by the USGS PAGER system, for the Nepal earthquake on April 25, 2015. The part of the dashed line uses a different time scale. *Source* http://earthquake.usgs.gov/earthquakes/pager/events/us/20002926/index.html

Table 9.1 Released PAGER estimates of the death toll for the Nepalese earthquake (courtesy of Dr. Kristin Marano)

Version	Time	Probability					Notes on the new data for the revision
		Less than 100 (%)	100–1000 (%)	1000–10,000 (%)	10,000–100,000 (%)	More than 100,000 (%)	
V 1.0	23 min	47	33	16	3	0	'Pending' (heads-up) alert
V 2.0	56 min	22	34	30	12	2	'Pending' (heads-up) alert
V 3.0	1 h, 30 min	26	35	27	10	2	Released widely and online
V 4.0	2 h, 5 min	26	35	27	10	2	Revised magnitude (to M7.8); Some reported intensities
V 5.0	4 h, 3 min	3	15	33	32	17	Fault dimension estimate added; …More reported intensity added
V 6.0	15 h, 36 min	3	14	31	33	19	Revised fault dimensions added; Reported intensities revised
V 7.0	1 week, 2 days	3	15	33	32	17	Revised fault dimension; Add station in Kathmandu; Add assigned intensities at key locations

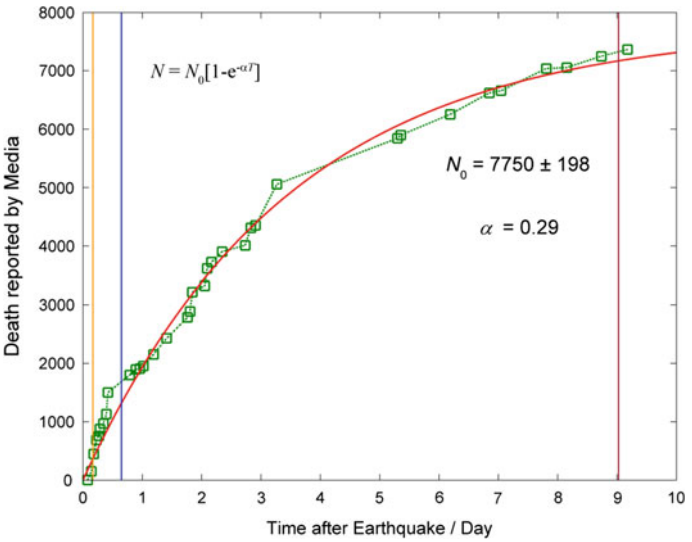

Fig. 9.2 Reported fatalities varying with time and fitting of the data to estimate the final death toll using Eq. (9.1). The yellow line represents the release time of version 5.0 of the USGS PAGER estimate, which gave that the total fatalities would be 1000–10,000 most likely. The blue line represents the release time of version 6.0 of the USGS PAGER estimate, which stated that the total fatalities would rise to 10,000–100,000 most likely. On May 5, 2015, the USGS PAGER system released version 7.0 estimate that the final death toll would be 1000–10,000 (the dark red line)

The Nepal earthquake highlighted the difficulty of the estimation which is based on databases and empirical relations between the fatalities and earthquake/intensity parameters.

9.4 The Self-correcting Estimate

After the Nepal earthquake, news media such as BBC and Sina News launched the special live web pages which collected and reported the news related to the deaths found by the rescue teams from a variety of resources. Figure 9.2 shows the report from those multiple media sources collected continuously after the earthquake (Table 9.2). For those reports in the form 'the death toll is at least X,' X is simply taken as the value of data at that moment. By fitting the data using Eq. (9.1), the parameters N_0 and α can be obtained. Shown in Fig. 9.2 is an example of the fitting that based on the data 9.5 days after the earthquake when the reported deaths are 7365, the estimate gives that the final death toll would be around 7750 $\pm$ 198. The rescue efficiency coefficient α is 0.29, falling into the empirical relation from previous earthquakes (Zhao et al. 2008).

Table 9.2 List of reported fatalities at different time and the estimated final death toll based on the data up to the time

Date	Time (UTC)	Fatalities reported	Source	Estimation with free α	Deviation	α calculated	Estimation (fixed $\alpha = 0.3$)	Deviation
2015/04/25	08:04	2	RT					
2015/04/25	09:35	150	CNN					
2015/04/25	10:32	449	Reuters					
2015/04/25	11:39	688	Reuters					
2015/04/25	12:35	758	Reuters					
2015/04/25	13:02	876	AFP	502,520	146	0.005	9314	150
2015/04/25	14:28	970	BBC	413,168	134	0.007	9481	138
2015/04/25	15:39	1130	Reuters	374,397	125	0.007	9662	129
2015/04/25	16:16	>1500	Kantipur TV	551,195	152	0.005	10,386	160
2015/04/26	01:08	>1800	The Guardian	4034	173	0.808	9584	186
2015/04/26	03:36	1896	The Guardian	3266	168	1.035	9056	198
2015/04/26	05:10	1910	AP	2956	163	1.170	8658	208
2015/04/26	06:36	1953	AFP	2809	158	1.249	8363	213

(continued)

Table 9.2 (continued)

Date	Time (UTC)	Fatalities reported	Source	Estimation with free α	Deviation	α calculated	Estimation (fixed $\alpha = 0.3$)	Deviation
2015/04/26	10:42	2152	AP	2784	152	1.265	8082	220
2015/04/26	16:03	2430	CCTV	2914	149	1.182	7833	225
2015/04/27	00:30	2789	CCTV	3189	152	1.029	7569	233
2015/04/27	01:30	2889	CCTV	3381	152	0.942	7432	232
2015/04/27	02:26	3218	AFP	3773	173	0.802	7457	226
2015/04/27	07:25	3326	BBC	4071	176	0.717	7420	221
2015/04/27	08:25	3617	AP	4558	193	0.610	7470	219
2015/04/27	10:11	3726	Xinhua	5023	202	0.532	7514	217
2015/04/27	14:28	3904	Xinhua	5508	206	0.468	7543	214
2015/04/27	23:48	>4010	AFP	5568	201	0.461	7490	212
2015/04/28	02:06	4310	AFP	5951	201	0.420	7495	208
2015/04/28	03:59	>4352	AP	6170	199	0.399	7493	204
2015/04/28	12:37	5057	AFP	7153	214	0.325	7564	214
2015/04/30	13:23	5844	AFP	7093	210	0.329	7528	211
2015/04/30	14:45	>5900	CNS	7118	206	0.328	7507	208

(continued)

Table 9.2 (continued)

Date	Time (UTC)	Fatalities reported	Source	Estimation with free α	Deviation	α calculated	Estimation (fixed $\alpha = 0.3$)	Deviation
2015/05/01	10:42	6254	Xinhua	7180	203	0.323	7495	204
2015/05/02	02:33	6621	AFP	7330	202	0.314	7507	202
2015/05/02	07:13	6659	Xinhua	7401	199	0.309	7515	199
2015/05/03	01:33	7040	AP	7542	201	0.300	7544	201
2015/05/03	09:51	7056	Xinhua	7608	199	0.296	7562	200
2015/05/03	23:48	7250	CNN	7684	199	0.291	7586	202
2015/05/04	10:25	7365	RUVR	7750	198	0.287	7610	204

Note The origin time of the Nepal earthquake is 06:11:26.0 (UTC)

Due to the properties of Eq. (9.1), the earlier the time, the more difficult for the fitting to obtain a correct estimate. As shown in Table 9.2, the early estimate based on the fitting with free α could not get a stable and reasonable estimate. To remedy this problem, taking into account the previous experiences (e g., Li et al. 2011), for the early estimate, we firstly take a fixed α based on the empirical relation with the magnitude of the earthquake. In the case of the Nepal earthquake with surface wave magnitude 7.8, the fixed α is taken as 0.3.

9.5 The Role of Very Early Data in the Self-correcting Estimate

After the occurrence of an earthquake, the rescue force cannot start the operation instantly, and little information is known about the stricken areas, then a period of 'recue vacuum' at the first several hours immediately after the occurrence of the earthquake is to much extent inevitable. With more and more information available, the 'black box' of the disastrous region may be illuminated gradually. Related to this phenomenon, Eq. (9.1) is not an appropriate description of the temporal variation of reported deaths at the very early stage (Yang et al. 2011), due to the entanglement of two factors, the finding of deaths by the rescue team, and the preparatory stage, or the 'pre-heating,' of the rescue action. If this very early stage plays an important role in the whole curve, then the fitting by Eq. (9.1) is naturally problematic. Considering this feature, we tried the estimate by eliminating the first N data, where N is somehow arbitrarily taken as 9 in Table 9.3 (which means the 'pre-heating time' is assumed to be 12 h). Actually, there is a trade-off of different factors in the fitting. On one hand, eliminating the first N data points (or the data of the first 12 h) may enhance the stability of the fitting, thus improves the accuracy of the estimate. On the other hand, eliminating the very early stage makes the estimate to need longer time for getting enough data, thus reduces the timing characteristics of the estimate.

9.6 Conclusions and Discussion

Uncertainty in the estimate of earthquake death toll is determined by many complicated factors. As a result, the modification of the estimate seems to be an inevitable stage for almost all the agencies providing information for earthquake emergency and rescue actions. Such uncertainty, and the resulted difficulty of the modification, was especially the case of the April 25, 2015, Nepal, great earthquake. To overcome such difficulty, in this paper, we discussed a 'self-correcting' method for the estimation of earthquake death toll and the ongoing updating of such estimate. The method is based on a simple model of the temporal variation of found deaths. The input data is the reported found deaths from the field. The approach highlights the role of the

Table 9.3 List of reported fatalities at different time and the estimated final death toll, with the data of the first 12 h removed

Date	Time (UTC)	Fatalities reported	Source	Estimation with fixed $\alpha = 0.3$ eliminating the first 9 data	Deviation	Estimation with free α eliminating the first 9 data	Deviation	α calculated
2015/04/25	08:04	2	RT					
2015/04/25	09:35	150	CNN					
2015/04/25	10:32	449	Reuters					
2015/04/25	11:39	688	Reuters					
2015/04/25	12:35	758	Reuters					
2015/04/25	13:02	876	AFP					
2015/04/25	14:28	970	BBC					
2015/04/25	15:39	1130	Reuters					
2015/04/25	16:16	>1500	Kantipur TV					
2015/04/26	01:08	>1800	The Guardian					
2015/04/26	03:36	1896	The Guardian					
2015/04/26	05:10	1910	AP					
2015/04/26	06:36	1953	AFP	7853	113	2170	11	2.259
2015/04/26	10:42	2152	AP	7664	130	2529	35	1.527
2015/04/26	16:03	2430	CCTV	7495	141	3086	56	1.043
2015/04/27	00:30	2789	CCTV	7300	161	3610	66	0.805

(continued)

Table 9.3 (continued)

Date	Time (UTC)	Fatalities reported	Source	Estimation with fixed $\alpha = 0.3$ eliminating the first 9 data	Deviation	Estimation with free α eliminating the first 9 data	Deviation	α calculated
2015/04/27	01:30	2889	CCTV	7213	158	3869	70	0.724
2015/04/27	02:26	3218	AFP	7280	157	4605	124	0.564
2015/04/27	07:25	3326	BBC	7273	148	5040	125	0.497
2015/04/27	08:25	3617	AP	7348	156	6008	151	0.393
2015/04/27	10:11	3726	Xinhua	7411	161	6959	160	0.326
2015/04/27	14:28	3904	Xinhua	7454	160	7801	160	0.283
2015/04/27	23:48	>4010	AFP	7413	159	6949	158	0.328
2015/04/28	02:06	4310	AFP	7429	154	7279	154	0.309
2015/04/28	03:59	>4352	AP	7434	149	7382	149	0.303
2015/04/28	12:37	5057	AFP	7514	174	8696	167	0.245
2015/04/30	13:23	5844	AFP	7485	171	7490	171	0.300
2015/04/30	14:45	>5900	CNS	7470	168	7385	167	0.306
2015/05/01	10:42	6254	Xinhua	7462	163	7370	163	0.307
2015/05/02	02:33	6621	AFP	7479	161	7480	161	0.300
2015/05/02	07:13	6659	Xinhua	7490	158	7527	158	0.297
2015/05/03	01:33	7040	AP	7522	164	7652	161	0.290
2015/05/03	09:51	7056	Xinhua	7542	164	7705	159	0.287
2015/05/03	23:48	7250	CNN	7568	168	7770	159	0.283
2015/05/04	10:25	7365	RUVR	7594	173	7827	159	0.279

news media and the internet in assisting the earthquake rescue and relief actions. In using this method, therefore, the nature and limits of information from the news media as well as the Internet, which depends on the infrastructure of communication and the openness of the society, have to be taken into consideration. In this sense, this 'dynamic' approach is to be used as a complement, rather than a substitute, of other ('static') approaches.

Additionally, considering the lessons of the 2004 Sumatra earthquake and the Indian Ocean tsunami (Liu et al. 2005), it has to be cautioned in the meantime that there exists a possibility that the curve has an abrupt change due to the complicated situations related to local rescue actions. For instance, in the Nepalese earthquake, a possible scenario is that in some stricken areas, the actual conditions may ill-informed in the early stage due to the poor transportation, and the number of fatalities may increase abruptly as rescue workers reach mountain villages. On the other hand, however, this situation can also be resolved by the method, since in principle the method is 'self-correcting.'

Acknowledgements Thanks are due to Dr. Kristin Marano and Prof. Max Wyss for personal communications on the products of the estimate.

References

Ashkenazi, I., B. Isakovich, Y. Kluger, R. Alfici, B. Kessel, and O.S. Better. 2005. Prehospital management of earthquake casualties buried under rubble. *Prehospital and Disaster Medicine* 20: 122–133. https://doi.org/10.1017/S1049023X00002302.

Badal, J., M. Vázquez-prada, and Á. González. 2005. Preliminary quantitative assessment of earthquake casualties and damages. *Natural Hazards* 34: 353–374. https://doi.org/10.1007/s11069-004-3656-6.

Gao, J.G., and Y. Jia. 2005. A study on the time of promulgating earthquake disaster—An index of earthquake rescue ability. *Journal of Catastrophology* 32–36.

Gutiérrez, E., F. Taucer, T. De Groeve, D.H.A. Al-Khudhairy, and J.M. Zaldivar. 2005. Analysis of worldwide earthquake mortality using multivariate demographic and seismic data. *American Journal of Epidemiology* 161: 1151–1158. https://doi.org/10.1093/aje/kwi149.

Jaiswal, K., and D. Wald. 2010a. An empirical model for global earthquake fatality estimation. *Earthquake Spectra* 26: 1017–1037. https://doi.org/10.1193/1.3480331.

Jaiswal K.S., and D.J. Wald. 2010b. Development of a semi-empirical loss model within the USGS Prompt Assessment of Global Earthquakes for Response (PAGER) system. In *Proceedings of the 9th US and 10th Canadian conference on earthquake engineering, reaching beyond borders*, 25–29.

Koshimura, S., T. Katada, H. Mofjeld, and Y. Kawata. 2006. A method for estimating casualties due to the tsunami inundation flow. *Natural Hazards* 39: 265–274. https://doi.org/10.1007/s11069-006-0027-5.

Lamontagne, M. 2008. Casualties directly caused by an earthquake in Canada: First contemporaneous written accounts from the M6.5 Charlevoix, Quebec, earthquake of 20 October 1870. *Bulletin of the Seismological Society of America* 98: 1602–1606. https://doi.org/10.1785/0120070227.

Li, Y.C., Z.L. Wu, and Y.Z. Zhao. 2011. Estimating the number of casualties in earthquakes from early field reports and improving the estimate with time. *Natural Hazards* 56: 699–708. https://doi.org/10.1007/s11069-010-9583-9.

Liu, Z., and Z.L. Wu. 2005. A simple model of reported casualties during earthquakes and earthquake-generated tsunamis. *Earthquake Res China* 21: 526–529.

Liu, Z., Z.L. Wu, M.J. Cai, and C.S. Jiang. 2005. Discussion on casualties during 2004 earthquake-generated tsunami in Indian Ocean. *Progress in Safety Science and Technology* 5: 2075–2077.

Lomnitz, C. 1970. Casualties and behavior of populations during earthquakes. *Bulletin of the Seismological Society of America* 60: 1309–1313.

Ohta, Y., N. Goto, and M. Ohashi. 1993. An empirical construction of equations for estimating number of victims at an earthquake. *Zisin* II: 463–466.

Samardjieva, E., and J. Badal. 2002. Estimation of the expected number of casualties caused by strong earthquakes. *Bulletin of the Seismological Society of America* 92: 2310–2322. https://doi.org/10.1785/0120010112.

Samardjieva, E., and K. Oike. 1992. Modelling the number of casualties from earthquakes. *Journal of Natural Disaster Science* 14: 17–28.

Spence, R.J., C. Scawthorn, and E. So. 2011. *Human casualties in earthquakes: Progress in modelling and mitigation*. Amsterdam: Springer Science & Business Media.

Tsai, Y.-B., T.-M. Yu, H.-L. Chao, and C.-P. Lee. 2001. Spatial distribution and age dependence of human-fatality rates from the Chi-Chi, Taiwan, earthquake of 21 September 1999. *Bulletin of the Seismological Society of America* 91: 1298–1309. https://doi.org/10.1785/0120000740.

Wu, X.Y., J.H. Gu, and H.Y. Wu. 2009. A modified exponential model for reported casualties during earthquakes. *Acta Seismol Sin* 31: 457–463.

Wyss, M. 2005. Human losses expected in Himalayan earthquakes. *Natural Hazards* 34: 305–314. https://doi.org/10.1007/s11069-004-2073-1.

Yang, X.L., Z.L. Wu, and Y.C. Li. 2011. Using Internet reports for early estimates of the final death toll of earthquake-generated tsunami: the March 11, 2011, Tohoku, Japan, earthquake. *Annuls of Geophysics* 54: 674–679.

Zhao Y.Z., Z.L. Wu, and Y.T. Li. 2008. Casualty in earthquake and tsunami disasters: internet-based monitoring and early estimation of the final death toll. In *Proceedings of the 14th world conference on earthquake engineering (WCEE)*, Beijing, Paper ID 09-01-0044.

Correction to: Earthquake and Disaster Risk: Decade Retrospective of the Wenchuan Earthquake

Yong-Gang Li

Correction to:
Y.-G. Li (ed.), *Earthquake and Disaster Risk: Decade Retrospective of the Wenchuan Earthquake,*
https://doi.org/10.1007/978-981-13-8015-0

The original version of the book was inadvertently published with an incorrect figure in Chapters 2, 3 and 6. Figures 2.2, 3.1 and 6.1 have been replaced with the correct figure in the updated version.

The updated versions of these chapters can be found at
https://doi.org/10.1007/978-981-13-8015-0_2
https://doi.org/10.1007/978-981-13-8015-0_3
https://doi.org/10.1007/978-981-13-8015-0_6

Y.-G. Li (ed.), *Earthquake and Disaster Risk: Decade Retrospective of the Wenchuan Earthquake*, https://doi.org/10.1007/978-981-13-8015-0_10